UNIVERSITY OF
LIVERPOOL

Search for Non-Prompt Photons in a Diphoton and Large Missing Transverse Momentum Final State at the ATLAS Detector

Thesis submitted in accordance with the requirements of
the University of Liverpool for the degree of Doctor in Philosophy
by

Allan Kenneth Lehan

September 2015

Abstract

A search for non-prompt photons in diphoton events with large missing transverse energy at the ATLAS detector is presented in this thesis. This search was performed using data collected from proton-proton collisions provided by the Large Hadron Collider at CERN at two energies: 4.8 fb^{-1}collected at a center of mass energy of 7 TeV in 2011 and 20.3 fb^{-1}collected at a center of mass energy of 8 TeV in 2012.

The theoretical motivation for this search lies in the Gauge Mediated Symmetry Breaking models in which the lightest neutralino can be long-lived and decay to a photon and a gravitino, which is stable and the source of missing transverse momentum in these models. The photons produced in these decays have two unique properties due to the finite lifetime of the neutralino: they will not point back to the primary collision vertex and they will arrive at the electromagnetic calorimeter delayed compared to promptly produced photons. These two signatures were used to search for non-prompt photons in a simplified model in which the only two free parameters are the lifetime of the neutralino and the effective supersymmetry breaking scale, corresponding to the mass of the neutralino. In the two datasets, no significant excess over the Standard Model predictions was observed. These results were used to set exclusion limits on the lifetime and mass of the lightest neutralinos at the 95% confidence level: neutralinos with lifetimes varying from 250 ps to 50 ns in the mass range of 95 GeV to 240 GeV were excluded by the 7 TeV analysis, neutralinos with lifetimes varying from 250 ps to 100 ns in the mass range of 120 GeV to 440 GeV were excluded by the 8 TeV analysis.

Acknowledgements

I would first like to acknowledge that the work presented in this thesis would not have been possible without the thousands of people who contributed to the design, build, and running of the LHC and ATLAS. The analyses presented were also developed as part of a team of researchers, who I feel lucky to have worked with, and have been documented in two published research papers[1][2].

I would like to thank all of the staff at the University of Liverpool for the support they have provided over the last four years. A special thanks has to go to my supervisors, Dr Sergey Burdin and Dr Helen Hayward, who have provided me with invaluable support and guidance at all stages of the PhD, I couldn't have asked for better supervisors.

I have met many amazing people over the course of this PhD that have helped make it feel less like an education and more like an adventure. A special mention goes to Adrian and Matt, I'll never forget our USA road trip, and to Chris, for keeping me topped up with the three "W"s (Wine, Whisky, and the Wire) at CERN.

On a personal level, I would like to the opportunity to name-drop my family (Dave, Shirley, Jon and Laura) and thank them, and my extended family, for their unconditional love and support and for putting up with me over the years. All of my friends deserve their own individual thanks, for many different reasons, but I will have to limit it to Gav and Will, for dealing with me on a day to day basis, and also to Justin and the Pineapples.

My final thanks is reserved for Jen, who's love and support has been invaluable during the final stages of this PhD and has shown me that my life after this PhD will be better than I ever imagined.

Finally, during the last four years I have only one regret, that we failed to win the Bubble Chamber.

Contents

List of Figures

List of Tables

Chapter 1

Introduction

The Standard Model of particle physics combines the theoretical framework of electroweak interactions, Quantum Chromodynamics, and the Brout-Englert-Higgs mechanism into a model that has been the foundation of particle physics since the experimental confirmation of quarks in deep inelastic scattering experiments at the Stanford Linear Accelerator in 1968 [3][4]. In the following decades, it successfully predicted the existence of every known elementary particle and hundreds of composite particles. It has also been remarkably successful at predicting the experimental results obtained at particle physics experiments; the discovery that neutrinos are not massless is the only experimentally confirmed [5, 6] result that disagrees with the SM prediction. There are, however, many observations that suggest that the Standard Model is not a complete description of nature but in fact a low energy approximation. These include: the lack of a dark matter candidate (see section 2.1.2), the hierarchy problem (see section 2.1.2), the inability to explain the extent of the matter anti-matter asymmetry in the Universe [7], and the absence of gravity in the model.

An elegant solution to the limitations of the Standard Model are found in the Supersymmetry (SUSY) models which predict the existence of a new family of particles that are partners to the Standard Model particles. SUSY contains a number of parameters that have yet to be constrained, leading to a number of different models. One such model is Gauge Mediated Symmetry Breaking (GMSB) where the lightest neutralino can be long lived and travel away from the primary vertex before decaying to a photon and a gravitino, which is a dark matter candidate. The long lifetime of the neutralino leads to

(non-prompt) photons having two unique properties that photons produced in prompt decays would not be expected to have: the shower in the electromagnetic calorimeter will not point back to the primary collision vertex (i.e. photons are non-pointing), and a non-prompt photon will arrive at the electromagnetic delayed compared to a prompt photon.

This thesis describes two analyses looking for evidence of GMSB with long-lived neutralinos decaying to a photon and a gravitino. These searches were performed using data from proton-proton (pp) collisions collected by the ATLAS collaboration at centre of mass energies of $\sqrt{s} = 7$ TeV and $\sqrt{s} = 8$ TeV (hereafter referred to as the 7 TeV analysis and the 8 TeV analysis). These analyses closely follow the strategy of a similar search for GMSB in a signal region consisting of final states containing two photons and a large amount of missing energy, where the neutralino decays promptly to a photon and gravitino [8] (hereafter referred to as the prompt analysis). One complication in these analyses is that it is not possible to estimate the number of background events in the signal region. The analyses presented in this thesis exploit the fact that the non-pointing and delayed timing distributions of non-prompt photons, from the decay of long-lived neutralinos, are different to those expected for background events in the signal region to extract limits on the number of observed signal events.

The structure of this thesis attempts to mirror the development of the analyses presented within. The theoretical concepts and arguments that justify these searches for GMSB in events with diphoton final states and a large amount of missing transverse energy are presented in chapter 2. This includes: an overview of the Standard Model and some of its limitations, an overview of SUSY and why it is an attractive theory, and details of the simplified GMSB model used in these analyses. The data used in this thesis to search for GMSB is collected by the ATLAS detector using pp collisions provided by the Large Hadron Collider (LHC); the design of both of these machines is described in chapter 3. In the ATLAS detector, the information from a number of different sub-detectors needs to be combined so that particles can be reconstructed and identified: this process is described in chapter 4. Signal Monte Carlo (MC) that has been produced with the expected kinematic properties of GMSB events is introduced in chapter 5. This MC allows the non-pointing and delayed timing nature of non-prompt photons to be investigated, and the potential impact this has on identification of non-prompt photons and the efficiency of events making it into the signal region to be studied. In

chapter 6, the pp data that was used in this thesis is introduced. In addition to the data in the signal region, it is separated into different control samples that are used to test the non-pointing and delayed timing distributions of non-prompt photons and model these in the expected background events. The method for fitting the signal and background distributions to those observed in the signal region is described in chapter 7. This is used to obtain the number of signal events and to set exclusion limits in the GMSB parameter space. The systematic uncertainties that can affect the expected signal yield or the shape of the pointing and timing distributions used to determine the number of observed signal events are described in chapter 8. In chapter 9, the results in the 7 TeV and 8 TeV signal regions are unveiled and the interpretation of these results in the GMSB parameter space used in these analyses is presented. In chapter 10, a study looking at the prospects of a similar search for non-prompt photons during run 2 of the LHC, which started in June 2015 with pp collisions at $\sqrt{s} = 13$ TeV, is presented. Finally, chapter 11 presents a summary of everything that has been presented in this thesis and the conclusions that can be drawn from it.

While the work presented in this thesis is a result of the collaborative effort of a small team of researchers, the author made a number of significant contributions to each of the analyses. In the 7 TeV analysis the author lead the efforts to understand how the shower of particles, produced when a non-prompt photon interacts with the electromagnetic calorimeter, develops as photons become more non-pointing and how this shower differs from showers produced by promptly produced objects. The author was also responsible for producing the 7 TeV limit plots which can be found in section 9.1.2. In the 8 TeV analysis, the author lead all aspects of the analysis relating to the non-pointing nature of photons, developed an independent cutflow which was used to produce all data and Monte Carlo samples, developed a new lifetime reweighting method (see Appendix B), and lead the efforts to estimate the systematic uncertainties that are present in this analysis (see chapter 8).

Chapter 2

Theory

In this chapter, the theoretical models that are relevant to the search for non-prompt photons are discussed. A brief introduction to the Standard Model (SM) of particle physics is given in section 2.1, including a discussion of some of the evidence that suggests that the SM is not a complete description of nature. In section 2.2 SUSY, a proposed extension to the SM is introduced and the specifics of the Gauge Mediated Symmetry Breaking (GMSB) model that will be used to interpret the results presented in this thesis is discussed.

2.1 The Standard Model of Particle Physics

The SM of particle physics was developed in the 1960s in an attempt to make sense of, and indeed prescribe order to, the vast array of new particles that were being discovered. The structure of the theory can be found in a variety of sources such as the original work [9, 10, 11, 12, 13, 14] (including the Brout-Englert-Higgs mechanism [15, 16, 17]), dedicated reviews [18], and many articles, theses and textbooks. As such, this section will only give a brief introduction to the particles and forces of the SM before discussing the need for extensions to the SM.

Quarks		
	Charge	Mass
u	$+\frac{2}{3}$	< 2.3 MeV
d	$-\frac{1}{3}$	4.8 MeV
s	$+\frac{2}{3}$	95 MeV
c	$-\frac{1}{3}$	1.275 GeV
t	$+\frac{2}{3}$	173.21 GeV
b	$-\frac{1}{3}$	4.18 GeV

TABLE 2.1: Mass and charge of the three generations of quarks. Masses taken from PDG group site where associated uncertainties can also be found [18].

2.1.1 Particles and Forces

In nature any conserved physical parameter is due to an underlying symmetry [19]. Symmetries therefore have played an important role in the development of many important theories and the SM is no exception. The SM is a relativistic quantum field theory in which the Lagrangian must be invariant under local gauge transformations. The symmetry of the SM is described by:

$$U(1)_Y \times SU(2)_L \times SU(3)_C, \tag{2.1}$$

where $U(1)_Y$ describes quantum electrodynamics (QED), $SU(2)_L$ describes the weak interaction, and $SU(3)_C$ describes the strong interaction (quantum chromodynamics, QCD). In this formalism particles are excited states of fields and it is the interaction between fields that has been interpreted in classical mechanics as forces.

The fundamental constituents of matter are spin half particles called fermions which can be subdivided into two families: quarks (q) and leptons (l). The two lightest quarks are the up (u) and down (d) quarks which have fractional charges of $+\frac{2}{3}e$ and $-\frac{1}{3}e$ respectively and are the basic building blocks of protons and neutrons (uud and udd). The u and d are the first of three generations of quarks, with each generation consisting of two quarks. In each generation, one quark has the same electric charge as the u quark and the other the same as the d quark, as shown in table 2.1. Each quark has an antiparticle ($\overline{q}$) which is identical to the quark except that the sign of the electric charge is inverted. Quarks are confined to composite particles known as hadrons, either in baryons with two other quarks (qqq or $\overline{qqq}$) or in mesons together with an antiquark ($q\overline{q}$).

Leptons		
	Charge	Mass
ν_e	0	< 0.002 MeV
e	-1	0.511 MeV
ν_μ	0	< 0.19 MeV
μ	-1	105.66 MeV
ν_τ	0	< 18.2 MeV
τ	-1	1776.82 MeV

TABLE 2.2: Mass and charge of the three generations of leptons. Masses taken from PDG group site where associated uncertainties can also be found [18].

Bosons					
	Symbol	Force	EM Charge	Mass [GeV]	Relative Strength
gluon	g	Strong (QCD)	0	0	10^{38}
photon	γ	Electromagnetic (QED)	0	0	10^{36}
W	$W^\pm$	Weak	± 1	80.385	10^{25}
Z	Z	Weak	0	91.188	10^{25}
graviton	G	Gravitational	-	-	1
Higgs	H	–	0	125.7	–

TABLE 2.3: Fundamental properties of SM Bosons. Information taken from PDG group site [18] Note: gravitons are not included in the SM but are included here so that the relative strength of the forces can be compared to gravity.

As with quarks, leptons also exist in three generations, the lightest of which contains the electron (e) and a corresponding neutrino (ν_e). The second and third generations of the leptons are populated by heavier versions of electrons called muons (μ) and taus (τ) together with corresponding neutrinos (ν_μ and ν_τ) as shown in table 2.2. Unlike quarks, leptons have integer charge and can be found isolated in nature. By definition charged leptons are negative and antileptons positive.

The interactions between these fundamental particles (fields) are mediated by the exchange of integer spin particles known as gauge bosons. The SM bosons, along with the force they mediate, are shown in table 2.3.

There is one important caveat to add when discussing the gauge bosons in table 2.3: the photon and Z bosons are not electroweak gauge eigenstates but arise due to the electroweak symmetry being broken at low energies [16]. Before electroweak symmetry breaking there are two neutral gauge eigenstates (W^0 and B^0) which mix to form the mass eigenstates (γ and Z) observed in nature.

2.1.2 Limitations

To date, predictions made using the SM agree with experimental results from particle colliders to a remarkable degree of accuracy [20]. However, there are known limitations to the model and there are observations from other fields of study that the SM is unable to account for. The mass of the Higgs boson and dark matter are two examples of these problems that are discussed in more detail below.

The Hierarchy Problem

The discovery in 2012 by the ATLAS and CMS collaborations [21, 22] of a new boson with properties consistent with that of a SM Higgs boson is an impressive example of the predictive power of the SM. However, the mass (m_H) it was discovered at highlights an inconsistency in the theory known as the hierarchy problem. The hierarchy problem arises due the vast difference in the strength of gravity relative to the other fundamental forces (see table 2.3). More specifically, if the quantum corrections to the mass of the Higgs boson are calculated they are on the order of the Planck mass which is many orders of magnitude larger than the observed mass of 126 GeV. Full treatment of the hierarchy problem can be found in the literature (e.g. [23]), however, the correction (Δm_H) due to a fermion f with N_f repetitions and coupling λ_f to the Higgs field can be simplified to:

$$\Delta m_H^2 = N_f \frac{\lambda_f^2}{8\pi^2}\left[-\Lambda^2 + 6m_f^2 \ln\left(\frac{\Lambda}{m_f}\right) - 2m_f^2\right] + \mathcal{O}\left(\frac{1}{\Lambda^2}\right) \tag{2.2}$$

where Λ is the cutoff scale up to which the SM is a valid theory, $\lambda_f^2 = 2m_f/v^2$ and v is the vacuum expectation value of the Higgs boson. From equation 2.2 it can be seen that $\Delta m_H^2 \propto \Lambda^2$ which, assuming the SM is valid up to the Planck scale ($M_P \sim \mathcal{O}(10^{19})$ GeV), implies that Δm_H due to SM fermions should be many orders of magnitude larger than m_H. That corrections this large could be cancelled out by chance seems unnatural and led many theorists to suggest that it hints at an undiscovered symmetry in nature (see section 2.2). This symmetry suggests that there is a family of undiscovered particles whose corrections to the Higgs mass naturally protect it from these quadratic divergences. If we assume there are N_s scalar particles with trilinear ($v\lambda_s$) and quadlinear (λ_s) couplings to the Higgs boson, then the corresponding correction to m_H is given by:

$$\Delta m_H^2 = \frac{\lambda_s N_s}{16\pi^2}\left[-\Lambda^2 + 2m_s^2 \ln\left(\frac{\Lambda}{m_s}\right)\right] - \frac{\lambda_s^2 N_s}{16\pi^2} v^2 \left[-1 + 2\ln\left(\frac{\Lambda}{m_s}\right)\right] + \mathcal{O}\left(\frac{1}{\Lambda^2}\right). \quad (2.3)$$

If it is also assumed that the couplings to the Higgs boson of the SM fermions and the new scalar particles are related in such a way that $-\lambda_s = 2m_f/v^2 = \lambda_f^2$ and that $N_s = 2N_f$, then equations 2.2 and 2.3 can be combined to give:

$$\Delta m_H^2 = \frac{N_f \lambda_f^2}{4\pi^2}\left[(m_f^2 - m_s^2)\ln\left(\frac{\Lambda}{m_s^2}\right) + 3m_f^2 \ln\left(\frac{m_s}{m_f}\right)\right] + \mathcal{O}\left(\frac{1}{\Lambda^2}\right). \quad (2.4)$$

From this equation it can be seen that the Λ^2 dependence has disappeared with only a $\ln(\Lambda)$ term remaining. Therefore, even if $\Lambda \sim M_P$ the correction to the Higgs mass will be relatively small. It can also be seen that if the symmetry is exact and $m_f = m_S$, then the correction disappears completely.

Dark Matter

Dark matter is a theoretical form of non-baryonic matter that does not interact via the electromagnetic (EM) force. Evidence for the existence of dark matter originally came from observations that galaxies rotate faster than general relativity allows [24] and that the bending of light from stars and galaxies [25] can be explained by the gravitational influence of matter that cannot be seen. This matter has also been shown to be responsible for creating the large scale structure of the Universe [26], requiring a large percentage of dark matter be non-relativistic. According to recent measurements of the cosmic microwave background radiation by the Planck satellite [27] there is considerably more dark matter in the universe than ordinary matter with dark matter accounting for 26.8% of the energy density of the universe compared to only 4.9% for ordinary matter.

The favoured theory to explain this dark matter is that non-relativistic particles that interact very weakly with SM particles were produced in the early Universe. Neutrinos are the only stable SM particles that interact weakly with baryonic matter, however the relativistic nature of neutrinos mean that they cannot explain the large scale structure of the Universe and can only be responsible for a small fraction of the dark matter content. Therefore, the discovery of particles that are dark matter candidates would be a clear sign of physics beyond the SM. Searches to discover dark matter particles indirectly, in

collider experiments (see for example [28]), or directly, in dedicated experiments (see for example [29]), have so far found no conclusive evidence.

2.2 Supersymmetry

Attempts to include the SM as part of a greater symmetry [30, 31, 32, 33] would develop into the basis for a group of related theories known today as supersymmetry (SUSY). A common feature of SUSY models is that they predict the existence of a whole family of undiscovered particles that are the superpartners to the SM particles.

The analyses presented within this thesis have made every attempt to be as model independent as possible. Therefore, a detailed handling of SUSY, while insightful, is beyond the scope of this thesis. This section will provide: an introduction to SUSY, why and how the symmetry could be broken, and an introduction to the simplified SUSY model that will be used to interpret the results presented in this thesis. If a more detailed handling of SUSY is required it can be found in dedicated reviews (e.g. [34, 35, 36]) and the sources referenced in this section.

2.2.1 Basics of Supersymmetry

In SUSY models, the new symmetry is a space-time symmetry relating SM fermions and bosons to their superpartners according to:

$$\begin{aligned} Q|\text{fermion}\rangle &= |\text{boson}\rangle \\ Q|\text{boson}\rangle &= |\text{fermion}\rangle \end{aligned} \tag{2.5}$$

where the generator Q acting on fermions is responsible for the transformation of fermions into bosons and vice-versa. If the symmetry is an exact symmetry, each SM particle and its superpartner will have the same quantum numbers other than spin. The underlying mathematics allows these partner particles to be arranged in a multiplet (supermultiplet) provided the number of fermionic and bosonic degrees of freedom are

equal. This requirement can be met if a supermultiplet contains a Weyl fermion [37] with two helicity states and two real scalars.

The naming convention for the new particles predicted in SUSY has been developed to highlight the connection between the SUSY particle and its SM partner. The superpartner to SM fermions have the same name with an 's' preceding it, so the superpartner to an electron would be a selectron. For the superpartners of the SM bosons the names are postfixed with an 'ino', i.e. the partner to a W is a wino and the partner to a gluon is a gluino. The notation also highlights the connection between the SUSY and SM particles with the SUSY particle having the same symbol as the SM particle with a $\widetilde{}$ added above.

2.2.2 The Minimal Supersymmetric Standard Model

The underlying theory of SUSY can be used to construct new theories with a large number of new particles and interactions. A theory developed to contain the minimum number of new particles and interactions required to reproduce the SM, as shown in table 2.4, is called the minimal supersymmetric standard model (MSSM). In order to avoid a gauge anomaly in the electroweak gauge symmetry a separate supermultiplet giving mass to up and down type quarks is needed, requiring there to be four Higgs boson gauge eigenstates. After electroweak symmetry breaking, mixing of these gauge eigenstates leads to there being 5 spin-0 Higgs boson mass eigenstates (only the lightest of which has been discovered) as shown in table 2.5. This results in two different Higgs doublets, one coupling to up type quarks and the other to down type quarks, requiring two separate Higgs superfields. Including the two Higgs fields in the superpotential introduces the Higgs mass parameter μ, the value and sign of which is currently unknown, which is required to give Higgsinos mass. The ratio of the vacuum expectation values of the Higgs fields ($\tan\beta$) is an important parameter in SUSY models.

In the same way that the Higgs boson gauge eigenstates mix after electroweak symmetry breaking, the Higgsino and electroweak gauginos mix to form mass eigenstates. The neutral wino and the bino mix with the neutral Higgsinos to form four mass eigenstates called neutralinos ($\widetilde{\chi}^0$). The charged winos mix with the charged Higgsinos to form two positive and two negative charginos ($\widetilde{\chi}^{\pm}$). The different mass eigenstates of the neutralinos and charginos are denoted by the subscript i, running from i =1-4 for neutralinos and i =1-2 for charginos, with $i = 1$ ($\widetilde{\chi}^0_1/\widetilde{\chi}^{\pm}_1$) indicating the lightest mass eigenstate.

Supermultiplets			
Name	spin-0	spin-1/2	spin-1
squarks and quarks	$(\widetilde{u}, \widetilde{d})_L$ $\widetilde{u_R}$ $\widetilde{d_R}$	$(u, d)_L$ $\widetilde{u_R^*}$ $\widetilde{d_R^*}$	
sleptons and leptons	$(\widetilde{\nu_e}, \widetilde{e})_L$ $\widetilde{e_R}$	$(\nu_e, e)_L$ $\widetilde{e_R^*}$	
gluinos and gluons winos and W bosons bino and B boson		$\widetilde{g}$ $\widetilde{W^{\pm}}\widetilde{W^0}$ $\widetilde{B^0}$	g $W^{\pm}W^0$ B^0
Higgs and Higgsino	(H_u^+, H_u^0) (H_d^-, H_d^0)	$(\widetilde{H_u^+}, \widetilde{H_u^0})$ $(\widetilde{H_d^-}, \widetilde{H_d^0})$	

TABLE 2.4: Supermultiplet combinations of particles in the MSSM. The quark and lepton supermultiplets are only shown for the first generation. The spin 0 squarks and sleptons are complex scalars. The subscript L and R indicate that the particle is left or right handed. Adapted from table in [34].

Eigenstates		
Names	Gauge	Mass
Higgs Bosons	$\widetilde{H_u^0}, \widetilde{H_u^+}, \widetilde{H_d^0}, \widetilde{H_d^-}$	$h^0, H^0, A^0, H^{\pm}$
neutralinos	$\widetilde{B^0}, \widetilde{W^0}, \widetilde{H_u^0}, \widetilde{H_d^0}$	$\widetilde{\chi_1^0}, \widetilde{\chi_2^0}, \widetilde{\chi_3^0}, \widetilde{\chi_4^0}$
charginos	$\widetilde{W^{\pm}}, \widetilde{H_u^+}, \widetilde{H_d^-}$	$\widetilde{\chi_1^{\pm}}, \widetilde{\chi_2^{\pm}}$

TABLE 2.5: Gauge and mass eigenstates of MSSM bosons. Taken from [34].

If SUSY is a local symmetry [38, 39] then general relativity is included automatically (as supergravity [40]) requiring the existence of a supermultiplet containing a spin-2 SM graviton (G, with 2 helicity states) and its the spin-3/2 superpartner the gravitino ($\widetilde{G}$, also with 2 helicity states).

2.2.3 R-Parity Violation

In the SM, every interaction that has been observed results in the total number of leptons (L) or baryons (B) staying constant. An important consequence of this apparent conservation law is that the proton, as the lightest baryon, is stable with a lifetime of at least 10^{33} years [41]. In MSSM however, baryon and lepton violating interactions are introduced that would result in the lifetime of the proton being much shorter than observed [34, 42].

To address the problem of proton decay in SUSY models a new symmetry is introduced, called R-parity, as defined by:

$$P_R = (-1)^{3(B-L)+2s} \tag{2.6}$$

where s is the spin of the particle. From this definition it is clear the all SM particles will have $P_R = +1$ and all SUSY particles $P_R = -1$. If R-parity is a conserved quantity then this leads to two important implications:

- A SM particle must decay to an even number of SUSY particles (e.g. 2). In addition to ruling out proton decay mechanisms this will result in two SUSY decay chains if SUSY particles are produced in a collider experiment.
- A SUSY particle must decay to an odd number of SUSY particles (e.g. one SUSY particle and one SM particle). Therefore the lightest SUSY particle (LSP) in any SUSY decay chain will be stable.

A consequence of stable LSPs is that if the LSP is neutral and only interacts via the weak and gravitational forces then it will be a dark matter candidate.

2.2.4 Symmetry Breaking

If SUSY is an exact symmetry then the SUSY particles will have the same mass as their SM partner particles. To date, no SUSY particles have been observed either at the SM particle masses or at larger energies, with many searches at ATLAS and CMS failing to see any evidence of SUSY particles at energies in excess of 1 TeV [43, 44]. It must then be concluded that SUSY is not an exact symmetry at low energies. If SUSY is an exact symmetry at high energies but broken at some intermediate energy, allowing the SUSY masses to be much larger than the SM masses, then the cancellation of quantum corrections to the Higgs mass in equation 2.4 will be preserved. SUSY is broken if supersymmetric transformations of the vacuum state are no longer invariant. This results in the minimum potential energy of the vacuum having a non-zero value, as shown in figure 2.1. Soft SUSY breaking [45] models are attractive since they retain the MSSM structure with the addition of a SUSY breaking mechanism. However, when

soft SUSY breaking is included in the MSSM there are 105 free parameters [46] (masses, phases and mixing angles) that have no SM counterpart.

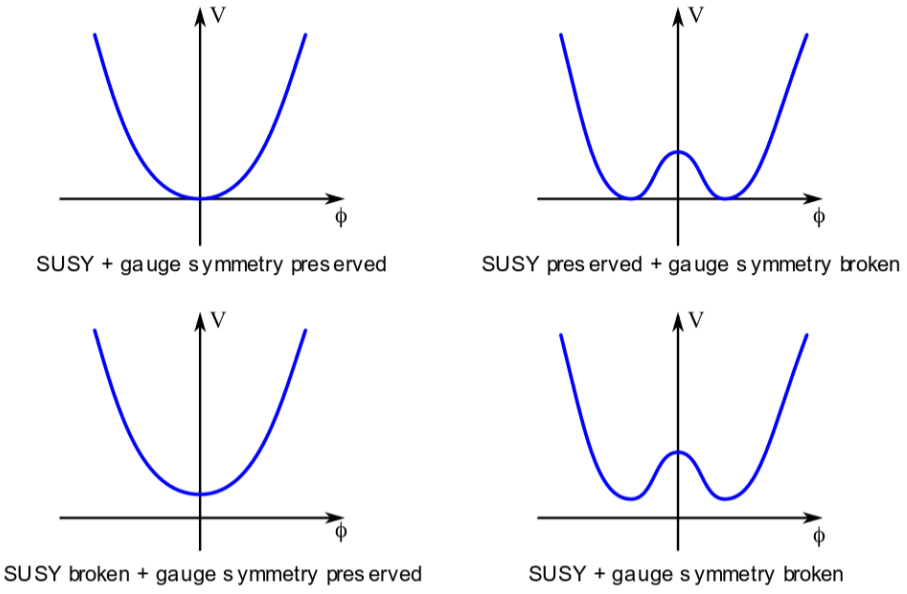

FIGURE 2.1: Various symmetry breaking scenarios: SUSY is broken, whenever the minimum potential energy, V, is non-zero. Gauge symmetry is broken whenever the potentials minimum is attained at a non-zero field configuration, ϕ, of a gauge non-singlet [47].

There are many proposed mechanisms by which SUSY could be broken, details of which can be found in the literature (e.g. [34, 35, 36]). This thesis focuses on GMSB models.

2.2.5 Gauge Mediated Symmetry Breaking

In GMSB models the SUSY breaking occurs in a hidden sector at high energies which does not couple to the MSSM sector [48]. The hidden sector contains a set of new supermultiplets and a new superpotential that leads to spontaneous supersymmetry breaking via O'Raifeartaigh models [49]. There also exists additional messenger chiral supermultiplets with N_m generations which couple to the hidden sector. The messenger particles gain mass in the hidden sector, which can be characterised by an overall mass scale (M_m) and mass splitting ($\sqrt{F}$). The messenger field transforms under the ordinary SM gauge interactions, mediating the symmetry breaking from the hidden sector to the MSSM sector via loops containing the messenger particles. SUSY gauginos receive mass

contributions in 1-loop interactions and MSSM scalars in 2-loop interactions. Due to gauge invariance in the SM, the SM gauge bosons are protected from mass corrections from the messenger particles. In minimal GMSB (mGMSB) models the soft masses of the gauginos ($\widetilde{M}_r$) and scalars ($\widetilde{m}_{\phi_i}$) are found to be defined by 3 parameters: α_r, their SM couplings; $\Lambda = F/M_m$, the effective SUSY breaking scale in the visible sector; and N_m. The masses are found to be [34]:

$$\widetilde{M}_r = \frac{\alpha_r}{4\pi}\Lambda \tag{2.7}$$

$$\widetilde{m}^2_{\phi_i} = 2\Lambda^2 \left[\left(\frac{\alpha_3}{4\pi}\right)^2 C_3(i) + \left(\frac{\alpha_2}{4\pi}\right)^2 C_2(i) + \left(\frac{\alpha_1}{4\pi}\right)^2 C_1(i) \right] \tag{2.8}$$

where $C_a(i)$ are quadratic Casimir invariants [34]. If these particles are to have masses on the order of 1 TeV, and therefore accessible at the LHC, then Λ is required to be of the order of 100 TeV.

SUSY breaking implies the existence of a goldstino fermion [50] which is absorbed by the gravitino giving it a mass of [34]:

$$m_{\widetilde{G}} = \frac{F_0}{\sqrt{3}M_P}, \tag{2.9}$$

where M_P is the Planck mass and F_0 is the fundamental symmetry breaking scale, related to symmetry breaking scale felt by the messenger sector by $C_{grav} = F_0/F$. Given that $M_P >> \sqrt{F_0}$ the gravitino will be the LSP, and therefore the dark matter candidate in any GMSB model. Having the gravitino as a dark matter candidate poses some important cosmological questions given that gravitinos would be produced with a large amount of kinetic energy and be classified as warm dark matter. While cold dark matter offers the simplest solutions to reproduce the large scale structure seen in the Universe, it has been shown that the gravitino as a warm dark matter can reproduce the large scale structure seen in the Universe [51] and be compatible with a Higgs boson with a mass of 125 GeV [52]. A warm dark matter candidate could also help explain the deficiency in the number of observed dwarf galaxies [53] and potentially explain the unidentified 3.5 keV x-ray line that has been observed in many galaxies [54].

The mGMSB models which are explored in this thesis are completely defined by six variables (sign(μ), tanβ, M_m, N_m, Λ, C_{grav}) rather than the 105 required by MSSM. An attractive feature of mGMSB models over other SUSY models with different mechanisms for symmetry breaking is that flavour changing neutral currents are naturally suppressed rather than requiring additional assumptions. This arises due to the fact that ordinary gauge interactions are blind to flavour and squarks and sleptons with the same quantum numbers are mass degenerate [55].

2.2.6 Signal Model

While mGMSB models reduce the number of free parameters that are yet to be constrained by experimental results to 6, this is still a large parameter space to explore experimentally. The Snowmass Points and Slopes [56] are a set of benchmark scenarios where either all (points) or all but one or two (slopes) of the free parameters are set at a fixed value. For the analyses presented in this thesis the SPS8 slope, which is specific to GMSB and reduces the number of free parameters to 2, is used as the signal model. All of the Snowmass Points and Slopes were originally of interest to theorists, and therefore merit experimental attention. However the SPS8 slope was chosen as the signal model for these analyses since the two free parameters in the model, Λ and C_{grav}, can result in some unique experimental signatures that will be introduced in this section and explained in more detail in chapter 5. In SPS8, the remaining four parameters needed to fully describe mGMSB set to:

$$\text{sign}(\mu) > 0,\ \tan\beta = 15,\ M_m = 2\Lambda,\ N_m = 1.$$

The relative mass of all SUSY particles in SPS8 is therefore fixed, with Λ setting the scale. This can be seen in figure 2.2 which shows the mass of SUSY particles for two different Λ values.

The fixed parameters in SPS8 are such that the next to lightest supersymmetric particle (NLSP) will always be the lightest neutralino. The Wino and Bino components of the neutralino allow a neutralino to decay to either a photon or a Z boson, which are mixtures of the SM partners to the $\widetilde{W}_0$ and $\widetilde{B}_0$, and a gravitino. The decay rate of a sparticle to its SM counterpart and a Goldstino (i.e. the gravitino) is given by [34]:

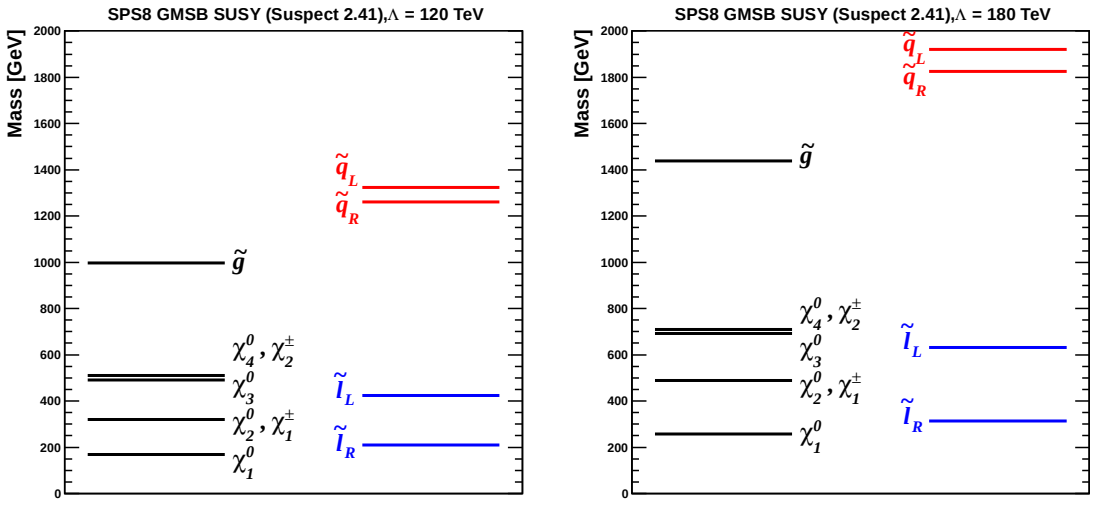

FIGURE 2.2: Spectrum of SUSY particle masses in the SPS8 GMSB model for $\Lambda = 120$ TeV (left) and $\Lambda = 180$ TeV (right) [57].

$$\Gamma\left(\widetilde{X} \to X\widetilde{G}\right) = \frac{\kappa m_{\widetilde{X}}^5}{16\pi {F_0}^2}\left(1 - \frac{m_X^2}{m_{\widetilde{X}}^2}\right)^4 \tag{2.10}$$

where κ is a mixing parameter. Which for $\widetilde{\chi_1^0} \to \gamma\widetilde{G}$ decays simplifies to:

$$\Gamma\left(\widetilde{\chi_1^0} \to \gamma\widetilde{G}\right) = \frac{\kappa m_{\widetilde{\chi_1^0}}^5}{16\pi C_{grav}^2 F^2} \tag{2.11}$$

where $F_0 = C_{grav}F$ has been substituted. The same treatment as above can be applied to the $\widetilde{\chi_1^0} \to Z^0\widetilde{G}$ decay rate resulting in a suppression factor proportional to $\left(1 - \frac{m_{Z^0}^2}{m_{\widetilde{\chi_1^0}}^2}\right)^4$ compared to the $\widetilde{\chi_1^0} \to \gamma\widetilde{G}$ decay rate. Given the large suppression factor to the $\widetilde{\chi_1^0} \to Z^0\widetilde{G}$ decay, the $\widetilde{\chi_1^0} \to \gamma\widetilde{G}$ decay is the dominant decay path accounting for approximately 85% of the branching fraction in the Λ region of interest. Note that due to the Higgsino content of the lightest neutralino, a decay to a gravitino and a neutral Higgs boson is also possible but the corresponding suppression factor for this decay is sufficiently large that the branching fraction can be safely ignored. For simplification, the analyses presented in this thesis have assumed that the branching fraction of $\widetilde{\chi_1^0} \to \gamma\widetilde{G}$ is 100%. Assuming R-parity conservation ensures that SUSY particles are produced in pairs and every SUSY event will result in a final state containing two photons and two gravitinos. A diagram of this decay chain is shown in figure 2.3.

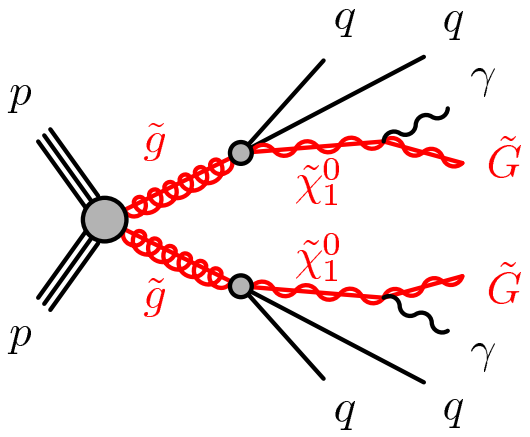

FIGURE 2.3: Diagram showing an SPS8 decay chain resulting in a final state containing two photons and two gravitinos [58].

From equation 2.11 it is trivial to convert the decay rate of the neutralino into a lifetime:

$$\tau\left(\widetilde{X_1^0}\right) = \frac{16\pi F^2}{\kappa m^5_{\widetilde{X_1^0}}} C^2_{grav}. \tag{2.12}$$

Noting that in SPS8 the mass of all sparticles and the value of F depends only on the value of Λ it becomes apparent that the decay lifetime of the neutralino for a constant Λ is determined by C_{grav}. Since C_{grav} is a free parameter in the model, equation 2.12 shows that the lifetime of the neutralino can instead be treated as the free parameter and take any value desired. In collider experiments, if neutralinos have short lifetimes they will decay promptly at the interaction vertex, while if the lifetime is very large neutralinos will travel through a detector and escape before decaying. This work focuses on the intermediate lifetime range where the decay is non-prompt but occurs within the detector.

The cross-section of SUSY production is dependent on the value of Λ, with the cross-section decreasing as Λ increases, as shown in figure 2.4 (left) and figure 2.5 (left) for a center of mass energy ($\sqrt{s}$) of 7 TeV and 8 TeV respectively. Since the cross-section is directly related to the number of SUSY events that will be produced, fewer SUSY events will be expected for higher Λ values. Figure 2.5 (right) highlights the dependence of the SUSY production cross-section on the $\sqrt{s}$ of pp collisions, with the cross-section increasing by approximately 50% across the Λ region of interest when $\sqrt{s}$ is increased from 7 TeV to 8 TeV. The relative number of SUSY events that are initiated by strong

production of coloured particles (i.e. pairs of squarks or gluinos) or via electroweak production (i.e. pairs of gauginos or sleptons) also changes as a function of Λ as shown in 2.4 (right). The process by which SUSY proceeds determines the particles that are expected to be found in the final state, with strongly produced events likely to contain a large number of jets while electroweak events are expected to contain fewer jets but with the possibility of charged leptons. By performing inclusive searches for final states of two photons and a large amount of missing energy the method of production can be ignored with only the total production cross-section affecting the predicted results.

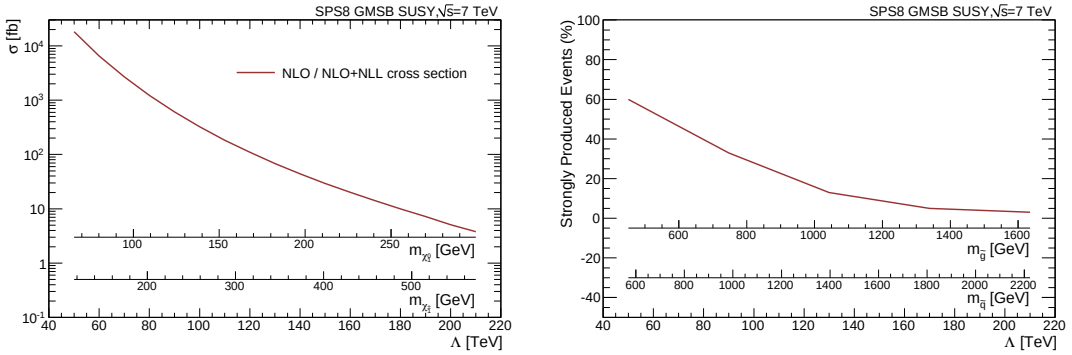

FIGURE 2.4: (Left) The total SUSY cross section (NLO) for the SPS8 GMSB model as a function of Λ for center of mass energy of 7 TeV. The dependence of the cross section on the masses of the lightest neutralino and chargino is shown on the interior axes. (Right) The fraction of strongly produced SUSY events as a function of Λ. The dependence of the fraction as a function of the gluino mass and typical squark mass is shown on the interior axes [57].

As has previously been noted, the mass scale of the SUSY particles is determined by Λ, with a larger value corresponding to the SUSY particles having larger masses. Figure 2.6 shows that as Λ increases the typical neutralino transverse momentum (p_{T}) also increases while the typical β value decreases, with important consequences for the detection of non-prompt photons. For example, if a neutralino with $\beta = 0.8$ and a lifetime of 5 ns decays inside a detector, the arrival time of the resulting photon would be delayed by approximately 1 ns compared to that expected for a photon produced promptly at the interaction point.

For non-prompt photons to be detected in a collider experiment, the neutralino must decay before the sub-detector responsible for identifying photons. In the ATLAS detector photon detection is performed by the electromagnetic calorimeter. Due to the spread in important kinematic variables, such as β, different neutralinos will travel different distances before decaying for a given neutralino lifetime and Λ. To estimate the expected

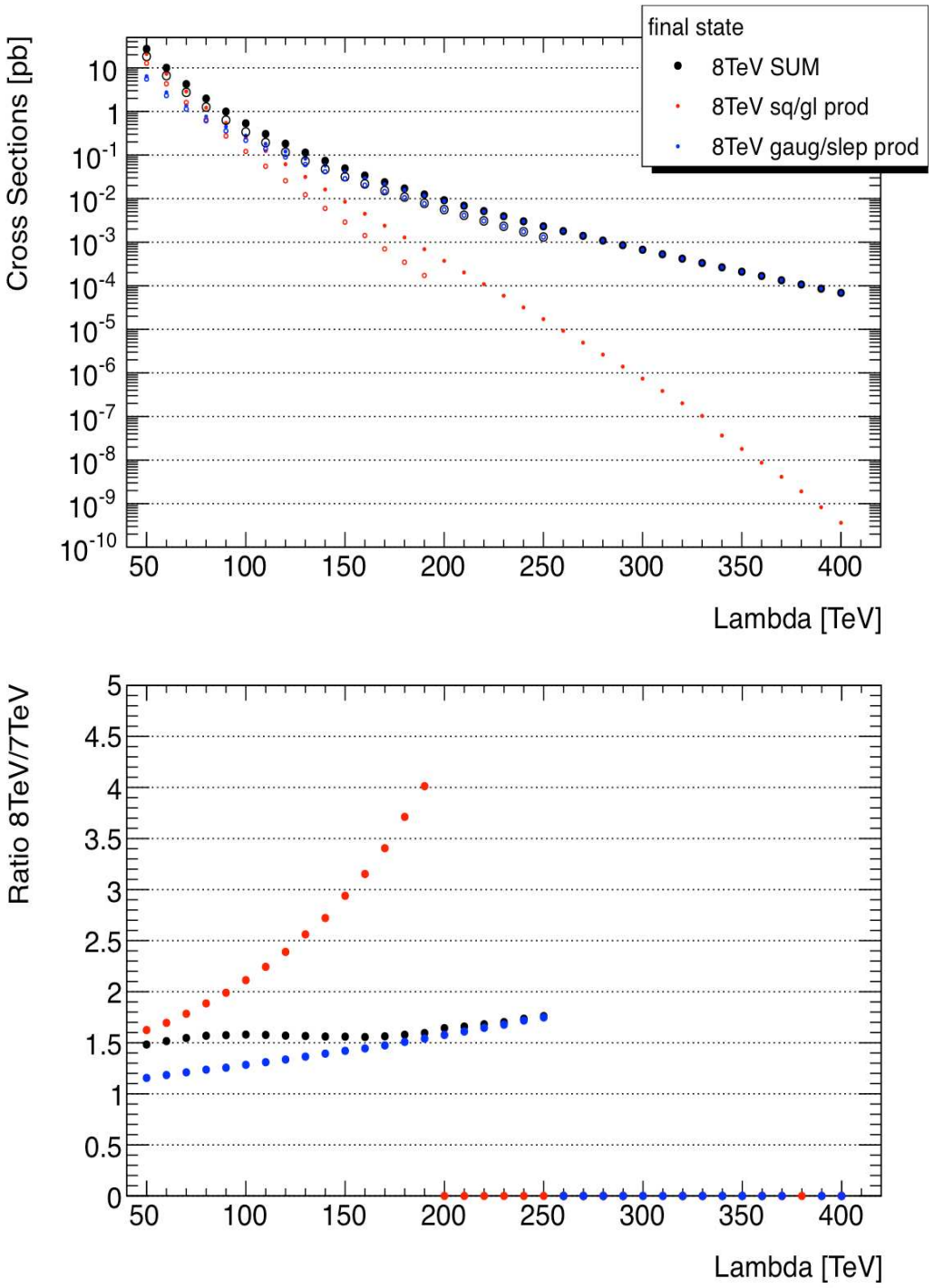

FIGURE 2.5: (Top) The total SUSY cross section (NLO+NLL) for the SPS8 GMSB model as a function of Λ for center of mass energy of 8 TeV (filled markers) and 7 TeV (hollow markers). (Bottom) The ratio of the SPS8 production cross-section inn 8 TeV and 7 TeV pp collisions, note that the ratio goes to 0 when there is no corresponding 7 TeV cross section. In both plots, the red points are for squark and gluino production, blue are for gaugino and slepton production and black is the total Λ [59].

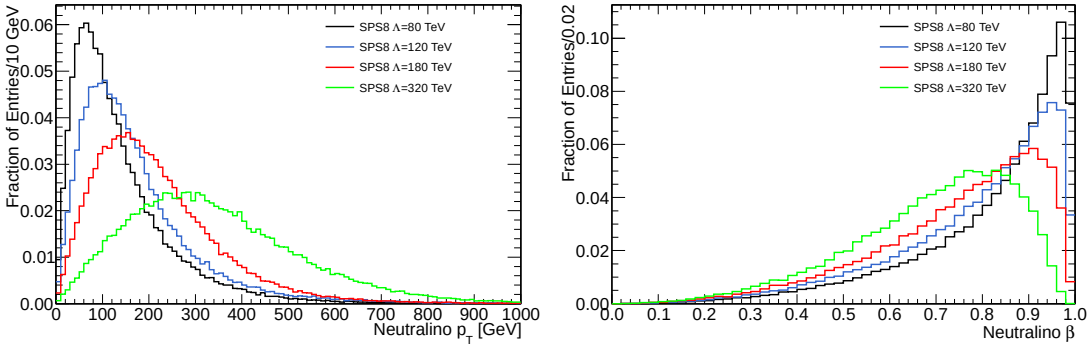

FIGURE 2.6: Unit-normalised distributions of (left) the neutralino transverse momentum and (right) the neutralino speed for several Λ values on the GMSB SPS8 model line [57].

fraction of non-prompt neutralinos that would be detectable at the ATLAS detector, a toy MC was produced using the kinematics expected in SPS8 events. Figure 2.7 shows that as the lifetime of the neutralino increases, the fraction of neutralinos decaying before the calorimeter decreases. It can also be seen that the fraction of neutralinos decaying before the calorimeter for a given lifetime increases for higher Λ values, which is to be expected when considering the trend of typical β values observed in figure 2.6. Searching for final states containing two photons therefore requires both of the neutralinos in an event to decay before the calorimeter. The corresponding probability of an event meeting this requirement can be estimated by squaring the probability of a single neutralino decaying. For a lifetime of 1 ns the probability of a neutralino decaying in the required volume is approximately 95% giving a probability of $\sim$ 90% that both neutralinos will decay. For a lifetime of 50 ns however, approximately 10% of neutralinos will decay resulting in an estimate of $\sim$1% of SUSY events meeting the diphoton requirement.

Taking into account the decrease in the number of expected SUSY events as Λ increases, due to a decreasing cross-section, and the decrease in the number of events observed as the neutralino lifetime increases, due to the decreasing probability of both neutralinos decaying before the calorimeter, it is expected that the SUSY discovery potential will decrease as either the value of Λ or neutralino lifetime increases.

2.2.7 Models With Long Lived Particles

The decay of a long-lived neutralino to a photon and a gravitino is an interesting feature of the SPS8 model of mGMSB, however it isn't the only BSM theory which predicts the

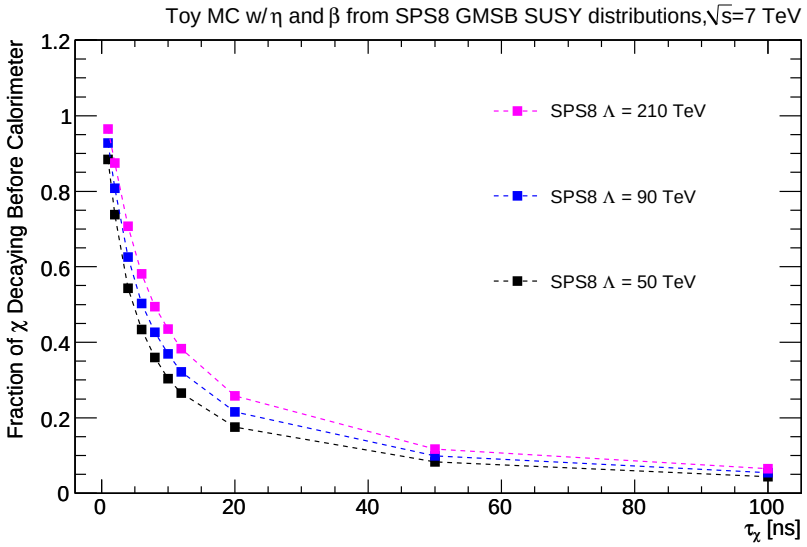

FIGURE 2.7: The fraction of neutralinos decaying before the calorimeter as a function of the neutralino lifetime. Curves are shown for three different Λ values and illustrate the dependence of the fraction on the speed of the neutralino. These distributions are for 7 TeV proton-proton collisions and are very similar for 8 TeV collisions [57].

existence of undiscovered long-lived particles. Many interesting searches are currently being performed looking for long-lived particles of varying lifetimes at the LHC [43, 44]. Therefore, while the discovery of long-lived neutral particles decaying to photons and missing energy would be proof of BSM physics it would not necessarily be proof of mGMSB. It would, however, provide impetus and direction to future searches for SUSY and other BSM theories and no doubt spark a flurry of new theories attempting to explain the exciting observations.

Chapter 3

The LHC and the ATLAS Experiment

The analyses presented in this thesis were performed using pp data collected by the ATLAS Collaboration using the ATLAS detector [60], one of the four main experiments at the LHC. In section 3.1, the LHC and important features relating to its operation and performance are described. Then in section 3.2, the various components of the ATLAS detector that are designed to detect the vast array of particles that are produced in the pp collisions are presented.

3.1 The Large Hadron Collider

The LHC [61] is a particle accelerator based at the European Organization for Nuclear Research (CERN) and is the highest energy particle accelerator in history. The LHC accelerates two beams of protons, in opposite directions, through vacuum evacuated beampipes in a 27 km circumference tunnel 100 m below the French and Swiss countryside. The two beams are then made to cross at four points around the ring where protons from opposite beams collide. At design energy, proton−proton (pp) interactions will have a center of mass energy of $\sqrt{s} = 14$ TeV, however, due to technical problems in 2008 [62] the center of mass of the pp collisions in 2011 (2012) was $\sqrt{s} = 7$ (8) TeV.

3.1.1 CERN Accelerator Complex

Before the protons can be injected into the LHC, they must first pass through the accelerator complex, a schematic of which is shown in figure 3.1. The first stage of preparing the protons for these extremely high energy collisions is to take hydrogen atoms from a bottle of hydrogen gas and apply a large electric field to separate the protons and the electrons. Protons are then injected into the Linac 2 where they are accelerated in 100 ms pulses to an energy of 50 MeV before being injected into the Proton Synchrotron Booster (PSB). Once the protons have reached the desired energy of 1.4 GeV they are then injected into the Proton Synchrotron (PS) and accelerated around the 628 m circumference of the ring until they reach an energy of 25 GeV, which allows them to be injected into the final accelerator before the LHC: the Super Proton Synchrotron (SPS). With a circumference of almost 7 km the SPS (the accelerator used to discover the W [63] and Z [64] bosons) is the second largest machine in the accelerator complex and injects protons into the LHC at an energy of 450 GeV.

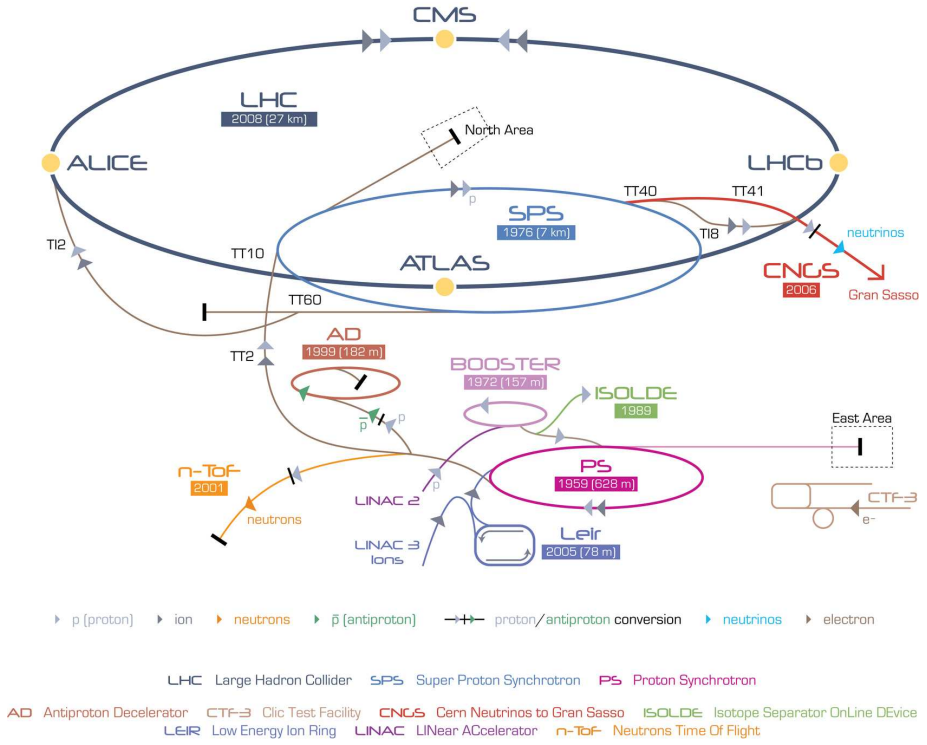

FIGURE 3.1: Schematic showing CERN accelerator complex, taken from [65].

3.1.2 LHC Operation

The protons are inserted into the LHC in bunches which consist of approximately 1.1×10^{11} protons. The LHC is designed so that a maximum of 2808 bunches can circulate in each beampipe with each bunch separated by a minimum of 25 ns. The actual number of bunches and the bunch separation in each beam varied over the 2011 and 2012 data taking periods with a maximum of 1380 bunches and a minimum spacing of 50 ns achieved in both periods. To direct protons around the LHC requires 1232 superconducting dipole magnets which can each supply a magnetic field of up to 8.6 T. As the bunches travel around the ring they will begin to defocus: 392 superconducting quadrupole magnets focus the bunches in the transverse plane.

To accelerate protons up to the desired collision energy radiofrequency (RF) cavities, with an alternating frequency of 400 MHz, are used to transfer energy to protons in the direction of the beampipe. Precise control over the trajectory of the proton bunches around the LHC allows the same RF cavity to supply energy to the beam travelling in the clockwise direction as well as the beam travelling in the anticlockwise direction. However, to achieve this requires very precise timing to ensure that the centre of a bunch travelling in the clockwise (anticlockwise) direction passes through the centre of the RF cavity when the amplitude of the RF is positive (negative) to provide a boost in energy in the direction of travel. The RF cavities are also able to focus proton bunches along the direction of the beampipe. The centre of each bunch is timed to reach the centre of the RF cavity as the amplitude is increasing, as shown in figure 3.2. Any proton that is ahead (behind) of the bunch will then receive less (more) energy than a proton in the centre of the bunch and return closer to the centre of the bunch, resulting in a smaller spread. However, a proton that is too far ahead (behind) the centre of the bunch could be accelerated by the RF cavity a full period or more before (after) the main bunch and fall into a stable orbit ahead (behind) the main bunch. These bunches are said to have fallen into a different RF bucket and are hereafter referred to as satellite bunches. Given the RF period of 2.5 ns buckets are expected to be separated by multiples of 2.5 ns

The amount of data that can be used in physics analyses by the experiments that are built around the LHC depends on the amount of instantaneous luminosity ($\mathcal{L}$) that is delivered. The instantaneous luminosity is a measurement of the rate of pp collisions, in

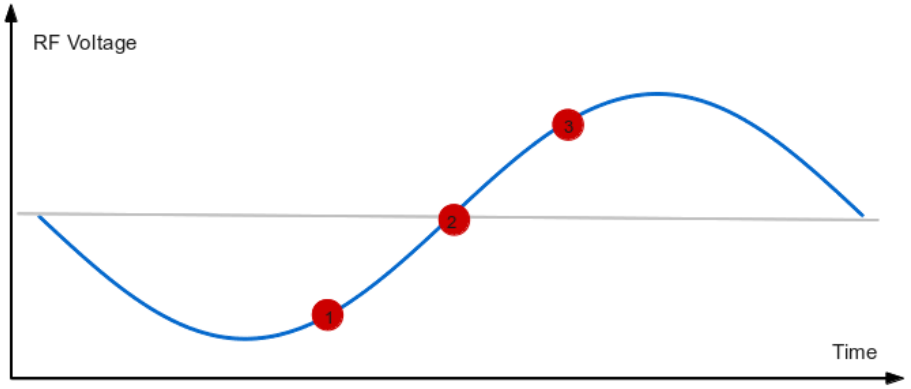

FIGURE 3.2: Cartoon showing how the voltage felt by particles in a bunch changes depending on the arrival time. Particle 1 which reaches the centre of the RF cavity early will receive less energy than particle 2 in the centre of the bunch. Particle 3, which reaches the centre of the RF cavity later than the centre of the bunch, will receive more energy than particle 2. The effect that this has on the spread of the bunch is explained in the text.

units of $\mathrm{cm}^{-2}\mathrm{s}^{-1}$, and can be calculated directly for a collider operating with a revolution frequency of f_r and n_b bunch pairs colliding per revolution:

$$\mathcal{L} = \frac{n_b f_r n_1 n_2}{2\pi \Sigma_x \Sigma_y} \tag{3.1}$$

where the number of protons in the bunch of beam 1 and beam 2 is given by n_1 and n_2 respectively, and $\Sigma_{x/y}$ characterises the horizontal/vertical profiles of the beams [66]. From this knowledge, the total integrated luminosity (L) for a given data taking period can be calculated and is related to the expected number of events for a physics process with cross-section (σ) by:

$$N = \epsilon \sigma L = \epsilon \sigma \int \mathcal{L} dt, \tag{3.2}$$

where ϵ is the detector efficiency and acceptance.

3.1.3 LHC Performance

Run 1 (2009−2013) was a very successful period of operation for the LHC with over 28 fb^{-1} of integrated luminosity delivered to ATLAS and CMS. As can be seen from figure 3.3 the majority of this was delivered in 2012, due to higher instantaneous luminosity used in the 8 TeV run. One way in which this increase in luminosity was achieved was to increase the number of collisions per bunch crossing. As can be seen in figure 3.4 the mean number of interactions per crossings increased from 9.1 in the 7 TeV dataset to 20.7 in the 8 TeV dataset. This effect, known as pileup, can cause problems for physics analyses because there will be multiple vertices in a single crossing producing a high flux of particles that can have overlapping signals, as shown in figure 3.5.

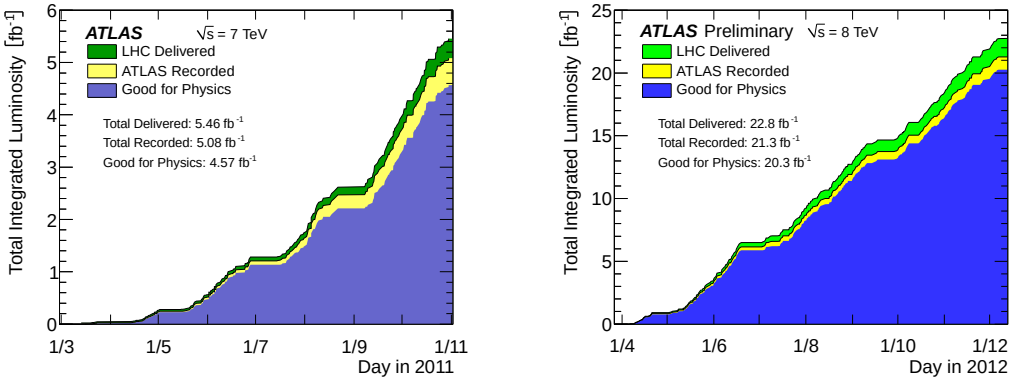

FIGURE 3.3: Breakdown of the total integrated luminosity delivered by the LHC and recorded by the ATLAS detector as a function of time for the 7 TeV (left) and 8 TeV (right) *pp* collisions[67].

Using the Longitudinal Density Monitor [69][70] it is possible to measure the distribution of protons in the LHC. Figure 3.6 shows that, as expected, the majority of protons arrive in the main bucket with a time centred on 0 seconds, albeit with a small spread. However, it also shows that other buckets (and therefore satellite bunches) are indeed populated by protons due clear peaks in the number of protons arriving at 5 ns intervals starting from ±5 ns.

3.2 The ATLAS Experiment

The ATLAS (**A** **T**oroidal **L**HC **A**pparatu**S**) detector, shown in figure 3.7, is a multi-purpose detector designed to discover the Higgs boson and search for signs of new physics

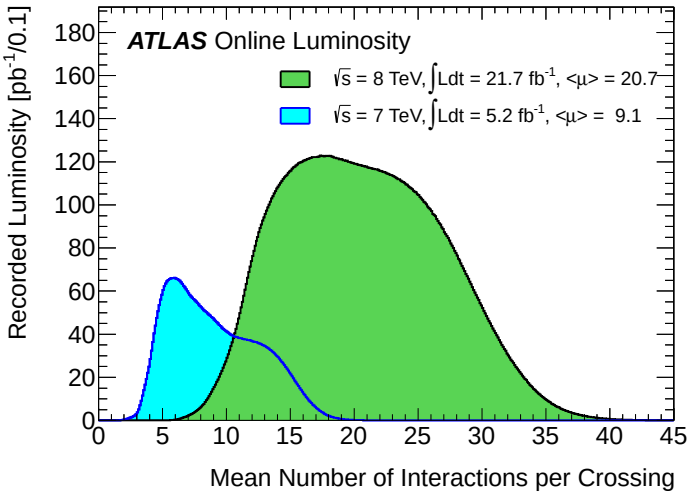

FIGURE 3.4: Average number of proton-proton interactions per crossing recorded at the ATLAS detector in 2011 and 2012 [67].

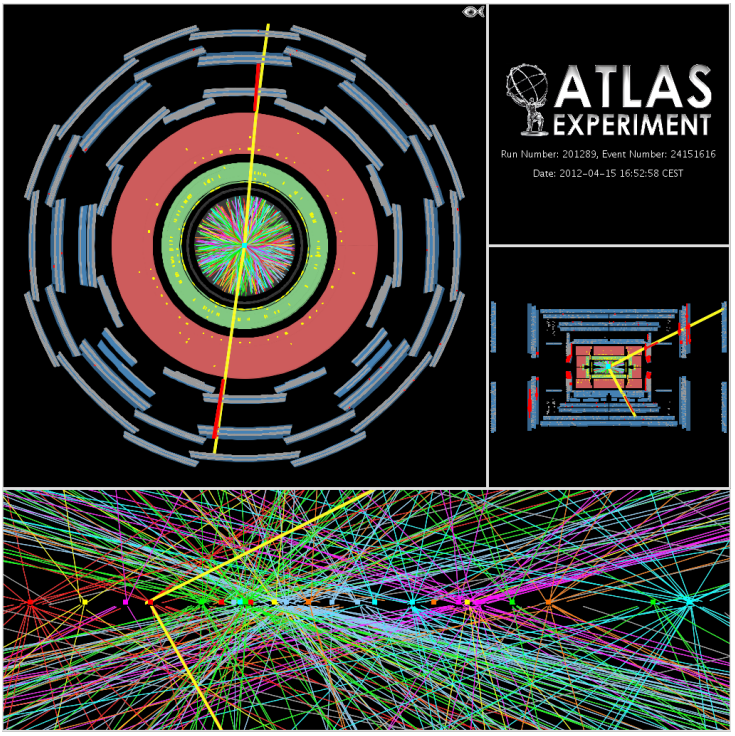

FIGURE 3.5: A candidate Z boson event in the dimuon decay with 25 reconstructed vertices. For this display the all tracks are required to have p_{T} of at least 0.4 GeV and at least 3 Pixel and 6 SCT hits [68].

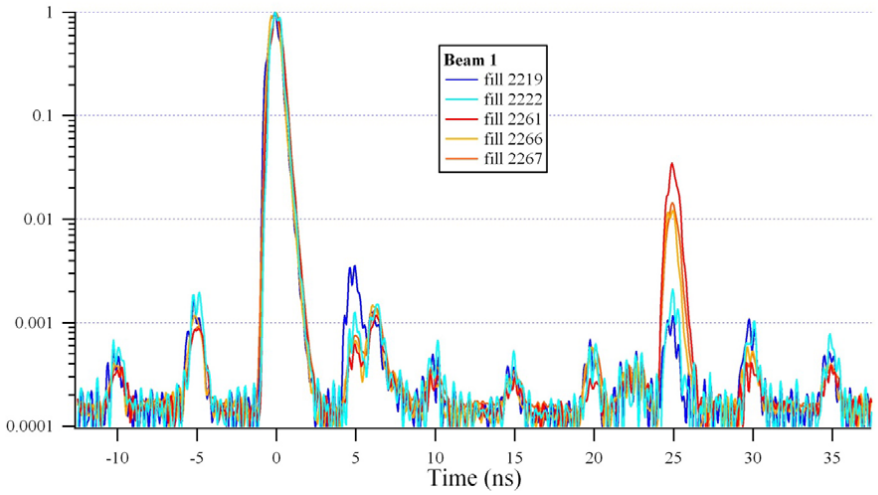

FIGURE 3.6: Measurement of the normalised population of LHC bunches using the Longitudinal Density Monitor for specified proton-proton fills in October 2011 with a bunch separation of 50 ns. Fills 2261, 2266 and 2267 had enhanced satellites at 25 ns [69].

beyond the Standard Model. Over 3000 scientists from over 100 countries work on ATLAS which, with a length of 45 m and diameter of 25 m, is the largest particle physics detector ever constructed.

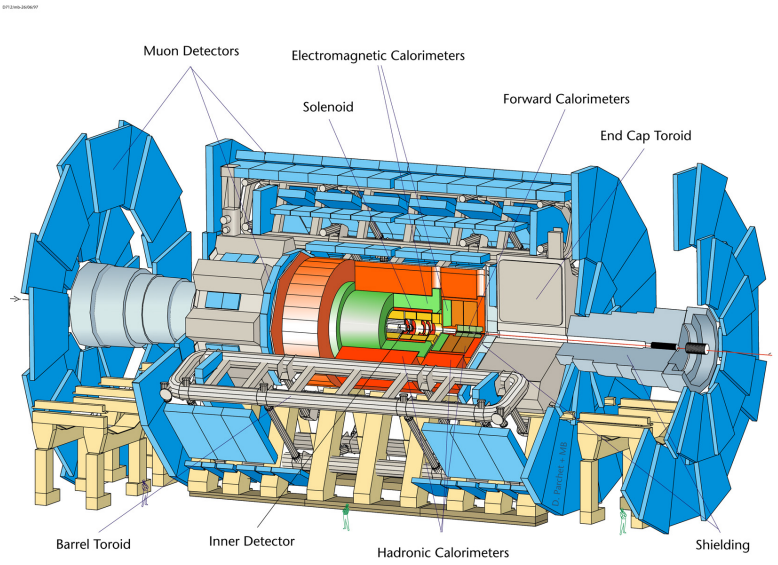

FIGURE 3.7: The ATLAS detector [60].

The ATLAS detector was designed to have a number of systems and components that provide complementary information to allow accurate reconstruction of all particles and events. Many of the ATLAS components are subdivided into two sections: the central

barrel region and the end-caps. The barrel provides 360^o coverage of the beampipe in the azimuthal direction for the volume that lies within $|\eta| < 1.37$ (see section 3.2.1 for more information on this coordinate system). The barrel is closed off at both ends by the end-caps, which are designed as disks, in order to maximise the region each sub detector is sensitive to. There is a small section of the detector between the barrel and endcap, see the next section for a more explicit definition, where not all of the sub-detectors provide complete coverage and some information relating to particles will be lost. This region will be referred to as the crack region and any particle detected in this region is not used in the physics analyses presented in this thesis due to the potential that it may not be correctly reconstructed.

This section gives an overview of the different components that combine to form the ATLAS detector.

3.2.1 The ATLAS Coordinate System

In order to describe the trajectory of particles and the corresponding regions where different parts of the ATLAS detector operate a coordinate system needs to be specified. The coordinate system used in this thesis is the ATLAS coordinate system which is right handed with the origin at the centre of the detector. The x-axis is in the direction of the centre of the LHC and the z-axis is along the beam pipe meaning that the y-axis is approximately 0.7^o off vertical due to the tilt of the tunnel, as shown in figure 3.8. The transverse direction (R) is the distance from the origin in the x-y plain defined as $R = \sqrt{x^2 + y^2}$. The direction of collision by-products are often described by ϕ, the angle from the x-axis in the x-y plane and the pseudorapidity η:

$$\eta = -\log \tan(\frac{\theta}{2}), \tag{3.3}$$

where θ is the polar angle from the z axis. These definitions can be used as a set of geometric coordinates to identify different parts of the detector based on the η and ϕ a neutral particle produced at the nominal interaction point would require to reach this point. For example, the crack region between the barrel and end-cap is defined as the $1.37 < |\eta| < 1.52$ region for all ϕ.

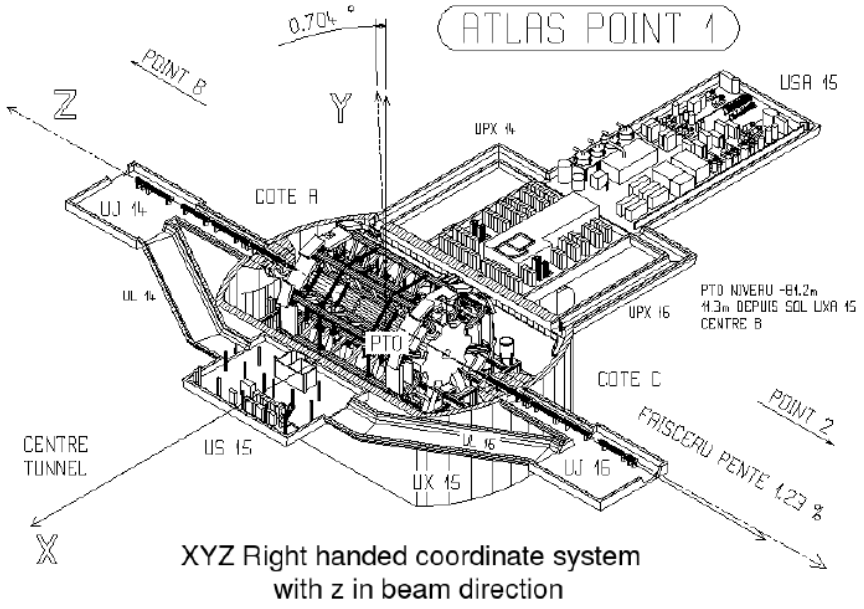

FIGURE 3.8: Diagram showing the coordinate system used at ATLAS [60].

3.2.2 Magnet System

The ATLAS Magnet System utilises superconducting magnets to provide a magnetic field throughout the detector. As shown in figure 3.9, it is composed of three sub-systems: the Central Solenoid (CS), the Barrel Toroid (BT) and the two End-Cap Toroids (ECT). The CS provides a 2 T axial magnetic field throughout the volume of the central tracking region which is primarily used for determining the charge and momentum of particles. Each of the toroidal magnets produce a 3.9 (4.1) T field in the barrel (endcap) which equates to an average field strength of $0.5 - 1.0$ T over the muon detector volume.

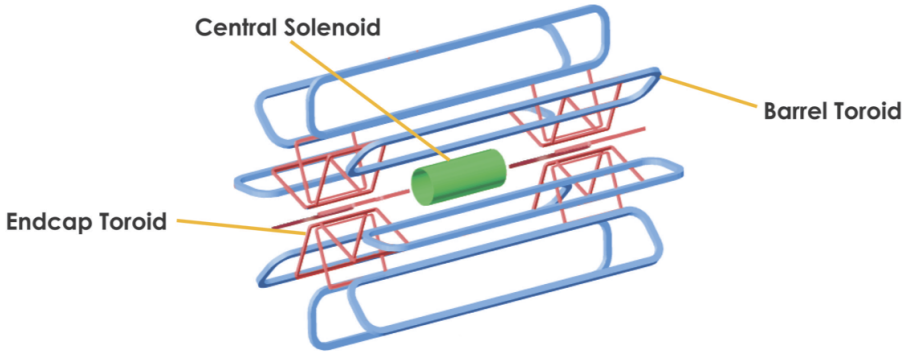

FIGURE 3.9: Layout of the ATLAS detector magnet system (taken from [71]).

3.2.3 Inner Detector

The Inner Detector (ID) provides almost complete coverage around the beampipe with an acceptance of $|\eta| < 2.5$ and contains a number of subsystems that provide complementary information used to help identify particles. By combining information from the subsystems, which are described in more detail below, the ID can accurately measure the position of charged particles as they pass through the detector. Due to the presence of the magnetic field from the CS magnet, charged particles will feel the Lorentz force causing the direction of travel to bend, allowing the charge and momentum to be calculated. Figure 3.10 shows the layout of the ID and figure 3.11 shows the approximate distance in R, from the nominal interaction point, of the ID sub-detectors in the barrel. These different sub-detectors are described below, starting from the beampipe and working out.

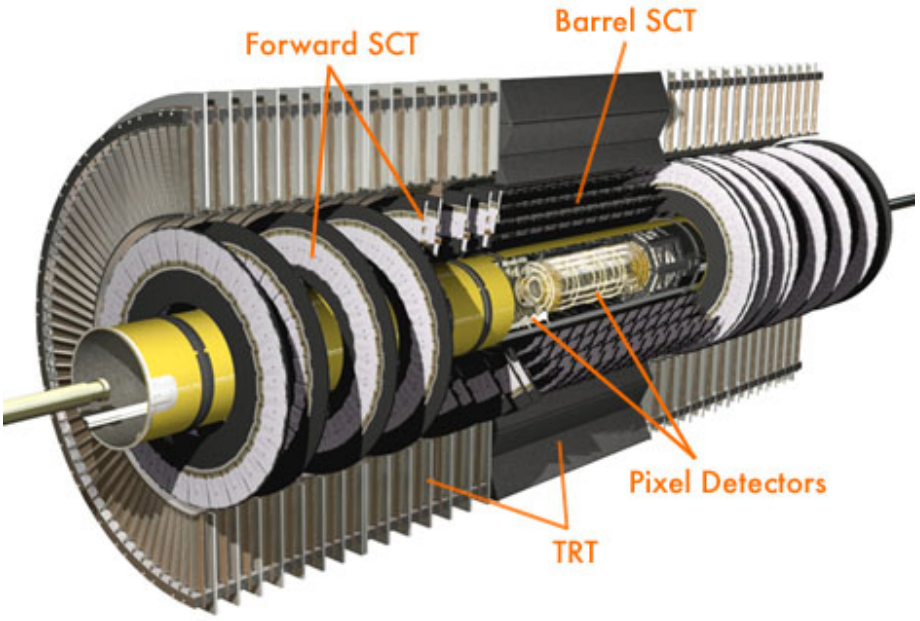

FIGURE 3.10: Image showing sub-detectors of the ATLAS Inner Detector [60].

3.2.3.1 Pixel Detector

Located 50.5 mm from the beampipe at its closest point the pixel detector is the closest part of the ATLAS Detector to the interaction point. Wafers of silicon are used to construct the pixel modules which each contain 47232 pixels, measuring 50×400 μm in $R - \phi \times z$ [72], arranged in three layers in both the barrel and either end-cap. Each

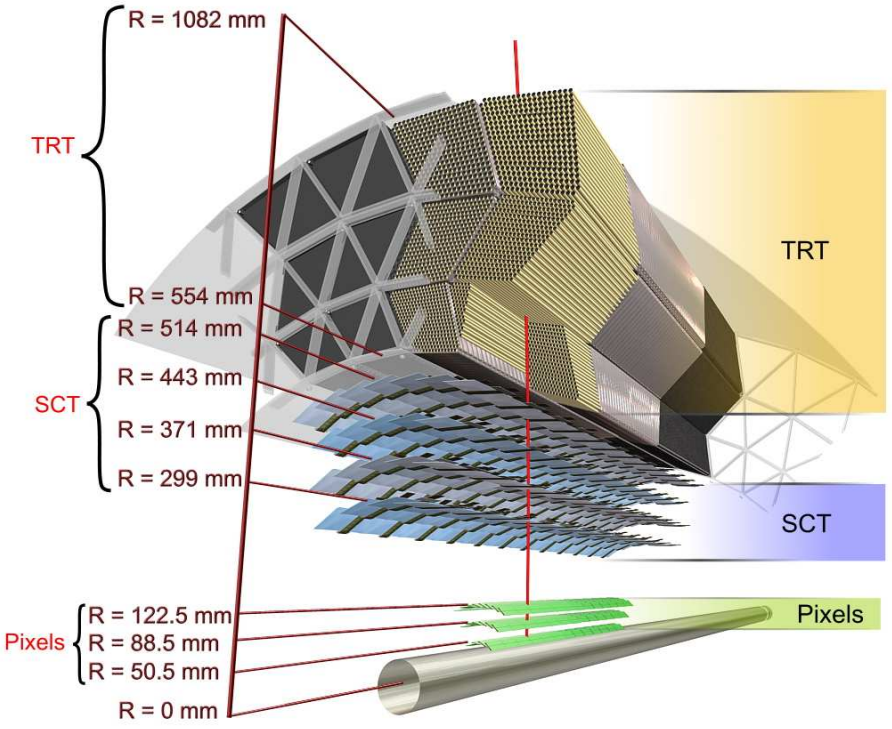

FIGURE 3.11: The approximate distance in R of the different inner detector subsystems in the barrel [60].

module is read out individually by 16 front-end chips allowing the pixel detector to operate in the high luminosity environment and results in there being approximately 80.4 million separate readout channels. The resolution of the pixels, which is on the order of 10μm in the $R-\phi$ direction and 115 μm in the z (R) direction in the barrel (end-cap), gives a good efficiency of identifying secondary vertices containing charged particles. The pixel detector is also therefore very important for differentiating between electrons from the conversion of a photon and electrons that originate from the primary vertex.

3.2.3.2 Semiconductor Tracker

The Semiconductor Tracker (SCT) is the second silicon based detector that particles from the collision point will traverse. Each SCT module is formed from two silicon strips attached back to back to another pair of silicon strips, but with a relative stereo angle of 40 mrad between them, providing one 3-dimensional measurement point. The SCT modules are arranged in 4 layers in the barrel, spanning the 299 mm to 514 mm in

the radial direction, and 9 layers in each of the end caps, in the region between 839 mm and 2720 mm in the z direction.

3.2.3.3 Transition Radiation Tracker

The Transition Radiation Tracker (TRT) is the third sub-detector of the ID and is different from the previous two due to not being silicon based. The TRT consists of straw tubes that contain a xenon based gas mixture and a tungsten-rhenium wire with a large potential difference through the centre. A charged particle that passes through a tube will ionise the gas mixture causing the electron to drift towards a cathode at the outer edge of the tube which, given the constant drift velocity of electrons, allows the drift time to be used to determine a precise measurement of the point where the charged particle entered the tube.

In addition to providing extra information about the track of charged particles, the TRT is also designed to distinguish between electrons and heavier charged particles. To achieve this polypropylene fibres (foils) are situated between drift tubes in the barrel (end-cap) creating a region with a constantly changing refractive index. The probability of a particle emitting transition radiation is inversely proportional to the mass of the particle meaning that for a fixed momentum, electrons are hundreds of times more likely to emit transition radiation than a charged hadron. The energy of transition radiation photons is an order of magnitude larger than the energy a minimum ionising particle deposits so the signals are easily distinguished.

In the barrel, the TRT tubes are arranged parallel to the z axis in three separate layers completely surrounding the beampipe and filling the volume between 554 mm and 1082 mm in the radial direction. In the end caps, the straws are arranged in layers perpendicular to the z axis in the region between 848 mm and 2710 mm in z and 617 mm to 1106 m in R so as not to overlap with the SCT. This design means that particles with $p_{\mathrm{T}} > 0.5$ GeV will be expected to cross over 30 tubes. However it is only sensitive to particles with $|\eta| < 2$.

3.2.4 Calorimetry

After particles have traversed the ID the aim is now to accurately measure their energy. This job is performed by the ATLAS calorimeter system which is made up of many different components, as shown in figure 3.12. These components are grouped into four separate sub-detectors: the presampler, the Electromagnetic Calorimeter, the Hadronic Calorimeter, and the Forward Calorimeter. The design and technologies employed in the calorimeters are described in further detail in the following sections.

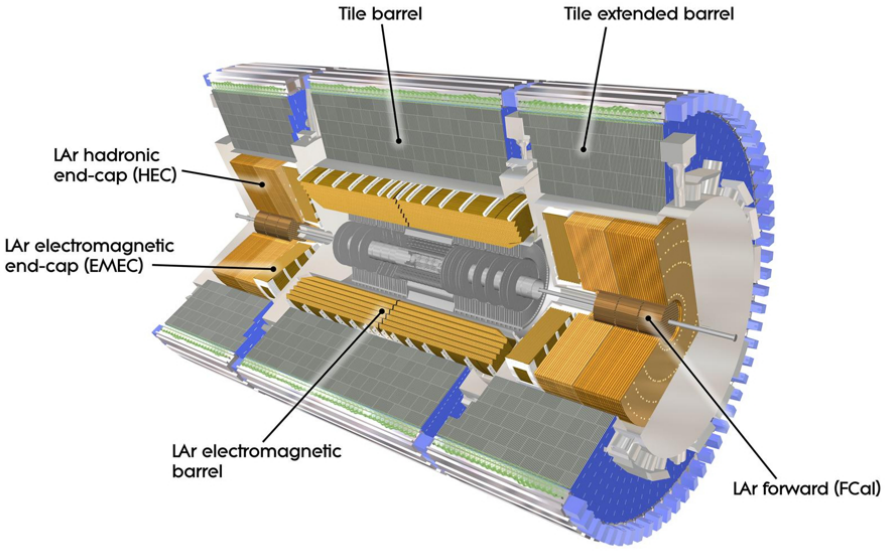

FIGURE 3.12: Layout of ATLAS calorimeter system [60].

3.2.4.1 Presampler

Before reaching the calorimeter system particles will have travelled through a large amount of material, not just the active regions of the ID and the CS but also many cables and support structures. During the design process the amount of material was kept to a minimum and is well known. As particles pass through matter they interact and lose energy via a number of processes [20], therefore no particle produced at the PV will reach the calorimeter with the energy it was created with. It is also possible for particles to induce a shower before the calorimeter; these particles will also interact with matter in the detector and arrive at the calorimeter with less energy than they were created with.

If the particles or particle showers that reach the calorimeter do not have the total energy they were created with then when the event is reconstructed the energy of that particle will be underestimated. This is a problem for analyses that look for particles that escape ATLAS undetected because badly reconstructed particle masses will introduce a source of missing energy (see section 4.5). Information about how much energy is lost before the is recovered by a thin layer of liquid argon called the presampler, located directly before the electromagnetic calorimeter covering the range $|\eta| < 1.8$ with an $\Delta\eta \times \Delta\phi$ granularity of 0.025×0.1. The amount of energy collected by the pre-sampler is combined with knowledge about the amount of material the particle will have travelled through in the inner detector, as shown in figure 3.13, to correct the reconstructed energy (see equation 4.1).

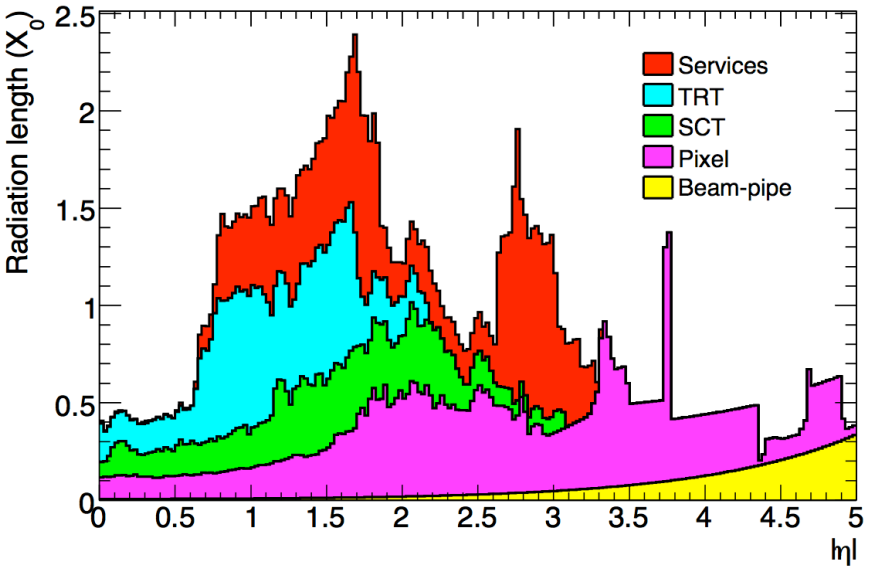

FIGURE 3.13: Material budget of ATLAS Inner Detector [73].

3.2.4.2 Electromagnetic Calorimeter

The Electromagnetic Calorimeter (EM calorimeter) is designed to accurately measure the energy of electromagnetic objects, such as photons and electrons. Test beam results using electrons have shown that, after electronic noise subtraction, the energy resolution can be described by the following function [74]:

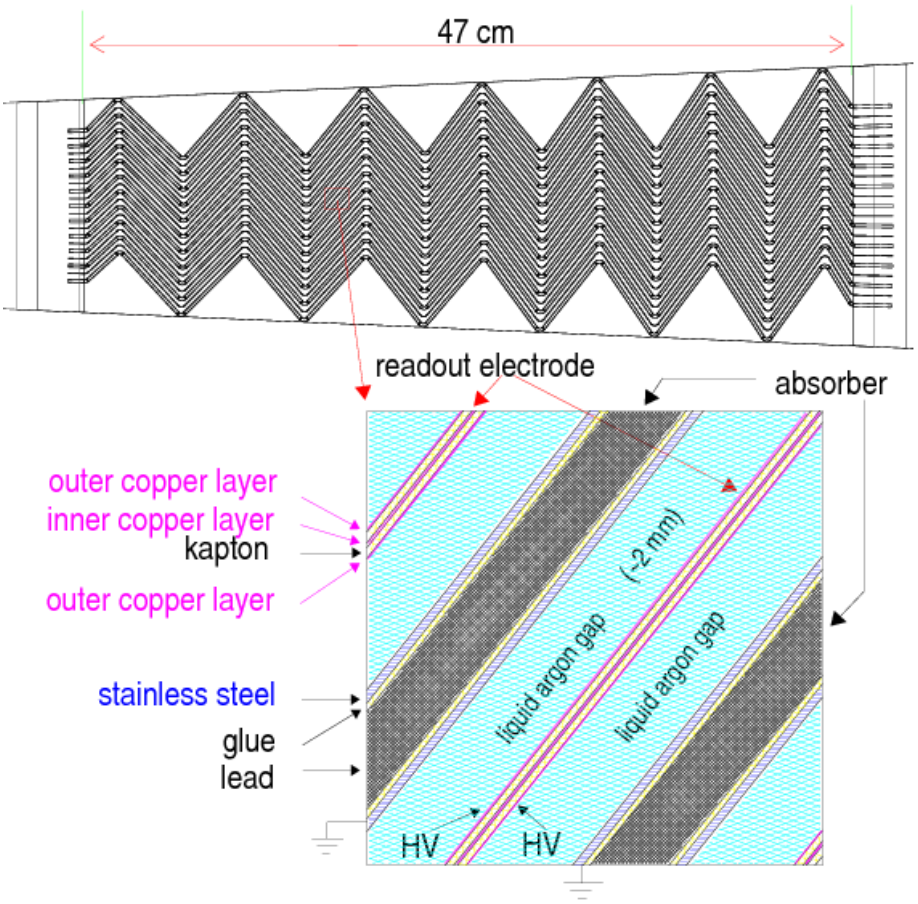

FIGURE 3.14: Accordion structure used in the electromagnetic calorimeter (top) zoomed in to show internal structure (bottom) [73].

$$\sigma_E/E = \frac{a}{\sqrt{E}} \oplus^1 b, \tag{3.4}$$

where a is the stochastic term, which takes into account the statistical fluctuations relating to the detection of the shower, that has been measured to be $10.1 \pm 0.1\% \cdot \sqrt{GeV}$ and b is a constant term, that includes detector instabilities and mis-calibration, which has been measured to be 0.2 ± 0.1.

The EM calorimeter consists of two half barrels that cover the central $|\eta| < 1.475$ region and two wheels, one at either end of the barrel calorimeter, that cover the $1.375 < |\eta| < 3.2$ region. Lead absorber plates in the EM calorimeter induce particle showers which then ionise the liquid argon (LAr) that fills the space between plates. The liquid argon between two lead plates also contains a copper electrode which provides

[1] This symbol means the terms are added in quadrature

	$\|\eta\|$ range	Cell η size	
		Layer 1	Layer 2
Barrel	0-1.4	0.025/8	0.025
	1.4-1.475	0.025	0.075
end-cap	1.375-1.425	0.05	0.05
	1.425-1.5	0.025	0.025
	1.5-1.8	0.025/8	0.025
	1.8-2.0	0.025/6	0.025
	2.0-2.4	0.025/4	0.025
	2.4-2.5	0.025	0.025

TABLE 3.1: Main parameters of the liquid argon electromagnetic calorimeter system, taken from [60].

a large electric field that attracts electrons liberated during the ionisation and causes the positive ion to drift towards the grounded absorber plate. The absorber plates and electrodes are structured in an accordion geometry, as shown in figure 3.14, so that the barrel component can completely encompass the beam pipe whilst maintaining an almost uniform material density as a function of η.

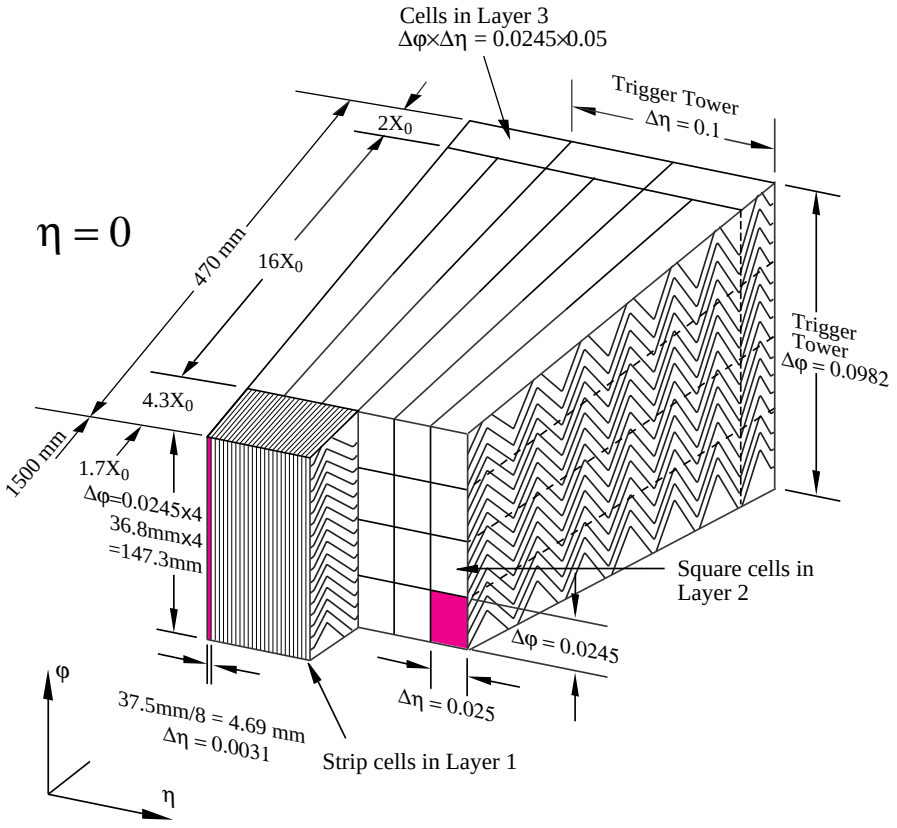

FIGURE 3.15: Schematic drawing highlighting the difference in granularity of the three different layers of the EM calorimeter. The effective radiation length of each layer is also shown [73].

Figure 3.15 shows that the EM calorimeter is divided into three layers, with the cells in each layer having different granularity. The η size of cells for different $|\eta|$ ranges for layers 1 and 2 can be seen in table 3.1. The ϕ size of the cells is 0.1 and 0.025 in layers 1 and 2 respectively. The primary role of layer 3 of the EM calorimeter is to estimate energy leakage into the hadronic calorimeter and as such has a coarser granularity of $\Delta\eta \times \Delta\phi = 0.05 \times 0.025$. A novel feature of the EM calorimeter is that the cells in each layer are arranged so that each points back to the nominal interac point. This allows the direction of travel of neutral particles, such as photons, to be determined even though they don't leave a track in the ID. To calculate this the cells at the centre of the shower in layers 1 and 2 of the EM calorimeter are assumed to lie on the path the photon would have travelled along, with the energy weighted barycentre of the shower giving the η and ϕ of the photon. This assumption, however, requires that all photons are produced at the nominal interaction point at the geometric centre of the detector and pass through different layers at the same η and ϕ point. There is actually a large spread in the position of the primary vertex along the z axis, even for a single fill (see figure 4.2). If a photon is produced from a vertex displaced in the z axis, as would be expected from the decay of long lived neutralinos in SPS8 events, then the η values of the centre of the shower in the first and second layers will be different and neither will give a reliable estimate for the η the photon was produced with (η_γ). Combining the η values from the first (η_1) and the second (η_2) layers, however, does provide a good estimate for η_γ:

$$\eta_\gamma = \sinh^{-1}\left(\frac{R_2 \sinh\eta_2 - R_1 \sinh\eta_1}{R_2 - R_1}\right) \tag{3.5}$$

where R_1 and R_2 are the shower depths in layers 1 and two respectively. The angular resolution of the calorimeter using this equation is approximately 60 mrad/$\sqrt{E}$ [60], where E is measured in GeV. The same variables can also be used to calculate the position of the photon production vertex on the z axis:

$$z_{DCA} = \frac{R_1 R_2}{R_2 - R_1}\left(\sinh\eta_1 - \sinh\eta_2\right) \tag{3.6}$$

which, for photons detected in the barrel with energy in the range of 50-100 GeV, gives a resolution of approximately 20 mm. However, due to the geometry of the calorimeter

the pointing resolution will be worse for photons detected in the end-caps. This pointing information is essential if the decay vertex of a long-lived neutral particle is to be determined. However, it is also useful in SM analyses such as the $H \rightarrow \gamma\gamma$ analysis which utilises the pointing information to provide a more accurate estimate of the Higgs production vertex and increase the accuracy of the Higgs mass calculation [75].

From Shower to Signal

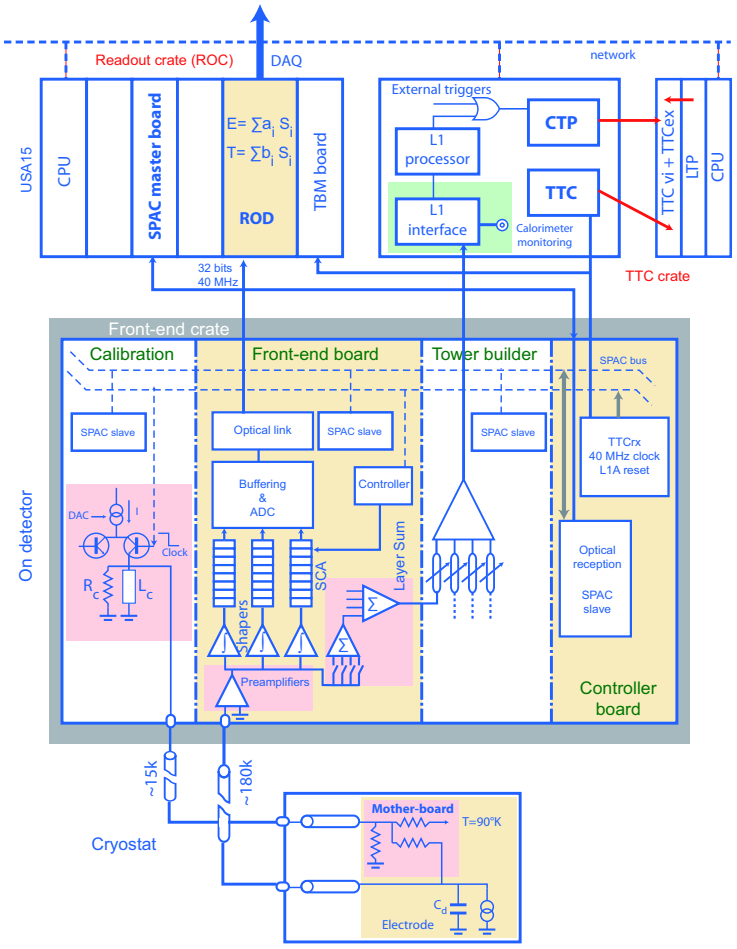

FIGURE 3.16: Block diagram depicting the architecture of the overall LAr readout electronics. The location of the different stages is given on the diagram, USA15 is the name given to the cavern the ATLAS detector is situated in [60].

After a particle has produced a shower in the EM calorimeter, the resulting current created from ionising the liquid argon layers are collected and need to be converted into a digital signal. The electronics system used, depicted in figure 3.16, is designed to be able to cope with energy deposits in the range of 20 MeV (noise) up to 3 TeV and has modules that are able to provide an estimate of the energy in less than 2.5 μs for use in the trigger system (see section 3.2.6). To achieve measurements at this rate requires

placing some of the electronics in the cryostat with the EM calorimeter, or in other parts of the detector, meaning that all components used in these areas need to be radiation hard.

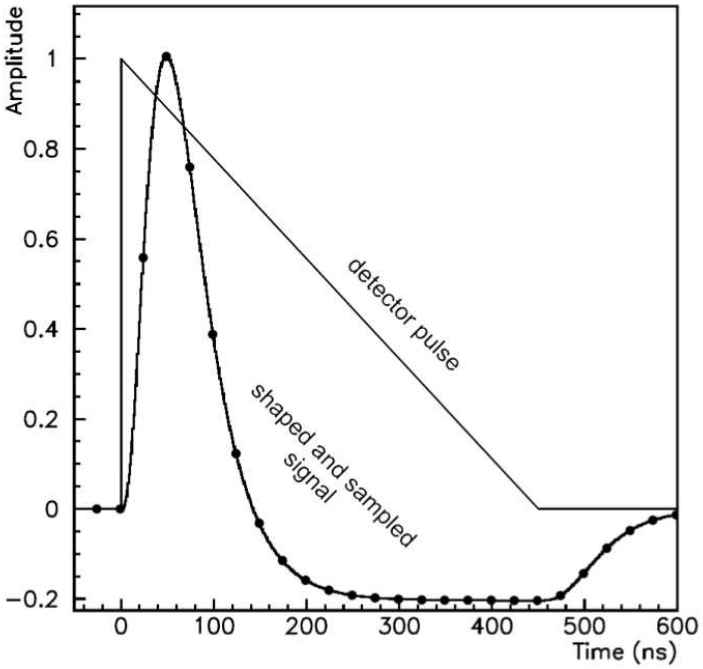

FIGURE 3.17: Amplitude versus time for triangular pulse of the current in a LAr barrel electromagnetic cell and of the FEB output signal after bi-polar shaping. Also indicated are the sampling points every 25 ns [60].

The signal that is read out by the electrodes in the calorimeter is a triangular pulse which is sent to the Front-end board (FEB) before being digitised. The signal sent to the FEB needs to be shaped to correct for the electron drift times, which are responsible for the triangular shape, and to minimise the different sources of noise. The shape of the signal before and after shaping can be seen in figure 3.17. Before shaping, the signal is amplified so that any noise already present, which can be corrected for, will dominate over any random noise introduced in the downstream electronics. The signal is split into three parallel channels which apply gains of 0.8 (LOW gain), 8.4 (MEDIUM gain) and 82 (HIGH gain), only one of which will be read out for digitisation to reduce the amount of information that needs to be stored. The gain that is kept is the one that has the highest gain without saturating the components, so that the affect of any downstream noise will be minimised. In practise, this means that cells with the highest energy (>400 GeV) will be read out with LOW gain and the cells with the lowest energy (<40 GeV) with HIGH gain.

The shaped signal in the FEB is sampled once every 25 ns, corresponding to the LHC bunch crossing frequency of 40 MHz, and sent to the Digital Signal Processor (DSP) where the cell energy (E_{cell}, in MeV) is reconstructed using the optimal filtering technique [76]. This calculation relies on coefficients that are measured in test beams, calibration runs where a known signal is injected into the electronics and with Monte Carlo simulations. Using these coefficients the cell energy for sample i is given as:

$$E_{\text{cell}} = F_{\mu A \to MeV} \times \frac{M_{cal}}{M_{phys}} \times R \times \sum_i a_i \left(ADC_i - P_i\right) \tag{3.7}$$

where F is a coefficient that converts the measured current into energy, the ratio M_{cal}/M_{phys} corrects for know differences in the shape of physics and calibration pulses, R gives the electronic gain (ADC $\rightarrow \mu$A), ADC_i is the digital reading for sample i, P_i is the ADC_i reading when there is no input (pedestal value), and a_i is an optimal filtering coefficient calculated from knowledge related to the shape of the pulse and the noise to estimate the pulse amplitude. Using this information the DSP is able to calculate the time of the peak of the pulse:

$$t_{\text{cell}} = \frac{1}{E_{\text{cell}}} \times \sum_i b_i \left(ADC_i - P\right) \tag{3.8}$$

where b_i is an optimal filtering coefficient calculated in a similar way to a_i.

A third value returned by the DSP is the quality factor (Q-factor) [60] given by:

$$\frac{\Sigma_{\text{cluster}} E_{\text{cell}}(Q > 4000)}{\Sigma_{\text{cluster}} E_{\text{cell}}} \tag{3.9}$$

which quantifies the quality of the reconstructed pulse compared to that expected for a physical signal. The higher the Q-factor of a cell the lower the quality of the pulse.

3.2.4.3 Hadronic Calorimeter

The hadronic calorimeter is located beyond, and surrounds, the EM calorimeter. Its purpose is to measure the energy of particles with masses that are much larger than electrons which interact hadronically and are able to penetrate the EM calorimeter

without stopping. In the $|\eta| < 1.6$ region, the hadronic calorimeter uses scintillating tiles as the active material and iron as the absorber of positive ions. This gives the hadronic calorimeter in this region a higher interaction length per unit length than the EM calorimeter, causing particles to stop in the calorimeter. The hadronic calorimeter end-cap covers the eta region $1.5 < |\eta| < 3.2$ which experiences a much higher flux of particles. To be able to operate in this environment the active material is liquid argon with copper plate absorbers for the positive ions.

3.2.4.4 Forward Calorimeter

The forward calorimeter (FCal) covers the $3.1 < |\eta| < 4.9$ range and experiences a higher flux of particles than any of the other calorimeter sub-systems. The FCal is separated into electromagnetic and hadronic sections, both of which use liquid argon as the active material, with the electromagnetic layer using copper as the absorber material and the hadronic section utilising tungsten.

3.2.5 Muon Spectrometer

The furthest sub detector from the nominal interaction point, and by far the largest in terms of volume occupied, is the Muon Spectrometer [77]. The Muon Spectrometer consists of two parts: a system for quick identification of muons and a second system for accurately measuring the momentum of muons. The quick identification of muons is achieved using Resistive Plate Chambers (Thin Gap Chambers) in the barrel (end-cap) arranged in three layers which are able to confirm the presence of a muon in ~ 1 ns.

Muons are not stopped in ATLAS so the momentum is determined by accurately determining the radius of curvature of the muon due to the presence of a magnetic field from the toroidal magnets. To determine the radius of curvature the position of the muon needs to be precisely known. This is achieved using monitored drift tubes in the $|\eta| < 2$ region, with an individual resolution of 80 μm, that are arranged into chambers consisting of 6 layers of tubes, with an effective resolution of 40 μm. The $2 < \eta < 2.7$ range experiences a higher flux of particles so Cathode Strip Chambers were installed which can provide an excellent position resolution of 60 μm and withstand the high level of radiation present in this region.

Stage	Time per Event	Rate of Information
L1	2.5 μs	75 kHz
L2	40 ms	3.5 kHz
EF	4 s	200 Hz

TABLE 3.2: Time each stage of the ATLAS trigger system spends analysing an event and the effective data rate after each stage [60].

3.2.6 Trigger System

When the LHC is operating at the design bunch spacing of 25 ns bunch crossings will occur with a frequency of 40 MHz. Combined with multiple interactions per crossing this results in more data being produced than ATLAS can store and keep for analysis. The amount of data that can be stored is determined by available technologies and resources and works out at roughly 200 Hz. Reducing the data down to a rate that can be stored whilst not losing information that is interesting for physics analyses is performed by the ATLAS Trigger and Data Acquisition systems (TDAQ), detailed descriptions of which can be found in [60] and [78].

The trigger system is divided into three different levels: Level 1 (L1), Level 2 (L2) and Event Filter (EF). The amount of time each trigger level spends analysing an event and the rate of data after the trigger is shown in table 3.2. To be able to make a decision in 2.5 μs, L1 triggers only use raw detector information from the calorimeter (with reduced granularity) and from the muon spectrometer (Resistive Plate Chambers and Thin Gap Chambers only) to search for events that contain high momentum objects or a large amount of missing energy. If an event passes an L1 trigger, any region of the calorimeter with transverse energy (E_{T}) above pre-determined thresholds will be marked as a region of interest and investigated in more detail using the full granularity of the calorimeter and the full muon spectrometer information. By accurately reconstructing only the particles in these regions of interest, the L2 trigger set reduces the amount of data to below 3.5 kHz and allows photons or electrons to be distinguished from jets. The EF triggers, the final stage of the trigger system, use information from every sub-detector to fully reconstruct every particle, including track reconstruction to separate photons and electrons, in the regions of interest in any event that passes an L2 trigger. Any event that passes an EF trigger is then permanently stored and made available for data analysis.

Egamma Trigger

Events which contain high energy or multiple photons or electrons (egamma objects) are useful for a number of different analyses. To ensure that these events are kept for later analysis, the egamma triggers have been designed to quickly identify events with single or multiple electrons or photons.

The basic unit of an egamma trigger [79] is the EM calorimeter trigger tower, as shown in figure 3.18. The trigger algorithm uses the energy deposits in a 4×4 array of trigger towers to assess whether they were caused by an egamma object. In the central 2×2 core of trigger towers the energy of any two adjacent towers is summed (i.e. 4 separate calculations), at least one of which must be above a minimum value (threshold) to turn on the trigger. Outside the central core of trigger towers the remaining 12 towers form an isolation ring in which the sum of the E_{T} is required to be below an isolation threshold. This is used ensure that the energy deposit is not due to multiple objects or other objects that are expected to deposit energy over a wider range of trigger towers, such as a jet.

In addition to using information from the EM calorimeter the egamma trigger algorithm also uses the corresponding 16 towers in the hadronic calorimeter. The E_{T} deposits in the 2×2 core and the surrounding ring of 12 towers are summed independently and required to be below pre-set thresholds, acting as two independent hadronic vetoes.

The trigger algorithm uses a 4×4 'overlapping, sliding window' method where, as the name suggests, the boundaries of the 4×4 window slides across all towers meaning each tower is in 16 different window calculations.

The naming convention for egamma triggers is best described with the use of an example: `EF_2g20_loose`. This trigger is used at the event filter stage and requires that there be at least 2 photons in the event that each have a $p_{\mathrm{T}} > 20$ GeV and pass the Loose IsEM menu (see section 4.2.2 for more information on the IsEM menu). If there was a similar trigger that required at least two electrons in an event, then the `g` would be replaced by an `e` and become `EF_2e20_loose`.

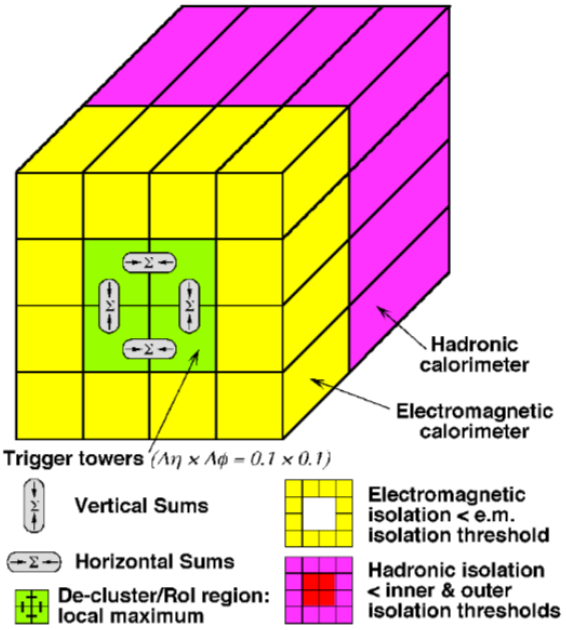

FIGURE 3.18: Diagram highlighting the egamma trigger operation [80].

Chapter 4

Object Reconstruction

In this thesis, the final state that is being searched for contains two photons and a large amount of missing energy from the two gravitinos. It is therefore important that these objects can be reconstructed from the information collected in the ATLAS detector. The reconstruction process for each event, which combines the information collected in the various sub-detectors described in section 3.2 to identify what physics object (i.e. particle) is responsible for the different energy deposits, is described in this chapter. The first stage of this process is to identify the pp interaction vertices and the tracks left by charged particles in the inner detector, as described in section 4.1. The process for reconstructing the different particles that are relevant to these analyses are described separately: electrons and photons in section 4.2, jets in section 4.3, and muons in section 4.4. A visualisation of how these particles are reconstructed is shown in figure 4.1 and more detailed information on the different quality cuts that are applied to these objects, so that they can be used in the 7 TeV and 8 TeV analyses, can be found in Appendix A. Additionally, the method for determining if there is any missing momentum in an event is described in section 4.5 and the method for ensuring that no single particle is reconstructed as two different particles is described in section 4.6.

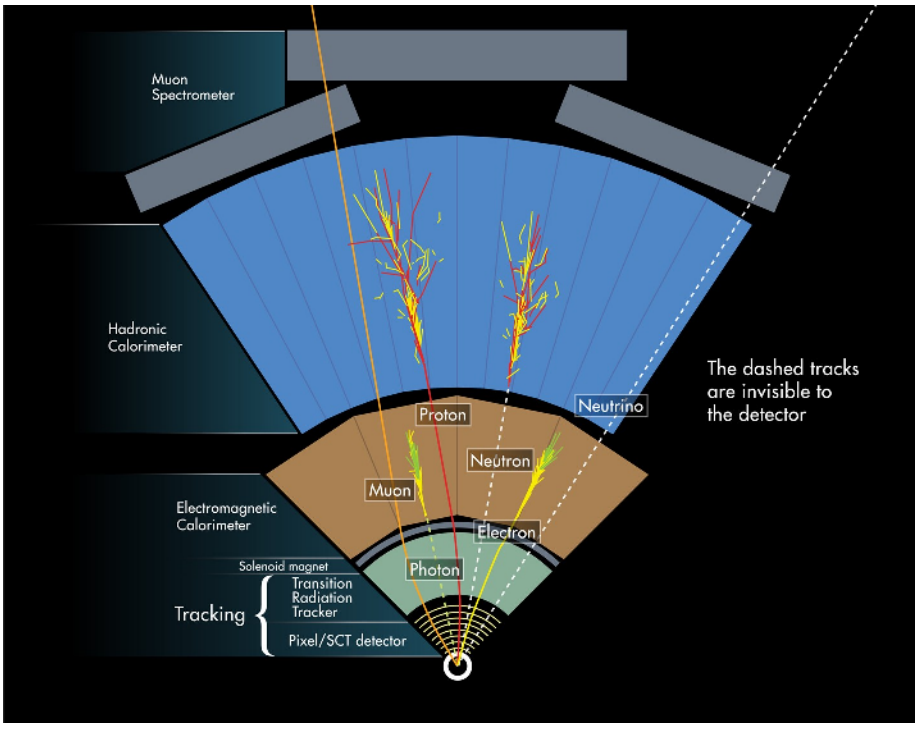

FIGURE 4.1: The signal left by particles in the different ATLAS sub-detectors [81].

4.1 Tracks and Vertices

4.1.1 Track Reconstruction

When a charged particle travels through the ID, the hits it leaves in the different sub-detectors are transformed into 3D SpacePoints [82] and used to reconstruct the path (track) it must have taken. Due to the high luminosity environment there will be multiple pileup interactions in a single beam crossing, see figure 3.4, resulting in a large number of hits that need to be resolved into separate tracks. Two complementary algorithms are used to reconstruct tracks: inside-out and outside-in track reconstruction [82].

The inside-out algorithm starts with SpacePoint pairs in the pixel or SCT detectors, adding new hits that lie in the potential path of a particle moving out into the TRT away from the interaction point. For each new point that could potentially lie on a track candidate, the momentum required for a particle to reach that new point is compared to the momentum required to produce the existing track and if they are compatible the point is added to the track. This process is then repeated for all remaining hits.

The outside-in algorithm starts by looking at track segments in the TRT and working back to hits in the SCT and pixel detector using the same logic as the inside-out algorithm. This is useful for finding secondary particles that may have few or no hits in the SCT or pixel detectors, such as from the conversion of a photon to two electrons. If no hits in SCT or pixel detectors are found to be consistent with a TRT track using this algorithm then a TRT only track is formed.

Given the large number of hits that are produced after every beam crossing many "fake" tracks that don't represent the path of a particle are identified using the two algorithms outlined above. This could be due to different tracks sharing hits or the algorithms extrapolating tracks beyond layers where no hits were observed, but would be expected if the track was produced by a particle, to unrelated hits further from the interaction point. The process of deciding which tracks likely represent a true particle is called ambiguity resolution and is described in a number of sources [82][83].

4.1.2 Primary Vertex Reconstruction

Once all of the tracks have been reconstructed, primary vertices where the initial interactions occurred are identified using the vertex finding algorithm [84]. This algorithm first requires that all tracks have a minimum p_{T} of 400 MeV, then identifies all tracks that are compatible with originating from the same vertex, and finally determines the best position for the vertex. Once all tracks have been associated with a vertex, all of the primary vertices are then ranked in terms of the sum of the p_{T}^2 of all the tracks associated with that vertex. In the 7 TeV and 8 TeV analyses, the primary vertex in any event is the one with the highest $\Sigma_{track} p_{\mathrm{T}}^2$ that also has a minimum of 5 tracks associated with it.

Throughout the course of data taking the radial position of the primary vertex changes very little due to very precise control of bunch spread by the LHC superconducting magnets. However, as can be seen in figure 4.2, there is a relatively large spread in the z position of the primary vertex with a number of collisions taking place with $|z| > 150$ mm. This spread in z can be explained by considering the spread in time of arrival of protons in the main bunch observed in figure 3.6; a spread in the arrival times of the protons is equivalent to the protons being spread along the z-axis and proton collisions can therefore occur away from the centre of the detector.

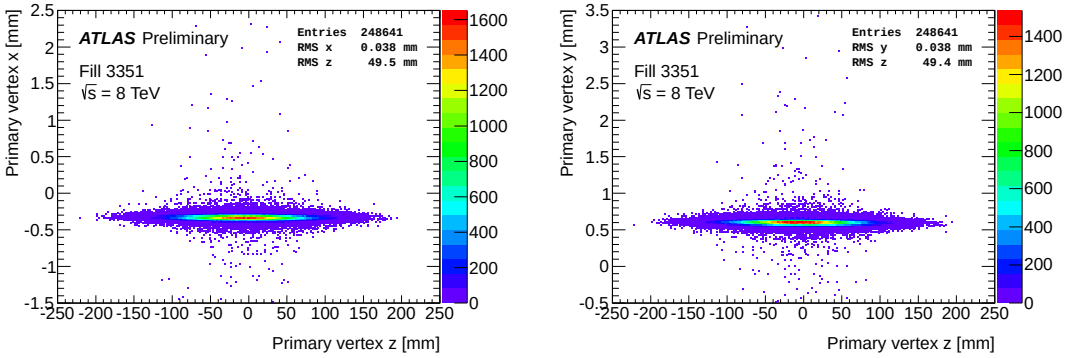

FIGURE 4.2: Primary vertex position in the x-z (left) and y-z (right) planes for a single fill. Per event, only the vertex which has the highest $\Sigma_{track} p_{\mathrm{T}}^2$ which also has 5 or more tracks is shown [85].

4.1.3 Secondary Conversion Vertex Reconstruction

When photons pass through matter there is a chance, proportional to the amount of material, that the photon will undergo a conversion and create an electron pair. The amount of material a photon passes through not only increases with the radius but is dependent on the η of the particle, with a peak at around $|\eta| = 1.7$, as shown in figure 3.13. This η dependence on the amount of material particles encounter results in the probability of a photon converting before the calorimeter system as a function of radius also being η dependent, as shown in figure 4.3.

4.2 Electrons and Photons

In the ATLAS detector, electrons and photons both produce electromagnetic showers in the EM calorimeter; discrimination between the two objects is primarily achieved by the success or failure of attempts to match a track in the inner detector to the shower. The process by which electrons and photons are reconstructed is described below.

4.2.1 Classifying Electrons and Photons

The first stage of identifying photons or electrons starts with an algorithm that searches every 5×5 (in $\eta \times \phi$) cluster of towers, using a sliding window algorithm [86], in the second layer of the EM calorimeter searching for cells with a local maximum energy. If a

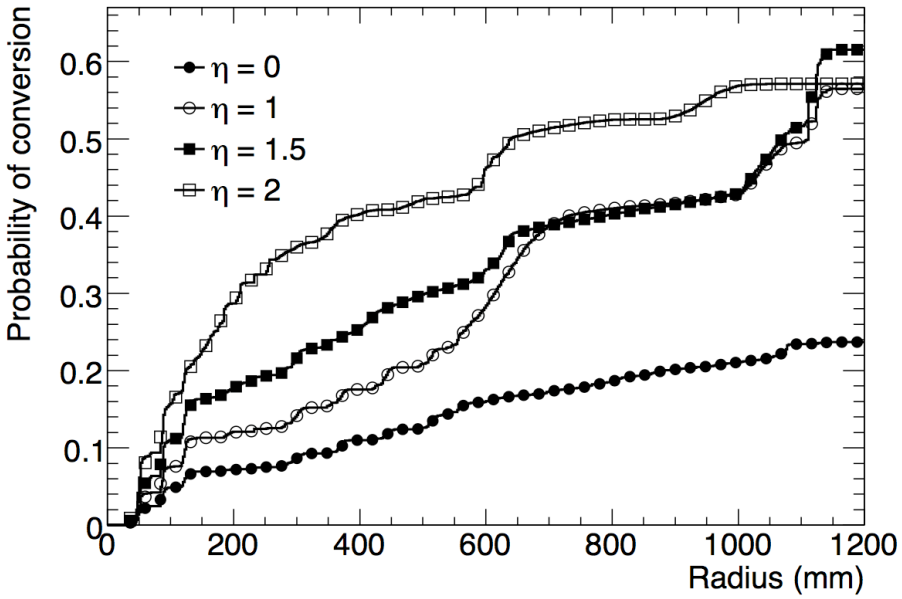

FIGURE 4.3: Probability of a photon to have converted as a function of radius for different values of pseudorapidity. All photons were required to have $p_{\mathrm{T}} > 1$ GeV [78].

maximum is found with E_{T} greater than 2.5 GeV then the energy from the other layers of the calorimeter in the same window are combined to create a seed cluster. The total energy of the cluster is combined using:

$$E_{rec} = \lambda(b + \omega_{PS}E_{PS} + E_1 + E_2 + \omega_3 E_3), \tag{4.1}$$

where E_i is the energy in the ith layer of the calorimeter with $i = PS$ corresponding to the energy in the presampler layer. The parameters λ, b, ω_{PS} and ω_3 are calculated by comparing the true and reconstructed energies of particles in Monte Carlo samples [87] with b correcting for energy lost before the presampler (see 3.2.4.1).

In addition to the energy of the particle it is also important to know the position in η and ϕ of the cluster so tracks can be matched to it. Initially, the energy-weighted barycentre of the cluster is calculated in each layer of the EM calorimeter separately and corrected for any biases which are known [87] to affect the position measurement. Once these corrections have been applied the measurements from the first and second layers are combined to give the position of the cluster.

Once a seed cluster has been identified and the position corrected the next task is to attempt to match a track from the ID to it. Tracks are extrapolated from the last hit in the ID into the EM calorimeter and must be within 0.05 in η and 0.10 in ϕ of the cluster. The momentum of the track and energy of the cluster are also required to be compatible with a maximum p/E ratio of 10. If more than one track passes these requirements then the tracks are ranked in order of the quality of the track and how close the track is to the cluster position as measured by $R = \sqrt{(\Delta\eta)^2 + (\Delta\phi)^2}$.

After the final track matching process has been completed the egamma object can now be classified as a photon or an electron:

- If a good quality track with hits in the pixel detector is matched to a seed cluster then the egamma object is an electron,
- If a good quality track that comes from a conversion vertex is matched to a seed cluster than the egamma object is a converted photon,
- If a good quality track cannot be matched to a seed cluster then the egamma object is a photon.

After the egamma object has been classified a final calibration is applied to the energy of the cluster. The number of towers in $\eta \times \phi$ in the window used to calculate the energy cluster in the EM calorimeter is optimised for clusters in the barrel, with a 3×7 window used for electrons or converted photons and a 3×5 window used for unconverted photons. This calibration is not applied to clusters in the end-cap because the effect of the magnetic field is smaller [86].

4.2.2 IsEM Menu

The photon identification algorithms are efficient at classifying prompt photons as photons, however, a lot of other objects can also be classified as photons and are referred to as fake photons. These objects can be broadly separated into two categories: electrons with badly reconstructed tracks, and jets (e.g. $\pi^0 \to \gamma\gamma$) which deposit a large fraction of their total energy in the EM calorimeter. A series of variables which describe how the EM shower produced by egamma objects develops (i.e. shower shaper) in the EM

Category	Description	Name	Loose	Tight
Acceptance	$\|\eta\| < 2.37$, $1.37 < \|\eta\| < 1.52$ excluded	-	✔	✔
Hadronic leakage	Ratio of E_T in the first sampling of the hadronic calorimeter to E_T of the EM cluster (used over the range $\|\eta\| < 0.8$ and $\|\eta\| > 1.37$)	R_{had1}	✔	✔
	Ratio of E_T in all the hadronic calorimeter to E_T of the EM cluster (used over the range $0.8 < \|\eta\| < 1.37$)	R_{had}	✔	✔
EM Middle layer	Ratio in η of cell energies in 3×7 versus 7×7 cells	R_η	✔	✔
	Lateral width of the shower	$w_{\eta 2}$	✔	✔
	Ratio in ϕ of cell energies in 3×3 and 3×7 cells	R_ϕ		✔
EM Strip layer	Shower width for three strips around maximum strip	w_{s3}		✔
	Total lateral shower width	w_{stot}		✔
	Fraction of energy outside core of three central strips but within seven strips	F_{side}		✔
	Difference between the energy associated with the second maximum in the strip layer, and the energy reconstructed in the strip with the minimal value found between the first and second maxima	ΔE		✔
	Ratio of the energy difference associated with the largest and second largest energy deposits over the sum of these energies	E_{ratio}		✔

TABLE 4.1: Shower shape variables used for the Loose and Tight photon definitions [88].

calorimeter have been identified to help separate true photons from this background. These shower shape variables (SSV) are described in table 4.1 and by comparing the distributions of these SSVs for jets and photons, as shown in figures 4.4 and 4.5, the IsEM cuts were developed to reduce the background in photon samples. For photons these cuts are separated into two menus, Loose IsEM and Tight IsEM, with the SSVs used in each menu highlighted in table 4.1. Any photon that passes the Tight IsEM cuts is labelled a Tight photon, while any photon that fails Tight but passes the Loose IsEM cuts is labelled a Loose photon.

The Loose IsEM set of cuts makes use the SSVs that measure energy leakage into the hadronic calorimeter and the SSVs in the second layer of the EM calorimeter. Figure 4.6 shows that, for both converted and unconverted photons, the efficiency of passing the Loose IsEM remains high for photons with $E_{\mathrm{T}} > 50$ GeV. The Tight IsEM cuts use the same discriminating variables used in the Loose cuts, with stricter cuts, combined with discriminating variables based on the EM shower in the first layer of the EM calorimeter. The higher granularity of the first layer of the EM calorimeter allows for cuts which are more optimised to true photons and remove as much background as possible. This can be seen in seen in table 4.2, which shows that the total rejection of jets in an MC sample increases by approximately an order of magnitude when going from Loose to Tight.

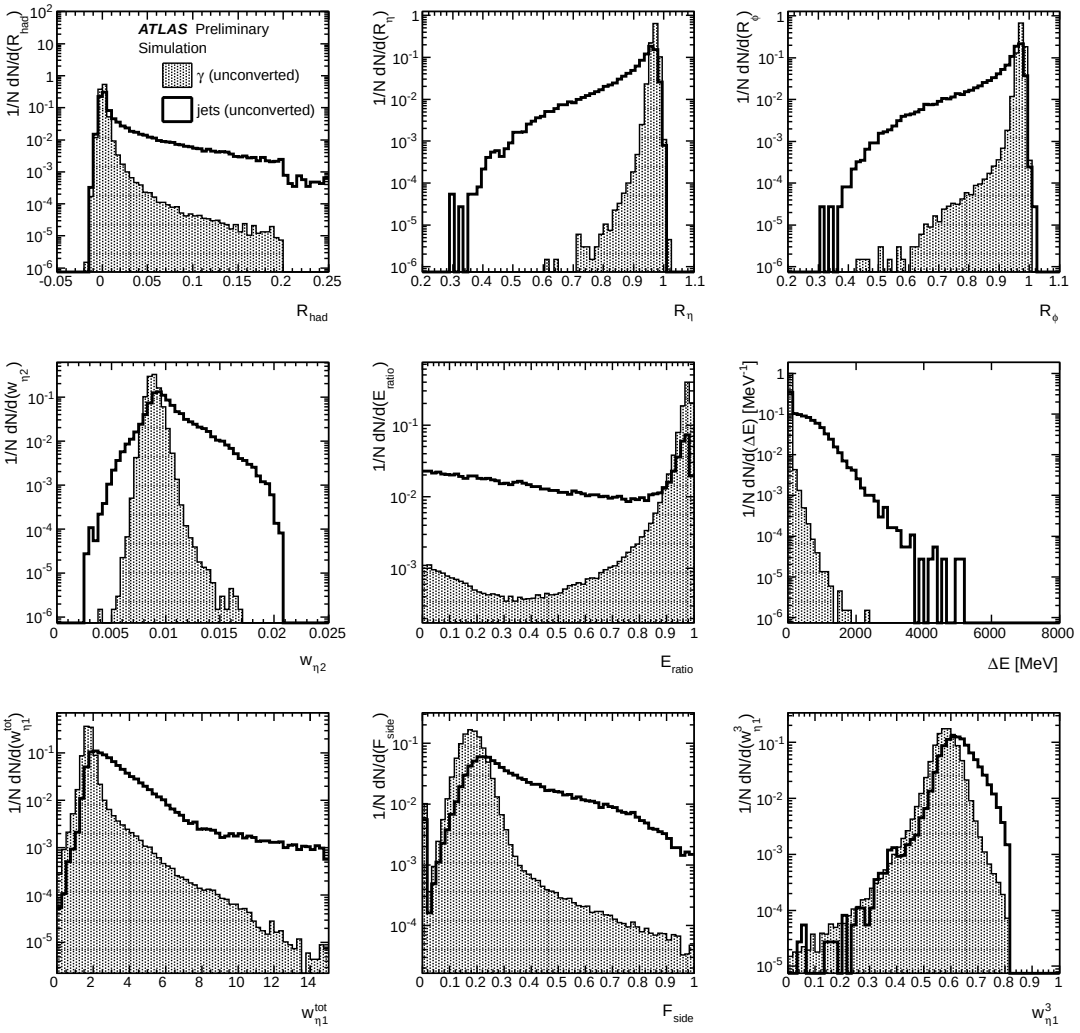

FIGURE 4.4: Normalised distribution of the shower shape variables for true and fake unconverted photons before selections have taken place. Photons have $E_{\mathrm{T}} > 20$ GeV and are in the range $0 < |\eta| < 0.6$ [89].

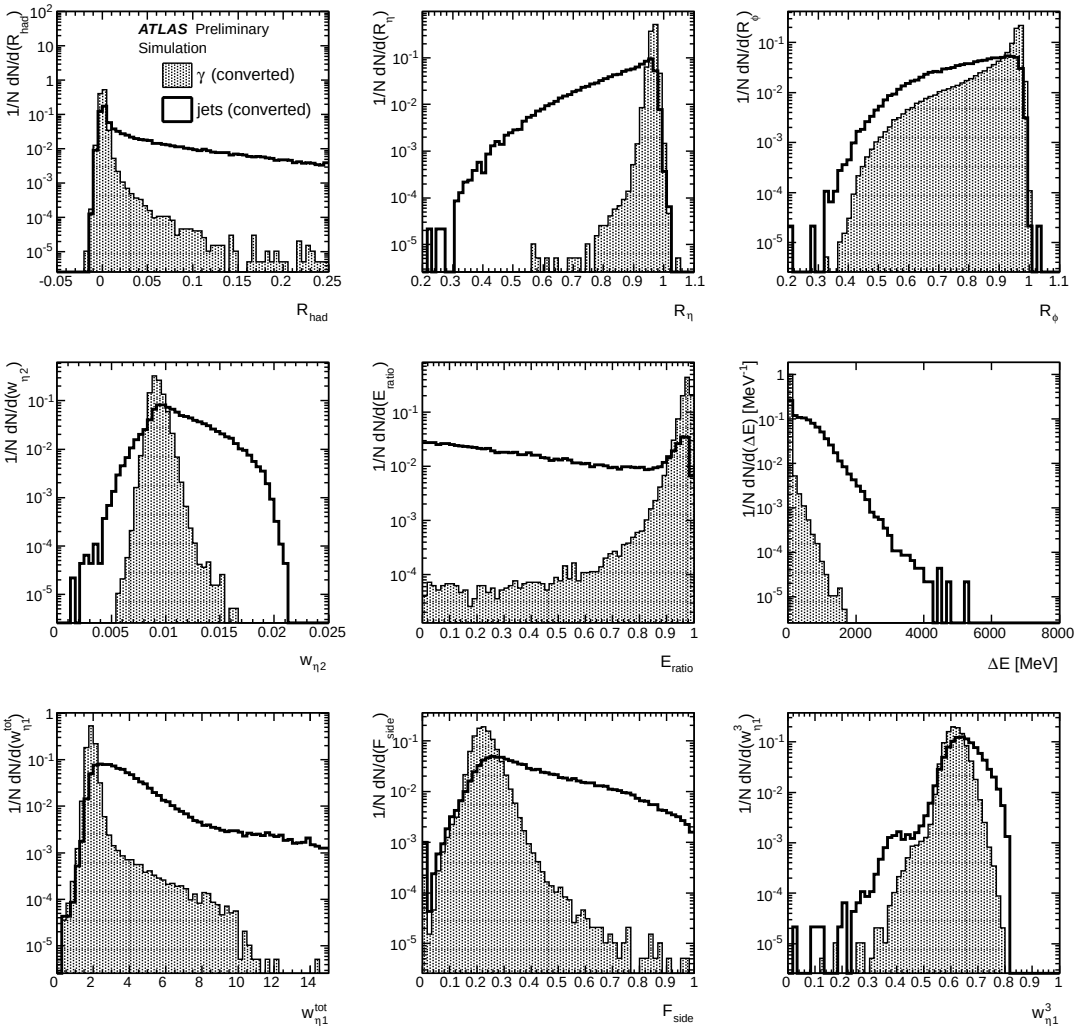

FIGURE 4.5: Normalised distribution of the shower shape variables for true and fake converted photons before selections have taken place. Photons have $E_{\mathrm{T}} > 20$ GeV and are in the range $0 < |\eta| < 0.6$ [89].

Loose IsEM			Tight IsEM		
all jets	quark jets	gluon jets	all jets	quark jets	gluon jets
940 ± 10	368 ± 6	2210 ± 60	5100 ± 200	1680 ± 60	20100 ± 1500

TABLE 4.2: Expected jet background rejection count, using the photon IsEM menu, for jets with $E_{\mathrm{T}} > 40$ GeV based on 0.1 pb^{-1} of MC produced at $\sqrt{s} = 10$ TeV. Quoted errors are statistical only [89].

This large increase in background rejection comes at the cost of small reduction in the efficiency of prompt photons passing the IsEM cuts, as can be seen in figure 4.6.

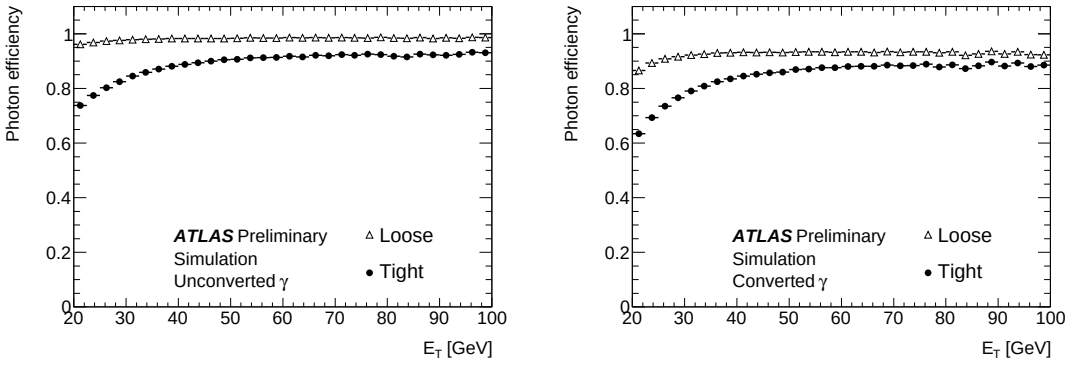

(a) (b)

FIGURE 4.6: Expected efficiency of simulated unconverted (a) and converted (b) photons passing the Loose and Tight IsEM cuts [89].

Due to the similarities in how the shower of photons and electrons develop, the IsEM cuts used to identify Loose photons are also used to identify Loose electrons. However, converted photons are expected to have showers that are wider than unconverted photons and the shower produced by electrons is expected to be wider still. These differences should be apparent in the first layer of the EM calorimeter, due to the fine granularity. Therefore, three separate Tight IsEM cut menus have been developed. The electron IsEM menu also contains an additional quality level, Medium, between Loose and Tight [90].

4.2.3 Electron and Photon Corrections

After photons have been reconstructed and identified in data and MC there are corrections that need to be made to correct for known issues in the reconstruction process. Firstly, the energy reconstructed in the EM calorimeter is not the true energy of a photon

as energy can be lost in a number of ways: to material upstream of the EM calorimeter, see section 3.2.4.1; beyond the EM calorimeter; and laterally due to the finite size of the cluster towers. Due to the design of the EM calorimeter, which has cells that point back to the nominal interaction point, the amount of energy lost will not only depend on the η and ϕ of a particle, but also the z position of the primary vertex. Studies using electrons from $Z \rightarrow ee$ decays [91] determined the corrections [92] that need to be made to the energy scale and resolution of electrons and photons to recover the lost energy.

In early data taking [93], it was apparent that the distributions of several of the shower shape variables used in the IsEM menus were different in data and MC. To ensure that the efficiency of electrons and photons passing the IsEM cuts menu is correctly modelled in MC, a procedure was introduced to shift the value of each shower shape variable in MC so that the data and MC distributions match [94].

4.3 Jets

The first step in reconstructing jets in the topological cluster algorithm [86] method is to identify the cells in the EM calorimeter with the highest energy as jet candidates. If the energy of one of these candidate cells is above the expected noise level in cells ($\sigma_{\text{cell,noise}}$) with a significance of $\Gamma = E_{\text{cell}}/\sigma_{\text{cell, noise}} > 4$ then that cell becomes a jet seed. The algorithm starts with the highest energy seed, adds all adjacent cells to the jet cluster, and then compares the energy of the cells that are adjacent to the expanded cluster to $\sigma_{\text{cell, noise}}$. If $|\Gamma| > 2$ for any of the adjacent cells they are added to the cluster. This process is repeated for any new cells that are added to the cluster until no cell has a neighbour with $|\Gamma| > 2$ that isn't already included in the cluster. The algorithm then starts again with the highest energy seed that isn't already in a cluster and iterates until all seeds are included in a cluster.

After topological clusters have been built around the jet seed cells, the anti-kt jet clustering algorithm [95] is used to determine if clusters contain more than one jet and to calculate the energy of each unique jet. An energy cone with R =0.4 is built around each jet seed with any cell in the topological cluster in this cone contributing to the energy of that jet. If one jet seed lies within ΔR <0.4 of another then the two jets are combined into one single jet with the position being an energy weighted combination of the two.

If two jets are separated by ΔR >0.4 but the cones overlap then the shared cells are assigned to the jet with the highest energy seed to avoid double counting. This results in the majority of the reconstructed jets being conical and having a regular shape which is not always the case in some jet reconstruction algorithms, as shown in figure 4.7.

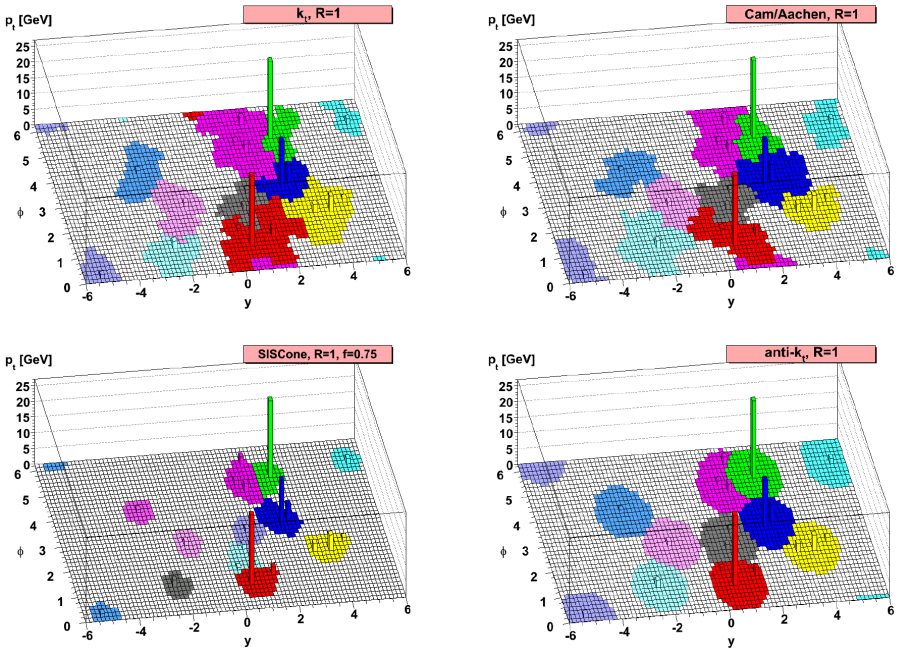

FIGURE 4.7: The results of four different jet algorithms with the same inputs [95].

4.4 Muons

Muons are not stopped by the ATLAS detector: they leave a track in the ID, calorimeter system, and muon spectrometer before escaping into the surrounding rocks. Several algorithms have been designed to attempt to match signals in the muon spectrometer with tracks in the ID and the calorimeter[96][97]. Different classes of muons are defined [98][99] based on which of the signals can be combined and are consistent with a single particle track. For the analysis work presented in this thesis only two categories of muons will be considered:

- **Combined Staco muons** are reconstructed by creating tracks from hits in the muon spectrometer and extrapolating this back to the ID where they are matched with a track. This is performed using using the staco [96] family of algorithms.

- **Stand alone muons** use the same method as the combined staco muons but no track in the ID can be matched. These are important for removing background sources of secondary muons such as the decay of pions or cosmic muons that don't pass through the centre of the detector.

Since they can pass through a large amount of material without stopping it is also possible for muons to reach ATLAS from the outside environment. Accurate reconstruction of muons is therefore essential to ensure this source of background (cosmic muons) is identified. Any event containing a cosmic muon is excluded from physics analyses.

4.5 Missing Transverse Momentum

Inferring the presence of a gravitino relies on the basic concept that protons in the LHC only have momentum in the z direction when they reach ATLAS. Therefore, the momentum in the transverse direction of all particles in any interaction must sum up to zero to conserve momentum. If a particle doesn't interact with the ATLAS detector then it will carry momentum away with it. When the p_{T} of all the remaining particles in this event is summed up it will not equal zero due to missing transverse momentum ($E_{\mathrm{T}}^{\mathrm{miss}}$). The $E_{\mathrm{T}}^{\mathrm{miss}}$ for a given event is calculated using a different method for the 7 TeV and 8 TeV analyses. For the 7 TeV analysis the $E_{\mathrm{T}}^{\mathrm{miss}}$ in the calorimeter [100] is calculated using equation 4.2:

$$\begin{aligned} E_{\mathrm{T}}^{\mathrm{miss}}(x)_{Cal} &\equiv -\sum_{i=1}^{N_{\mathrm{cell}}} E_i \sin\theta_i \cos\phi_i \\ E_{\mathrm{T}}^{\mathrm{miss}}(y)_{Cal} &\equiv -\sum_{i=1}^{N_{\mathrm{cell}}} E_i \sin\theta_i \sin\phi_i \\ E_{\mathrm{T}}^{\mathrm{miss}} &\equiv \sqrt{\left(E_{\mathrm{T}}^{\mathrm{miss}}(x)_{Cal}\right)^2 + \left(E_{\mathrm{T}}^{\mathrm{miss}}(y)_{Cal}\right)^2} \end{aligned} \tag{4.2}$$

where E_i is the energy in any calorimeter cell that has been associated to any reconstructed object in the event with $|\eta| < 4.9$. These energies are calibrated using the Local Hadron Calibration [101] method, as described in section 4.3, which includes corrections for energy loss upstream of the calorimeter ($METLocHadTopo$). The energies

also need to be corrected due to the presence of muons, which deposit a fraction of their energy in the calorimeter. The total energy as calculated from the muon spectrometer ($METMuonBoy$) needs to be corrected for the energy deposited in the calorimeter ($METRefMuonTrack$), which is already included in the original $E_{\mathrm{T}}^{\mathrm{miss}}$ calculation, before being applied as a correction to the $E_{\mathrm{T}}^{\mathrm{miss}}$ components from equation 4.2:

$$\begin{aligned} E_{\mathrm{T}}^{\mathrm{miss}}(x) \equiv \quad & E_{\mathrm{T}}^{\mathrm{miss}}(x)_{Cal} + METLocHadTopo(x) + METMuonBoy(x) \\ & - METRefMuonTrack(x) \end{aligned} \tag{4.3}$$

In the 8 TeV analysis the $E_{\mathrm{T}}^{\mathrm{miss}}$ calculation [102] is also performed using equation 4.2, however the sum is over objects in the event that have been reconstructed with any calibrations to the energy already applied.

A problem common to both the 7 TeV and 8 TeV analyses that affects the resolution of the $E_{\mathrm{T}}^{\mathrm{miss}}$ calculation is the contribution from pileup in the detector. Assigning a particle to the wrong primary vertex introduces momentum that won't be balanced by other particles in the event and will be a source of fake $E_{\mathrm{T}}^{\mathrm{miss}}$. The potential impact on the $E_{\mathrm{T}}^{\mathrm{miss}}$ has been studied [100][102] and is included in these analyses as part of the pileup systematic uncertainties in section 8.1.8.

4.6 Overlap

After all energy deposits and hits have been assigned to objects, it is possible for an object to be pass all of the cuts for more than one type of particle and be present in the final object samples more than once. The following overlap removal process prevents double counting of objects:

- If the clusters of a photon and an electron are found within $\Delta R < 0.01$, the object is classified as an electron and the overlapping photon is removed from the photon sample.
- If a photon (electron) and a jet are found within $\Delta R < 0.2$, the object is classified as a photon (electron) and the overlapping jet is removed from the jet sample

- If a photon (electron) and a jet are found within 0.2 $\Delta R < 0.4$, the object is classified as a jet and the overlapping photon (electron) is removed from the photon (electron) sample.

- If a muon and a jet are found within $\Delta R < 0.4$, the object is classified as a jet and the overlapping muon is removed from the muon sample

Chapter 5

Signal Monte Carlo Samples and Studies

In this chapter, the signal Monte Carlo (MC) that is produced to model SPS8 events is introduced and studies performed with this MC are presented. The procedure used to generate the MC and the cross section for different signal samples is given in section 5.1. As previously stated, non-prompt photons from the decay of long-lived neutralinos will leave two distinctive signatures in the ATLAS detector: they will arrive delayed compared to prompt photons, primarily due to the β distribution of the neutralinos; and the shower produced in the EM calorimeter does not point back (i.e. it is non-pointing) to the PV. These variables and how they are measured are described in section 5.2. Many of the predictions made for SPS8 events cannot be verified in data since there is no data sample with events that cover the same expected pointing and timing ranges of signal photons. Therefore, it is not possible to test the detector response to very non-pointing or delayed photons. This is particularly important for the non-pointing photons since changes in the shower shape could affect the efficiency of photons passing the IsEM cuts. Investigations into the reliability of the Monte Carlo predictions for non-pointing photons are presented in section 5.3. In section 5.4, the efficiency of SPS8 events making it into the signal region and the expected signal yields are given for a range of Λ values and neutrino lifetimes.

5.1 Signal Monte Carlo

5.1.1 Generation and Theoretical Cross-sections

All of the MC used in this thesis was produced centrally using the ATLAS simulation infrastructure [103], where events in a GEANT4 [104] based simulation of the ATLAS detector are reconstructed with the same algorithms used to reconstruct the data. The detector pileup in the 7 TeV and 8 TeV signal samples was designed to replicate the pileup observed in data (see figure 3.4) as closely as possible. However, pileup conditions changed over the different data taking periods and the signal MC samples need to be reweighted [105] so that the pileup distribution exactly matches the distribution observed in the diphoton data.

All of the signal MC was generated using the HERWIG++ generator, version 2.4.2 [106], with MRST 2007 LO [107] parton density distributions. The samples were generated as mGMSB events with 4 of the model parameters fixed to the values stated in section 2.2.6 (sign(μ) >0, tanβ =15, M_m =2Λ, N_m =1) for a range of Λ and neutralino lifetime (τ) values. As has previously been stated in section 2.2.6, in these analyses the branching ratio of $\widetilde{\chi_1^0} \rightarrow \gamma\widetilde{G}$ is set to 100 % even though the theoretical value is closer to 85 %. Putting these parameters into ISAJET [108] (version 7.80) the full SPS8 mass spectrum, branching ratios, and cross-sections can be calculated.

For the 7 TeV analysis, MC signal samples were generated containing between 10000 and 40000 events for 15 different Λ values from 70 TeV to 210 TeV, with at least 1 τ value for each Λ. To be able to explore SPS8 models with different τ values a reweighting procedure was applied, as described in Appendix B, to produce a 2D signal grid in Λ and τ. The samples that were generated are shown in table 5.1 along with the LO and NLO + NLL cross sections and the associated uncertainty.

For the 8 TeV analysis all MC signal samples were generated containing 40000 events and were generated for 28 different Λ values from 70 TeV to 400 TeV. Samples with lower Λ values were generated with τ = 6 ns while samples with larger Λ values were generated with τ = 2 ns. As in the 7 TeV analysis, a reweighting procedure described in Appendix B was applied so that models with different τ values can be explored. The samples that were generated are shown in 5.2 along with the NLO + NLL cross section and the associated uncertainty.

Λ[TeV]	τ[ns]	σ(LO)[pb]	σ(NLO + NLL)[pb]	Uncert.(%)	Events
70	2	1.71	2.69	6.3	40000
80	2	0.794	1.23	6.4	20000
90	1	0.403	0.609	6.3	20000
90	2				40000
90	4				20000
90	6				40000
100	1	0.221	0.324	6.1	20000
100	2				40000
100	4				20000
100	6				40000
110	1	0.129	0.184	5.8	20000
110	2				40000
110	4				20000
110	6				40000
120	0	79.5×10^{-2}	0.110	5.5	10000
120	1				20000
120	2				40000
120	4				20000
120	6				40000
120	10				40000
130	1	51.2×10^{-2}	68.4×10^{-2}	5.2	20000
130	2				40000
130	4				20000
130	6				40000
140	2	34.0×10^{-2}	44.2×10^{-2}	4.9	20000
150	2	23.2×10^{-2}	29.4×10^{-2}	4.7	20000
160	2	16.2×10^{-2}	20.2×10^{-2}	4.7	20000
170	2	11.5×10^{-2}	14.1×10^{-2}	4.7	20000
180	2	8.30×10^{-3}	9.98×10^{-3}	4.8	20000
190	2	6.06×10^{-3}	7.17×10^{-3}	4.7	20000
200	2	4.44×10^{-3}	5.12×10^{-3}	4.9	20000
210	2	3.30×10^{-3}	3.78×10^{-3}	5.0	20000

TABLE 5.1: The total LO and NLO cross sections for the 7 TeV SPS8 signal points generated for this analysis, together with their PDF and scale uncertainties (see Appendix C) [57] .

Λ[TeV]	τ[ns]	σ(NLO + NLL)[pb]	Uncert.(%)
70	6	4.25	12.3
80	6	1.98	12.6
90	6	0.993	13.1
100	6	0.535	13.3
110	6	0.304	13.4
120	6	0.182	13.2
130	6	0.114	13.0
140	6	7.38×10^{-2}	12.8
150	6	4.93×10^{-2}	12.2
160	6	3.38×10^{-2}	11.7
150	2	4.93×10^{-2}	12.2
160	2	3.38×10^{-2}	11.7
170	2	2.38×10^{-2}	11.3
180	2	1.71×10^{-2}	10.9
190	2	1.25×10^{-2}	10.5
200	2	9.20×10^{-3}	10.2
210	2	6.87×10^{-3}	10.1
220	2	5.18×10^{-3}	9.70
230	2	3.94×10^{-3}	9.81
240	2	3.02×10^{-3}	9.91
250	2	2.32×10^{-3}	9.47
260	2	1.80×10^{-3}	9.75
270	2	1.40×10^{-3}	9.75
280	2	1.09×10^{-3}	9.84
290	2	8.55×10^{-4}	9.92
300	2	6.71×10^{-4}	9.89
310	2	5.29×10^{-4}	10.1
320	2	4.19×10^{-4}	10.5
350	2	2.10×10^{-4}	11.3
400	2	6.87×10^{-5}	14.1

TABLE 5.2: The total NLO+NLL cross sections for the 8 TeV SPS8 signal points generated for this analysis, together with their PDF and scale uncertainties (see Appendix C) [59].

5.1.2 SPS8 Signal Kinematics

The SPS8 MC samples were used to study the properties of the final state in signal events and how this is expected to change for different Λ and τ values. This is essential for developing an analysis strategy that is able to distinguish between signal and background events. For these analyses, part of this strategy is determining a minimum value for the p_{T} of photons that removes as many background events as possible while still having a good efficiency for signal events. A similar trade off between background suppression and signal efficiency is involved in the selection of the $E_{\mathrm{T}}^{\mathrm{miss}}$ cut for the signal region.

To avoid biasing the analysis by optimising for specific lifetimes, only the kinematics of prompt SPS8 signal samples, as shown in figure 5.1, were considered during the selection of the signal region.

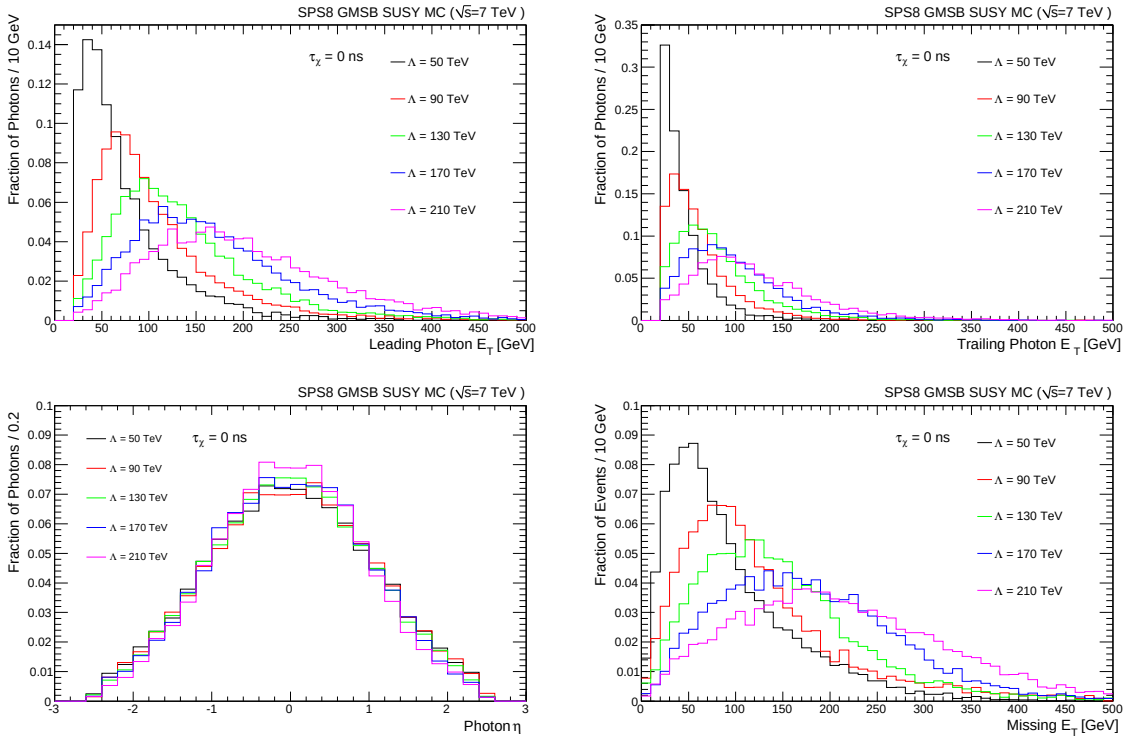

FIGURE 5.1: Unit-normalised distributions of several kinematic variables for several Λ values on the GMSB SPS8 model line. The variables plotted are (upper left) p_{T} of the leading photon, and (upper right) p_{T} of the sub-leading photon, (lower left) η spectra of the two photons, and (lower right) $E_{\mathrm{T}}^{\mathrm{miss}}$. [57]

5.1.3 Signal Region

SPS8 events are expected to contain at least two photons and a large amount of $E_{\mathrm{T}}^{\mathrm{miss}}$ in the final state, however there are many SM processes that can result in a similar final state. In the 7 TeV analysis a signal region was constructed requiring one photon to be Tight, to reduce the number of events containing fake photons, and the other to be at least Loose and detected in the barrel, to increase the sensitivity to non-pointing photons (see section 5.3.1), in what is called a Tight-Loose (TL) selection. As will be explained in section 7.1, only the information from the Loose photon will be used in the limit setting procedure. Therefore, if both photons pass the Tight cuts one photon will be assigned the Loose tag: if only one is detected in the barrel this will be given the Loose tag, if both are detected in the barrel then the Loose tag will be assigned to

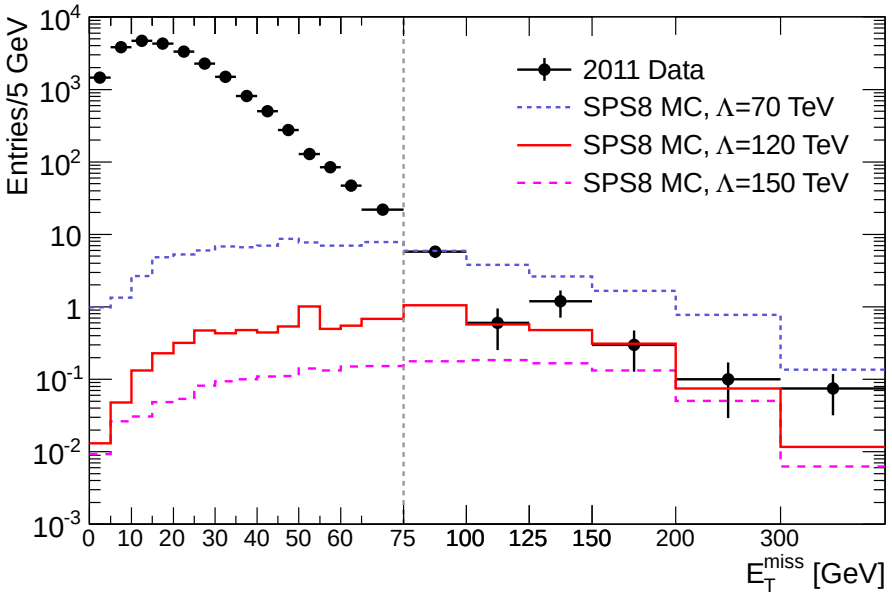

FIGURE 5.2: The $E_{\mathrm{T}}^{\mathrm{miss}}$ distribution for events in the selected diphoton sample using the full 2011 dataset. The predicted SPS8 signal contributions are shown for three reference grid points with a neutralino lifetime of 10 ns. The right-most bin contains all events with values of $E_{\mathrm{T}}^{\mathrm{miss}}$ beyond 300 GeV [57].

the photon with the lowest energy. Figure 5.2 shows that a large $E_{\mathrm{T}}^{\mathrm{miss}}$ cut can greatly reduce the number of diphoton events relative to the expected number of signal events. Analysing data from period K (see section 6.1) showed that an $E_{\mathrm{T}}^{\mathrm{miss}}$ cut of 75 GeV reduces the number of background diphoton events by over 99.8% with a much smaller impact on the various signal models. This $E_{\mathrm{T}}^{\mathrm{miss}}$ cut was found to be efficient across the entire signal grid, allowing a single signal region to be constructed for the entire analysis.

In the 8 TeV analysis, better understanding of the signal and background samples allowed the loosening of the photon identification requirements to a Loose-Loose (LL) selection to further increase the sensitivity to non-prompt photons. The $E_{\mathrm{T}}^{\mathrm{miss}}$ cut of the signal region was kept at 75 GeV as it was found to still be an efficient cut across the signal grid.

5.2 Non-Prompt Photons

In this section the non-pointing and delayed timing measurements that will be used to increase the sensitivity to SPS8 events in the signal region are introduced. The

relationship between the two variables for signal and background events is also discussed in section 5.2.3.

5.2.1 Non-Pointing Measurement

As figure 5.3 highlights, when a long-lived neutralino decays to a photon the resulting shower produced in the EM calorimeter will point back to the decay vertex of the neutralino, and therefore a different point on the z axis (z_{DCA}), rather than the primary vertex (z_{PV}) where the neutralino was produced. Using equation 3.6, z_{DCA} can be calculated for a non-prompt photon, with neutralinos that decay further away from the primary vertex expected to produce photons with larger z_{DCA} values. However, since both z_{DCA} and z_{PV} are measured relative to the nominal interaction point, a large displacement in the primary vertex will also result in a large z_{DCA} value even for prompt photons. Figure 4.2 shows that during data taking the primary vertex can be displaced from the nominal interaction point by up to 250 mm. To remove the contribution to the pointing measurement from the primary vertex position a new pointing variable, z_{γ}, defined as:

$$z_{\gamma} = z_{\mathrm{DCA}} - z_{\mathrm{PV}} \tag{5.1}$$

is used to quantify how non-pointing a photon is.

To be able to use z_{γ} as the pointing variable, the resolution of the calorimeter needs to be determined for the range of z_{DCA} that will be used in the analyses. However, no data sample exists with z_{DCA} values that are as large as those predicted for SPS8 events. Instead, electrons from $Z \rightarrow ee$ data and MC samples are used to model the resolution of the calorimeter, over the range where there is enough statistics, and compared to the resolution predicted by the signal MC. If the resolutions agree, this suggests that the MC is correctly modelling how the shower develops as photons become more non-pointing and the signal MC can be used to estimate the resolution at larger z_{DCA} values. The reasons why the $Z \rightarrow ee$ sample can be used to model photons, including a basic description of the tag and probe method used in this study, are given in section 6.2.3. For this study, z_{PV} from the electrons is used to model z_{DCA}, rather than the z_{DCA} measurement from the electron shower, due to it being more accurate. The calorimeter

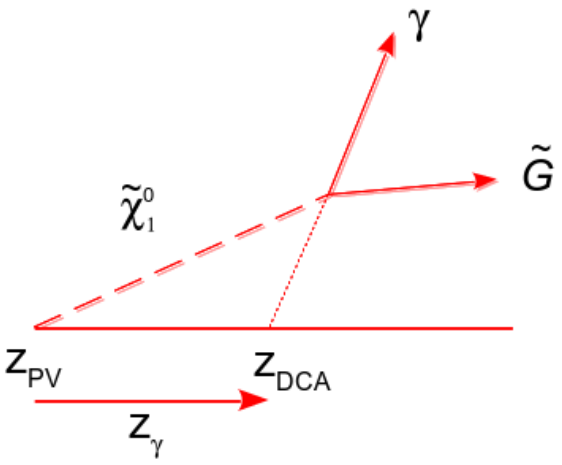

FIGURE 5.3: Cartoon showing how the decay of a long-lived neutralino to a photon can result in the shower in the EM calorimeter pointing back to the neutralino decay vertex and a point on the z axis (z_{DCA}) different to the primary vertex (z_{PV}). As explained in the text, the difference between z_{PV} and z_{DCA} is the pointing variable z_γ.

resolution is estimated using the $Z \rightarrow ee$ samples by taking the difference between the z_{PV} and z_{DCA} values for electrons over different z_{PV} ranges and then fitting a Gaussian function to the distributions. For the SPS8 signal MC, the calorimeter resolution for photons is calculated by taking the difference between the z_{DCA} value that is used as an input to produce the MC and the z_{DCA} value after the MC has been reconstructed, over different z_{DCA} ranges and then fitting a Gaussian function to the distributions.

Figure 5.4 (left) compares the calorimeter resolution for two prompt diphoton MC samples and a di-electron sample and it can be seen that they are in good agreement. Figure 5.4 (right) compares the calorimeter resolution for two different $Z \rightarrow ee$ data samples with a $Z \rightarrow ee$ MC sample and shows that they are in good agreement. Taking figure 5.4 as a whole shows that, over the z_{PV} range where data exists, the calorimeter response to photons and electrons in MC is similar and that the electron MC agrees with the data collected at 7 TeV. Therefore, since SPS8 signal MC is found to agree with $Z \rightarrow ee$ MC and data at small and intermediate z_{DCA} values, as shown in figure 5.5, it can be used to estimate the calorimeter resolution for large z_{DCA} values. A similar method to estimate the calorimeter resolution was performed for the 8 TeV data which also found the $Z \rightarrow ee$ MC and data to be in good agreement with the photon samples, as shown in figure 5.6.

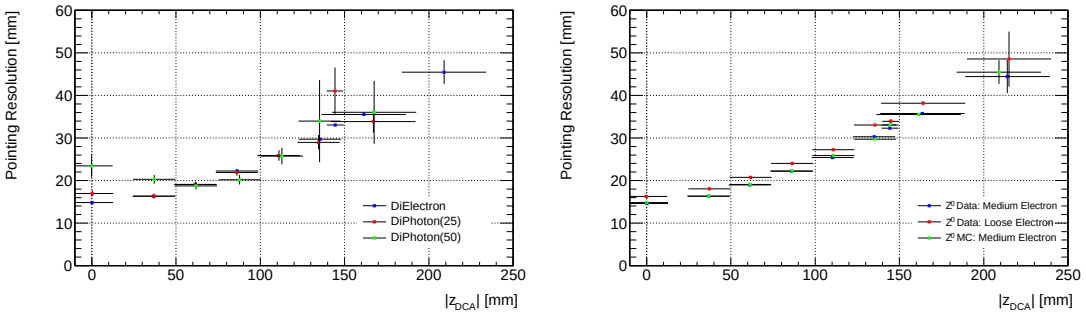

FIGURE 5.4: Pointing resolution, as a function of z_{DCA}, for prompt diphoton and di-electron samples at 7 TeV detected in the barrel. (Left) resolutions for a 25 GeV di-electron and 25 GeV & 50 GeV diphoton MC samples. (Right) resolution for electrons from $Z^0 \rightarrow ee$ data and MC samples. In both figures, the electron resolution is the difference between z_{PV} and z_{DCA} while the photon resolution is the difference between z_{DCA} value used as an input for the MC and the z_{DCA} value after the MC has been produced and the photon reconstructed.

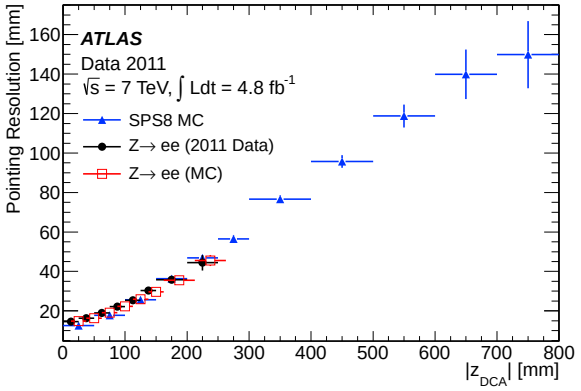

FIGURE 5.5: Pointing resolution,as a function of z_{DCA}, for non-prompt photons detected in the barrel in a 7 TeV SPS8 signal MC sample shown. Superimposed is the calorimeter resolution for $Z \rightarrow ee$ MC and data events

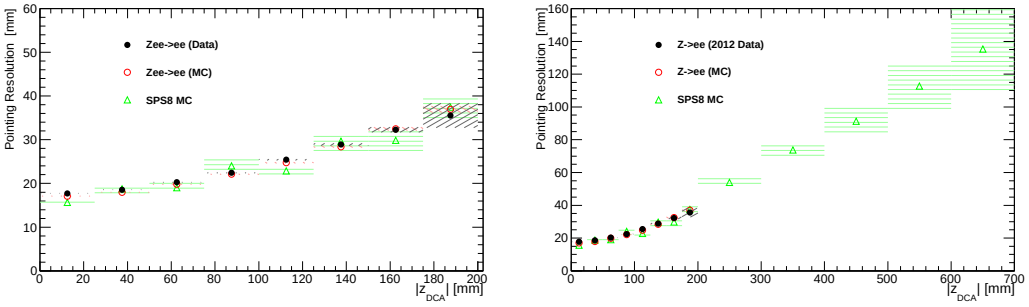

FIGURE 5.6: The pointing resolution, as a function of $|z_{\mathrm{DCA}}|$, is compared for non-prompt photons and electrons, from $Z \rightarrow ee$ data and MC events, detected in the barrel of the EM calorimeter. For the $Z \rightarrow ee$ samples, $|z_{\mathrm{pv}}|$ is used to model $|z_{\mathrm{DCA}}|$. Both plots show the same data, except that the right hand plot shows an expanded $|z_{\mathrm{DCA}}|$ range.

5.2.2 Delayed Timing Measurement

As has previously been stated, non-prompt photons from the decay of long-lived neutralinos will be expected to arrive at the EM calorimeter delayed compared to promptly produced photons, mostly due to the β distribution of the neutralino (figure 2.6). The arrival time of photons (t_γ) can be calculated from the energy deposits left in cells in the EM calorimeter using equation 3.8, with a resolution of approximately 1 ns. This resolution, however, can be improved by calibrating the timing measurement using $Z \rightarrow ee$ and $W \rightarrow e\nu$ samples [109]. The calibration process involves applying a number of corrections, including but not limited to: correcting the flight path so that it originates from the primary vertex, not the centre of the detector; corrections to various offsets for different channels; and corrections to the timing relating to energy dependence. The resulting timing resolution in the 7 TeV data is shown in figure 5.7 for showers where the cell with the maximum energy is in the HIGH gain region (see section 3.2.4.2 for a definition of the different gain regions) and found to be approximately 300 ps, including a contribution of 220 ps from the spread in the arrival time of proton bunches observed in figure 3.6. Improvements made to the calibration process for the 8 TeV data result in a resolution of 256 ps (299 ps) for HIGH (MEDIUM) gain cells, as shown in figure 5.8, with a contribution of approximately 220 ps from the spread in the arrival time of proton bunches still present. The worse resolution observed in MEDIUM gain is attributed to the smaller statistics available in this channel in the $W \rightarrow e\nu$ sample, details of which and the improvements made in the calibration method can be found in [110]. In both the 7 TeV and 8 TeV datasets there are too few events with max E_{cell} energies large enough to make it into the LOW gain category, so it was not possible to calibrate the timing measurement for these events. Due to the poor t_γ resolution, LOW gain photons are rejected in the 8 TeV analysis. For the SPS8 signal MC samples, this results in a negligible decrease in the efficiency of events making it into the signal region of less than 1%.

The methods used to calibrate the timing measurement to obtain the resolutions observed in figures 5.7 and 5.8 can be applied to any electron or photon sample to obtain the same resolution. However, MC samples do not contain a spread in the arrival time of proton bunches or many of the other features that produce the resolution observed in data. Therefore, a procedure was developed to smear the timing distribution in MC

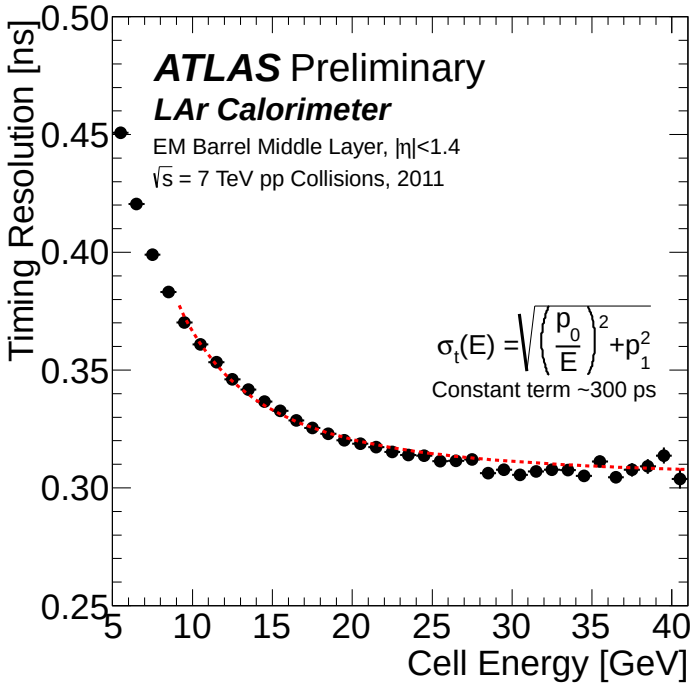

FIGURE 5.7: Time resolution obtained for EM showers in the ATLAS LAr EM barrel calorimeter, as a function of the energy deposited in the second-layer cell with the maximum deposited energy, in 7 TeV *pp* collisions. Superimposed is the result of the fit described in the text. The data are shown for electrons read out using high gain, and the errors shown are statistical only [1]

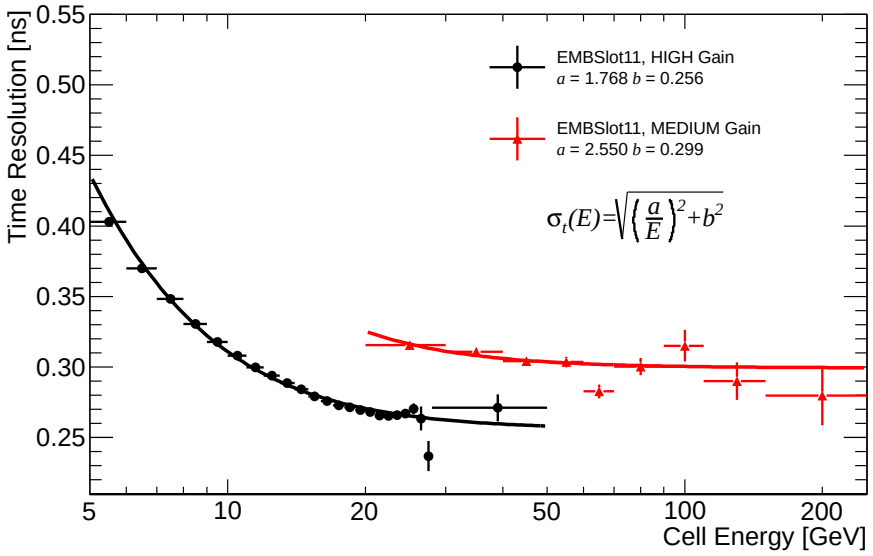

FIGURE 5.8: Time resolution, as a function of the energy in the middle-layer cell with the maximum energy, obtained from $Z \rightarrow ee$ events, for electrons with $|\eta| < 0.4$, and for both High and Medium gains in 8 TeV *pp* collisions. Similar results are obtained over the full coverage of the EM calorimeter [2]

samples, allowing the underlying resolution observed in data to be reproduced in any MC sample. In figure 5.9, a 7 TeV (left) and 8 TeV (right) $Z \rightarrow ee$ MC sample has been smeared using this method and both can be seen to agree with the timing distribution observed in the corresponding $Z \rightarrow ee$ data samples. Also shown in figure 5.9 are SPS8 MC signal samples, with different neutralino lifetimes, that have had this smearing contribution added to the delay due to the neutralino speed, to highlight the expected difference in the timing distribution of prompt and non-prompt photons.

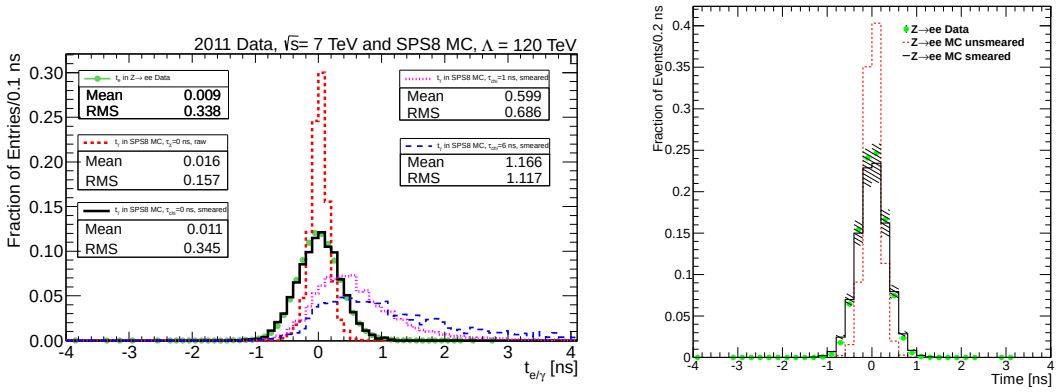

FIGURE 5.9: (Left) 7 TeV timing distribution for $Z \rightarrow ee$ data events (green points), prompt $Z \rightarrow ee$ MC sample (red) and a prompt SPS8 sample after applying smearing method (black). Also shown are two SPS8 signal samples (magenta and dark blue) with finite neutralino lifetimes [57]. (Right) 8 TeV timing distribution for $Z \rightarrow ee$ data events (green) and $Z \rightarrow ee$ MC before (red) and after (black) smearing has been applied with associated errors shown.

During the calibration of the timing measurement, secondary peaks in the timing distribution were observed at ± 5 ns, as can be seen in figure 5.10. It was determined that these events are due to collisions between protons that populate the satellite bunches, visible in figure 3.6, that arrive at the centre of the detector within ± 5 ns of the main bunch. To ensure that particles produced in these satellite collisions do not interfere with the results of the 8 TeV analysis, a timing cut requiring $|t_\gamma| < 4$ ns was placed on all photons in the analysis.

5.2.3 Relationship between t_γ and z_γ

As previously described, t_γ is calculated by measuring how much energy is deposited in the calorimeter as a function of time (see equation 3.8) while z_γ is calculated by determining the barycentre, in η, of the shower in the first and second layers of the EM calorimeter (see equation 3.6). Therefore, since the time of arrival of objects does not

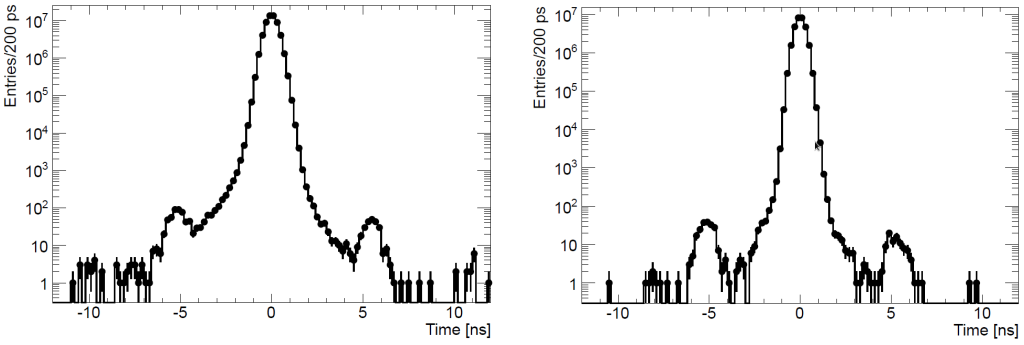

FIGURE 5.10: Measured time distributions for electrons in $W \rightarrow e\nu$ and $Z \rightarrow ee$ events, detected in the EM calorimeter barrel (left) and end-cap (right). The presence of 'shoulders' at ± 5 ns have consequences for searches for non-prompt photons as explained in the text. [111]

determine how the shower develops in the calorimeter, the two variables are independent for Standard Model events, as can be seen in figure 5.11. The correlation factor between t_γ and $|z_\gamma|$ for diphoton events in the 8 TeV data is 0.037, confirming that the two variables can be treated as independent. Figure 5.11 also shows that photons from SPS8 signal events tend to have larger positive t_γ and $|z_\gamma|$ values than photons from diphoton events in the 8 TeV data, as expected due to the non-prompt decay of the neutralino, with a correlation factor of 0.33 for this signal sample. Due to the obvious differences between the t_γ and z_γ distributions of photons produced in Standard Model events and SPS8 signal events, these distributions will be used to distinguish between signal events and background events, as explained in chapter 7.

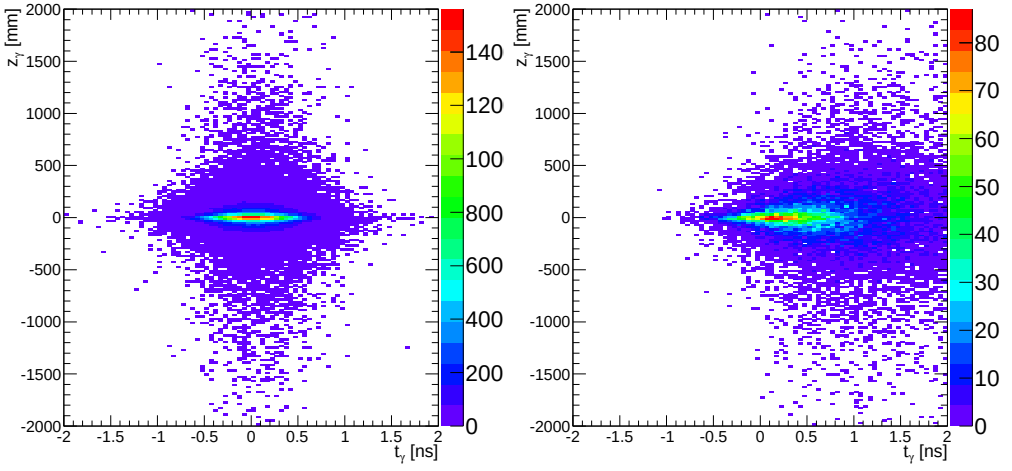

FIGURE 5.11: Plot showing the relationship between t_γ and z_γ for diphoton events collected at 8 TeV center of mass energy with $E_{\mathrm{T}}^{\mathrm{miss}} < 20$ GeV (left) and for diphoton events with $E_{\mathrm{T}}^{\mathrm{miss}} > 75$ GeV in an SPS8 signal MC with $\Lambda = 300$ TeV and $\tau = 2$ ns (right). Every event is required to contain at least two Loose photons that both have $p_{\mathrm{T}} > 50$ GeV and one of which must be detected with $|\eta| < 1.37$.

5.3 Non-Pointing Photon Studies

Due to the pointing geometry of the EM calorimeter, the shower from a non-pointing photon is likely to deposit energy over more cells in η than a prompt photon, making it appear 'wider'. Many of the variables used during photon identification to determine the quality of a photon candidate (section 4.2.2) use the spread of the shower in η to determine if an object is a photon or a different object, such as a jet, faking a photon. As such it is expected that as non-prompt photons become more non-pointing they will fail one or more of the shower shape variable (SSV) cuts. The impact this has on the IsEM efficiencies is studied for signal MC in section 5.3.1. A data driven method using the $Z \rightarrow ee$ tag and probe samples (described in section 6.2.3) is then used in section 5.3.2 to provide confidence that the MC is correctly predicting how these efficiencies change as photons become more non-pointing. In section 5.3.3, the changes in the SSVs for very non-pointing photons, that are beyond the z_γ range available in data, are studied and the potential impacts of mis-modelling these variables on the IsEM efficiencies are estimated. In section 5.3.4, the efficiency of non-prompt photons passing the photon trigger is studied to determine if there is any dependence on how non-pointing a photon is.

5.3.1 Impact on Photon Quality

Using the SPS8 signal MC samples, the efficiency of non-prompt photons passing the different IsEM menus is shown in figure 5.12. It can be seen that the efficiency of non-prompt photons passing the Loose cuts remains almost flat at approximately 95% until z_γ is greater than 200 mm, at which point the efficiency begins to fall as z_γ increases further. When z_γ reaches 400 mm the efficiency of non-prompt photons passing the Loose cuts remains high, having fallen to approximately 80 %, however it continues to decrease as z_γ increases, falling to less than 40% when z_γ is greater than 800 mm. The decrease in the efficiency of non-prompt photons passing the Tight cuts as a function of z_γ is much steeper than for the Loose cuts. The efficiency starts at approximately 85%, however this falls to approximately 60% when z_γ reaches 200 mm and below 40% when z_γ is in excess of 400 mm.

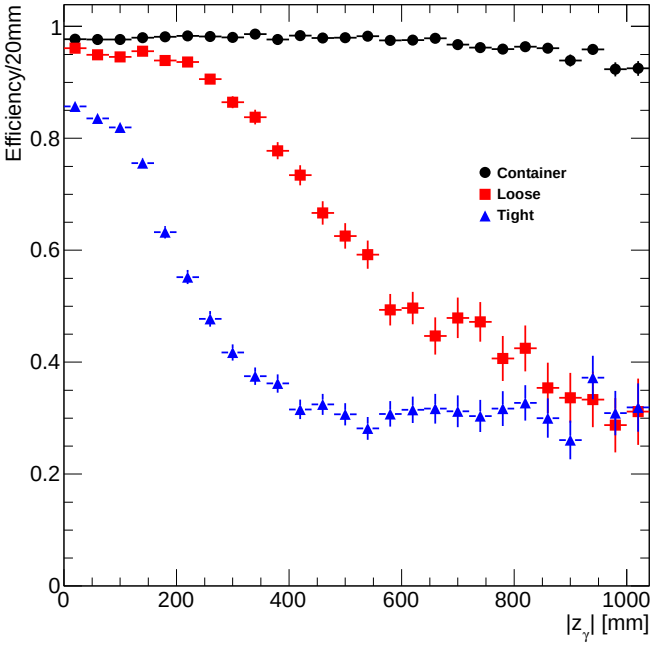

FIGURE 5.12: The photon container, Loose and Tight photon efficiencies as a function of z_γ for photons from the 7 TeV SPS8 signal MC samples.

5.3.2 IsEM Efficiency Studies

The Loose IsEM cuts applied to the shower shape of photons are identical to those that are applied to electrons. Given the similarities of the showers produced in the EM calorimeter by an electron and a photon, it is expected that the efficiencies of photons and electrons passing the Loose IsEM cuts should be similar. Figure 5.13 shows the efficiencies of the electron and photon samples passing the Loose IsEM cuts with z_{PV} modelling z_γ for the electron samples. As expected, the samples do agree fairly well over the z_γ range where $Z \rightarrow ee$ data and MC exist, although it should be noted that due to the low statistics for events with large z_{PV} in the $Z \rightarrow ee$ samples the associated error bars become large.

While the efficiency of electrons and photons passing the Loose IsEM cuts shows good agreement over the range where $Z \rightarrow ee$ events exist, figure 5.12 shows that the efficiency is expected to be flat over this region. In the same region the efficiency of signal MC photons passing Tight IsEM cuts is expected to decrease rapidly. If the efficiency of electrons and photons passing the Tight IsEM cuts shows good agreement in this region then it will be provide confidence that the changes in shower shape are being correctly handled in MC and that the expected Loose IsEM efficiency at large z_γ values can be

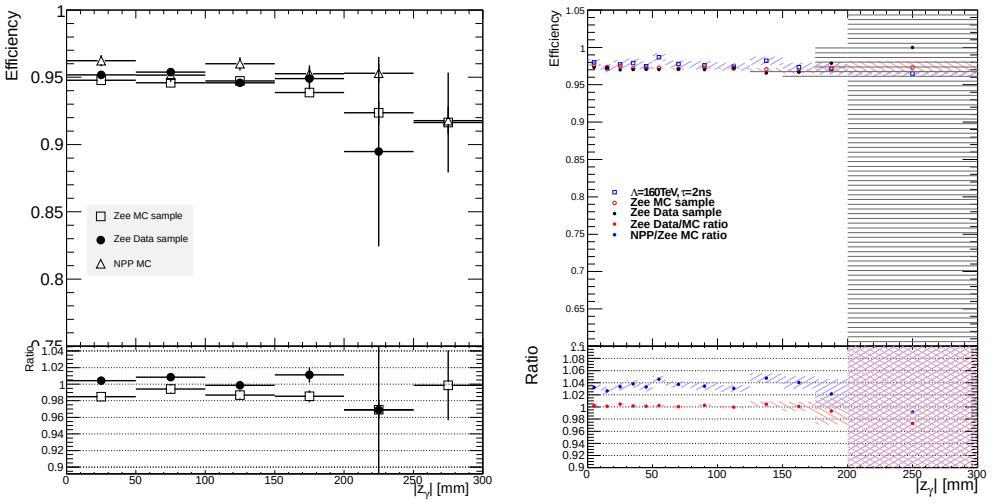

FIGURE 5.13: The efficiency of the probe electron, from Data and MC $Z \rightarrow ee$ Tag and Probe samples, passing the Loose IsEM shower shape variable cuts is plotted on the same graph as the efficiency of non-prompt photons, from signal MC, passing the Loose IsEM cuts in 7 TeV. The ratio plots shown in the lower third of the figure are calculated relative to the signal MC values.

trusted. Figure 5.14 shows that the efficiency of the probe electron from the $Z \rightarrow ee$ MC and data samples passing the Tight IsEM cuts for electrons agree over the range where events exist, however they show a very different trend to the efficiency of non-pointing photons passing the Tight IsEM cuts for photons. This, however, is to be expected since there are some differences in the shower produced by electrons and photons due to the effect of the magnetic field in the inner detector. The fine granularity of the first layer of the EM calorimeter allows these small differences to be measured, and separate Tight IsEM cuts have been optimised for electrons and photons.

A more appropriate test is to determine if the EM shower is being correctly modelled for non-pointing photons is to measure the efficiency of the probe electron passing the Tight IsEM cuts that have been optimised for photons. If the same dependence on z_γ that is observed in the SPS8 MC samples is also observed in the $Z \rightarrow ee$ samples then it will provide confidence that the changes in the shower of non-prompt photons, as they become more non-pointing, is being correctly modelled in the MC. Figure 5.15 shows that when the Tight IsEM cuts that have been optimised for photons are applied to the $Z \rightarrow ee$ samples, the efficiency of the probe electron passing the cuts is reduced compared to the electron cuts. This is to be expected since the shower produced by an electron is expected to be slightly wider than one produced by a photon and the average E_{T} of the electrons is less than the average E_{T} of signal photons (see section

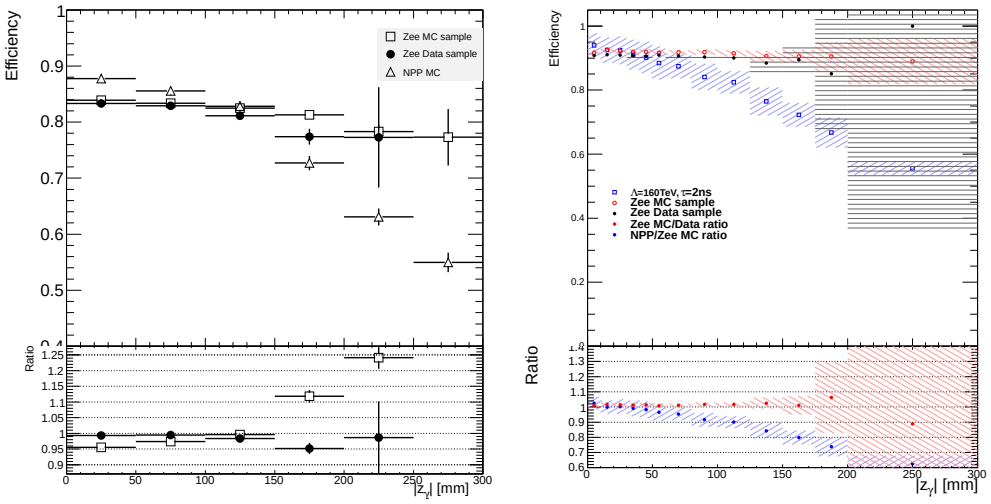

FIGURE 5.14: The efficiency of the probe electron, from Data and MC $Z \rightarrow ee$ Tag and Probe samples, passing the Tight IsEM shower shape variable cuts that have been optimised for electrons is plotted on the same graph as the efficiency of non-prompt photons, from signal MC, passing the Tight IsEM cuts that have been optimised for photons. The left plot shows the different efficiencies for 7 TeV samples and the right plot shows the same efficiencies for 8 TeV samples.

8.3.1). More importantly for these analyses is how the efficiency of the probe electron passing the photon cuts changes as z_γ increases, which is shown to be similar for the $Z \rightarrow ee$ data and MC samples and comparable to the non-prompt signal MC. This shows that the MC is correctly reproducing the dependence of the shower development on z_γ and provides confidence that the prediction for the loose efficiency in figure 5.13 can be trusted.

5.3.3 Shower Shape Variables Studies

As described in section 4.2.3, differences between the distributions of the different photon SSVs in data and MC are corrected for by shifting the MC values. These corrections, however, were validated using prompt photons and any differences in the SSV distributions for non-prompt photons in MC and data have not been corrected. If the signal MC is incorrectly predicting how the distribution of an SSV changes as photons becomes more non-pointing then this could affect the efficiency of non-pointing photons passing the IsEM cuts and therefore change the expected signal yield.

The SSV distributions in SPS8 signal MC samples were studied for a range of z_γ values to see if they are predicted to be stable in MC. If an SSV is stable as z_γ increases then the method described in section 4.2.3 will correctly account for any differences between

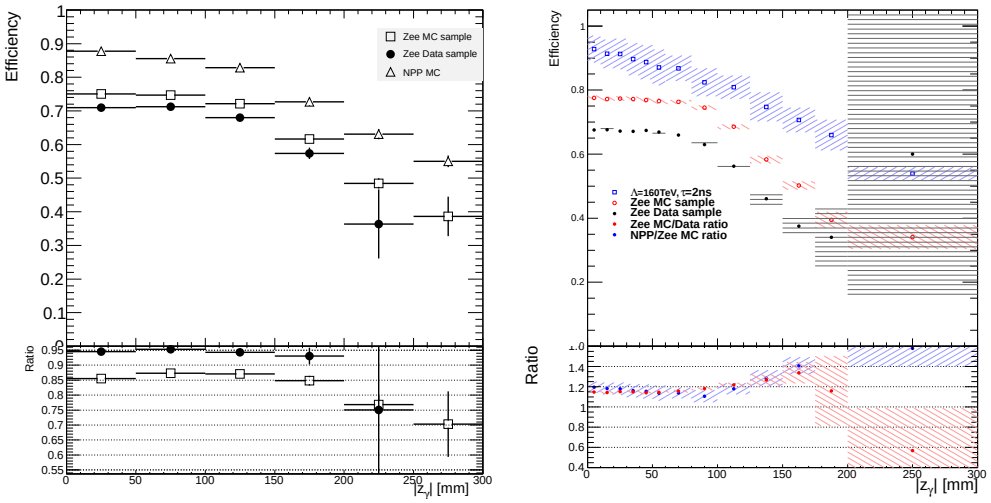

FIGURE 5.15: The efficiency of the probe electron, from Data and MC $Z \rightarrow ee$ Tag and Probe samples, passing the Tight IsEM shower shape variable cuts that have been optimised for converted photons is plotted on the same graph as the efficiency of non-prompt photons, from signal MC, passing the Tight IsEM cuts that have been optimised for photons. The left plot shows the different efficiencies for 7 TeV samples and the right plot shows the same efficiencies for 8 TeV samples.

data and MC. Figure 5.16 shows how different SSVs change as z_γ increases and it can be seen that the biggest shift in a Loose IsEM variable (see table 4.1 for definitions) occurs in $w_{\eta 2}$ and the biggest shift in a Tight IsEM variable occurs in w_{s3}. To test if these trends are observed in data, the mean and RMS of the $Z \rightarrow ee$ data and MC samples were compared as a function of z_{PV} as shown in figure 5.17. It can be seen that the difference between data and MC values are stable for the mean and RMS of the $w_{\eta 2}$ distributions and also for the mean of the w_{s3} distributions, however there is a clear relationship between the difference of the RMS of the w_{s3} distributions over the z_{PV} range. Extrapolating this trend up to a z_{PV} value of $\sim$ 500 mm, beyond which Tight IsEM reconstruction is very inefficient, results in a disagreement between MC and data of approximately 40%. To test if this disagreement could affect the efficiency of non-pointing photons passing the Tight IsEM cuts, the w_{s3} distribution of photons in an SPS8 signal MC sample was smeared by $\pm$ 40% and the new efficiency of passing the Tight IsEM was calculated. As can be seen in figure 5.18, the change in efficiency is very small for larger z_γ values with a change of less than $\pm$ 2%. A larger change in efficiency can be seen in smaller z_γ values, however a smear of 40 % is a large overestimation of the actual difference in this range and since the change in efficiency is negligible and within the statistical uncertainties for larger z_γ it is ignored.

In the 8 TeV analysis SR photons are only required to pass the Loose IsEM cuts, therefore

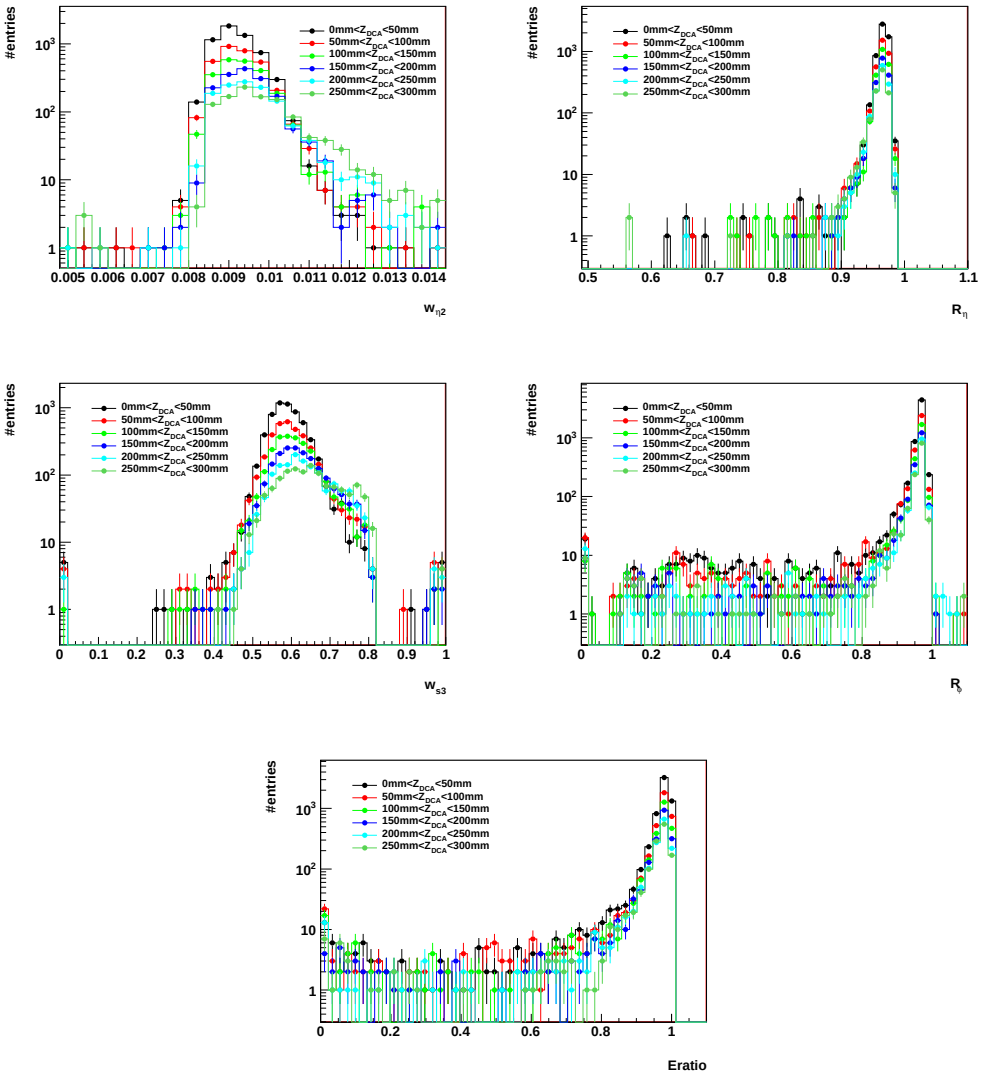

FIGURE 5.16: Shower shape variables for photons from 7 TeV SPS8 signal MC over different z_γ ranges. The top two plots show Loose IsEM variables, while the other three show Tight IsEM variables. Details of the shower shape variables can be found in table 4.1.

the SSV study from the 7 TeV analysis was only repeated for the Loose IsEM SSVs, as shown in figure 5.19. As expected from the 7 TeV study, it is the distribution of the $w_{\eta 2}$ variable that shows the biggest shift as z_γ increases. When this variable is studied for $Z \rightarrow ee$ MC and data events, as shown in figure 5.20, it is found that the RMS is fairly stable over the z_{PV} range where enough statistics exist. However, the mean of the distributions shows a clear dependence on z_{PV} and this dependence is slightly different for data and MC. It was found that this discrepancy was best described by a linear fit with a maximum value of $\pm$ 4% at $z_\gamma = 2000$ mm. This fit was then used as a z_γ dependent function to shift the mean value of the $w_{\eta 2}$ distribution for an SPS8 MC

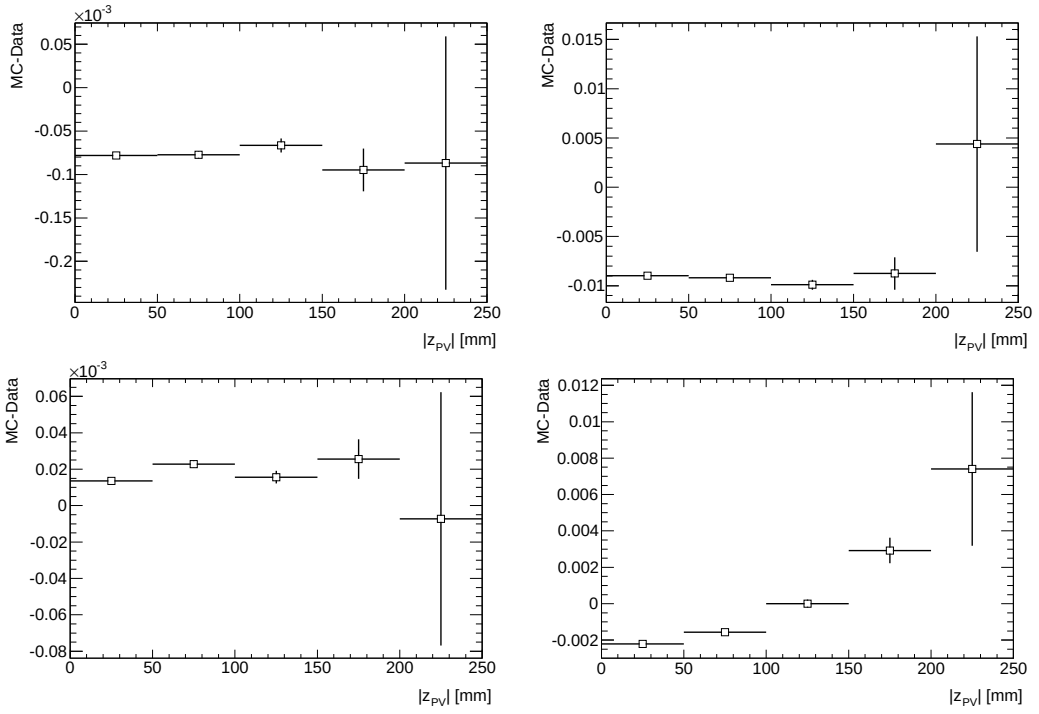

FIGURE 5.17: The difference between 7 TeV $Z \rightarrow ee$ data and MC in the (top row) mean values and (bottom row) RMS values of the shower shape variables (left) $w_{\eta 2}$ (used in Loose ID) and (right) W_{s3} (used in Tight ID), as a function of z_{PV}.

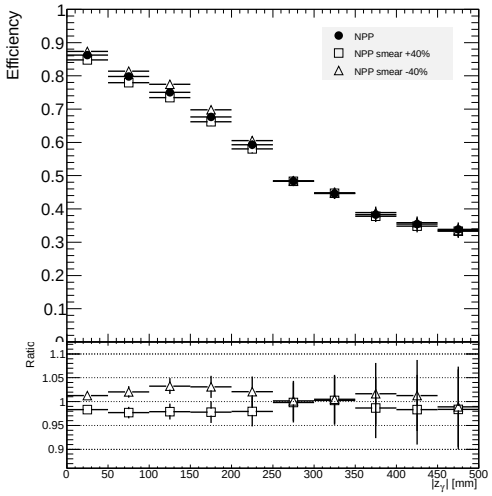

FIGURE 5.18: Comparisons of the Tight photon efficiency in the 7 TeV non-pointing photon signal selection, with and without the additional smearing described in the text.

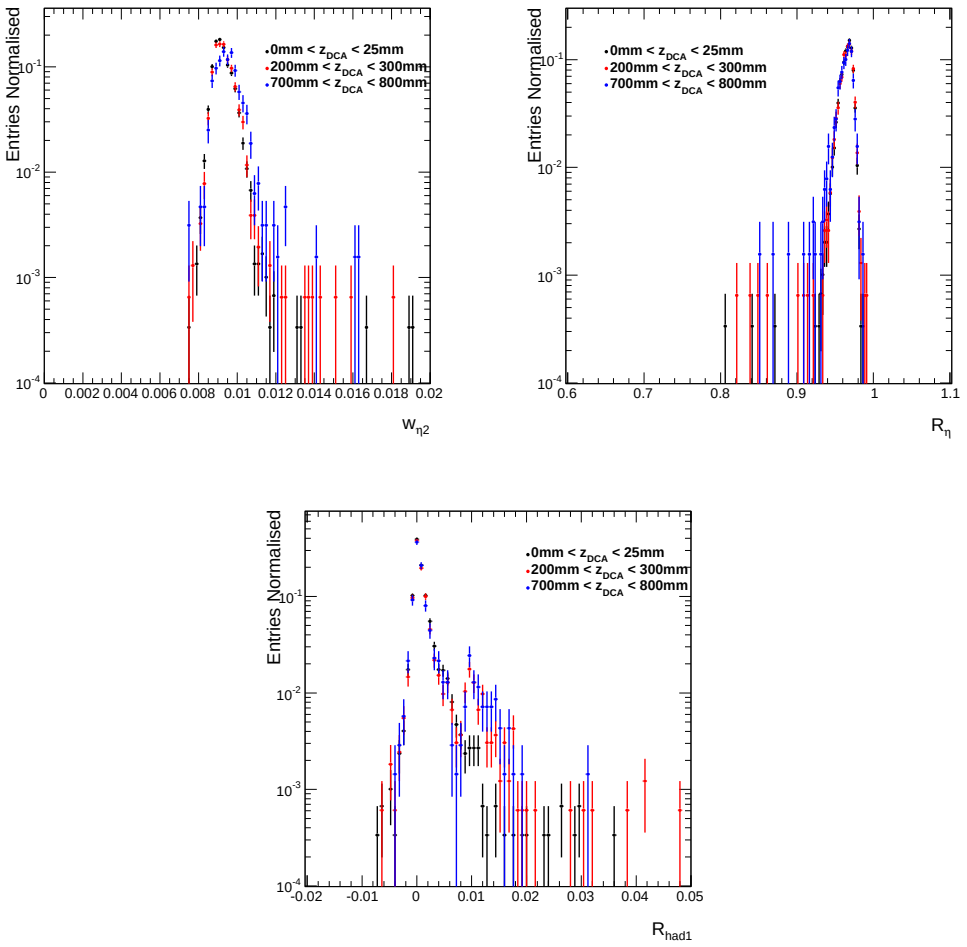

FIGURE 5.19: Shower shape variables for photons from 8 TeV MC signal samples with different z_γ ranges. The top two plots show Loose IsEM variables measured in the middle layer of the calorimeter, while the other plot shows the variable that measures the fraction of energy that is deposited in the hadronic calorimeter (R_{had1}).

signal sample as shown in figure 5.21. It can be seen that there is very little change in efficiency of photons passing the Loose IsEM cuts with a total change of efficiency in the entire sample of less than 1%.

In summary in both the 7 TeV and 8 TeV analyses the potential impact on the signal yield due to the SSVs of non-pointing photons being incorrectly modelled in SPS8 signal MC is negligible and no systematic uncertainty will be included in the limit setting procedure.

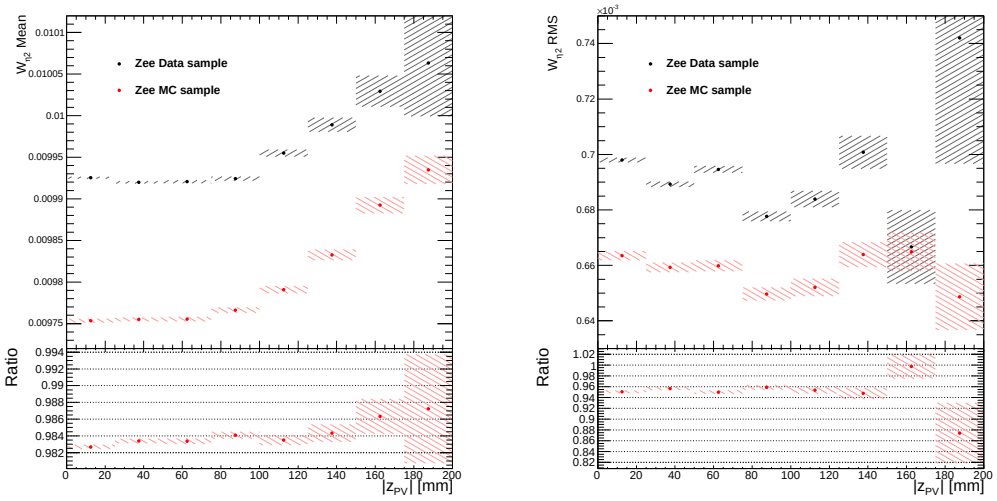

FIGURE 5.20: The left (right) plot shows how the mean (RMS) of the $w_{\eta 2}$ distribution changes as a function of z_{PV} for $Z \rightarrow ee$ MC and data electrons.

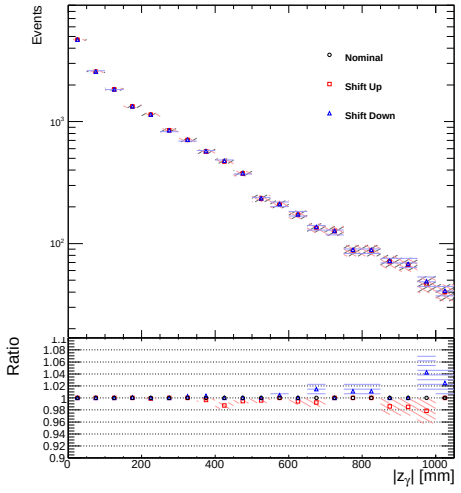

FIGURE 5.21: Comparisons of the number of non-pointing photons from an 8 TeV SPS8 signal sample passing the $w_{\eta 2}$ cuts with and without the shift described in the text.

5.3.4 Trigger Efficiency

As will be discussed in section 6.1, the `EF_2g20_loose` trigger (see section 3.2.6 for information on the trigger naming convention) was used in the 7 TeV analysis. This has been found to be reliable for prompt photons produced in SPS8 events [112]. However, further study is required to determine if the efficiency of non-prompt photons passing the trigger is correctly modelled in MC and if there is any dependence on z_γ.

To determine if the MC is correctly modelling the trigger efficiency the $Z \rightarrow ee$ tag and probe samples were used to model non-prompt photons. Since the tag and probe

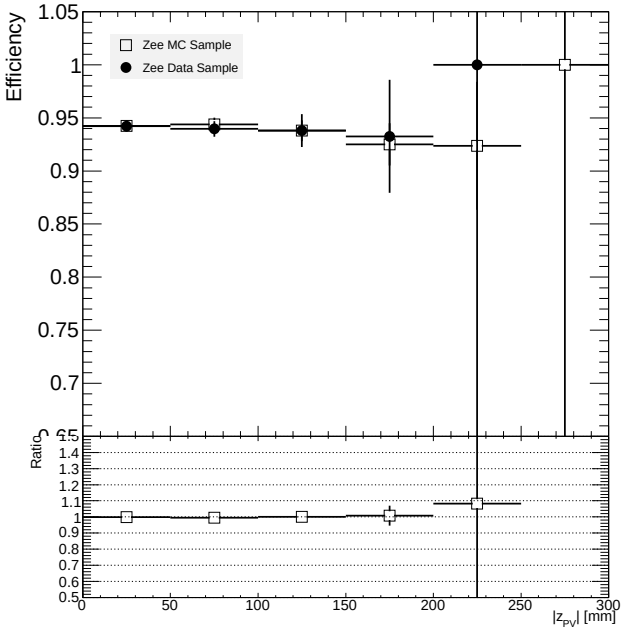

FIGURE 5.22: Trigger efficiency, defined as the fraction of $Z \rightarrow ee$ events selected via a pre-scaled single electron trigger that also pass the 2g20_loose trigger requirements, as a function of the z coordinate of the primary vertex. Superimposed on the data result is the prediction from MC.

selection requires the tag electron to pass a single electron trigger this would bias the efficiency of the event passing the `EF_2g20_loose` trigger. Therefore, the efficiency of the probe electron passing a single electron trigger as a function of z_{PV} is explored instead, as shown in figure 5.22. It can be seen that the efficiency is fairly flat with only a small drop in efficiency over the z_{PV} range where data exists. It can also be seen that there is good agreement between data and MC over the range where data is available, showing that the MC is correctly reproducing how the development of the shower depends on z_{PV}.

The method outlined above is data driven which means it is limited to the regions where data exists. Signal MC is used to determine if the trigger efficiency has any dependence on the shower shape when non-prompt photons are very non-pointing. It has already been shown that data and MC agree over the range where data exists, implying that the development of the shower shape for larger z_{DCA} values in MC can be trusted. The Loose photon cuts applied at the trigger stage are not addressed in this section as they are similar to the IsEM menu and are therefore covered by the studies presented in the previous sections. Instead, the efficiency of a cell passing the L1 cluster seed requirements is investigated. As explained in section 3.2.4.2, the cells in the

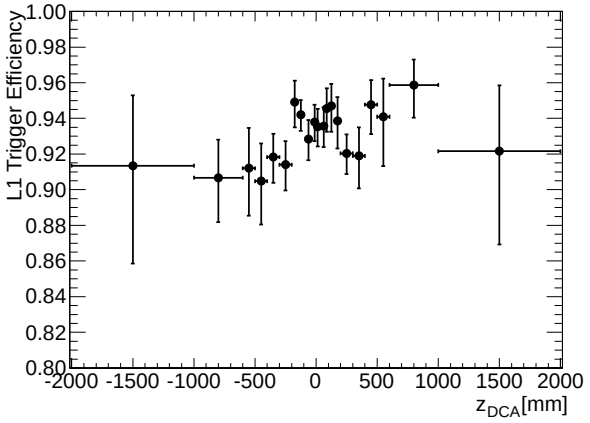

FIGURE 5.23: L1 Trigger efficiency in 7 TeV signal MC for loose photons in the signal region matched to emulated L1 Trigger objects, versus the extrapolated photon point of origin on the beam axis. The efficiency is defined as the fraction of photons with matched L1 Trigger object EM Cluster sums over the nominal selection threshold of 50 GeV [57].

EM calorimeter are designed so that they point back to the nominal interaction point. Therefore, if a photon is very non-pointing, and has a wide shower, it may deposit a large percentage of its energy over multiple cells with no single cell having enough energy to pass the L1 trigger requirements. To test this, a study was performed attempting to match L1 trigger objects to Loose photons in signal MC. The photons were required to pass the standard photon cuts with no IsEM requirement and be matched, within a cone of $\Delta R < 0.015$, to an L1 trigger object with an EM Cluster energy over the photon p_{T} requirement of 50 GeV. The L1 trigger efficiency in figure 5.23 is defined as the fraction of signal photons that pass the event cuts that can be successfully matched to an L1 trigger object and is presented as a function of z_{DCA}. The best fit to figure 5.23 is a horizontal line at approximately 93$\pm$2 %, implying that changes in the shower shape introduce no bias in the trigger efficiency even for very non-pointing photons. Even though the trigger efficiency was found to have no dependence on how non-pointing a photon is, a flat systematic uncertainty (see chapter 8) of $\pm$2% is assigned to the L1 trigger efficiency to account for any possible deviation from the standard efficiency.

The efficiency of the `EF_g35_loose_g25_loose` trigger that was used in the 8 TeV analysis, see section 6.1, has been found to be stable for prompt photons [113]. The study from the 7 TeV analysis matching L1 trigger objects to reconstructed Loose photons in signal MC was repeated for different 8 TeV samples as shown in figure 5.24. For the $\Lambda = 160$ TeV sample there appears to be some small dependence on z_γ, however all

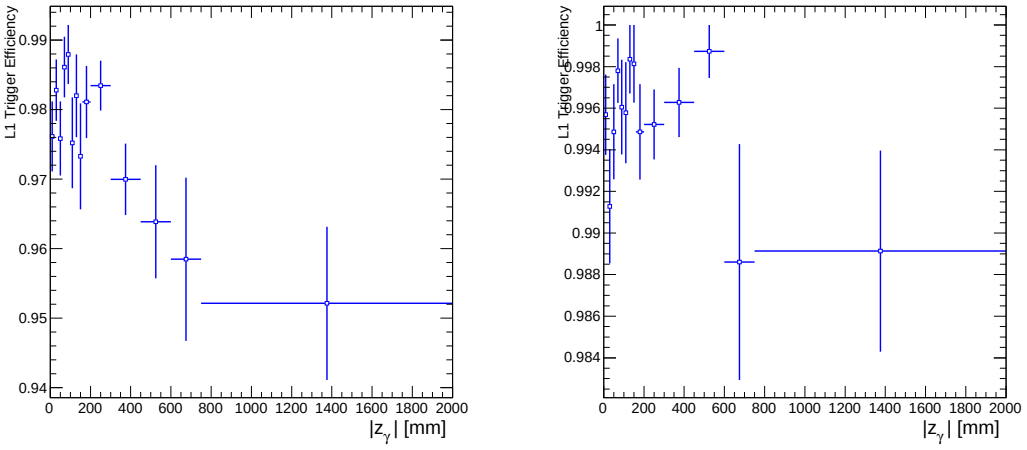

FIGURE 5.24: L1 Trigger efficiency in 8 TeV signal MC for loose photons in the signal region matched to emulated L1 Trigger objects, versus the extrapolated photon point of origin on the beam axis. The efficiency is defined as the fraction of photons with matched L1 Trigger object EM Cluster sums over the nominal selection threshold of 50 GeV. The plot on the left shows the efficiency for signal MC with $\Lambda = 160$ TeV, while the plot on the right shows the trigger efficiency for signal MC with $\Lambda = 300$ TeV.

values lie within a $\pm$ 2% band corresponding to the systematic uncertainty observed in the 7 TeV L1 trigger efficiency study. For higher Λ samples, such as the 300 TeV sample also shown in figure 5.24, there is much less variation in the L1 trigger efficiency. Therefore, the systematic uncertainty assigned to the L1 trigger efficiency in the 7 TeV analysis of $\pm$ 2% is also assigned to the L1 trigger efficiency in the 8 TeV analysis and is a conservative estimate across much of the signal grid.

5.4 Signal Efficiencies and Event Yields

The total signal event selection efficiency for SPS8 signal events, defined as the signal acceptance $\times$ efficiency, was determined using the MC signal samples. The efficiency of SPS8 signal events passing the SR event selection is shown versus neutralino lifetime for a selection of Λ values in figure 5.25, with the 7 TeV and 8 TeV event selections shown separately. Tables showing the selection efficiency for a wider range of Λ values and neutralino lifetimes are included in Appendix C. The number of signal events that are expected in the 7 TeV and 8 TeV datasets for different Λ and neutralino lifetimes can be calculated by substituting the relevant cross section (from tables 5.1 and 5.2) into equation 3.2. This calculation also requires the relevant efficiency from Appendix C

to take into account the efficiency and acceptance of the analysis. The expected yields in the signal region of the 7 TeV and 8 TeV analyses are shown in tables 5.3, 5.4, 5.5 and 5.6.

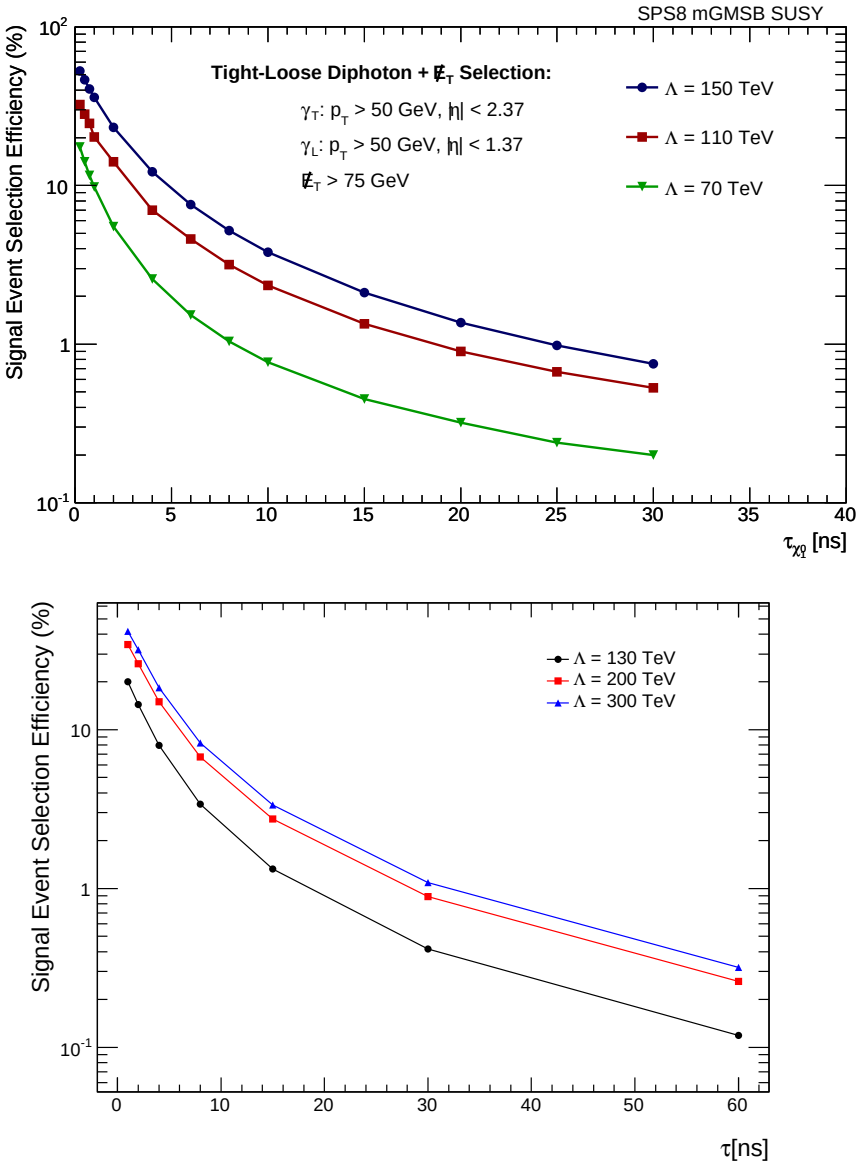

FIGURE 5.25: Product of GMSB SPS8 signal acceptance × efficiency versus neutralino lifetime for several Λ values. The top plot was produced using the 7 TeV [57] signal selection and the bottom plot using the 8 TeV signal selection.

Λ (TeV)	Neutralino lifetime (ns)											
	0.25	0.5	0.75	1	2	4	6	8	10	15	20	25
210	10.0	9.7	9.2	8.5	6.0	3.2	2.0	1.4	1.0	0.55	0.34	0.25
200	13.9	12.8	11.9	10.9	7.7	4.1	2.6	1.8	1.3	0.71	0.46	0.32
190	17.9	17.6	16.5	15.2	10.5	5.6	3.4	2.3	1.7	0.94	0.61	0.44
180	23.4	22.9	21.5	19.9	13.7	7.3	4.5	3.0	2.2	1.2	0.77	0.55
170	35.6	32.4	29.6	26.9	18.3	9.7	6.1	4.2	3.1	1.7	1.1	0.80
160	45.1	42.1	39.3	36.1	25.0	13.2	8.2	5.6	4.1	2.2	1.4	1.0
150	60.2	57.3	53.0	48.4	33.0	17.4	10.7	7.3	5.4	2.99	1.95	1.39
140	82.2	79.4	73.8	67.3	45.4	23.8	14.7	10.1	7.4	4.1	2.7	1.9
130	118.7	112.3	104.2	90.4	63.7	33.3	21.3	14.7	10.8	6.2	4.1	3.02
120	199.6	176.7	155.5	127.7	86.9	46.6	28.8	19.6	14.7	8.16	5.4	3.93
110	242.4	221.6	203.7	179.3	124.7	61.6	41.0	28.1	20.8	11.9	8.0	5.92
100	359.0	340.9	308.7	261.2	178.9	92.1	55.3	37.9	28.3	16.2	10.9	8.03
90	563.1	526.5	474.0	411.6	268.1	139.8	85.4	58.6	43.4	25.0	16.9	12.64
80	909.8	835.8	747.8	661.9	411.4	199.4	119.9	81.7	60.3	34.7	23.7	17.9
70	1844.1	1618.8	1404.3	1214.1	717.5	336.9	200.8	136.7	101.2	59.1	41.2	31.6

TABLE 5.3: The predicted NLO signal yield (in events), for $4.8fb^{-1}$ at $\sqrt{s} = 7$ TeV, after the Tight-Loose photon selection and $E_{\mathrm{T}}^{\mathrm{miss}}$ cut for the signal grid, for neutralino lifetimes up to 25 ns in SPS8 events [57].

Λ (TeV)	Neutralino lifetime (ns)				
	30	40	60	80	100
160	0.78	0.50	0.28	0.19	-
150	1.06	0.68	0.39	0.28	-
140	1.5	0.96	0.55	0.38	-
130	2.37	1.6	1.0	0.77	-
120	3.05	2.1	1.2	0.88	-
110	4.67	3.3	2.1	1.6	1.3
100	6.31	4.4	2.7	2.0	1.6
90	10.03	7.1	4.6	3.5	2.9
80	14.3	10.3	6.9	5.4	4.5
70	25.9	19.4	13.8	11.3	10.0

TABLE 5.4: The predicted NLO signal yield (in events), for $4.8fb^{-1}$ at $\sqrt{s} = 7$ TeV, after the Tight-Loose photon selection and $E_{\mathrm{T}}^{\mathrm{miss}}$ cut for the signal grid, for a range of neutralino lifetimes from 30 ns up to 100 ns [57].

Λ	Neutralino lifetime (ns)											
(TeV)	0.1	0.3	0.5	0.7	1	2	4	6	8	10	15	20
350	2.05	2.04	2.06	2.02	1.92	1.46	0.84	0.54	0.376	0.278	0.153	0.0974
320	3.9	3.95	3.96	3.88	3.68	2.82	1.65	1.07	0.745	0.551	0.304	0.193
310	5.06	5.05	4.95	4.81	4.57	3.51	2.05	1.32	0.922	0.682	0.376	0.239
300	6.03	5.98	6.07	5.99	5.73	4.38	2.53	1.62	1.13	0.836	0.46	0.293
290	7.54	7.65	7.78	7.65	7.29	5.55	3.21	2.06	1.43	1.06	0.583	0.37
270	12.2	12.1	12.2	12	11.5	8.78	5.07	3.25	2.26	1.67	0.916	0.581
260	15	15.9	15.9	15.5	14.7	11.3	6.53	4.19	2.92	2.16	1.19	0.755
250	18.9	19.5	19.8	19.4	18.6	14.2	8.22	5.27	3.67	2.71	1.49	0.943
240	29.6	26.2	25.6	24.9	23.6	18	10.4	6.68	4.66	3.44	1.9	1.21
230	35.6	33.1	32.7	31.9	30.4	23.3	13.5	8.64	6.02	4.44	2.44	1.55
220	40.5	41.5	41.4	40.4	38.4	29.3	16.8	10.8	7.48	5.51	3.02	1.92
210	47.7	52.9	52.9	51.7	49.2	37.7	21.9	14.1	9.82	7.26	4.01	2.55
200	74.9	71.2	70.4	68.3	64.6	48.8	28.2	18.1	12.7	9.36	5.16	3.28
190	99.1	91.5	90.2	87.7	83.1	62.5	35.6	22.6	15.7	11.5	6.29	3.97
170	170	159	156	152	144	109	62.6	40	27.8	20.5	11.2	7.11
160	201	211	209	202	190	142	80.3	50.9	35.1	25.7	13.9	8.76
150	263	271	274	267	252	189	107	67.9	46.9	34.5	18.8	11.9
140	586	421	391	369	340	246	136	85.4	58.4	42.5	22.9	14.3
130	854	605	546	508	466	336	185	116	79	57.5	30.9	19.4
120	870	897	840	771	689	478	260	163	111	81.1	43.7	27.4
90	2630	2270	2340	2250	2040	1370	719	442	300	218	117	73
80	3610	3470	3330	3130	2870	2010	1090	683	469	343	186	117

TABLE 5.5: The predicted NLO signal yield (in events), for $20.3fb^{-1}$ at $\sqrt{s} = 8$ TeV, after the Loose-Loose photon selection and $E_{\mathrm{T}}^{\mathrm{miss}}$ cut for the signal grid, for neutralino lifetimes up to 20 ns in SPS8 events.

Λ	Neutralino lifetime (ns)					
(TeV)	25	30	40	60	80	100
350	0.0675	0.0496	0.0301	0.0145	0.00852	0.0056
320	0.134	0.0981	0.0594	0.0286	0.0168	0.011
310	0.166	0.122	0.0738	0.0355	0.0209	0.0137
300	0.203	0.149	0.0903	0.0435	0.0256	0.0168
290	0.257	0.189	0.114	0.0551	0.0324	0.0213
270	0.402	0.295	0.179	0.0859	0.0504	0.0331
260	0.523	0.384	0.233	0.112	0.0658	0.0432
250	0.653	0.479	0.29	0.139	0.0817	0.0537
240	0.838	0.616	0.374	0.18	0.106	0.0697
230	1.07	0.788	0.477	0.23	0.135	0.0887
220	1.33	0.973	0.589	0.283	0.166	0.109
210	1.77	1.3	0.787	0.379	0.223	0.146
200	2.28	1.67	1.01	0.489	0.288	0.189
190	2.74	2.01	1.21	0.582	0.341	0.224
170	4.92	3.61	2.18	1.05	0.615	0.404
160	6.02	4.4	2.65	1.26	0.739	0.484
150	8.22	6.02	3.64	1.75	1.02	0.673
140	9.8	7.14	4.28	2.03	1.19	0.776
130	13.3	9.68	5.8	2.76	1.61	1.06
120	18.8	13.7	8.23	3.92	2.29	1.5
90	50	36.4	21.8	10.4	6.06	3.97
80	80.6	58.9	35.5	17	9.91	6.5

TABLE 5.6: The predicted NLO signal yield (in events), for $20.3fb^{-1}$ at $\sqrt{s} = 8$ TeV, after the Loose-Loose photon selection and $E_{\mathrm{T}}^{\mathrm{miss}}$ cut for the signal grid, for a range of neutralino lifetimes from 25 ns to 100 ns in SPS8 events.

Chapter 6

Data Samples

In this chapter, the data that are used in this thesis is introduced. In section 6.1, the total data that was collected at 7 TeV and 8 TeV is presented, divided into different periods of operation. The different subsamples of the data that are used as control samples to model background events in the signal region, to test signal MC predictions and to test the analysis methods, are described in section 6.2. In section 6.3, potential sources of background events in the signal region and how these are modelled are discussed.

To avoid biasing the analyses, a blinding procedure was adopted whereby the diphoton events are separated into different control regions, defined by the $E_{\mathrm{T}}^{\mathrm{miss}}$ in the event. Only the pointing and timing distributions from events with the lowest $E_{\mathrm{T}}^{\mathrm{miss}}$, and therefore least signal like, are used to develop the analysis strategy. The rest of the diphoton data, other than a small subsection of the signal region, was blinded and not investigated until the procedures described in chapter 7 had been finalised.

6.1 Data Sample

The data used in these analyses are from pp collision events recorded at the ATLAS detector over two data taking periods with different center of mass energies, as such the datasets were analysed independently.

The center of mass energy of the pp collisions in the 2011 dataset was $\sqrt{s} = 7$ TeV. The standard Good Run List (GRL) [114], which removes all data collected in periods when

any ATLAS sub-detector was not operating as expected, is applied so that the data is suitable for physics analyses. This results in a total of 4.8 $\text{fb}^{-1}$of data available for physics analyses, which is shown in table 6.1 split into the different periods of operation, corresponding to different LHC pp runs. The diphoton events that are used to construct the signal region and the control region samples described in section 6.2.1 are taken from the subsample of events that pass the `EF_2g20_loose` diphoton trigger, which had the lowest p_{T} threshold out of any diphoton trigger used at ATLAS during the 7 TeV run.

Period	Run range	Luminosity [pb^{-1}]
B2	178044–178109	11.7
D	179710–180481	166.7
E	180614–180776	48.8
F	182013–182519	136.1
G	182726–183462	537.5
H	183544–184169	259.5
I	185353–186493	386.2
J	186516–186755	226.4
K	186873–187815	600.1
L	188902–190343	1401.9
M	190503–191933	1037.6
Total	178044–191933	4812.3

TABLE 6.1: Integrated luminosity used in the 7 TeV analysis. For each data taking period the run range and the integrated luminosity are given. Note that Period K, which was unblinded as part of the development of the analysis strategy, represents only $\approx 12\%$ of the full data sample [57].

In 2012 the center of mass energy of the pp collisions was increased to $\sqrt{s} = 8$ TeV. As for the 7 TeV analysis, the standard GRL was applied resulting in a total integrated luminosity of 20.3 fb^{-1}being available for physics analyses. The breakdown of the 8 TeV dataset into different run periods can be seen in table 6.2. The diphoton events that are used to construct the signal region and the control region samples described in section 6.2.1 are taken from the subsample of events that pass the `EF_g35_loose_g25_loose` diphoton trigger, which had the lowest p_{T} threshold out of any diphoton trigger used at ATLAS during the 8 TeV run.

6.1.1 Event Veto

Even after applying the good run list, there are still a number of events that need to be rejected from the data sample used for physics analyses due to detector issues or the

Period	Run range	Luminosity [pb^{-1}]
A	200804 – 201556	795.91
B	202660 – 205113	5113.61
C	206248 – 207397	1409.06
D	207447 – 209025	3297.54
E	209074 – 210308	2534.11
G	211522 – 212272	1279.54
H	212619 – 213359	1449.04
I	213431 – 213819	1018.45
J	213900 – 215091	2605.48
L	215414 – 215643	841.634
Total	200804 – 215643	20344.37

TABLE 6.2: Integrated luminosity used in the 8 TeV analysis. For each data taking period the run range and the integrated luminosity are given. Note that Period E, which was unblinded as part of the development of the analysis strategy, represents only $\approx 12\%$ of the full data sample [59].

presence of cosmic muons. The procedures for removing these events are applied to both data and MC as described below.

LAr Error Flag. During data taking it was discovered that large noise bursts that are not associated with any particle appear in the EM calorimeter and last on the order of 5 μs. A procedure was developed to identify these noise bursts and remove any data collected within ± 0.5 s of the burst to ensure that physics analyses are not impacted [115].

LAr Calorimeter Hole Veto. On the 30th April 2011 a power failure resulted in the loss of approximately 0.4% of the EM calorimeter cells [116]. This impacted the efficiency and reliability of reconstructing photons and electrons in the affected region. This also resulted in the energy deposited in the EM calorimeter by jets in the affected region being underestimated, introducing a source of $E_{\mathrm{T}}^{\mathrm{miss}}$. A "smart veto" procedure was developed by the SUSY group to veto events that are negatively affected by this hole without significantly reducing the amount of data that is available for physics, as described in [116]. All affected cells in the middle layer of the EM calorimeter were restored in July 2011 so this hole only effects data collected in periods E-H in the 7 TeV analysis.

Cosmic Muon Veto. If a cosmic muon is included in an event this could affect the $E_{\mathrm{T}}^{\mathrm{miss}}$ measurement due to the muon momentum not being balanced by other particles in the event. Also, if there is any overlap between a cosmic muon and energy deposits

in the EM calorimeter it could alter the shape of the deposits and introduce a source of non-pointing. To avoid this, any event which has a muon that is present after overlap removal with an axial impact parameter $|z_0| > 1$ mm or a transverse impact parameter $|d_0| > 0.2$ mm is removed from the sample.

6.2 Control Samples

In the following sections the various control samples used in this thesis are described. All diphoton events with $E_{\mathrm{T}}^{\mathrm{miss}} < 75$ GeV are separated into different control region samples, as explained in section 6.2.1. A control sample to model promptly produced photons and electrons is constructed from $Z \to ee$ data events as described in section 6.2.2. In section 6.2.3, the $Z \to ee$ data and MC samples that are used in tag and probe studies to model non-prompt photons are described.

6.2.1 Diphoton Control Regions

In these analyses three separate diphoton control regions (CRs) in the data have been defined so that the analysis strategy can be tested before the signal region is unblinded. Three control region samples (CR, CR1 and CR2) are created that have the same event requirements and treat the data the same as the signal region, except that the minimum p_{T} of photons in the CR sample is increased to 60 GeV (see section 8.3.2) and they have a different $E_{\mathrm{T}}^{\mathrm{miss}}$ range, as shown in table 6.3. As will be explained in section 6.3.3, the CR is also a background sample that is used to model jet contributions to the signal region.

Sample	$E_{\mathrm{T}}^{\mathrm{miss}}$ range (GeV)
CR	$E_{\mathrm{T}}^{\mathrm{miss}} < 20$
CR1	$20 < E_{\mathrm{T}}^{\mathrm{miss}} < 50$
CR2	$50 < E_{\mathrm{T}}^{\mathrm{miss}} < 75$
SR	$75 > E_{\mathrm{T}}^{\mathrm{miss}}$

TABLE 6.3: $E_{\mathrm{T}}^{\mathrm{miss}}$ range of the different control regions (CR) and the signal region (SR)

As will be explained in chapter 7, the signal region data is blinded until the final stages of the analysis to ensure that the signal region distributions do not influence the development of the analysis strategy. Due to having higher $E_{\mathrm{T}}^{\mathrm{miss}}$ thresholds than the

CR, CR1 and CR2 are also blinded until the full analysis strategy, including calculation of systematics and the limit setting procedure, has been finalised. CR1 is unblinded first and if the data behaves as expected then CR2 also can be unblinded and tested. However, if there are unexpected features in the data then these can be investigated to ensure that the behaviour of the signal and background is fully understood before the signal region is unblinded.

6.2.2 Prompt Electron Sample

This sample is derived from candidate $Z \rightarrow ee$ data events collected at ATLAS. The electrons in this sample are subject to the standard electron reconstruction method described in section 4.2, with the additional requirements that: the electrons must pass the diphoton trigger used in the signal region (see section 6.1), have p_{T} greater than 35 GeV (see section 8.3.1), be oppositely charged, have an invariant mass between 81 GeV and 101 GeV, and originate from the same PV. All electrons are also required to pass the Medium IsEM cuts and be detected outside of the crack region that was defined in section 3.2.1.

6.2.3 $Z \rightarrow ee$ Tag and Probe Sample

As has already been described in section 5.2.1, no data samples exist with large z_γ. Therefore a $Z \rightarrow ee$ data sample is used to model non-prompt photons, with the spread in z_{PV} over the different data taking periods being used to model z_γ. This is then extrapolated to larger values of z_γ, which are not available in data, using signal MC. Electrons from the $Z \rightarrow ee$ samples are able to model non-pointing photons by using a modified tag and probe method. The tag and probe method works by requiring one electron (tag) to pass the Tight IsEM cuts to identify the event as a good quality event. It is the information from the second electron (probe) that will be used to model z_γ. The probe electron is required to pass the Tight IsEM cuts relating to the quality of the track but no requirements are placed on the quality of the shower in the EM calorimeter. This ensures that the probe has a good quality track and only changes in the shower will affect any z_γ dependent variables, making it a good model for photons. If both electrons in an event pass the Tight IsEM cuts, then the tag and probe electrons are randomly assigned to the electrons in the event to remove any potential bias.

To avoid biasing the results by placing a quality requirement on the probe electron, the $Z \rightarrow ee$ events are only required to pass a single electron trigger. For all events that meet the above criteria, extra conditions are enforced to ensure that the samples are as pure as possible. Both electrons in the event are required to have p_{T} greater than 25 GeV, come from the same PV, be oppositely charged, and must have an invariant mass of between 81 GeV and 101 GeV.

MC $Z \rightarrow ee$ samples are also required, to ensure that what is being observed in data is being correctly reproduced in MC. If the $Z \rightarrow ee$ data and MC agree with the non-prompt photon samples over the range where data is available then it provides confidence that the MC is correctly modelling how the shower shape changes as z_{γ} increases and predictions made by the signal MC samples can therefore be trusted. The $Z \rightarrow ee$ MC samples used in these analyses are treated identically to the data samples.

6.3 Background Considerations

There is no SM candidate for a long lived neutral particle that decays to a photon and a dark matter candidate. However, it is possible for other SM processes or artefacts of the data taking environment to recreate the same expected signal of a diphoton and $E_{\mathrm{T}}^{\mathrm{miss}}$ final state and therefore populate the signal region.

In the limit setting procedure (see chapter 7) the number of events that are due to signal events or background events is determined by fitting the z_{γ} (7 TeV analysis) and t_{γ} (8 TeV analysis) distributions of the signal and background samples to the data in the signal region to determine the number of events that could be due to SPS8 signal events. If the expected number of events for SPS8 with a given Λ and τ combination from section 5.4 is larger than the number of signal events observed, then this combination is ruled out. It is therefore essential that the z_{γ} and t_{γ} distributions of the backgrounds used in the limit setting procedure correctly describe the background events that are present. The expected z_{γ} and t_{γ} distributions of the background will be modelled using data, this ensures that features such as the spread in z_{PV} will be correctly modelled.

The following sections will explain the different sources of background events and how these events are modelled for use in the limit setting procedure.

6.3.1 Primary Collision Backgrounds

Backgrounds arising from prompt SM sources in pp collisions account for the overwhelming majority of background events in the signal region in these analyses. As previously described in section 4.2.2, the Loose IsEM cuts are less powerful at distinguishing between true photons or objects commonly misidentified as photons, such as electrons or jets. Therefore potential candidates for the Loose photon(s) in the 7 TeV (8 TeV) analysis could either be true prompt photons, electrons or jets. By requiring at least one of the signal region photons in the 7 TeV analysis to pass the Tight IsEM cuts, the probability that this photon is a fake photon is greatly reduced. Signal region events could therefore be: QCD events decaying to $\gamma + X$, where X is either a photon, electron or jet; $W + \gamma$, where the electron from the $W \rightarrow e\nu$ fakes the loose photon; or $t\bar{t}$ events where the final state includes at least one true photon. The same decay channels are likely to be the dominant source of background events in the 8 TeV LL analysis except that the lack of the Tight requirement means it is possible that both objects in the final state could be fake photons.

6.3.2 Other Backgrounds

In addition to backgrounds originating from the collision of the main bunches there are a number of other sources of background that could potentially result in the required signal region final state of diphoton and $E_{\mathrm{T}}^{\mathrm{miss}}$. The majority of these sources are events where one of the final state objects does not originate from the PV collision. An example of a possible event is a $W \rightarrow e\nu$ interaction at the PV being produced in conjunction with a true photon from a pileup collision or the collision of satellite bunches. Since the photon is not produced at the PV, it will have a larger z_γ than would be expected if the photon was produced at the PV and therefore appear to be more like a signal event than a collision background event.

To estimate the total number of these background events that can be expected in the signal region, it is useful to first estimate the total number of inelastic collisions that will have taken place at ATLAS. Combining the full integrated luminosity measurement of the 7 TeV dataset of approximately 5 fb^{-1}with the total inelastic cross-section of 69.4 mb [117] using equation 3.2 gives the total number of inelastic collisions to be

approximately 3.5×10^{14}. The 7 TeV cross-section for producing $W \rightarrow e\nu$ interactions is found to be 4.791 nb [118] when the following requirements are met: the electron has $E_{\mathrm{T}} > 20$ GeV, $E_{\mathrm{T}}^{\mathrm{miss}} > 25$ GeV, the transverse mass of the $W > 40$ GeV. This gives a probability of 6.9×10^{-8} that a collision will produce a W that decays in such a way. The cross-section of producing a prompt isolated photon at ATLAS with $E_{\mathrm{T}} > 45$ GeV has been measured to be 5.88 nb [119], giving a probability per collision of 8.5×10^{-8}.

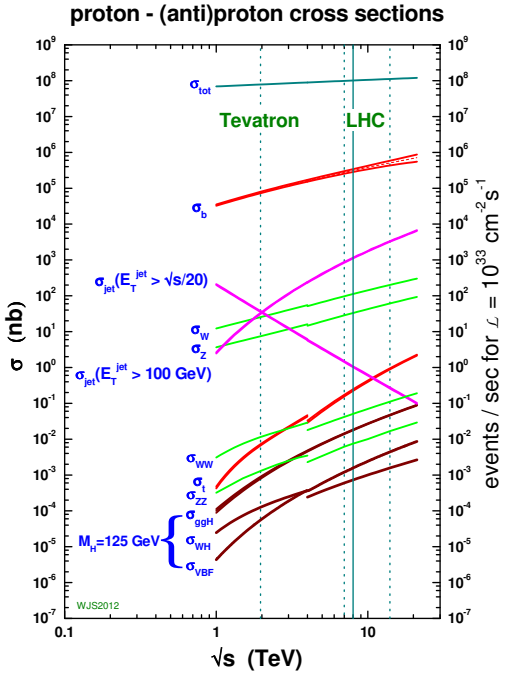

FIGURE 6.1: Standard Model cross sections at the Tevatron and LHC colliders[120].

When these probabilities are combined together with an average pileup rate of 10 collisions per bunch crossing in 2011, it is expected that there will be approximately 21 bunch crossings where a $W \rightarrow e\nu$ interaction overlaps with a prompt photon. However, the signal region thresholds for the minimum $E_{\mathrm{T}}^{\mathrm{miss}}$ of an event is much larger than that used in the calculations above. As highlighted by figure 6.2, the probability of a $W \rightarrow e\nu$ interaction having an $E_{\mathrm{T}}^{\mathrm{miss}}$ of between 25 GeV and 75 GeV is approximately two orders of magnitude larger than the probability of the interaction having an $E_{\mathrm{T}}^{\mathrm{miss}}$ larger than 75 GeV. Also, the event selection identifies all electrons that pass the medium IsEM cuts and removes them from the analysis during the overlap removal process (4.6). It can be seen in figure 6.3 that the medium IsEM cuts have an efficiency of approximately 90%, therefore only a maximum of 1 in every 10 $W \rightarrow e\nu$ decays will produce an electron that could fake a photon.

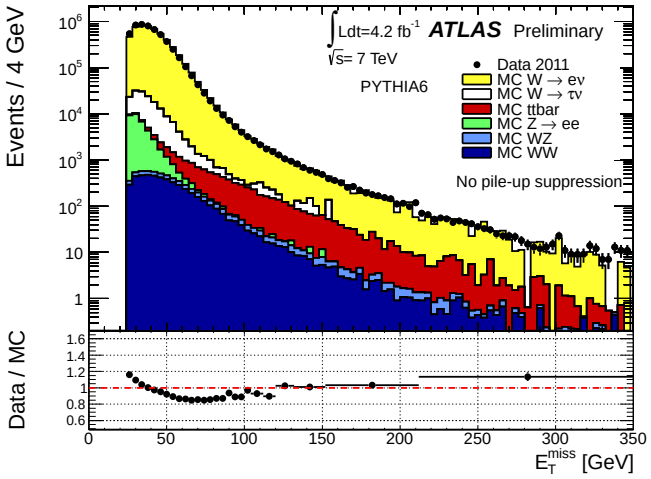

FIGURE 6.2: Distribution of $E_{\mathrm{T}}^{\mathrm{miss}}$ as measured in a data sample of $W \to e\nu$ events. The expectation from Monte Carlo simulation (Pythia6) is superimposed and normalised to data [121].

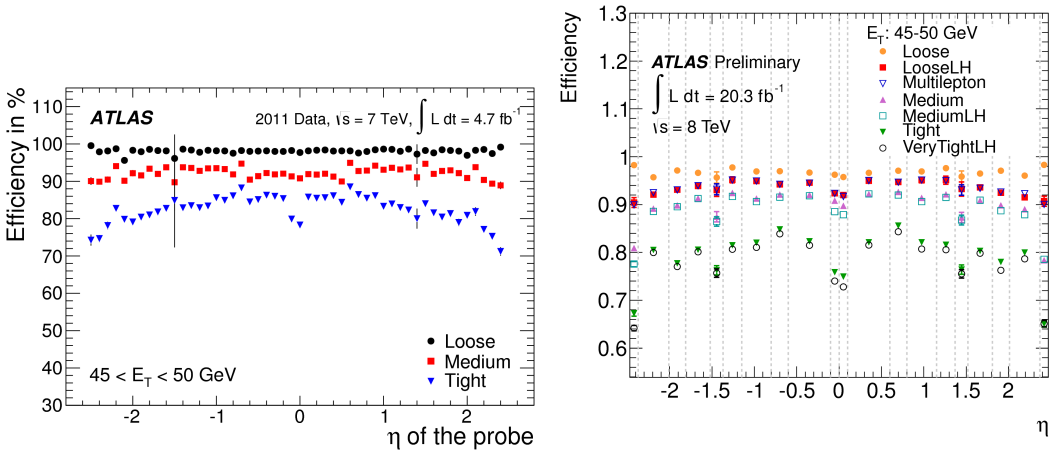

FIGURE 6.3: Measured identification efficiency for the various IsEM selections as a function of η for electrons in the E_{T} 45-50 GeV range for 7 TeV (left) and 8 TeV (right) pp collisions. More information on the methods used to calculate the efficiencies can be found in [90] and [122] for the 7 TeV and 8 TeV analyses respectively.

Taking these two effects into account, the expected number of bunch crossings with a $W \to e\nu$ decay overlapping with a prompt photon from a pileup collisions is reduced to approximately 0.02 in the 7 TeV data sample. This is still a conservative estimate since extra suppression factors from the increased E_{T} threshold of signal region objects, requiring an electron to pass the photon IsEM cuts and other inefficiencies in the selection criteria have yet to be taken into account.

In the 8 TeV analysis, the expected number of a $W \to e\nu$ decays overlapping with a

prompt photon from a pileup collision in the signal region will increase. This is due to the increase in the size of the dataset, the increase in the number of pileup events (see figure 3.4), and effects due to the increase in collision energy, such as a small increase in the cross-section of W production (see figure 6.1) and an increase in the E_{T} (and therefore $E_{\mathrm{T}}^{\mathrm{miss}}$) spectrum of particles. However, the expected contribution to the signal region sample is still expected to be less than one and therefore not taken into account when modelling the expected background.

In these analyses the background is modelled using data. Using a similar argument as above, the CR is expected to contain very few $W \rightarrow e\nu$ overlap events due to the $E_{\mathrm{T}}^{\mathrm{miss}}$ being less than 20 GeV. If these overlap events are more common than estimated above, they should appear in CR1 where the $E_{\mathrm{T}}^{\mathrm{miss}}$ range matches the $E_{\mathrm{T}}^{\mathrm{miss}}$ of $W \rightarrow e\nu$ decays. If during the unblinding process CR1 or CR2 looked more signal like than the CR, further investigation into the shape of these backgrounds would be required before the unblinding of the signal region could proceed.

In both the 7 TeV and 8 TeV analyses the probability of a collision between satellite bunches overlapping with a collision in the main bunch is many orders of magnitude lower than that of a pileup event due to the much lower occupancies in these bunches. As explained in section 5.2.2, a requirement placed on all photons in the 8 TeV analysis of $|t_{\gamma}| < 4$ ns ensures that these collisions will not impact the results. This cut also has an added benefit that it is stricter than the standard timing cut of ± 10 ns that reduces the sensitivity of analyses to cosmics, which is particularly important to this analysis due to the potential of cosmics having a non-pointing or delayed timing measurement. A study has shown that the impact of cosmics is negligible in diphoton + $E_{\mathrm{T}}^{\mathrm{miss}}$ events: a conservative upper limit of 0.46 ± 0.32 [123] can be placed on the number of events in the signal region of the 7 TeV analysis that are due to cosmics. When the equivalent numbers are calculated for the 8 TeV analysis, taking into account the 4 ns timing cut, this number is reduced to less than 0.2 ± 0.1. Therefore, the impact of cosmics on the signal region distributions can be neglected in both analyses.

6.3.3 Modelling the Background

In the previous two sections it has been discussed that the SM background to SPS8 signal events is dominated by collision backgrounds containing prompt photons, electrons

and jets. As shown in section 5.2.1, the development of the EM shower of photons and electrons is expected to be similar resulting in a similar pointing resolution in the calorimeter. The timing resolution of photons and electrons is also expected to be similar due to the timing measurement being performed only using information from the cell in the middle layer of the EM calorimeter with the maximum energy. Therefore, the $Z \rightarrow ee$ sample described in section 6.2.2 is used to model the z_γ and t_γ distributions of both photons and electrons from SM backgrounds. This sample is referred to as the e/γ sample.

In contrast to electrons, where a pure sample can be obtained by placing requirements relating to $Z \rightarrow ee$ kinematics, there is no way of obtaining a clean sample of jets. Instead the CR, which is dominated by QCD events containing jets and photons, is used to model the jet contribution. However, this sample will be contaminated by events containing prompt electrons and photons meaning that only a fraction (f_{jet}) of the events in the sample will be jets. Due to this e/γ contribution the central region of the z_γ distribution of the CR will be similar to the e/γ distribution. Jets are expected to have a wider shower than e/γ objects, resulting in the z_γ distribution of jets having a tail containing more events at larger values. Due to collision backgrounds being promptly produced and the t_γ measurement depending on energy deposited, not shower shape, the t_γ distribution of e/γ and CR samples will be similar, with f_{jet} having little impact on the shape. This can be seen in figure 6.4, which also shows that the t_γ distributions agree very well over different z_γ ranges, with the mean and RMS of the different t_γ distributions given in table 6.4. While the disagreements between the e/γ and CR distributions are small they are not unexpected, for example due to PV misidentification. The timing measurement has a correction to take into account the position of the PV so if it is misidentified this correction will be wrong and t_γ will not be correct. Since different backgrounds have a different probability of the PV being misidentified this will affect the e/γ and CR distributions differently as described in chapter 8. Also, PV misidentification results in a small shift in the z_γ value, introducing a small correlation between t_γ and z_γ.

While the jet and e/γ distributions can be modelled, the probability of jets and electrons faking photons is not accurately described in MC, therefore it is difficult to predict either the number of background events in the signal region or the fraction that will be due to jets or prompt e/γ objects. The fraction of the loose photon objects in the signal region sample that will be jets or e/γ objects is also expected to change for different $E_{\mathrm{T}}^{\mathrm{miss}}$

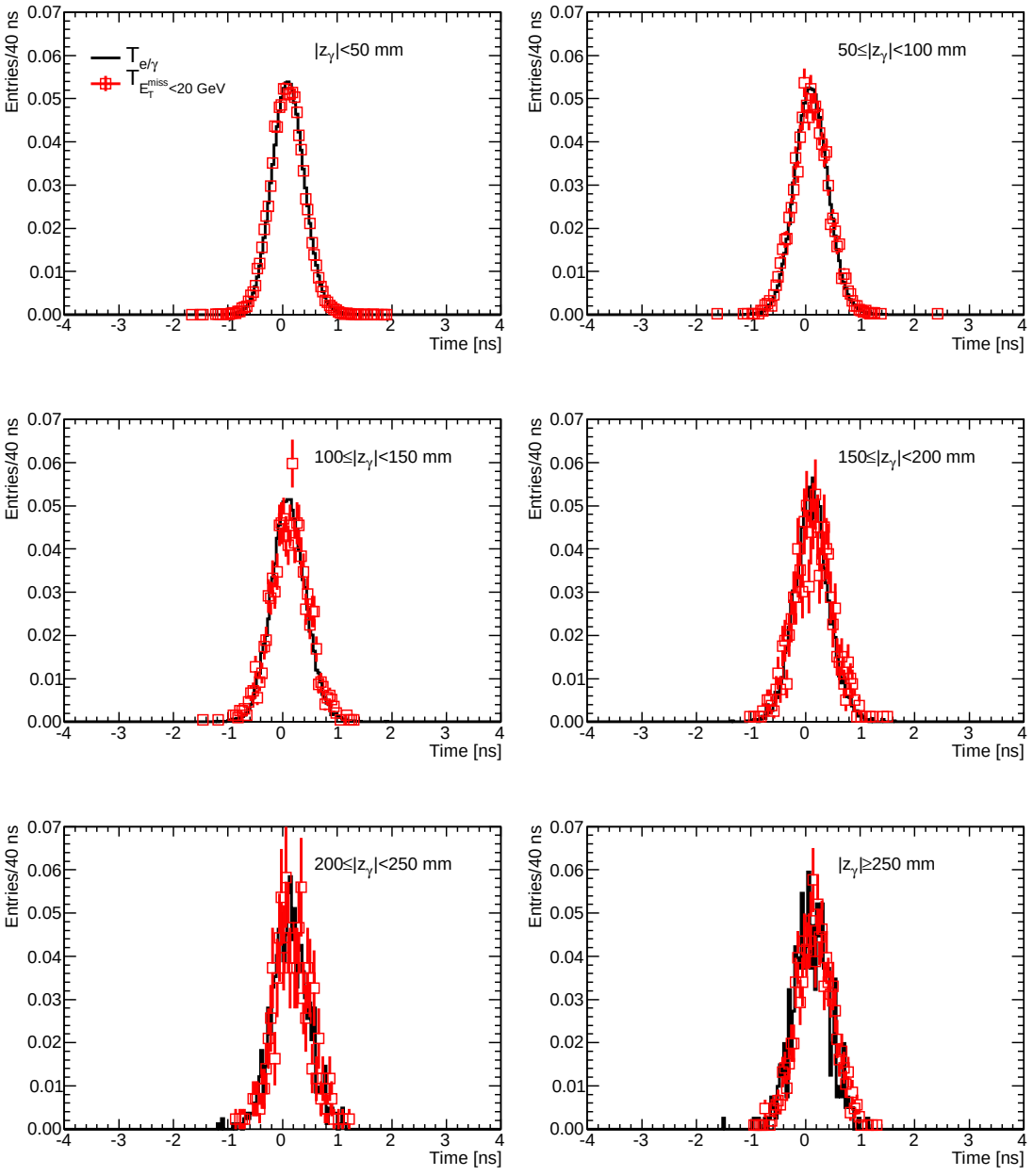

FIGURE 6.4: Superimposed unit-normalised t_γ distributions for the $Z \rightarrow ee$ and $E_{\mathrm{T}}^{\mathrm{miss}} < 20$ GeV 8 TeV control samples, for the various categories defined according to z_γ, with z_{DCA} modelling z_γ for the $Z \rightarrow ee$ sample. [59].

$\lvert z_\gamma \rvert$ Range (mm)	$Z \to ee$ Sample			$E_{\mathrm{T}}^{\mathrm{miss}} < 20$ GeV Sample			Max. $\lvert\Delta(t)\rvert$ [ps]
	No. of Entries	Mean [ps]	RMS [ps]	No. of Entries	Mean [ps]	RMS [ps]	
[0, 50)	3,456,008	101	300	25,614	91.8	306	9 ± 2
[50, 100)	193,320	105	311	5,013	103	326	4 ± 1
[100, 150)	22,325	110	321	1,957	124	341	23 ± 8
[150, 200)	3,792	111	321	798	138	359	37 ± 13
[200, 250)	822	138	338	429	173	323	72 ± 16
[250, ∞)	403	96.8	339	1,058	169	338	68 ± 10
[0, ∞)	3,676,670	101	301	34,869	100	314	1 ± 2

TABLE 6.4: Number of entries, mean and RMS of the jet and prompt e/γ 8 TeV timing background templates, for each of the categories defined according to z_γ, as well as (in the last row) for the inclusive distributions (i.e. all categories together). The last column shows the determination of the shift used as the systematic uncertainty for that category, determined as the absolute value of the maximum difference in means between the e/γ and $E_{\mathrm{T}}^{\mathrm{miss}} < 20GeV$ distributions in that category and the inclusive $Z \to ee$ sample, along with its statistical error [59]

regions so f_{jet} from the CR cannot be used to predict the f_{jet} of the signal region. The method for determining the number of signal and background events that are observed in the signal region is described in chapter 7. The templates used to model the t_γ and z_γ distributions for jets and e/γ objects can be found in sections 7.1.2 and 7.2.2 for the 7 TeV and 8 TeV analyses respectively.

Chapter 7

Analysis

As described in section 6.3.3, it is not possible to predict the number of background events in the signal region of this analysis using MC. Therefore, templates are created from the pointing and timing distributions for non-prompt photons and background events which are then fitted to the distributions observed in the signal region to determine the number of observed signal events. Due to the similarity between the pointing distributions of SPS8 samples with very low τ and the background templates, the minimum neutralino lifetime explored in these analyses is 250 ps. In this chapter the method of fitting signal and background templates to the pointing and timing distributions observed in the signal region is described, and how this is used to set limits in the SPS8 parameter space is outlined. Due to major differences in the template fitting strategy followed in the 7 TeV and 8 TeV analyses they are described separately in sections 7.1 and 7.2, however, each section follows a similar structure. First, the variables that are chosen for the signal and background templates are described in sections 7.1.1 and 7.2.1. Next, the templates used in the template fitting method are described in sections 7.1.2 and 7.2.2. Finally, the template fitting strategies are described in sections 7.1.3 and 7.2.3 and how the fits are performed and the results used to set limits in the SPS8 signal space are described in sections 7.1.4 and 7.2.4. Additionally, the optimisation of the bins and categories used in the limit setting procedure in the 8 TeV analysis is outlined in section 7.2.3.1.

7.1 7 TeV Analysis

7.1.1 Discriminating Variables

In the 7 TeV analysis the pointing variable z_γ is used as the only discriminating variable in the template fitting method to determine the number of signal events, with the t_γ measurement used as a cross-check. An event based analysis was pursued with the z_γ from the Loose photon in each event used to construct the pointing template.

7.1.2 Pointing and Timing Templates

SPS8 Signal Events z_γ Templates

Examples of the unit normalised z_γ distributions for SPS8 signal events in the 7 TeV analysis are shown in figure 7.1. As expected the distribution is wider for samples with larger neutralino lifetimes.

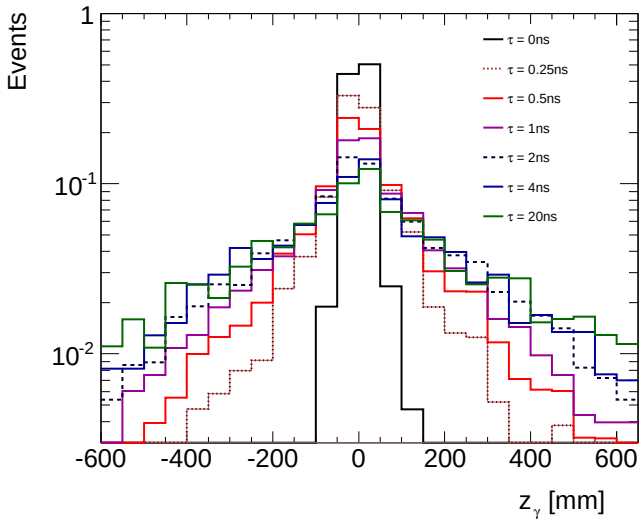

FIGURE 7.1: Unit-normalised z_γ templates for SPS8 $\Lambda = 120$ TeV MC signal samples of various neutralino lifetimes [57].

Background Events z_γ Template

The templates for the e/γ and CR z_γ distributions, as described in section 6.3.3, can be seen in figure 7.2 for the 7 TeV analysis.

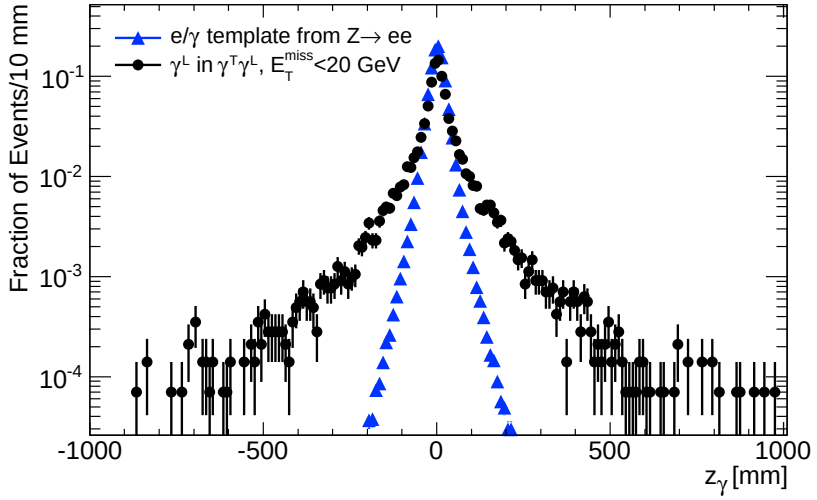

FIGURE 7.2: Expected shape of z_γ distributions for background contributions from jet ($E_{\mathrm{T}}^{\mathrm{miss}}$ <20 GeV) and e/γ objects at 7 TeV [57].

SPS8 Signal Events t_γ Templates

The t_γ template for SPS8 signal events in the 7 TeV analysis is shown in figure 7.3. It is only used as a cross-check in this analysis. A detailed description of this variable is provided in the corresponding section for the 8 TeV analysis.

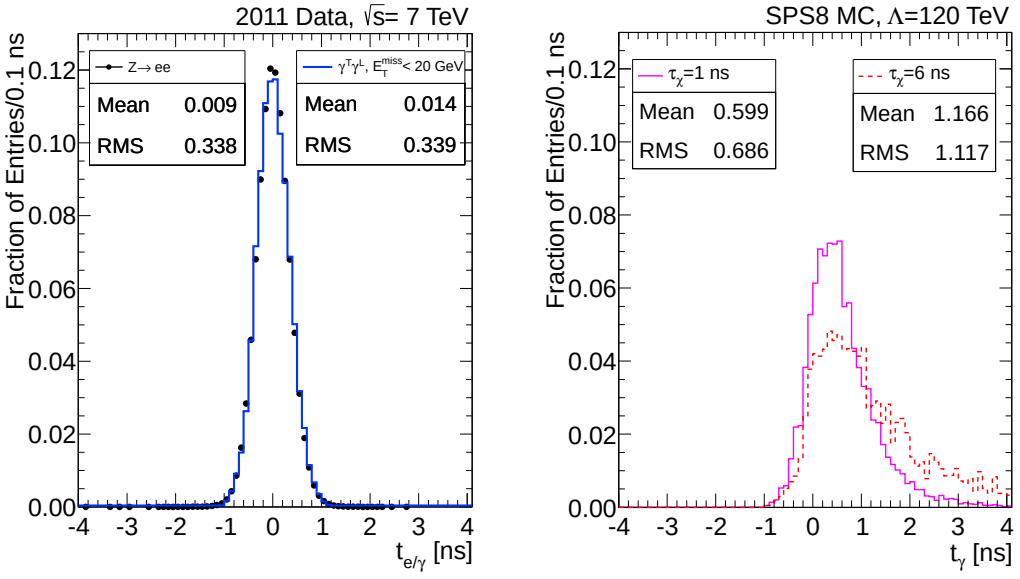

FIGURE 7.3: The left plots shows the timing templates as determined for prompt electrons/photons from two data samples: the e/γ distribution from a $Z \rightarrow ee$ sample (points) and the TL sample (blue) from the CR with $E_{\mathrm{T}}^{\mathrm{miss}} < 20$ GeV. The right plot shows the timing distributions for two SPS8 signal samples with $\tau = 1$ ns (solid pink) and $\tau = 6$ ns (dashed red) [57].

Background Events t_γ Template

It has already been shown in section 6.3.3 that the background objects in this analysis, prompt e/γ objects and jets, have similar t_γ distributions. Also, the t_γ for the 7 TeV analysis is not involved in the limit setting procedure. Therefore, due to the higher statistics in the sample, the e/γ t_γ distribution shown in figure 7.3 was the only background t_γ template developed for the 7 TeV analysis.

7.1.3 Fit Strategy

The signal MC template (T_{sig}) and background templates, for prompt e/γ objects ($T_{e/\gamma}$) and for jets (T_{jet}), are normalised to the number of events observed in the SR and separated into 9 bins with the following boundaries:

$$|z_\gamma| = 0,\ 20,\ 40,\ 60,\ 80,\ 100,\ 200,\ 400,\ 600,\ 2000\ [\text{mm}].$$

This choice of bins is a compromise between sensitivity, statistics, and CPU power. The more bins that are used in a fitting procedure, such as the one described below, the more sensitive the analysis is to changes in the shape of distributions. However, if there are many bins which are expected to have a low background count, then the analysis would be vulnerable to statistical fluctuations. This choice of bins was selected so that there are more bins at low z_γ, which is expected to be background dominated, to constrain the shape of the background fit at larger z_γ, which is expected to be signal dominated.

For each bin (i) the number of events (Z^i_{data}) will be the sum of the number of signal (N_{sig}) and background (N_{bkg}) events given by:

$$Z^i_{data} = N_{bkg} \cdot \left[f^{SR}_{jet} \cdot T^i_{jet} + \left(1 - f^{SR}_{jet}\right) \cdot T^i_{e/\gamma} \right] + N_{sig} \cdot T^i_{sig}, \tag{7.1}$$

where f^{SR}_{jet} is the jet fraction of the signal region.

As described in section 6.3.3, the CR template (T_{CR}) is used to model the jet template. However, it is also noted that a fraction of the loose objects in this sample will be prompt e/γ objects ($f^{CR}_{e/\gamma}$). Therefore, the jet template can be defined as:

$$T^i_{jet} = \frac{\left(T^i_{CR} - f^{CR}_{e/\gamma} \cdot T^i_{e/\gamma}\right)}{\left(1 - f^{CR}_{e/\gamma}\right)}. \tag{7.2}$$

Combining equations 7.1 and 7.2, Z^i_{data} can be rewritten as:

$$Z^i_{data} = N_{bkg} \cdot \left[F_{jet} \cdot T^i_{CR} + (1 - F_{jet}) \cdot T^i_{e/\gamma}\right] + N_{sig} \cdot T^i_{sig} \tag{7.3}$$

where the difference between the jet content of the CR and SR is accounted for by the modified jet fraction:

$$F_{jet} = \frac{f^{SR}_{jet}}{\left(1 - f^{CR}_{e/\gamma}\right)} \ . \tag{7.4}$$

Therefore, using equation 7.3, the fit to the SR can be performed with only three free parameters: F_{jet}, N_{sig}, and N_{bkg}. In addition to these free parameters, the normalised z_γ templates and the associated shape systematic uncertainties described in chapter 8 are required as inputs to the fit. This fit was performed using the method described in the next section for each point in the SPS8 signal grid used in this analysis.

7.1.4 Limit Setting Procedure

The limit setting in the 7 TeV analysis is performed within the RooStats framework [124]. As outlined in this section, the limit setting procedure follows the confidence limits (CL_S) method [125] of hypothesis testing used in analyses at ATLAS searching for signs of new physics. More detailed information, including explanations and discussion, on these methods can be found in the source material [125][126].

7.1.4.1 Likelihood Function

For each bin (i) of the fit, the number of expected events is given by:

$$N_i = L(\mu\sigma_i + \beta_i)$$

where L is the integrated luminosity, μ is the signal strength, σ_i is the effective signal cross-section for bin i, and β_i is the background cross-section in bin i. In this analysis, μ is determined separately for each signal grid point by dividing the number of signal events returned from the fit by the predicted number of events from tables in section 5.4. From this definition it is clear that $\mu = 0$ for the background only hypothesis and $\mu = 1$ for the signal + background hypothesis.

For each bin, a Poisson probability term can be used to calculate the likelihood for measuring k_i events given that N_i events are expected:

$$\mathcal{L}_i = \text{Pois}(k_i|N_i) = \frac{(N_i)^{k_i} e^{-N_i}}{k_i!}$$

which is iterated over all N bins in the fit to give:

$$\mathcal{L}_{\text{Stat.}} = \prod_{i=1}^{N} \mathcal{L}_i = \prod_{i=1}^{N} \frac{(N_i)^{k_i} e^{-N_i}}{k_i!}.$$

If systematic uncertainties are included, the number of expected events is now given by:

$$N_i = L\mu\sigma_i \prod_l (1 + \epsilon_l^S \delta_l^S) + L\beta_i \prod_k (1 + \epsilon_k^B \delta_k^B),$$

where the sources of systematic uncertainty affecting the signal distributions are denoted by l, with the relative uncertainty on the signal efficiency associated with that systematic given by ϵ_l^S. The corresponding background systematic uncertainties and relative uncertainty on the background cross-section are given by k and ϵ_k^B. All systematic uncertainties are treated as nuisance parameters, denoted by δ, which are constrained by a distribution $\mathcal{G}$. These constraining distributions are typically Gaussian for symmetric uncertainties, with a width equal to the systematic uncertainty. The total combined likelihood function is now given by:

$$\mathcal{L}_{\text{Total}} = \mathcal{L}_{\text{Stat.}} \cdot \prod_l \mathcal{G}(m_{\delta_l^S}|\delta_l^S) \cdot \prod_k \mathcal{G}(m_{\delta_k^B}|\delta_k^B),$$

$$\mathcal{L}_{\text{Total}} = \prod_{i=1}^{N_i} \frac{(N_i)^{k_i} e^{-N_i}}{k_i!} \cdot \prod_l \mathcal{G}(m_{\delta_l^S} | \delta_l^S) \cdot \prod_k \mathcal{G}(m_{\delta_k^B} | \delta_k^B).$$

The m_δ terms are the input values of the corresponding nuisance parameters, calculated when estimating the systematic uncertainties.

7.1.4.2 Test Statistic

A test statistic q_μ, based on the profile likelihood ratio [126][127], is constructed to set upper limits on the observed signal strength compared to a hypothesis:

$$q_\mu = \begin{cases} -2\ln(\frac{\mathcal{L}(\mu,\hat{\hat{\theta}})}{\mathcal{L}(\hat{\mu},\hat{\theta})} & 0 \leq \hat{\mu} \leq \mu, \\ -2\ln(\frac{\mathcal{L}(\mu,\hat{\hat{\theta}})}{\mathcal{L}(0,\hat{\theta})} & \hat{\mu} < 0, \\ 0 & \hat{\mu} > \mu \end{cases} \tag{7.5}$$

where the values of the nuisance parameters that maximise $\mathcal{L}$ for a given value of μ are represented by $\hat{\hat{\theta}}$, and the values of the signal strength and nuisance parameters that give the absolute maximum value of $\mathcal{L}$ are represented by $\hat{\mu}$ and $\hat{\theta}$ respectively. If a negative signal contribution is required to maximise $\mathcal{L}$ then $\hat{\mu}$ is set to 0 in the fit, since a negative signal contribution is unphysical. Also, if more signal than the signal + background hypothesis ($\hat{\mu} > \mu$) is required to maximise $\mathcal{L}$ then q_μ is set to 0 as this does not suggest a disagreement between the observed data and the signal model. Therefore, large values of q_μ will only occur when there is a large disagreement between the signal + background hypothesis and the observed data due to the signal model being a poor description of the data.

To test the quality of the background only fit, the test statistic becomes:

$$q_0 = \begin{cases} -2\ln(\frac{\mathcal{L}(0,\hat{\hat{\theta}})}{\mathcal{L}(\hat{\mu},\hat{\theta})} & \hat{\mu} > 0, \\ 0 & \hat{\mu} < 0. \end{cases} \tag{7.6}$$

This results in q_0 only having a value greater than 0 if the best fit to the observed data requires some signal contribution.

7.1.4.3 p-Values and Confidence Limits

To quantify the level of disagreement between the observed data and either of the background only or signal + background hypotheses, a p-value is calculated:

$$p_\mu = \int_{q_\mu,\text{obs}}^{\infty} f(q_\mu|\mu)\,\mathrm{d}q_\mu, \tag{7.7}$$

where $q_{\mu,\text{obs}}$ is the value of q_μ observed in the data, and $f(q_\mu|\mu)$ is the probability density function of q_μ for a given μ. In this analysis q_μ is calculated by generating pseudo experiments, handled within the RooStats framework.

To set upper limits across the signal grid, a $\mathrm{CL_S}$ value [125] is defined as:

$$\mathrm{CL_S} = \frac{P\left(q \geq q_{\text{obs}}|s+b\right)}{P\left(q \geq q_{\text{obs}}|b\right)} = \frac{p_{s+b}}{1-p_b}. \tag{7.8}$$

Any grid point in the Λ vs τ signal grid is considered to be excluded at 95% confidence level if it has a $\mathrm{CL_S}$ value of less than 0.05.

7.2 8 TeV Analysis

7.2.1 Discriminating Variables

For the 8 TeV analysis, both t_γ and z_γ were used to construct the templates used in the template fitting method, increasing the sensitivity of the analysis to SPS8 signal events. As explained in section 7.2.3.1, t_γ is more powerful at separating signal and background than z_γ. Therefore, to pursue an event based analysis, the photon with the maximum t_γ value in every event was selected to construct the timing and pointing templates. However, it has already been stated that only photons detected in the barrel will be used in this analysis due to the better pointing resolution. Therefore, it is only in events where both photons are detected in the barrel (BB events) that the photon with the maximum t_γ value will be selected. In events where one photon is detected in the barrel and one is detected in the end-cap (BE events) the barrel photon will be selected. The

difference in the shape of the z_γ and t_γ distributions due to this selection is addressed in section 8.3.3.

7.2.2 Pointing and Timing Templates

SPS8 Signal Events t_γ Templates

The 8 TeV t_γ distributions are shown in figure 7.4 for various neutralino lifetimes and Λ values.

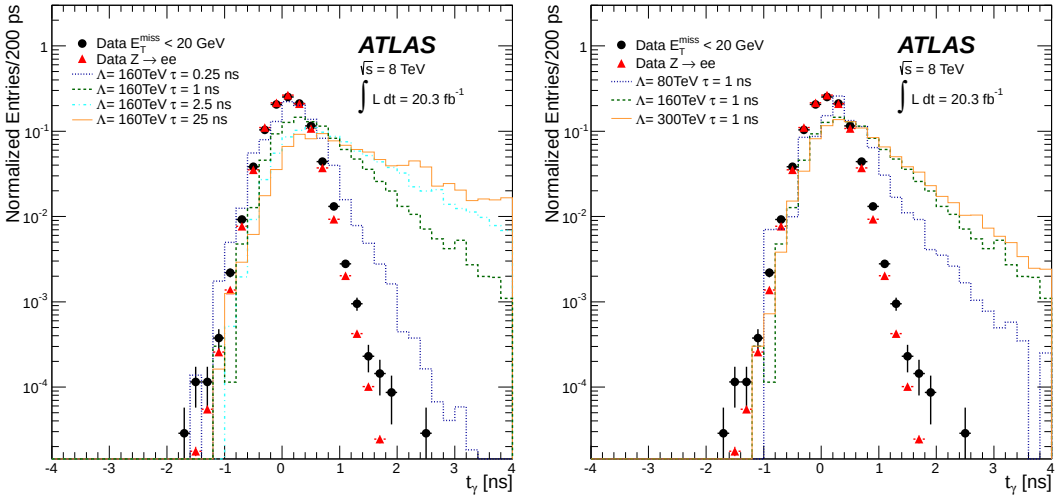

FIGURE 7.4: The timing templates for the $E_{\mathrm{T}}^{\mathrm{miss}}$ less than 20 GeV (black) and $Z \rightarrow ee$ (red) background templates. The left plot compares the background timing distributions to signal distributions with $\Lambda = 160$ TeV and various different neutralino lifetimes. The right plot compares the background timing distributions to signal distributions with various Λ values with a neutralino lifetime of 1 ns.

Background Events t_γ Template

As described in the next section, in the 8 TeV analysis the CR template is used to model the t_γ distribution of the prompt background distribution with the e/γ distribution used as a systematic uncertainty on the shape. The templates can be seen in figure 7.5 and compared to expected signal distributions in figure 7.4.

SPS8 Signal Events z_γ Templates

In figure 7.6 the z_γ templates for various SPS8 signal MC samples with different Λ values and neutralino lifetimes are shown alongside the background templates. The left plot of figure 7.6, which shows the z_γ template for four different MC signal samples with $\Lambda = 160$ TeV and different neutralino lifetimes, agrees with the trend seen in figure 7.1.

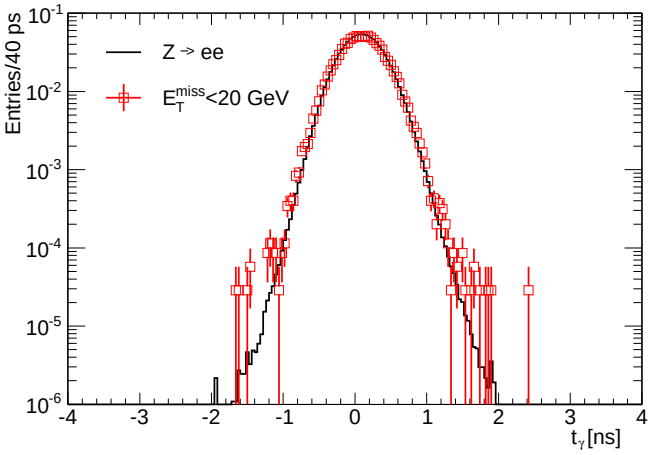

FIGURE 7.5: Expected shape of the t_γ distributions for jet ($E_{\mathrm{T}}^{\mathrm{miss}}$ <20 GeV) and e/γ ($Z \rightarrow ee$) contributions to the 8 TeV background [59].

The right plot of 7.6, shows z_γ templates for three different MC signal samples with different Λ values and $\tau = 1$ ns. It can be seen that the z_γ distribution is expected to be wider for signal samples with larger Λ values, however the shape differs by much less than that observed for different neutralino lifetimes.

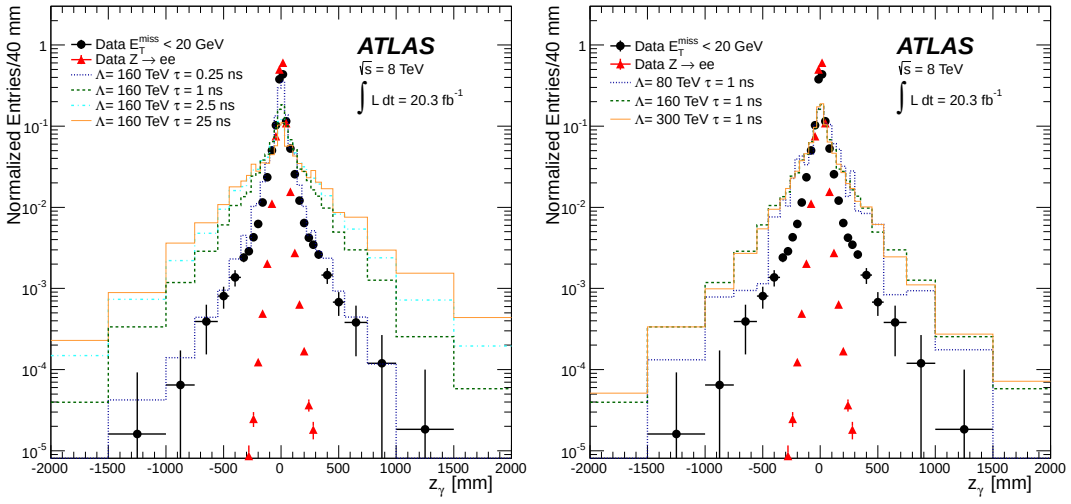

FIGURE 7.6: The pointing templates for the $E_{\mathrm{T}}^{\mathrm{miss}} < 20$ GeV (black) and $Z \rightarrow ee$ (red) background templates. The left plot compares the background pointing distributions to signal distributions with $\Lambda = 160$ TeV and various different neutralino lifetimes. The right plot compares the background pointing distributions to signal distributions with various Λ values with a neutralino lifetime of 1 ns.

Background Events z_γ Template

The templates for the e/γ and CR z_γ distributions can be seen in figure 7.7 and compared to expected signal distributions in figure 7.6 for the 8 TeV analysis.

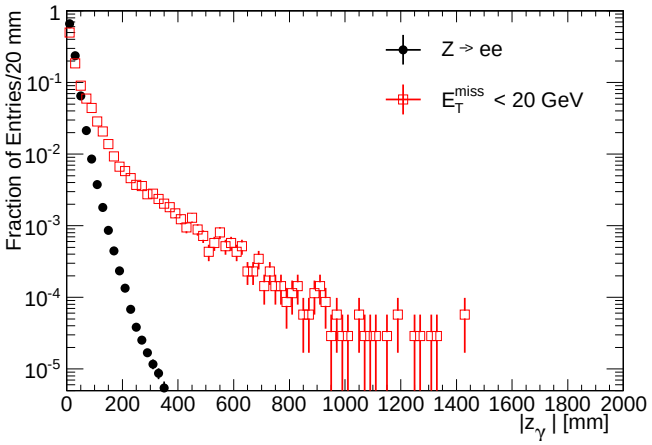

FIGURE 7.7: Expected shape of the z_γ distributions for jet (E_T^{miss} <20 GeV) and e/γ ($Z \rightarrow ee$) contributions to the 8 TeV background [59].

7.2.3 Fit Strategy

As has previously been described, the 8 TeV analysis makes use of the timing variable t_γ in addition to the pointing variable z_γ that was used as the only discriminating variable in the 7 TeV analysis. The background in this analysis is derived from data samples that contain limited statistics, especially in the larger t_γ and z_γ regions where larger amounts of signal events are predicted, therefore a full 2D fit is not suitable for this analysis. Instead, the z_γ distribution of the SR is split into categories creating multiple mutually exclusive samples of photons. Due to the difference in the z_γ shape of the signal and background, each of these samples will contain a different signal-to-background ratio. Therefore, a 1D fit of the signal and background to the t_γ of the SR is performed independently for each z_γ category. The difference in the z_γ shape of the jet and e/γ backgrounds means that the content of the background is also expected to change for the different categories, therefore the background normalisation in each category is treated as an independent nuisance parameter. However, since the t_γ shape of the e/γ and CR distributions has been shown to be very similar in section 6.3.3, only one template needs to be included in the fitting procedure. The background is expected to be a combination of prompt e/γ objects and jets, therefore the CR sample was chosen as the only t_γ background template, with any differences between the CR and e/γ distributions accounted for in a systematic uncertainty, as explained in section 8.3.4.

The boundaries of the different z_γ categories and the t_γ bins used in the limit setting

procedure were optimised to increase the sensitivity of the analysis, as explained in section 7.2.3.1. Due to the SPS8 t_γ and z_γ distributions appearing more similar to the background distributions for low τ values, two separate sets of boundaries were optimised: one for signal points with $\tau \leq 4$ ns and one for signal points with $\tau > 4$ ns. These boundaries are given in table 7.1.

τ Range	Category Boundaries for $\lvert z_\gamma \rvert$ [mm]						
$\tau \leq 4$ ns	0	40	80	120	160	200	2000
$\tau > 4$ ns	0	50	100	150	200	250	2000
τ Range	Bin Boundaries for t_γ [ns]						
$\tau \leq 4$ ns	-4.0	0.5	1.1	1.3	1.5	1.8	4.0
$\tau > 4$ ns	-4.0	0.4	1.2	1.4	1.6	1.9	4.0

TABLE 7.1: Values of the optimised ranges of the z_γ categories and t_γ bins for both low and high neutralino lifetime (τ) samples used in the 8 TeV analysis.

7.2.3.1 Optimisation of Category and Bin Boundaries

In this analysis, the amount of expected signal relative to the amount of expected background can change by many orders of magnitude for different z_γ and t_γ ranges. Therefore, standard approaches to optimisation do not provide an accurate estimate of the significance across the entire signal grid [126]. Instead, the boundaries in z_γ and t_γ were optimised by maximising the median expected discovery significance ($med[Z_0|1]$), derived from the Poisson likelihood for a fit to "perfect" signal-plus-background Asimov data [126]. The statistical significance can be approximated, for a single category (i) and bin (j), to:

$$med[Z_0^{ij}|1] = \sqrt{q_0^{ij}} = \sqrt{2[(S_{ij} + B_{ij})\ln(1 + \frac{S_{ij}}{B_{ij}}) - S_{ij}]},$$

where S_{ij} is the expected number of signal events for a signal strength of $\mu = 1$, and B_{ij} is the total number of expected background events. Both S_{ij} and B_{ij} are determined using the signal and background templates and correspond to the median expectations for the signal and background yields. In this analysis there are multiple bins and categories, therefore the significance is added in quadrature:

$$med[Z_0|1]^2 = \sum_{i}^{\text{categories}} \sum_{j}^{\text{bins}} med[Z_0^{ij}|1]^2.$$

The boundaries in t_γ and z_γ that correspond to the maximum significance were calculated for every signal point in the Λ vs τ signal grid, an example of which is shown in figure 7.8. In these plots, it can clearly be seen that the t_γ variable provides a greater significance than the $|z_\gamma|$ variable and is therefore more powerful at separating signal and background in this analysis.

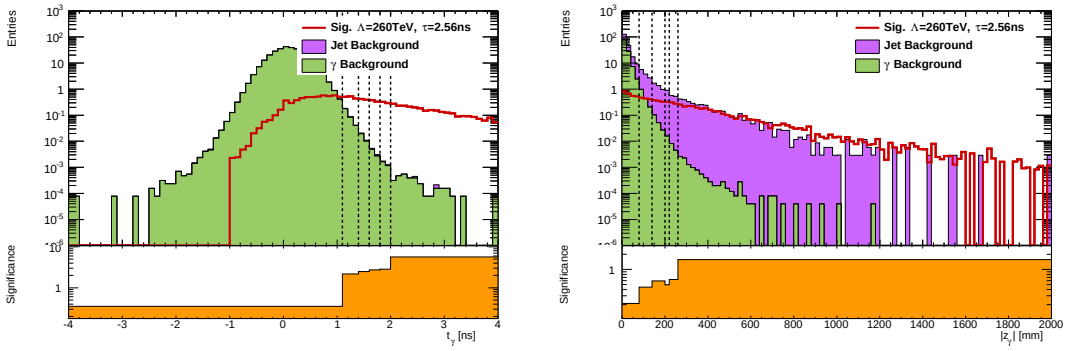

FIGURE 7.8: The optimal bin boundaries in t_γ (left) and category boundaries in z_γ (right) for the signal grid point with $\Lambda = 260$ TeV and $\tau = 2.56$ ns. The vertical dashed lines indicate the positions of the divisions between categories. The sub-plot provides the counting significance in each category [59].

It is important to note that the limited statistics in the background samples at large t_γ and z_γ values, and also in some signal samples, means that it is possible that the optimisation procedure may be affected by statistical fluctuations. To avoid this affecting the results, two sets of global boundaries were produced by averaging the position of the different boundaries over every signal grid point: one for grid points with $\tau \leq 4$ ns and one for grid points with $\tau > 4$ ns. These boundaries can be seen in table 7.1.

7.2.4 Limit Setting Procedure

The limit setting procedure for the 8 TeV analysis is implemented using the procedure developed to determine the Higgs Boson spin in the $H \rightarrow \gamma\gamma$ decay channel, more details of which can be found in [128], rather than in the RooStats framework. It follows the same logic as laid out in section 7.1.4, except for two important differences. The signal region in the 8 TeV analysis is separated into z_γ categories and t_γ bins, therefore the likelihood functions described in section 7.1.4 will need to be iterated over two dimensions. Also, a different approach is used to determine the q_μ distribution. Wilk's [129] and Wald's [130] theorems state that if a sample is sufficiently large then the test

statistic q_μ will take an asymptotic form and $f(q_\mu|\mu) \sim \chi^2_1$. This asymptotic approach to producing limits is pursued in the 8 TeV analysis, in contrast to the pseudo experiment approach pursued in the 7 TeV analysis.

Chapter 8

Systematic Uncertainties

In the template fitting method presented in the previous chapter, signal and background templates are fitted to the signal region to determine the number of observed signal events over the SPS8 parameter space. Therefore, if the shape of the signal or background templates are incorrectly modelled, the number of observed signal events returned by the template fitting will be incorrect. Any factor that could lead to the shape of the templates being incorrect is investigated in this chapter with a systematic uncertainty covering the potential variation in the shape calculated for each. The theoretical predictions and signal efficiencies that went into the signal yield estimates in section 5.4, which are used in the limit setting procedure, will also be subject to uncertainties that need to be estimated. Due to this the systematics have been divided into three categories: 'flat' systematic uncertainties that are common to all events are described in section 8.1, systematics due to uncertainties about the shape of the signal distributions are described in section 8.2, and systematics due to uncertainties related to the shape of the background distributions are described in section 8.3.

A summary of the uncertainties that are relevant to the 7 TeV analysis is shown in table 8.1 and the uncertainties that are relevant to the 8 TeV analysis is shown in table 8.2. In both analyses the uncertainty on the shape of the SM background is the dominant systematic uncertainty.

Impact	Source of Uncertainty	Value	Comment
Signal Yield	Integrated Luminosity	±1.8%	Section 8.1.1
	L1 Trigger Efficiency	±2%	Section 8.1.2
	HLT Efficiency	±0.5%	Section 8.1.2
	Photon E_T Scale/Resolution and Photon Identification	±4.4%	Section 8.1.3
	Photon Isolation	±1.4%	Section 8.1.3
	Object Quality and LAr Hole Flags	±0.2%	Section 8.1.3
	$E_{\mathrm{T}}^{\mathrm{miss}}$: Topocluster Energy Scale	$\pm 1.0 - 6.4\%$	Section 8.1.5
	$E_{\mathrm{T}}^{\mathrm{miss}}$ Resolution	$\pm 0 - 4.9\%$	Section 8.1.5
	Signal MC Statistics	$\pm 0.7 - 5\%$	Section 8.1.6
	Signal PDF and Scale Uncertainties	$\pm 4.7 - 6.4\%$	Section 8.1.7
	Signal Template	Shape	Section 8.2
Background	e/γ Template	Shape	Section 8.3.1
	$E_{\mathrm{T}}^{\mathrm{miss}} < 20$ GeV Template	Shape	Section 8.3.2

TABLE 8.1: Summary of systematic uncertainties for the 7 TeV analysis [57]

Impact	Source of Uncertainty	Value	Comment
Signal Yield	Integrated Luminosity	±2.8%	Section 8.1.1
	Trigger Efficiency	±2%	Section 8.1.2
	Photon E_T Scale/Resolution	±1%	Section 8.1.4
	Prompt Photon ID and Isolation	±1.5%	Section 8.1.4
	$E_{\mathrm{T}}^{\mathrm{miss}}$	±1.1 %	Section 8.1.5
	Signal MC Statistics	$\pm 0.81 - 3.6\%$	Section 8.1.6
	Signal Reweighting	$\pm 0.5 - 5\%$	Section 8.1.6
	Signal PDF and Scale Uncertainties	$\pm 9.9 - 13.4\%$	Section 8.1.7
	Signal Template	Shape	Section 8.2
Background	e/γ Template	Shape	Section 8.3.1
	$E_{\mathrm{T}}^{\mathrm{miss}} < 20$ GeV Template	Shape	Section 8.3.2
	Background Composition	Shape	Sections 8.3.3 & 8.3.4

TABLE 8.2: Summary of systematic uncertainties for the 8 TeV analysis

8.1 Flat Systematic Uncertainties

These systematic uncertainties have no dependence on t_γ or z_γ and are therefore the same for every event in the signal region.

8.1.1 Luminosity

The uncertainty on the integrated luminosity, described in section 3.1.2, collected by ATLAS during pp runs will propagate through to an uncertainty on the number of expected signal events via equation 3.2. The uncertainty is dominated by the uncertainty on the van der Meer scans [131][132] used to determine the horizontal and vertical profiles

of the proton beams and has been found to be ±1.8% [66] in the 7 TeV analysis and ±2.8%, using the same techniques as described in [133], in the 8 TeV analysis.

8.1.2 Trigger

As described in section 5.3.4, the L1 trigger shows no z_γ dependence and a conservative systematic of ±2% is adopted in the 7 TeV and 8 TeV analyses to cover any potential deviations. In the 7 TeV analysis an additional systematic of ±0.5% is assigned to account for uncertainty in the high level trigger efficiency, as described in [112].

8.1.3 7 TeV Photon Identification Efficiency

Diphoton Identification: As described in section 5.3.3, any differences in data and MC relating to the photon identification efficiency and shower shape variables were independent of z_γ in the 7 TeV analysis. Therefore any uncertainty due to differences between the efficiency of identifying photons in data and MC will be the same for prompt and non-prompt photons. This systematic was calculated to be ±4.4% [112] and covers the effects of photon E_{T} scale and resolution as well as the efficiency of both photons passing the Tight IsEM. Due to the stricter cuts, the uncertainty of a photon passing the Tight IsEM cuts is larger than for a photon passing the Loose IsEM, implying that this is a conservative estimate for the Tight-Loose selection used in this analysis.

Isolation: To calculate the systematic uncertainty due to isolation the difference in the isolation cone around electrons in the $Z \to ee$ tag and probe MC and data samples were compared. The mean of the isolation in a cone of $\Delta R < 0.2$ around the electrons in MC and data was found to differ by 0.4 GeV [112]. Therefore, for a range of signal samples the isolation cut was shifted by ±0.4 GeV and the efficiency of photons from that sample passing the new isolation cut was recorded in table 8.3. It can be seen that the maximum deviation from the nominal efficiency is 1.4%. Since this is negligible compared to other systematic uncertainties in the analysis, this value was taken as a flat symmetric systematic for every sample.

Λ (TeV)	τ (ns)	Efficiency difference (%) when lowering isolation cut to 4.6 GeV	Efficiency difference (%) when raising isolation cut to 5.4 GeV
90	2	-0.8	+0.8
90	6	-1.4	+0.6
100	2	-1.0	+0.7
100	6	-0.8	+0.9
120	2	-0.7	+0.6
120	10	-1.1	+0.9
150	2	-0.9	+0.6
200	2	-0.9	+0.6

TABLE 8.3: Change in signal efficiency for a sample of signal grid points as the isolation cut is changed by ±0.4 GeV [57].

8.1.4 8 TeV Photon Identification Efficiency

Energy Scale and Resolution: Any difference in the photon energy scale in data and MC creates uncertainty on the expected signal yield by changing the efficiency of photons passing the 50 GeV p_{T} cut. Similarly, any uncertainty on the energy resolution of the EM calorimeter will create uncertainty on the efficiency of photons passing the 50 GeV p_{T} cut. The photon E_{T} scale and resolution systematic uncertainty was calculated using the standard method developed by the ATLAS Egamma Working Group [92]. This method involves smearing the photon E_{T} distribution within the known uncertainties and recalculating the new efficiency of photons passing the 50 GeV p_{T} cut. The difference in efficiency compared to the nominal value was found to be ±1%.

IsEM Identification Efficiency: The ATLAS Egamma Working Group [134] gives the uncertainty on the efficiency of all photons with energy greater than 40 GeV passing the Tight IsEM cuts as ±1.5%, except for unconverted photons detected with $|\eta| > 1.81$ which have an uncertainty of ±2.5%. This uncertainty was calculated for photons that pass the standard isolation cut and also includes any uncertainties relating to the isolation requirements. This uncertainty is considered to be conservative due to requiring photons to pass the Tight IsEM cuts rather than the Loose IsEM cuts used in this analysis.

Shower Shape Variables As described in section 5.3.3 no additional systematic is required to account for any potential difference between data and MC in the reconstruction of SSVs at large z_{γ}.

Isolation In the 8 TeV analysis, the uncertainty due to the isolation cut is included in the IsEM identification systematic. However, this was calculated for prompt photons and does not take into account any uncertainties that may arise due to photons being non-pointing. Figure 8.1 compares the efficiency of probe electrons from $Z \rightarrow ee$ data and MC samples passing the isolation requirement and shows that they are in good agreement even as z_γ increases. Also shown in figure 8.1 is the efficiency of photons from a prompt and non-prompt signal sample passing the isolation requirements and it can be seen that they are in good agreement in the z_γ range where the prompt sample has statistics. The right hand plot in figure 8.1 shows the isolation of a signal sample extended to much larger z_γ values and it can be seen that the efficiency remains flat, therefore no additional uncertainty is applied.

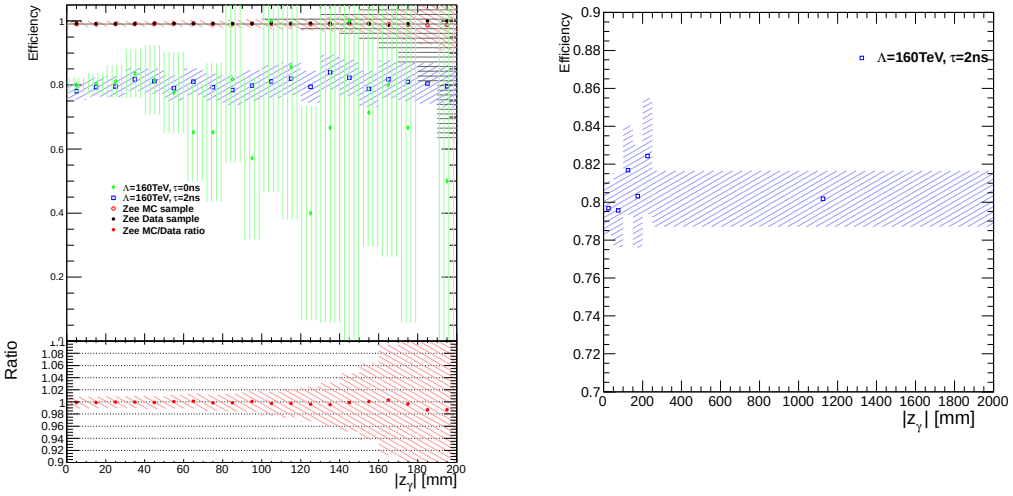

FIGURE 8.1: The left plot shows the isolation efficiency of electrons in data and MC $Z \rightarrow ee$ tag and probe samples and photons in a prompt and 2 ns SPS8 sample as a function of z_γ. The figure on the right shows the isolation efficiency of photons in a 2 ns SPS8 sample over an expanded range of z_γ.

Object Quality and LAr Hole Flags - 7 TeV analysis: As described in section 6.1.1, events are rejected if any particle fails the object quality cuts or if any particle is reconstructed in the EM calorimeter hole. These effects were included in certain MC samples and it was found that the efficiency of a single photon passing this veto in data and MC differed by 0.1% [115]. Incorrectly assuming that both photons in the final state are completely correlated would give a, negligible and conservative, estimate of $\pm 0.2\%$ for this systematic uncertainty in diphoton events.

8.1.5 $E_{\mathrm{T}}^{\mathrm{miss}}$ Uncertainties

The $E_{\mathrm{T}}^{\mathrm{miss}}$ measurement used in these analyses is calculated by summing up the transverse energy of every object in an event as described in section 4.5. Therefore, any uncertainties on the measured energy of these objects will propagate through to an uncertainty on the amount of $E_{\mathrm{T}}^{\mathrm{miss}}$ in an event. A different method was used to estimate the uncertainty on the $E_{\mathrm{T}}^{\mathrm{miss}}$ calculation in the 7 TeV and 8 TeV analyses. The different methods are outlined separately below.

7 TeV Analysis: The calculation of the systematic uncertainty on the scale and resolution of the $E_{\mathrm{T}}^{\mathrm{miss}}$ measurement in the 7 TeV analysis followed the recipe of scaling and smearing the $E_{\mathrm{T}}^{\mathrm{miss}}$ measurements developed by the prompt analysis team [135][136]. The systematics are calculated independently for each signal grid point and found to vary between 1.0% and 6.4% for the uncertainty on the $E_{\mathrm{T}}^{\mathrm{miss}}$ scale and between 0-4.9% for the uncertainty on the $E_{\mathrm{T}}^{\mathrm{miss}}$ resolution. More details on the method used and the uncertainty for each individual grid point can be found in Appendix D.

8 TeV Analysis: The ATLAS working group that developed the procedures for measuring the $E_{\mathrm{T}}^{\mathrm{miss}}$ in events calculated the uncertainty associated with all of the objects that contribute towards the $E_{\mathrm{T}}^{\mathrm{miss}}$ measurements and included them in a tool that can be used by analysis teams [137]. This tool was used to estimate the impact of these uncertainties on the efficiency of events passing the $E_{\mathrm{T}}^{\mathrm{miss}}$ cut of this analysis for a range of SPS8 signal MC samples. In addition to this systematic uncertainty there is also a well documented bug in ATLAS MC samples that results in the $E_{\mathrm{T}}^{\mathrm{miss}}$ of events being incorrectly calculated [138, 139]. The uncertainty in the $E_{\mathrm{T}}^{\mathrm{miss}}$ measurement due to this bug was combined quadratically with the standard $E_{\mathrm{T}}^{\mathrm{miss}}$ uncertainty for every MC signal sample with a maximum value of 1.1% obtained across the entire grid. This maximum value is taken as the $E_{\mathrm{T}}^{\mathrm{miss}}$ uncertainty across the entire signal grid since as it is negligible compared to other systematic uncertainties and provides a conservative estimate for the majority of signal samples.

8.1.6 Signal MC statistics and Reweighting Systematic

The uncertainty on the signal efficiency due to signal MC statistics varies depending on the sample selected. The efficiency and corresponding uncertainty for a range of Λ and

lifetimes can be found in Appendix C and typically lies between 0.7 - 5% for the 7 TeV samples and 0.81 - 3.6% for the 8 TeV samples. For the 8 TeV analysis the uncertainty due to the reweighing technique must also be considered. As shown in figure B.9, the uncertainty is found to depend on the lifetime of the signal samples with values varying between 0.5 - 5%.

8.1.7 Signal PDF and Scale Uncertainties

For the 7 TeV analysis the signal PDF and scale uncertainties are shown in table 5.1. For the 8 TeV analysis the signal PDF and scale uncertainties are shown in table 5.2. These are uncertainties on the k-factor for the cross section of each signal point and are used to create the theoretical errors in the limit setting procedure.

8.1.8 Pileup

This section deals with background events being assigned to the wrong PV due to pileup. For the effects of pileup on the shape of the signal distributions see section 8.2.3.

As shown in figure 3.4 there are multiple pileup interactions for every bunch crossing. It was also shown in section 6.3.2 that it is unlikely that a diphoton and $E_{\mathrm{T}}^{\mathrm{miss}}$ event could be constructed due to a photon from a pileup collision being assigned to an event with genuine $E_{\mathrm{T}}^{\mathrm{miss}}$. However, it is still possible that interactions can be assigned to the wrong PV, widening the z_γ and t_γ distributions.

Due to the electron tracks originating from the PV there will be little impact on the shape of the t_γ and z_γ distributions due to pileup in the e/γ sample. In contrast, it is known that some PV misidentification does occur in the CR sample, however this will be correctly handled since the template is derived from data. While it is correctly handled for events with $E_{\mathrm{T}}^{\mathrm{miss}}$ less than 20 GeV, PV misidentification is expected to increase slightly as $E_{\mathrm{T}}^{\mathrm{miss}}$ increases due to the presence of more and higher energy objects in each event. However, as shown in figure 4.2, the spread in the beamspot is approximately 50 mm and the impact on the z_γ and t_γ distributions will be negligible when compared with the expected signal values. Therefore, no systematic uncertainty is included for the PV misidentification due to pileup.

8.2 Signal Shape Systematic Uncertainties

The signal templates used in the template fitting method were created using the signal MC described in section 5.1. In this section, data driven methods are used to determine if the MC is correctly predicting the shape of the t_γ and z_γ distributions for non-prompt photons. However, there is no clean data sample that contains non-prompt photons or electrons which could be used to model the MC predictions. Therefore, the prompt control samples introduced in section 6.2 are used to model non-prompt photons as they become more non-pointing and delayed over the t_γ and z_γ range where data exists. Any discrepancy between the MC and data are investigated below and the impact this could have on the shape of the t_γ and z_γ distributions are covered by systematic uncertainties.

8.2.1 Pointing Resolution

The pointing measurement and resolution are described in detail in section 5.2.1. It has been shown that there is good agreement between the $Z \rightarrow ee$ data and MC samples over the range where data exists, with any disagreements present on the order of a few mm. If long lived neutralinos are produced at ATLAS it is expected that the resulting non-prompt photons would have z_γ values larger than 100 mm, therefore an uncertainty on the order of a few mm is negligible and ignored.

8.2.2 Timing Resolution and Measurement

The method for smearing the MC timing measurement, so that the resolution matches that observed in data, is described in detail in section 5.2.2. Given that the resolution is smeared so that it matches that observed in data there is no uncertainty attached to the timing resolution for signal MC photons. However, there is an uncertainty associated with the method used to obtain the time of arrival of photons. As explained in section 3.2.4.2, a set of optimal filter coefficients are used in equations 3.7 and 3.8 to calculate the cell energy and time respectively. The method for calculating these coefficients involves a Taylor expansion in which the quadratic terms are neglected [76]. This gives an accurate measurement for the time of the cell if particles are in time, however as particles become more out of time the measurement becomes less reliable. A study [111] into the timing measurement of collisions between particles populating satellite bunches at ± 5 ns shows

that they are reconstructed with mean times of approximately +5.5 ns and -5.2 ns. Taking the least accurate out of the two measurements gives an uncertainty of 10% on the reconstructed timing measurement for satellite collisions. The timing measurement for the 8 TeV analysis is restricted to $|t_\gamma| < 4$ ns, to exclude satellite collisions, and so would therefore be expected to be more reliable than the reconstruction of satellite events due to being more in time. However, as a conservative estimate an uncertainty of $\pm 10\%$ is adopted for the timing measurement of all signal photons.

8.2.3 Pileup

Due to the large number of Standard Model particles that should be produced with large p_{T} in any SPS8 decay chain it is expected that the correct PV will always be selected. However it is still possible that an event will be assigned to the wrong PV, which would impact the z_γ and t_γ measurements and change the shape of the signal templates.

The MC signal samples used in these analyses were produced so that each sample contains events with a range of different pileup collisions, however this doesn't match the distribution of pileup collisions observed in data. To correct this, the standard ATLAS pileup tool [105] is used to reweight events and reproduce the pileup distribution observed in data. To investigate if the pileup has an effect on the shape of the signal distributions, a signal sample was split into two subsamples, one with high pileup and one with low pileup.

In the 7 TeV signal MC, there are roughly an equal number of events with less than 6 pileup collisions as there are events with greater than or equal to 6 pileup collisions so this was chosen to be the boundary to separate the two new subsamples. The z_γ distributions for the low and high pileup samples were compared to the full sample and found to be in fairly good agreement as shown in figure 8.2. While the agreement is good in general, the disagreement can be as large as 15%. These two samples are therefore included as the shape systematic for the signal distributions in the 7 TeV analysis.

In the 8 TeV signal MC, there are roughly an equal number of events with less than 13 pileup collisions as there are events with greater than or equal to 13 pileup collisions. In contrast to the 7 TeV analysis, this was not chosen as the boundary between the low and high pileup samples but instead the central range of pileup interactions is not

included in either sample so that the two samples would be more distinct. Therefore, the high pileup sample contains all events with pileup greater than or equal to 16 and the low pileup sample contains all events with less than 11 pileup collisions. The z_γ and t_γ distributions of these samples were compared to the signal distributions, as shown in figure 8.2, and found to be in fairly good agreement. The disagreements between the high/low pileup samples and the full MC sample are included as shape systematics in the limit setting procedure.

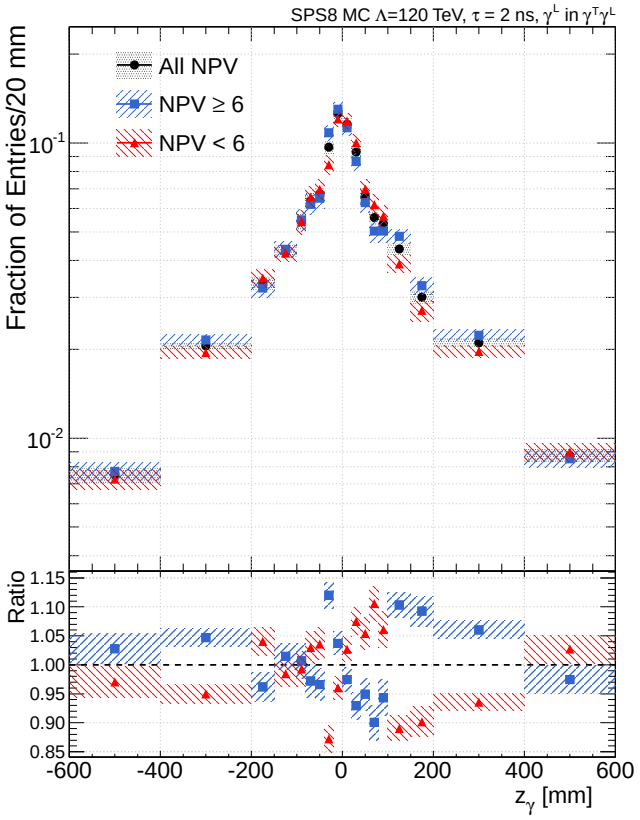

FIGURE 8.2: The shape of the unit-normalised signal template (T_{sig}) for the full 7 TeV signal MC dataset with $\Lambda = 120$ TeV and neutralino lifetime of 2 ns, and for low/high pileup subsamples, separated by the number of primary vertices in the event (NPV) as defined in the text. The lower section of the plot shows the ratio of the low/high pileup sample divided by the full MC sample [57].

8.2.4 Material Uncertainties

When a particle travels through matter it interacts and loses energy. When reconstructing photons and electrons, corrections are made to the amount of energy collected in the EM calorimeter to correct for energy lost in these interactions in the inner detector.

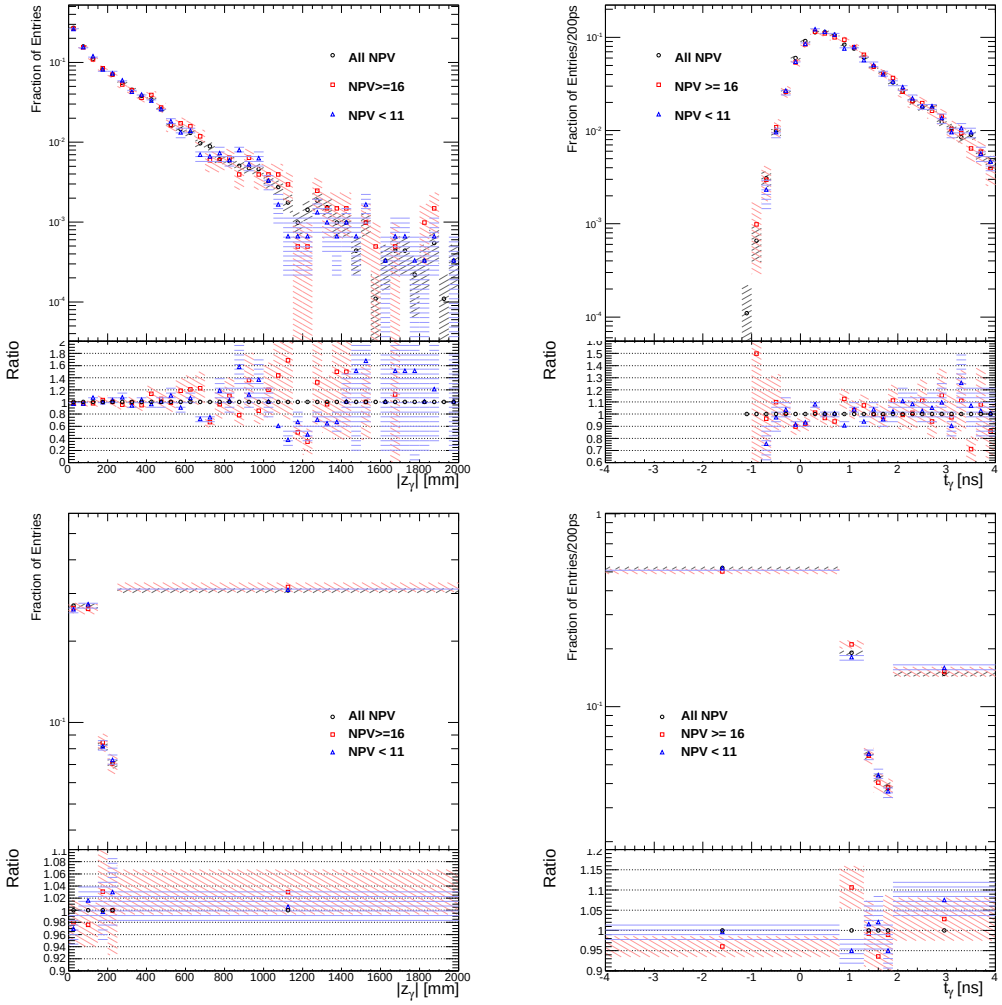

FIGURE 8.3: The shape of the unit-normalised signal template for the full 8 TeV signal MC dataset with $\Lambda = 160$ TeV and neutralino lifetime of 2 ns, and for low/high pileup subsamples as defined in the text. The lower two plots show the same data as the plots above but are separated into the categories used in the limit setting procedure. Each plot is subdivided into two sections, with the lower section showing the ratio of the low/high pileup sample divided by the full MC sample.

Therefore, it is important to know the amount of material in the inner detector, see figure 3.13, so that it can be accurately reproduced in MC simulations. Any discrepancy in the amount of material in the inner detector in MC simulations will lead to uncertainties on the energy of photons and also on the probability of photons converting.

To address these concerns a signal MC sample was produced with the same kinematics as a normal SPS8 MC signal sample except that it contains extra material in the inner detector. Figure 8.4 shows that the z_γ distribution for the 7 TeV MC signal sample with extra material is very similar to the sample with the normal geometry. It can be seen that they both have means consistent with 0, have similar RMS values, and the

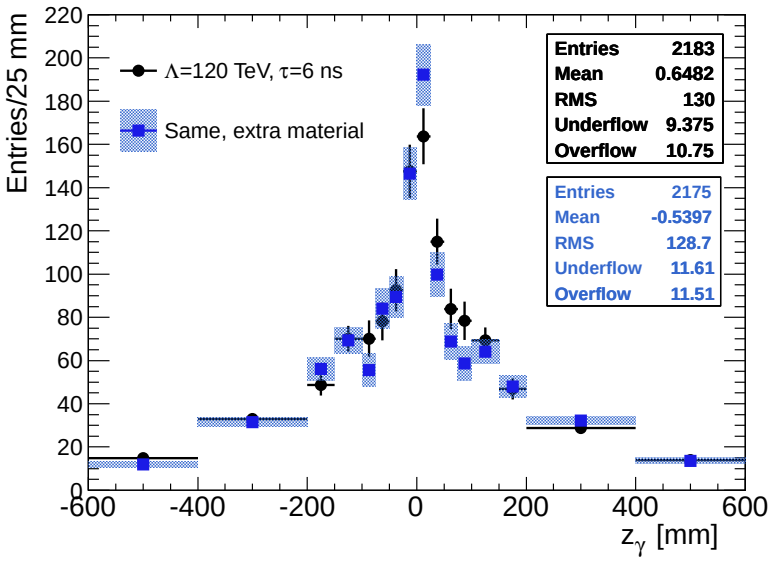

FIGURE 8.4: The pointing distribution for the nominal 7 TeV signal MC sample with $\Lambda = 120$ TeV and $\tau = 6$ ns, and for the sample with the same signal parameters but with additional material in the inner detector [57].

tails at larger z_γ values are very similar. Figure 8.5 shows how the z_γ and t_γ values for the 8 TeV MC signal sample with extra material compares to the sample with normal geometry. It can be seen that when statistical uncertainties are taken into account the two samples are also very similar even at larger z_γ and t_γ values. Given how similar the signal distributions are for samples with and without extra material, especially compared to the much larger shape uncertainties in these analyses, any differences arising due to the uncertainty on the amount of material in the inner detector is neglected.

8.3 Background Shape Systematic Uncertainties

As described in section 6.3.3, the background samples used in these analyses are derived from data samples. As outlined in section 7.1.3, in the 7 TeV analysis the z_γ shape of the e/γ and CR distributions are fitted to the signal region data to determine how many events can be attributed to background events. Therefore, systematic uncertainties relating to the shape of the z_γ distribution for these two distributions are considered below. In contrast, the 8 TeV signal region data is divided into z_γ categories and the t_γ distribution of the CR template is fitted to the signal region distribution to determine how many events can be attributed to background events. Therefore, uncertainties

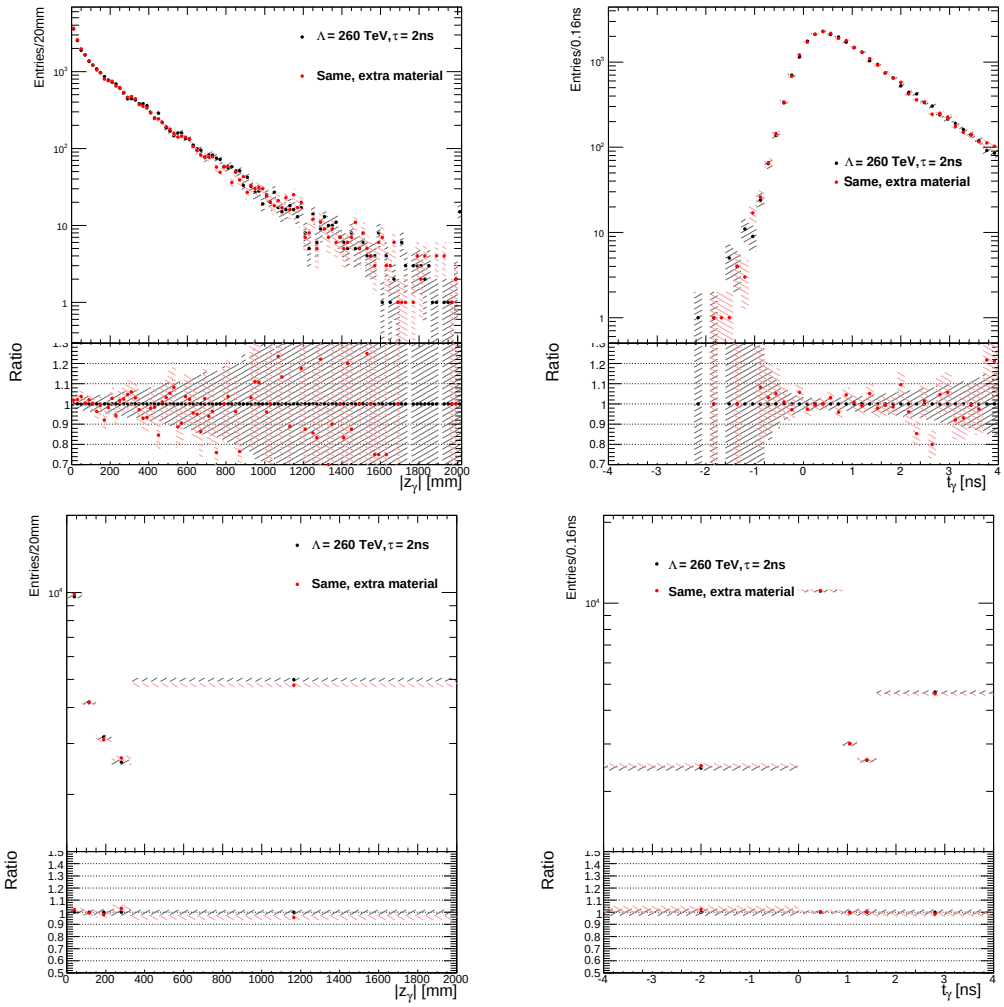

FIGURE 8.5: The pointing and timing distributions for the nominal 8 TeV signal MC sample with $\Lambda = 260$ TeV and $\tau = 2$ ns, and for the sample with the same signal parameters but with additional material in the inner detector. The lower two plots show the same data as the plots above but are separated into the categories used in the limit setting procedure.

on the shape of the t_γ distributions have more impact on the 8 TeV analysis than uncertainties on the shape of the z_γ distributions.

In this section: the systematic uncertainty described in section 8.3.1 is only relevant to the 7 TeV analysis, the systematic uncertainty described in section 8.3.2 is relevant to both analyses, while the rest of the systematics are only relevant to the 8 TeV analysis.

8.3.1 Impacts on Shape of e/γ Templates

As described in section 6.3.3, in order to model prompt photons the e/γ template is constructed from electrons from $Z \to ee$ decays. However, there are two ways in which

the e/γ z_γ distribution is expected to differ from the z_γ distribution of background events in the signal region.

Firstly, the pointing resolution of electrons is expected to differ slightly compared to the pointing resolution of converted and unconverted photons. In figure 8.6, the pointing resolution of prompt-photons, with the same p_{T} cut as used in the $Z \rightarrow ee$ sample, is compared to the pointing resolution of electrons from the $Z \rightarrow ee$ sample. It can be seen that distribution of converted photons is wider than the electrons whereas the distribution of unconverted photons is narrower.

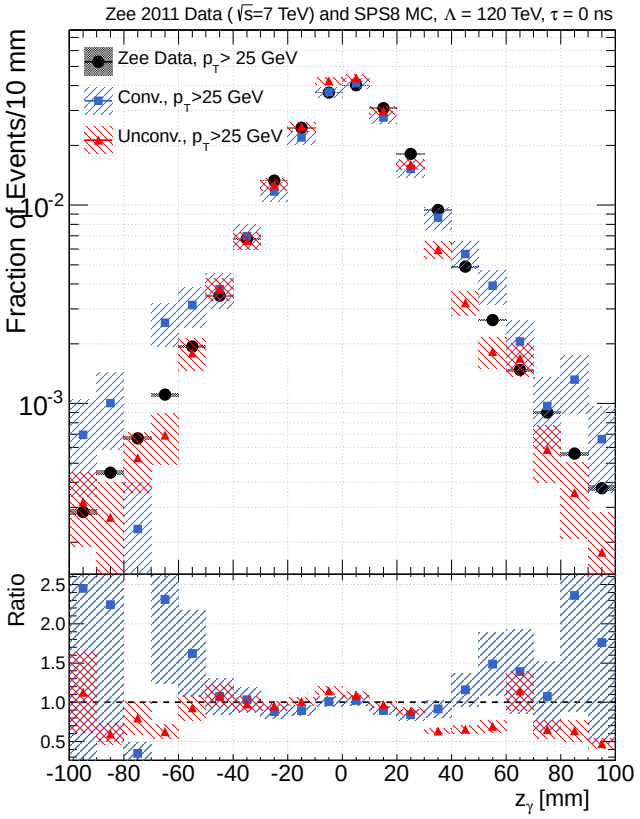

FIGURE 8.6: Normalised pointing distributions for electrons from 7 TeV $Z \rightarrow ee$ data events and for unconverted and converted photons, selected from the $\Lambda = 120$ TeV, $\tau = 0ns$ MC signal sample, with similar kinematics [57].

Secondly, the photon objects in the signal region are likely to have a higher p_{T} distribution than the electrons in the $Z \rightarrow ee$ sample. This will impact the shape of the z_γ distribution because higher p_{T} objects are expected to have a better pointing resolution. This is illustrated in figure 8.7 which compares the z_γ of electrons from MC and data $Z \rightarrow ee$ samples, with a 25 GeV p_{T} cut, to the z_γ of converted and unconverted prompt-photons, with the standard 50 GeV p_{T} cut. With this higher p_{T} cut, both the

converted and unconverted photons have a narrower z_γ distribution than the e/γ distribution, however this is less drastic than in figure 8.6. This suggests that e/γ is a good estimate of the z_γ distribution of prompt photons and electrons in the signal region.

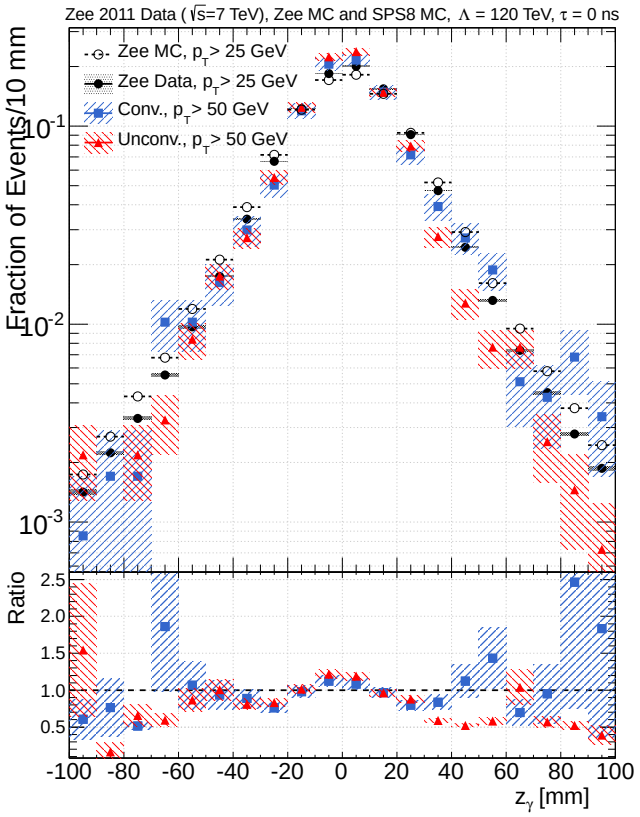

FIGURE 8.7: Normalised pointing distributions for electrons from 7 TeV $Z \rightarrow ee$ data and MC events, with $p_{\mathrm{T}} > 25$ GeV. Superimposed are the distributions for unconverted and converted photons, selected from the $\Lambda = 120$ TeV, $\tau = 0$ ns MC signal sample, passing the signal region cut of $p_{\mathrm{T}} > 50$ GeV [57].

As highlighted in figures 7.2 and 7.6 the pointing distribution of the e/γ template is much narrower than both the CR and signal MC templates. It is therefore likely that the e/γ template will contribute most to the fit in the central region of the signal region z_γ distribution. At larger z_γ, the shape of the CR template will dominate the fit and the relatively large disagreements observed in figures 8.6 and 8.7 at around $|z_\gamma| = 100$ mm are not important. It is only the central regions of the templates that are relevant and they show better agreement with the prompt photon samples. To estimate the systematic uncertainty on the shape of the e/γ template, converted and unconverted photon templates from figure 8.6 are included in the limit setting procedure to give a conservative estimate of the variations on the shape of the e/γ distribution.

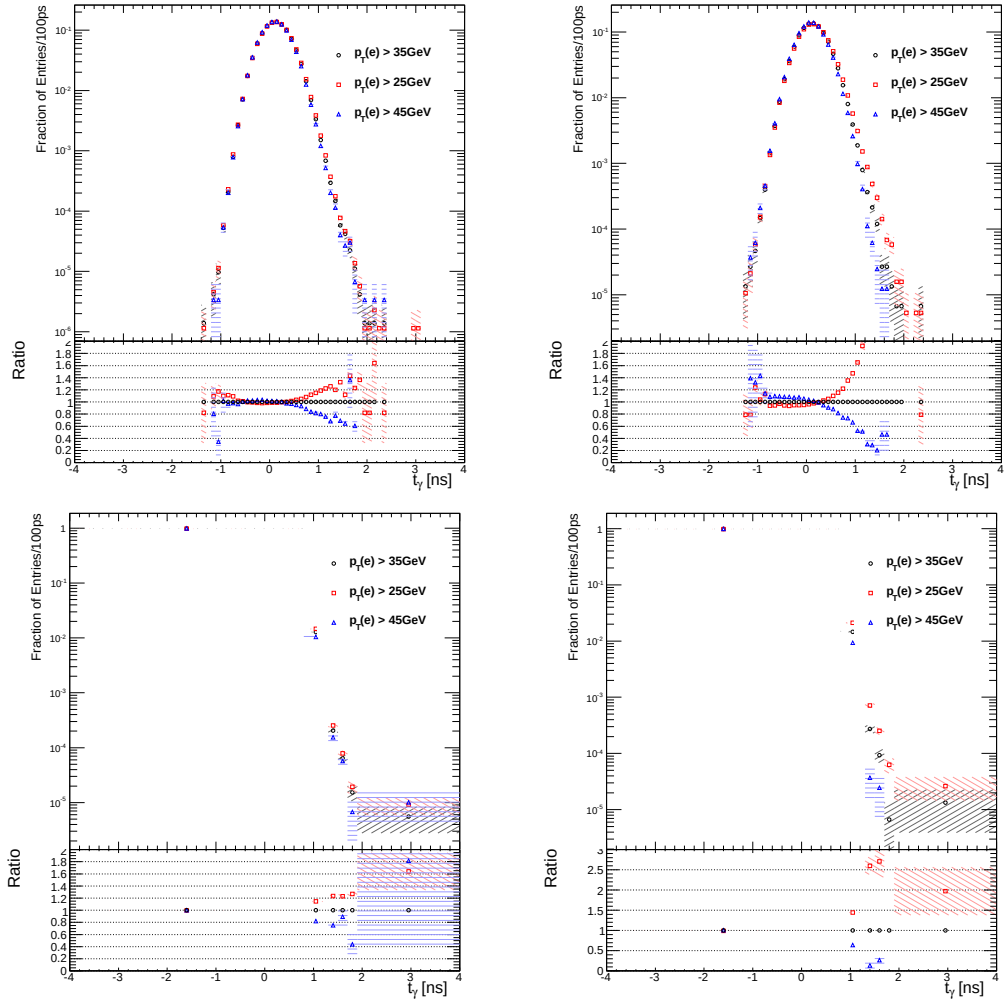

FIGURE 8.8: The shape of the unit-normalised e/γ t_γ template with minimum p_{T} cuts on the photons of 25, 35 and 45 GeV. The data sample is shown on the left, and the results for the MC sample is shown on the right as a cross-check. The upper plots show fine binning, while the lower ones show the same data with the final optimized binning.

It is explained in section 8.3.2 that the resolution of the timing measurement is sensitive to the energy distribution of photons/electrons. Therefore, the impact of changing the p_{T} cut on the t_γ distribution of the $Z \to ee$ sample is investigated in figure 8.8 for data and MC. It can be seen that the higher the p_{T} cut the more narrow the distribution becomes for both data and MC. While the 45 GeV p_{T} cut would be expected to have an energy distribution more similar to objects in the signal region, the more stringent cut drastically reduces the number of events in the final t_γ bin in the limit setting procedure, which would reduce the predictive power of the analysis. Therefore, as a compromise, the $Z \to ee$ sample with an p_{T} cut of 35 GeV is chosen for the e/γ template, while the samples with p_{T} cuts of 25 GeV and 45 GeV are included as systematic uncertainties on the shape of the e/γ distribution. It is interesting to note that the disagreement

between the different samples with different cuts is more extreme in the MC $Z \rightarrow ee$ sample, although due to the e/γ distribution being derived completely from the $Z \rightarrow ee$ data sample this is only a cross check and did not affect the p_{T} cut choice.

8.3.2 Impact of Event Kinematics on Shape of CR Templates

The CR template is derived from a data sample of diphoton events as described in section 6.3.3. It is expected that the lower $E_{\mathrm{T}}^{\mathrm{miss}}$ cut, compared to the signal region, imposed on this sample will result in the photons having a lower p_{T} distribution compared to the photons that will populate the signal region. As illustrated in section 8.3.1, the width of the pointing distribution is correlated with the p_{T} of the photons. It is also known that the timing resolution depends on the energy of the photons. Therefore, if the CR template is to accurately describe the shape of the z_γ and t_γ distributions of background events in the signal region then they will need to have similar kinematics.

$E_{\mathrm{T}}^{\mathrm{miss}}$ Range of Control Region	Photon p_{T} Cut (GeV)	Mean Photon p_{T} (GeV)
0 - 20 GeV	50	70.0
	65	88.1
50 - 75 GeV	50	79.7

TABLE 8.4: The mean value of the photon p_{T}, listed for a variety of 7 TeV TL control samples defined according to their $E_{\mathrm{T}}^{\mathrm{miss}}$ range and minimum photon p_{T} cut [57]

As expected, it can be seen in table 8.4, for 7 TeV events, and in table 8.5, for 8 TeV photons, that the mean photon p_{T} in the $E_{\mathrm{T}}^{\mathrm{miss}}$ less than 20 GeV sample is less than the mean photon p_{T} in the CR2 sample, which has $E_{\mathrm{T}}^{\mathrm{miss}}$ in the range of 50-75 GeV. It can also be seen that increasing the p_{T} cut on the CR sample increases the mean p_{T} of photons, with a cut of 60 GeV increasing the mean p_{T} above that observed in CR2 to a level which should be similar to that in the signal region.

$E_{\mathrm{T}}^{\mathrm{miss}}$ Range of Control Region	Photon p_{T} Cut (GeV)	Mean Photon p_{T} (GeV)
0 - 20 GeV	50	74.6
	60	85.4
50 - 75 GeV	50	81.3

TABLE 8.5: The mean value of the photon p_{T}, listed for a variety of 8 TeV control samples defined according to their $E_{\mathrm{T}}^{\mathrm{miss}}$ range and minimum photon p_{T} cut.

To investigate how this change in p_{T} cut, and therefore photon p_{T} distribution, affects the pointing distribution the z_γ distribution for three different p_{T} cuts are plotted together in figure 8.9, for 7 TeV photons, and in figure 8.10, for 8 TeV photons. In both figures, a second plot is included which shows the same information for a higher $E_{\mathrm{T}}^{\mathrm{miss}}$ region sample as a cross check. As expected the higher the p_{T} cut the more narrow the pointing distribution becomes. Therefore, since a p_{T} cut of 60 GeV gives a better description of the signal region this is the CR z_γ template that is included in the limit setting procedure in the 7 TeV analysis, with the 50 GeV and 70 GeV distributions included as systematic uncertainties on the shape of this template. While the 8 TeV pointing distribution shows a similar dependence on the p_{T} cut applied, these templates are not included as systematic uncertainties since uncertainties on the shape of the z_γ template have a negligible impact on the statistical analysis, as explained previously.

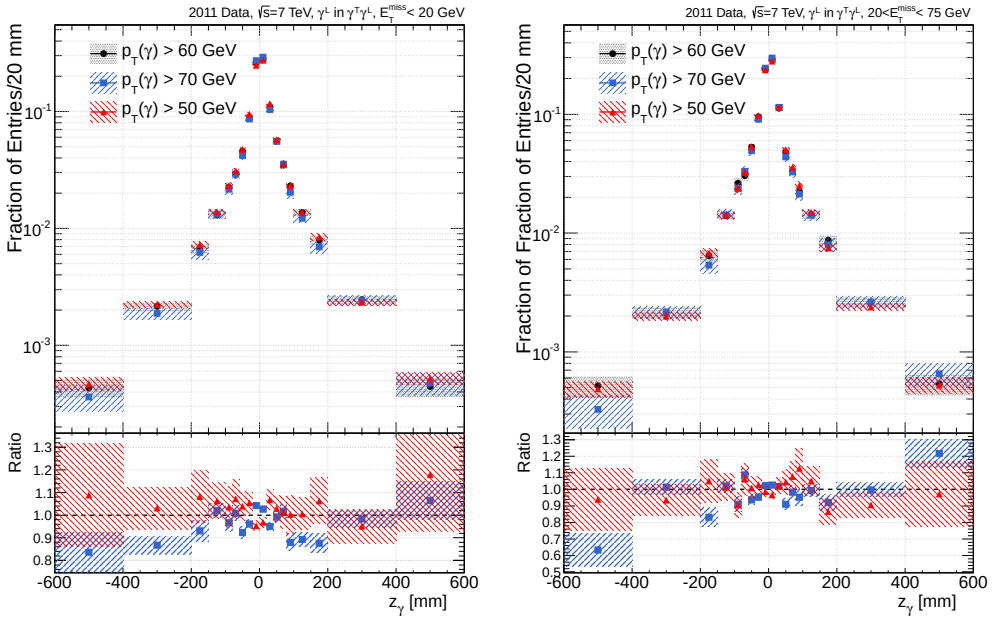

FIGURE 8.9: The t_γ shape of unit-normalised CR templates with minimum p_{T} cuts on the photons of 50, 60 and 70 GeV. The $E_{\mathrm{T}}^{\mathrm{miss}} < 20$ GeV control sample is shown on the left, and the results for the $20 < E_{\mathrm{T}}^{\mathrm{miss}} < 75$ GeV control sample is shown on the right as a crosscheck [57]

For the 8 TeV it is more important that any impact on the shape of the t_γ distribution is understood. Therefore the t_γ distributions of the three samples used in figure 8.10 are plotted in figure 8.11, with samples from a higher $E_{\mathrm{T}}^{\mathrm{miss}}$ region again used as a crosscheck. It can be seen that the three samples are in very good agreement in the central t_γ region but diverge in the tails as the statistics become more limited. Even though the three samples show good agreement within the statistical uncertainties, the

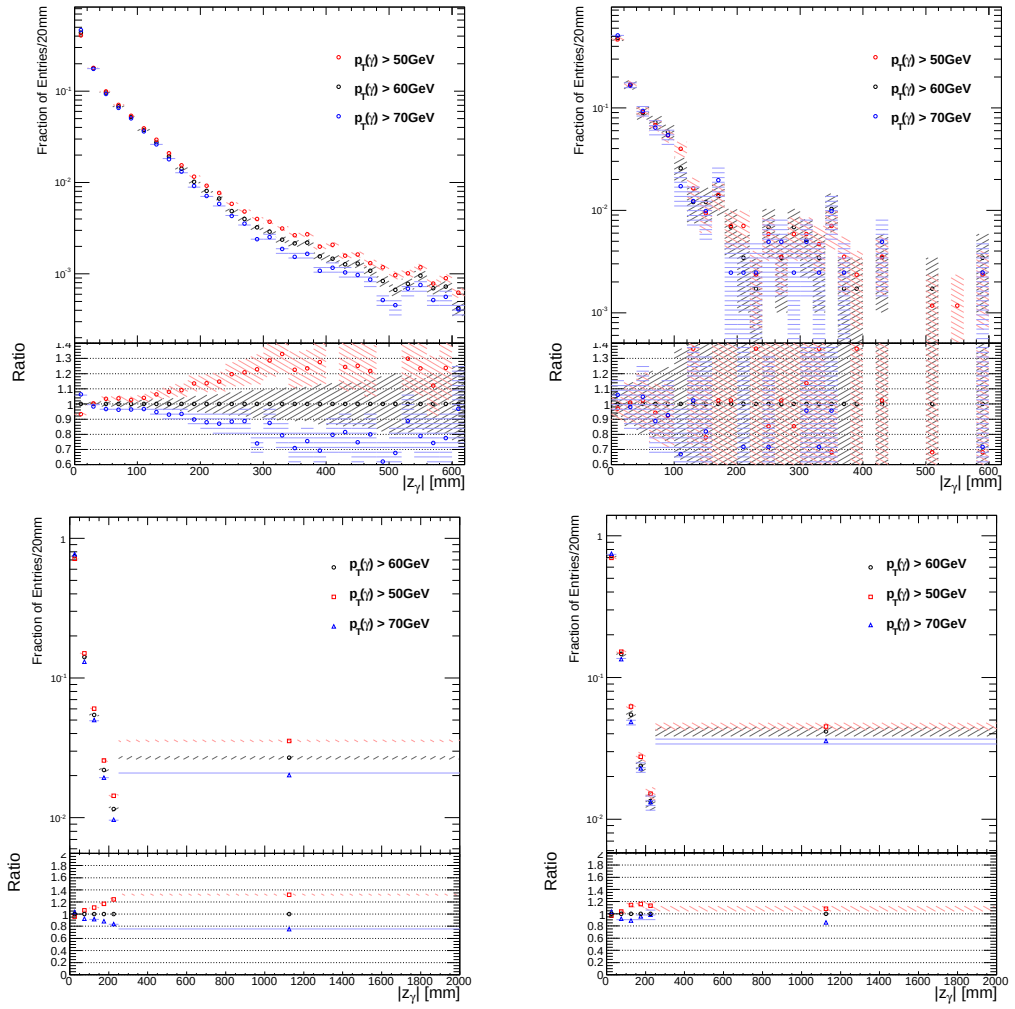

FIGURE 8.10: The shape of unit-normalised CR z_γ templates used in the 8 TeV analysis with minimum E_{T} cuts on the photons of 50, 60 and 70 GeV. The $E_{\mathrm{T}}^{\mathrm{miss}} < 20$ GeV control sample is shown on the left, and the results for the $20 < E_{\mathrm{T}}^{\mathrm{miss}} < 50$ GeV control sample is shown on the right as a crosscheck. The upper plots show fine binning, while the lower ones show the same data with the final optimized binning.

t_γ shape of the sample with a 60 GeV cut is included in the limit setting procedure as the nominal CR distribution with the distributions after a cut of 50 GeV and 70 GeV used as the systematic uncertainties on the shape of the CR template.

8.3.3 Background Rates of BB and BE Events

As explained in section 7.2.1, for BB events the t_γ and z_γ from the photon with the maximum t_γ are used in the limit setting procedure, while for BE events it is the t_γ and z_γ from the barrel photon. The selection of the photon with the maximum t_γ in BB events will cause the t_γ distribution to shift towards larger positive t_γ values compared

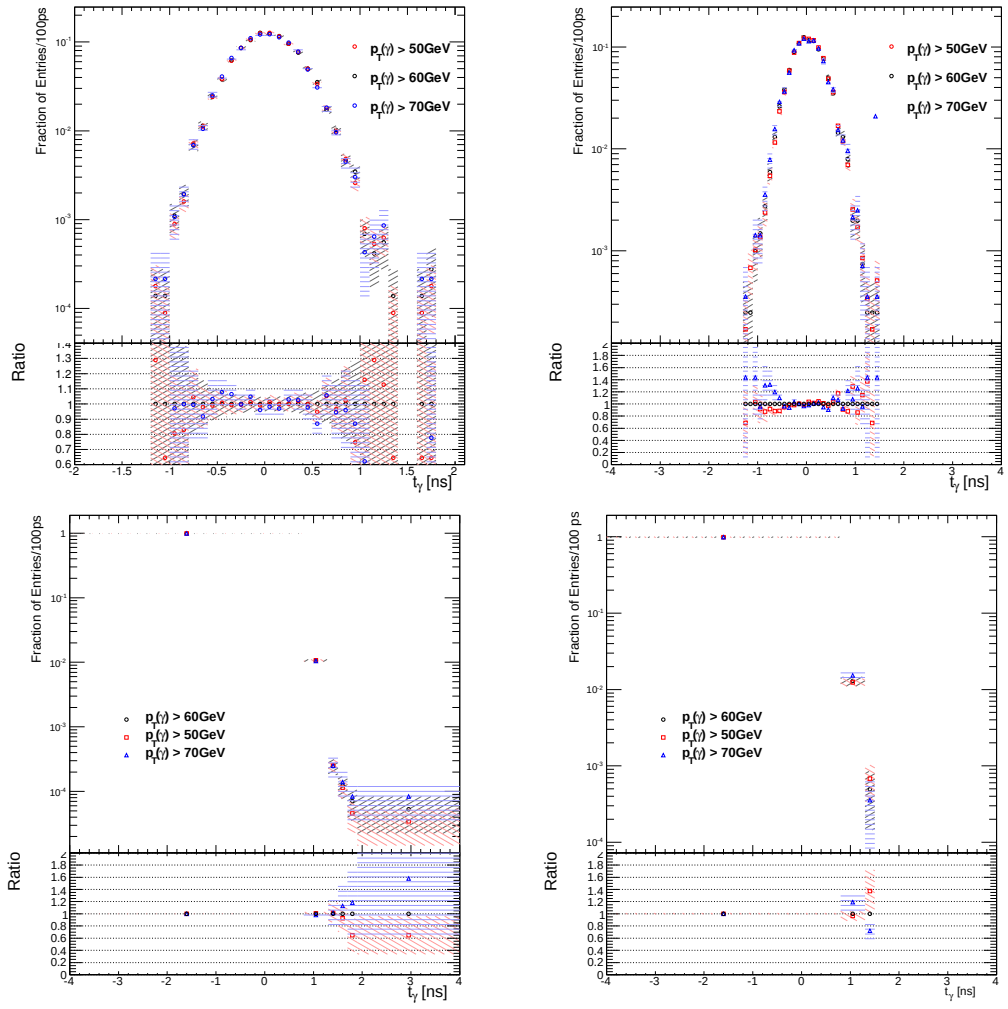

FIGURE 8.11: The shape of the unit-normalised CR t_γ templates used in the 8 TeV analysis with minimum E_{T} cuts on the photons of 50, 60 and 70 GeV. The $E_{\mathrm{T}}^{\mathrm{miss}} <$ 20 GeV control sample is shown on the left, and the results for the $20 < E_{\mathrm{T}}^{\mathrm{miss}} < 50$ GeV control sample is shown on the right as a crosscheck. The upper plots show fine binning, while the lower ones show the same data with the final optimized binning.

to the t_γ distribution from the barrel photon in BE events, which is expected to be centred on and symmetrical about 0. The difference in the t_γ distributions for BB and BE events can be seen in figure 8.12 for the $E_{\mathrm{T}}^{\mathrm{miss}} < 20$ GeV and $Z \rightarrow ee$ samples, with the bias towards positive t_γ values visible in the BB distribution.

Due to the difference in the t_γ shape of BB and BE events it is essential that the templates used in the limit setting procedure contain the same fraction of BB events (f_{BB}) that is present in the signal region. The production of the signal MC samples ensures that the f_{BB} is what would be expected for SPS8 events in the signal region. However, as has already been shown in the previous few sections, the kinematics of events in the CR and e/γ samples are different to the kinematics expected in the signal region, implying that

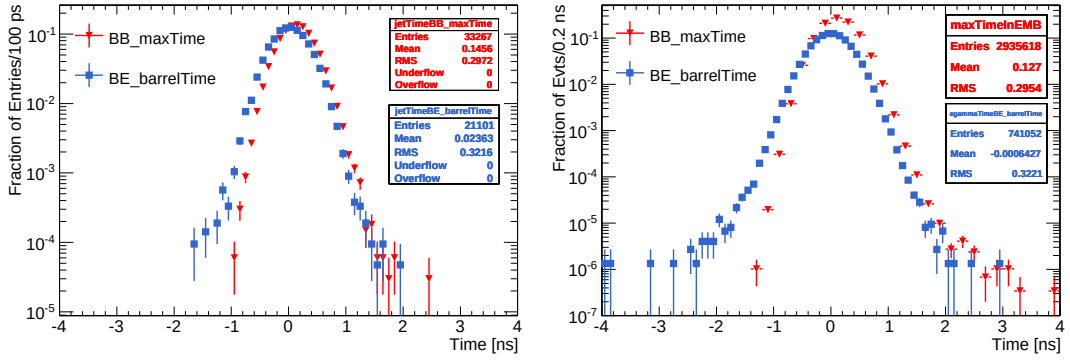

FIGURE 8.12: Background t_γ distributions used in the 8 TeV analysis, shown separately for BB and BE events. The left plot is for the $E_{\mathrm{T}}^{\mathrm{miss}} < 20$ GeV sample while the right plot is for the $Z \rightarrow ee$ sample [59].

the fraction of BB events in the background template ($f_{BB}^{Template}$) isn't necessarily the same as for background events in the signal region (f_{BB}^{SR}). A simple solution to determine the correct value for f_{BB}^{SR} would be to use the f_{BB} in the signal region once it has been unblinded. However, since signal and background events can have different f_{BB} and the signal region could contain signal events it could bias the observed value. Instead, the f_{BB} from the control samples in table 8.6 that will have negligible signal content are used to estimate f_{BB}^{SR}. CR2 will be expected to have some signal contamination due to the larger $E_{\mathrm{T}}^{\mathrm{miss}}$ cut so the events in this sample are restricted to those with negative timing, which is expected to be dominated by background events, as shown in figure 7.4. Table 8.6 shows that the CR and CR1 both have a similar f_{BB} of $\sim 61\%$ while the negative timing region of CR2 has a larger value of $\sim 63\%$. In contrast, the signal region events in the unblinded period E data contain a lower f_{BB} than the CR with a value of $\sim 57\%$. It was possible that period E contained signal events, so it was not necessary for the f_{BB} in this region to be the same as f_{BB}^{SR}, however a central value of 61% was selected for f_{BB}^{SR} with a conservative systematic uncertainty of $\pm$ 4% used to cover the variations observed in table 8.6.

$E_{\mathrm{T}}^{\mathrm{miss}}$ Range of Control Region	Total Number of Events	Number of BB Events	Number of BE Events	Value of BB/(BB+BE) (%)
0 - 20 GeV	54,241	33,247	20,994	61.3 ± 0.2
20 - 50 GeV	50,751	31,182	19,569	61.4 ± 0.2
50 - 75 GeV	3,591	2,268	1,323	63.2 ± 0.8
>75 GeV (Per. E)	54	31	23	57.4 ± 6.7

TABLE 8.6: Numbers of events in the various low and intermediate $E_{\mathrm{T}}^{\mathrm{miss}}$ control regions, as well as the Period E data in the signal region with $E_{\mathrm{T}}^{\mathrm{miss}} > 75$ GeV, along with the contributions from BB and BE events.

In the limit setting procedure, the background templates were reweighted so that $f_{BB}^{Template} = f_{BB}^{SR}$ by reweighting BB and BE events with separate coefficients defined as

$$C_{BB} = \frac{f_{BB}^{SR}}{f_{BB}^{Template}}$$

$$C_{BE} = \frac{1 - f_{BB}^{SR}}{1 - f_{BB}^{Template}}$$

which preserves the normalisation of the templates. The reweighted background CR template with the correct f_{BB}, and therefore correct t_γ distribution, for background events in the signal region is shown in figure 8.13 with the associated systematic uncertainty on the f_{BB}.

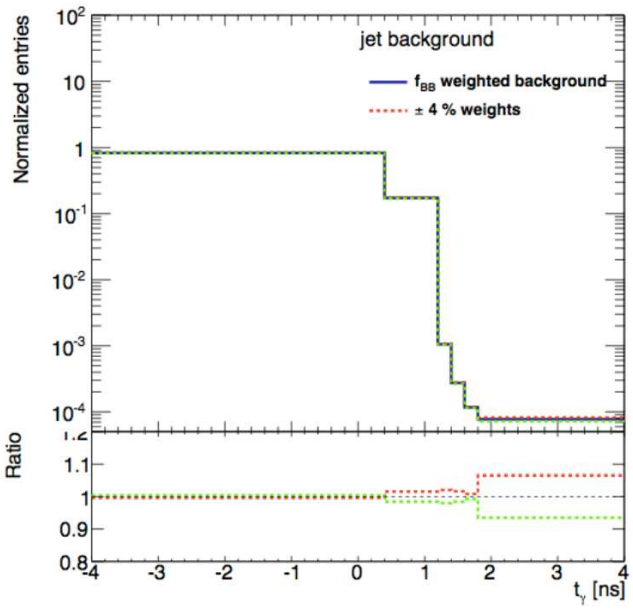

FIGURE 8.13: Background time distribution, reweighted to a BB event fraction of 61%, along with the associated systematic uncertainties from the procedure [59]. For more details, see the text.

8.3.4 Background Composition

As described in section 7.2.3, due to the similarities between the t_γ distributions of the CR and e/γ samples the CR distribution can be used as the background t_γ template, with the difference between the shape of the two distributions covered by a systematic uncertainty in each timing bin. This uncertainty is derived from the differences in the mean of the t_γ distributions for the different background samples shown in table 6.4,

with a maximum difference of $\sim$ 70 ns. The difference between the shape of the two distributions and the systematic uncertainty is shown in figure 8.14. While the uncertainty at large t_γ values is relatively large and dominates the systematic uncertainties, this has very little impact on the sensitivity of the analysis due to the large statistical uncertainties in the signal region.

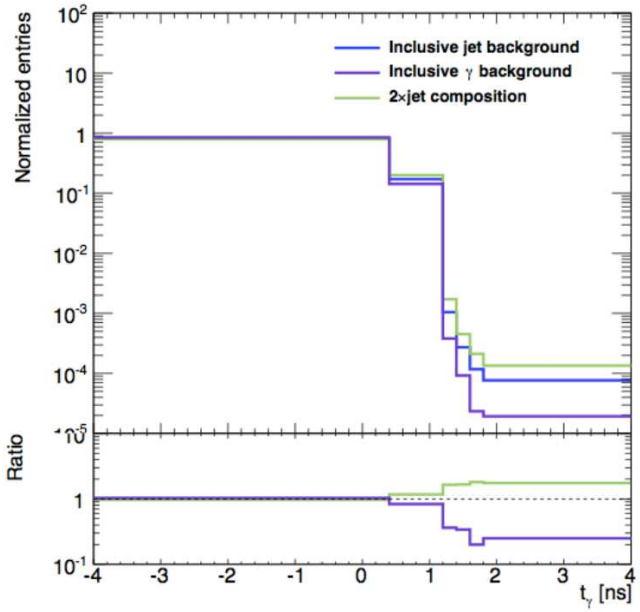

FIGURE 8.14: Background time distribution for 8 TeV events, and the symmetric systematic uncertainties assigned to account for variations in the background composition. For more details, see the text. [59]

Chapter 9

Results and Interpretation

In this chapter the t_γ and z_γ distributions for events that are in the higher $E_{\mathrm{T}}^{\mathrm{miss}}$ control regions and the signal region are presented separately for the 7 TeV and 8 TeV analyses. The results and interpretation of the template fitting and limit setting procedures are also presented and discussed.

9.1 Results of 7 TeV Analysis

9.1.1 Results in the Control Regions

Before the signal region distributions are unblinded, the CR1 and CR2 distributions are first unblinded and the limit setting procedure is applied to them. Due to CR2 having an $E_{\mathrm{T}}^{\mathrm{miss}}$ distribution that is more similar to the SR, this allows the analysis method to be tested before the signal region is unblinded.

Figure 9.1 shows the z_γ distribution of the 8568 events in CR1. Also shown is the result of fitting the background using equation 7.3, which returned an F_{jet} value of 0.92±0.02. It can be seen that, within errors, the background only fit is a good description of the observed data with no significant excess observed in any bin.

Figure 9.2 shows the z_γ distribution of the 303 events in CR2. Also shown is the result of fitting the background using equation 7.3, which returned an F_{jet} value of 0.88±0.10. It can be seen that in general the background only fit gives a good description, within errors, of the observed data. If signal events were present in CR2, it is expected that

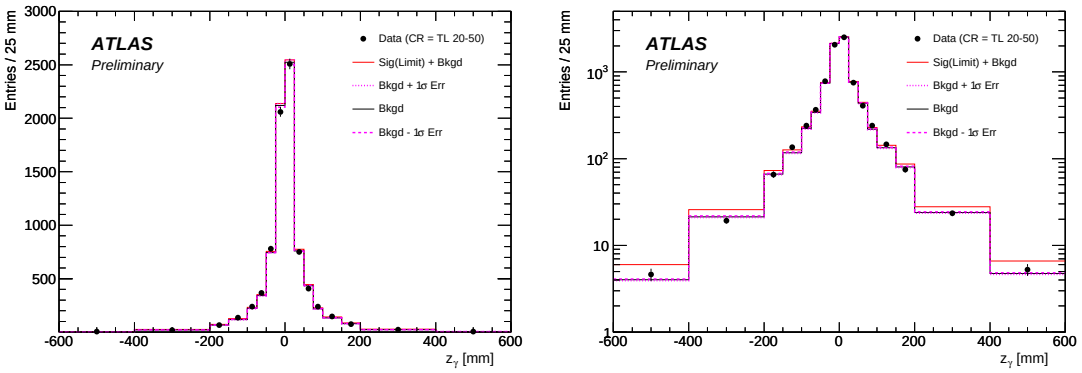

FIGURE 9.1: The z_γ distribution for the TL control sample in the 7 TeV analysis with $20 < E_{\mathrm{T}}^{\mathrm{miss}} < 50$ GeV, on (left) linear and (right) log scales. Superimposed are the results of the fit, including the best-fit background curve, the $\pm 1\sigma$ variations on the background, and a curve showing the best-fit background plus the number of signal events equal to the 95% CL limit [57].

they would have larger z_γ values resulting in wider tails in the z_γ distribution. This is clearly not the case in figure 9.2 where there is in fact a deficit of events with large positive z_γ values. It is, therefore, more likely that the limited statistics in this sample has resulted in the asymmetry present in the central, background dominated, region of the z_γ distribution.

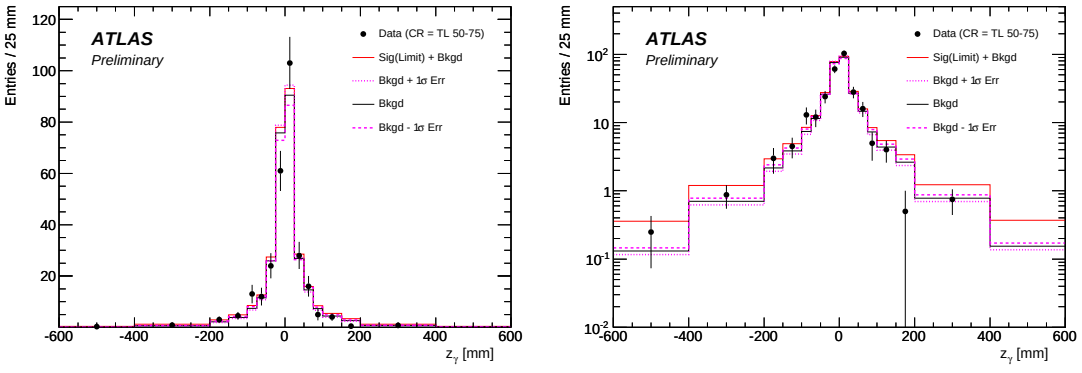

FIGURE 9.2: The z_γ distribution for the TL control sample in the 7 TeV analysis with $50 < E_{\mathrm{T}}^{\mathrm{miss}} < 75$ GeV, on (left) linear and (right) log scales. Superimposed are the results of the fit, including the best-fit background curve, the $\pm 1\sigma$ variations on the background, and a curve showing the best-fit background plus the number of signal events equal to the 95% CL limit [57].

9.1.2 Results in the Signal Region

After unblinding the 7 TeV signal region it was found that there were 46 events, the z_γ distribution of these events is shown in figure 9.3. It can be seen that the distribution is

narrow, the majority of the events are in the central $|z_\gamma| < 60$ mm region, with the lack of an obvious tail at large z_γ values suggesting that little signal can be present. This conclusion is enhanced by fitting only the background templates to the signal region distribution, as in figure 9.3, and observing that this gives a very good description of the data. There are however three events with $|z_\gamma| >200$ mm, which is more than would be expected if the data is to be explained only as background. These will be discussed in more detail below.

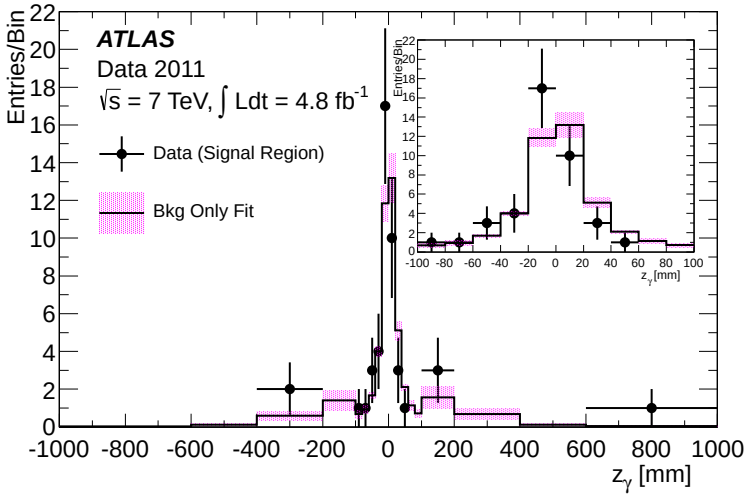

FIGURE 9.3: The z_γ distribution for the 46 loose photons from the events in the signal region in the 7 TeV analysis. Superimposed are the results of the background-only fit. The hatching shows the total uncertainties in each bin for the signal-plus-background fit. The inlay shows an expanded view of the central region, near $z_{DCA} = 0$ [57].

The t_γ distribution is not used in the limit setting procedure, however fitting the t_γ distribution of the expected background to the observed signal region t_γ distribution provides additional information. The result of this fit, alongside the t_γ distribution of the signal region events, is shown in figure 9.4. It can be seen that the background only fit gives a very good description of the data distribution and, as for the z_γ distribution, there is no obvious sign of signal events in the tail of the distribution.

The z_γ and t_γ information for the three 'outlier' events with the largest z_γ values are given in table 9.1. It can be seen that the photon with the largest z_γ value has a t_γ value of approximately zero. This suggests that it is more likely to be a promptly produced jet, in the tail of the z_γ distribution, faking a photon. This hypothesis is supported by information in Appendix E that suggests this 'Loose photon' is more likely to be a prompt jet with a leading π^0. It can be seen that the photon with the third largest $|z_\gamma|$ also has a relatively large value of t_γ, although this timing measurement was read out

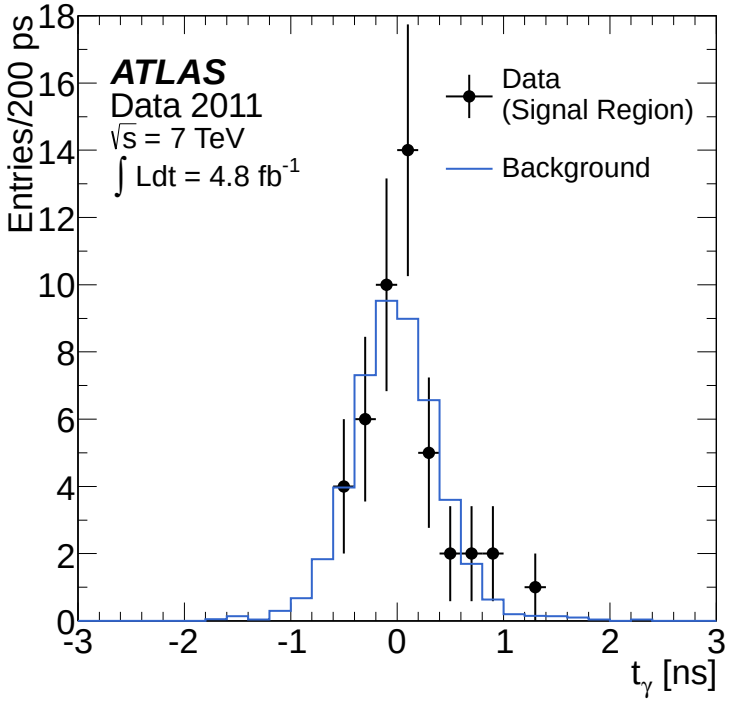

FIGURE 9.4: The distribution of arrival times (t_γ) for the 46 loose photon candidates from the events in the signal region of the 7 TeV analysis. Superimposed for comparison is the shape of the timing distribution expected for background only, normalised to 46 total events [1].

using MEDIUM gain which has a worse resolution than measurements read out with HIGH gain, as explained in section 5.2.2, and is therefore unreliable.

$E_{\mathrm{T}}^{\mathrm{miss}}$ [GeV]	Loose Photon			Tight Photon		
	E_T [GeV]	z_γ [mm]	t_γ [ns]	E_T [GeV]	z_γ [mm]	t_γ [ns]
77.11	75.87	-274.0	0.360	71.96	21.5	0.575
77.28	59.42	-261.8	1.207	87.21	-118.4	0.242
77.86	56.61	751.6	0.002	54.17	4.5	-0.197

TABLE 9.1: Some relevant parameters of the three "outlier" events, mentioned in the text, in the 7 TeV analysis.

When the signal templates are included in the fitting procedure, the best fit to the data is obtained for the $\Lambda = 120$ TeV, $\tau = 6$ ns sample. This combined signal + background (S+B) fit is shown in figure 9.5 and gives a total of 5.7±5.1 signal events. The breakdown of these events into the different z_γ bins is given in table 9.2 along with the number of events observed in the data and the breakdown for the background only fit. As expected from figure 9.3 the background only fit does a good job of describing the amount of data observed in every bin except for the $|z_\gamma| > 600$ mm bin. This excess results in

the background only fit having a p_0 value of ~ 0.060, which is equivalent to the data disagreeing with the background only fit with a significance of $\sim 1.55\sigma$.

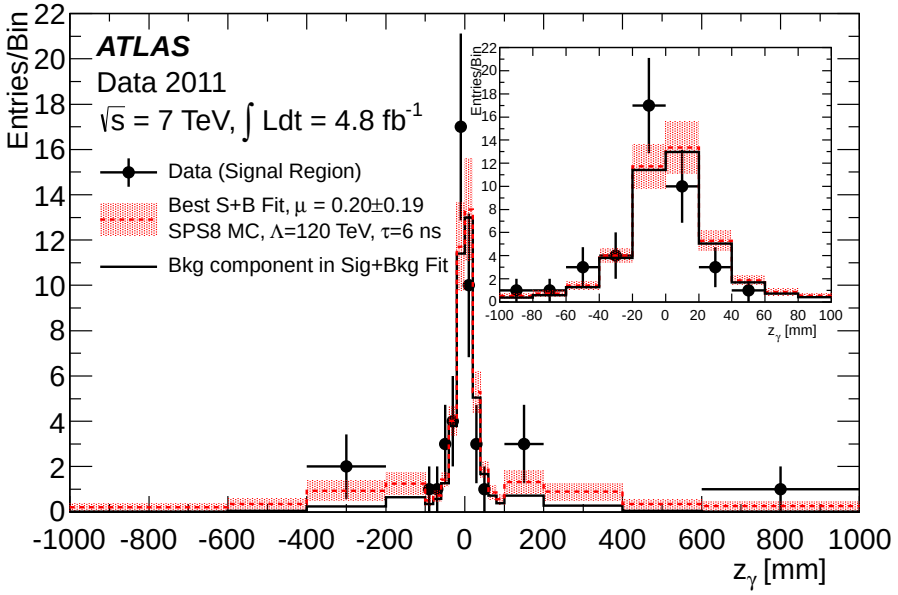

FIGURE 9.5: The z_γ distribution for the 46 loose photons from the events in the signal region of the 7 TeV analysis. Superimposed are the results of the signal-plus-background fit(for the case of $\Lambda = 120$ TeV and $\tau = 6$ ns), as well as the contribution from the background to that fit. The hatching shows the total uncertainties in each bin for the signal-plus-background fit. The inlay shows an expanded view of the central region, near $z_\gamma = 0$ mm [57].

Fit Type	Event Type	Range of $\lvert z_\gamma \rvert$ Values [mm]						
		$0-20$	$20-60$	$60-100$	$100-200$	$200-400$	$400-600$	>600
-	Data	27	11	2	3	2	0	1
Bkg Only	Bkg	25.04±2.22	12.90±1.09	3.47±0.89	2.97±1.10	1.29±0.53	0.24±0.10	0.08±0.03
Signal Plus Bkg	Total	25.05±4.18	12.60±2.17	2.65±0.97	2.57±1.00	1.82±0.81	0.70±0.45	0.47±0.36
	Sig	0.66±0.60	0.85±0.78	0.61±0.55	1.22±1.10	1.29±1.16	0.60±0.54	0.43±0.39
	Bkg	24.39±4.22	11.75±2.36	2.04±1.30	1.35±1.47	0.53±0.69	0.10±0.13	0.04±0.04

TABLE 9.2: Integrals over various $\lvert z_\gamma \rvert$ ranges of the distributions shown in Figure 9.5 for the 46 loose photons in the signal region of the 7 TeV analysis. The numbers of events observed in data are shown, as well as the results of a background-only fit and a signal-plus-background fit for the case of $\Lambda = 120$ TeV and $\tau = 6$ ns. The total fitted number of signal events is 5.7 ± 5.1. The errors shown correspond to the sum of both statistical and systematic uncertainties. The numbers of signal and background events from the signal-plus-background fit are negatively correlated. Note that some of the z_γ categories have been combined in this table, the full version can be found in [1].

The S+B fit was performed for a wide range of Λ and τ values and the observed number of signal events, with a 95% CL, were collected together for each Λ, an example of which is shown in figure 9.6. Also shown is the expected number of signal events, calculated by taking the F_{jet} value observed in the signal region of 0.68 ± 0.28 and producing pseudo-data from the background templates with this F_{jet}. The large difference between the

expected and observed limit on the number of signal events is primarily due to the three events with large $|z_\gamma|$ values. The number of SPS8 signal events that would be expected for the integrated luminosity collected at 7 TeV, signal cross-section, and the signal efficiencies is also shown for a sample with a given Λ and τ.

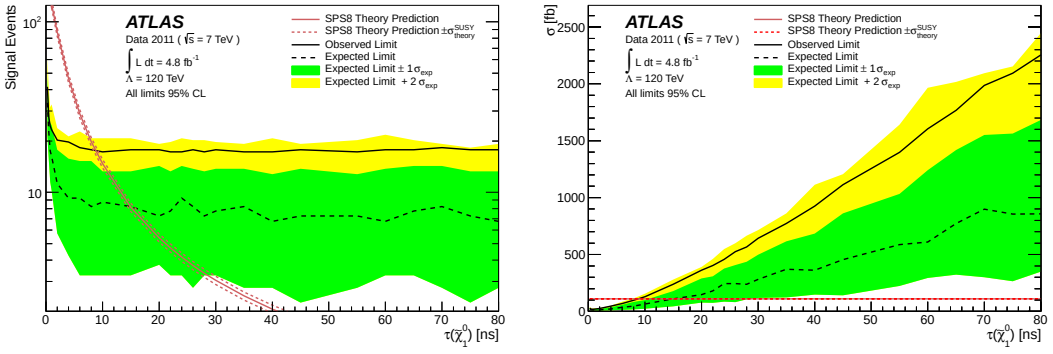

FIGURE 9.6: 95% CL limits on (left) the number of signal events and (right) the signal cross section, as a function of neutralino lifetime, for a Λ value of 120 TeV in the 7 TeV analysis.

To calculate which points in the 2D signal grid of $\Lambda \times \tau$ have been excluded by the analysis required analysing the information in the 1D limit plots. In these plots, any point at which the number of SPS8 events predicted in theory is larger than the number observed in the S+B fits to the signal region data is excluded with a 95% CL. This information was collected for each Λ value studied and the results are shown in figure 9.7. The range of Λ and τ values that have been excluded by this analysis are less than what would be expected from the pseudo-data, due to the three events with a large z_γ value, however the observed limits are within 2σ of the expected limits.

9.2 Results of 8 TeV Analysis

9.2.1 Results in the Control Regions

The z_γ and t_γ distributions for CR1 and CR2 can be seen in figure 9.8 alongside the control region distributions. It can be seen that for both z_γ and t_γ the three samples are in good agreement, with only small differences visible in the tail of the t_γ distributions. To test if the small differences in the t_γ distributions are due to the presence of signal events, the fitting and limit setting procedure was applied to CR1 and CR2. However, both CR1 and CR2 contain many more events than would be expected in the signal

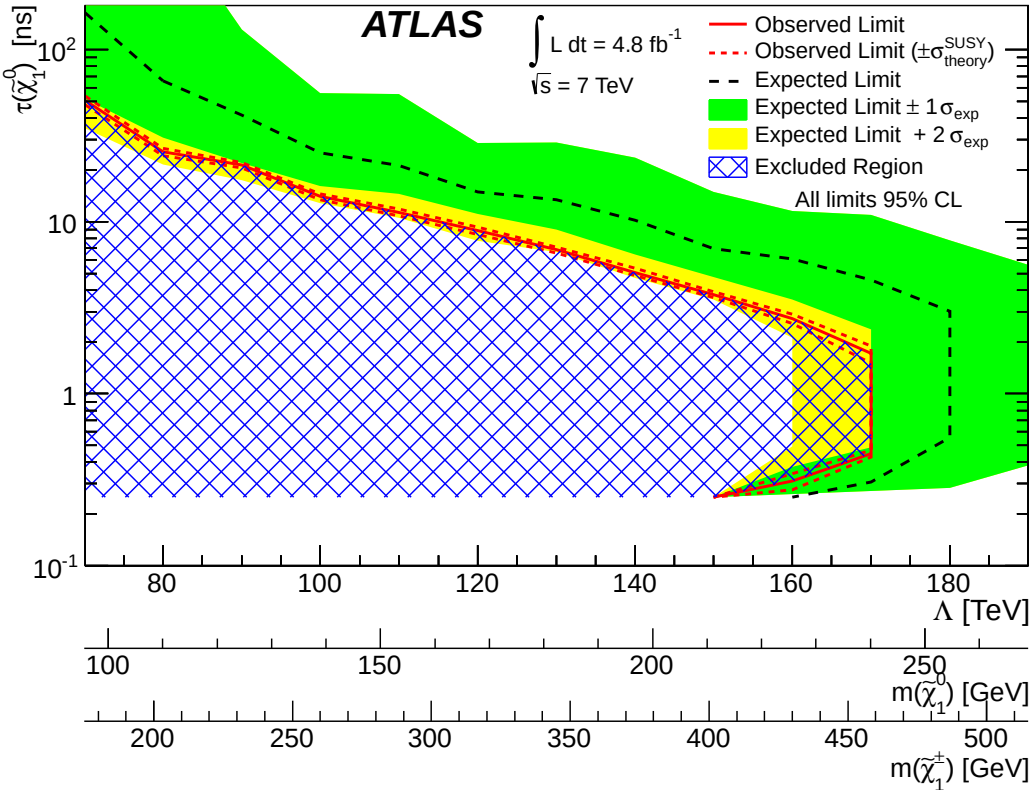

FIGURE 9.7: The expected and observed limits in the SPS8 plane of neutralino lifetime versus Λ (or, equivalently, versus the neutralino mass), in the 7 TeV analysis. Note that models with $\tau < 250$ ps were not considered in this analysis due the z_γ distibution being too similar to the z_γ distribution of prompt e/γ objects.

region so they were normalised to the 450 events that were predicted to exist in the signal region[1]. This stops any small differences in the extremity of the tails, that would have an insignificant contribution in the signal distribution due to the much smaller statistics, causing a discrepancy with the background distribution. When this procedure is applied to CR1 and CR2 it gives a maximum disagreement with the background distributions of 0.64σ and 1.21σ respectively, proving that any disagreements are small. These maximum disagreements both come from signal samples with $\tau = 160$ ps, which is unsurprising considering it has been shown that the z_γ and t_γ distributions of signal samples with small τ values closely resemble the background distributions. This is, therefore, a conservative estimate of the maximum disagreement, since the minimum τ value that will be used in the analysis of the signal region is 250 ps.

[1]Taking the 54 signal events observed in the unblinded period E and scaling up to the total integrated luminosity of the 8 TeV dataset yields a prediction of 434 ± 59 events in the signal region, which was rounded to 450 events in these studies

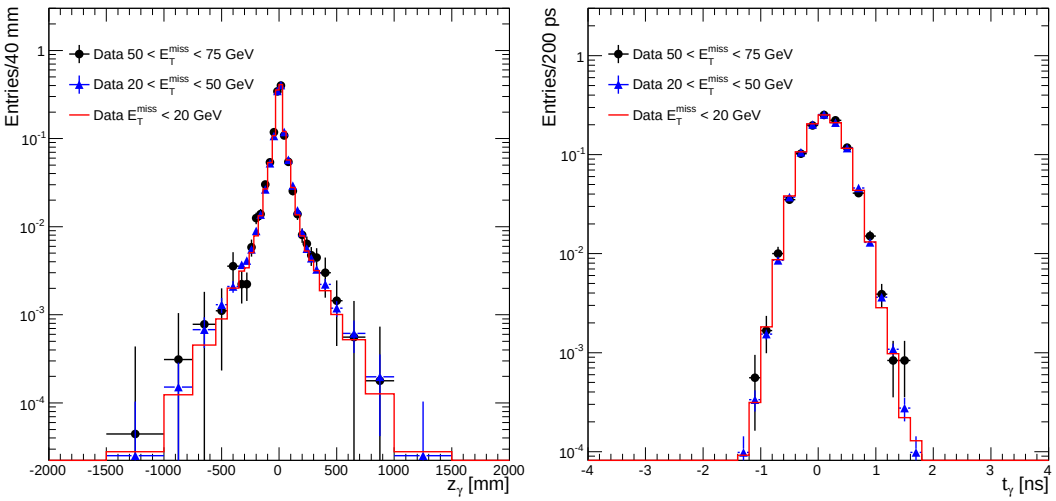

FIGURE 9.8: The pointing and timing distributions for 8 TeV diphoton data events observed in the different $E_{\mathrm{T}}^{\mathrm{miss}}$ control regions used in this analysis.

9.2.2 Results in the Signal Region

After unblinding the 8 TeV signal region it was found that 386 signal events are observed, in agreement with the expectation of 434 ± 59. The z_γ and t_γ distributions of the signal events are shown in figure 9.9, alongside the control region distributions and two signal MC distributions with different τ values. As expected from the CR1 and CR2 results, the distribution of both variables in the signal region are relatively narrow and agree, within errors, with the control region distributions. Crucially, there is no evidence of a tail at large positive t_γ values that would be expected if GMSB signal events were present.

Using the method outlined in chapter 7, the signal MC and background t_γ templates were fitted to the distribution observed in the signal region across the grid of Λ and τ values. As for the 7 TeV analysis, a 95% CL on the number of GMSB signal events that could be present in the signal region are calculated across the grid and collected together in plots such as figure 9.10. Also shown on this plot is the expected number of signal events, calculated from the signal cross-section, integrated luminosity collected at 8 TeV, and signal efficiencies. Any point on the plot where the limit on the number of GMSB events observed in the signal region is below the theoretical value is excluded at 95% CL.

Figure 9.11 shows the limits obtained from analysing plots such as figure 9.10 in the two dimensional GMSB signal space in the SPS8 model. Figure 9.11 also shows the

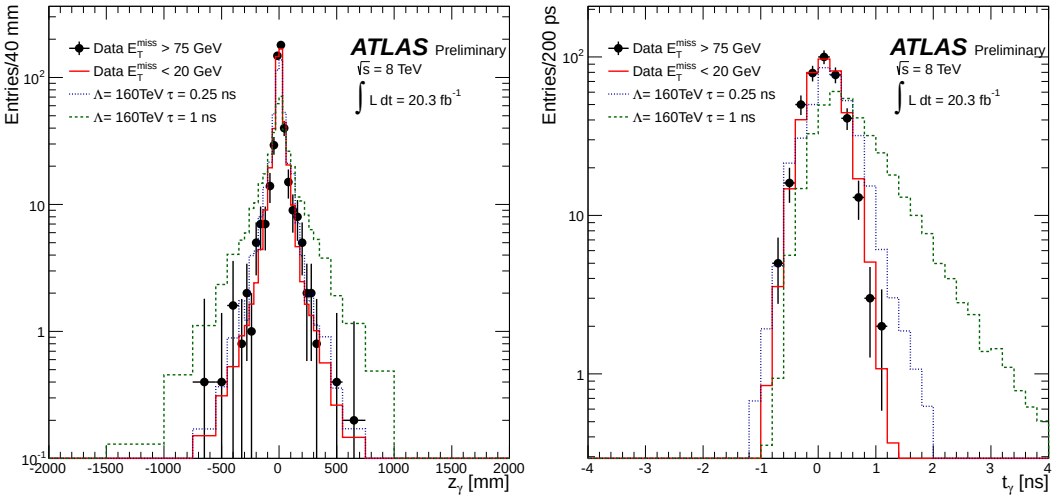

FIGURE 9.9: The pointing and timing distributions for 8 TeV diphoton data events observed in the $E_{\mathrm{T}}^{\mathrm{miss}}$ greater than 75 GeV signal region (black) and $E_{\mathrm{T}}^{\mathrm{miss}}$ less than 20 GeV control region (red). Also shown is the corresponding distributions for the background and two signal MC samples with $\Lambda = 160$ TeV.

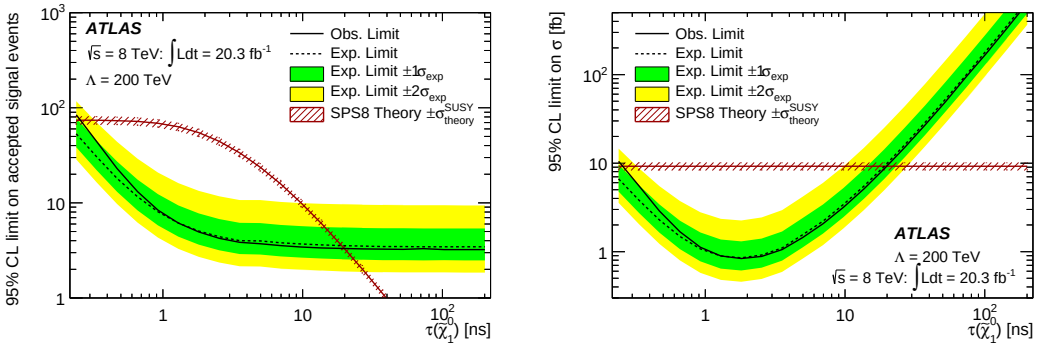

FIGURE 9.10: 95% CL limits on (left) the number of signal events and (right) the signal cross section, as a function of neutralino lifetime, for a Λ value of 200 TeV in the 8 TeV analysis. [2]

equivalent limits obtained from the analysis of the 7 TeV data, indicating that the 8 TeV analysis has excluded a much larger area of the signal space at 95% CL.

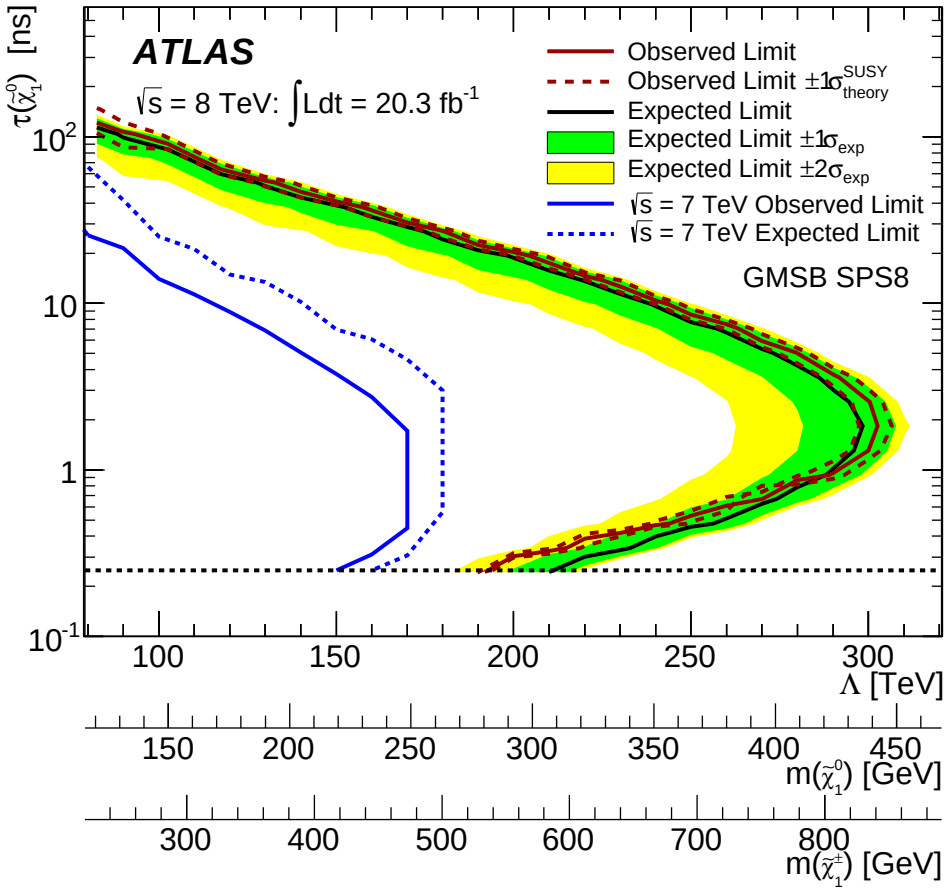

FIGURE 9.11: The observed and expected 95% CL limits from the 8 TeV analysis in the two-dimensional GMSB signal space of $\widetilde{\chi}_1^0$ lifetime versus Λ, the effective scale of SUSY breaking, and also versus the corresponding $\widetilde{\chi}_1^0$ and $\widetilde{\chi}_1^\pm$ masses in the SPS8 model. For comparison, the results from the 7 TeV analysis are also shown. The regions to the left of the limit curves are excluded at 95% CL. The horizontal dashed line indicates the lowest lifetime value, namely $\tau = 250$ ps, for which the analysis is applied. [2]

Chapter 10

LHC Run 2 Outlook

In this chapter an initial study looking ahead to the prospects of the search for non-prompt photons during run 2 of the LHC is presented.

This study focuses on the impacts of changes in the ATLAS trigger menu [140] for run 2. The changes to the trigger menu will have a big impact on the ability to perform a similar search for non-prompt photons primarily due to the removal of the diphoton trigger that is fired by Loose photons. This trigger will be replaced by a diphoton trigger that requires both photons to pass the, new to run 2, Medium IsEM cuts. The impact of this change in photon ID requirements will be investigated once new signal MC samples are available. However, as has been shown in section 5.3.1, the efficiency of detecting photons that have z_γ beyond 100 mm is drastically reduced if the photons are required to pass the Tight IsEM rather than the Loose IsEM cuts, so it is expected that the efficiency will also reduce for Medium IsEM. If it is found that the diphoton triggers available in run 2 are not suitable for use in the non-prompt photon search, it is possible that a single photon trigger, an $E_{\mathrm{T}}^{\mathrm{miss}}$ trigger, or a combination of both could be used instead.

Figure 10.1 shows the efficiency of SPS8 events passing different $E_{\mathrm{T}}^{\mathrm{miss}}$ cuts for a range of Λ values. It can be seen that if the $E_{\mathrm{T}}^{\mathrm{miss}}$ cut is increased above the value of 75 GeV used in the 7 TeV and 8 TeV analyses then the efficiency of events passing the cuts drops for all Λ values. This is most severe for samples with smaller Λ values, that have already been excluded for a range of τ values, and is considered a conservative estimate since increasing the center of mass energy of the pp collisions should also increase the

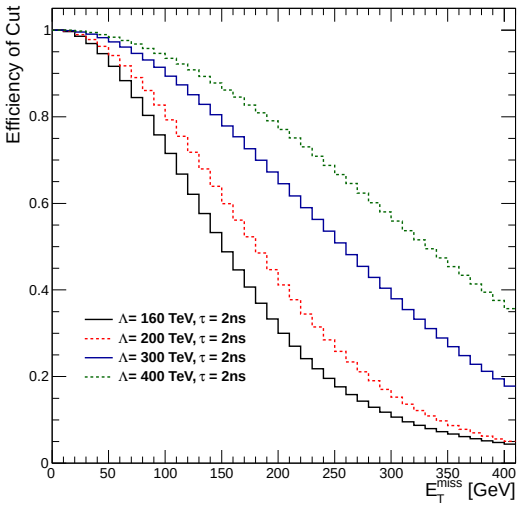

FIGURE 10.1: Efficiency of GMSB events passing an $E_{\mathrm{T}}^{\mathrm{miss}}$ cut as a function of the value of the $E_{\mathrm{T}}^{\mathrm{miss}}$ cut. This plot was produced using signal MC produced for the 8 TeV analysis.

amount of $E_{\mathrm{T}}^{\mathrm{miss}}$ in the events. However, the trigger with the lowest $E_{\mathrm{T}}^{\mathrm{miss}}$ requirements is currently set at 100 GeV so it is expected that this would result in the loss of some efficiency in the analysis.

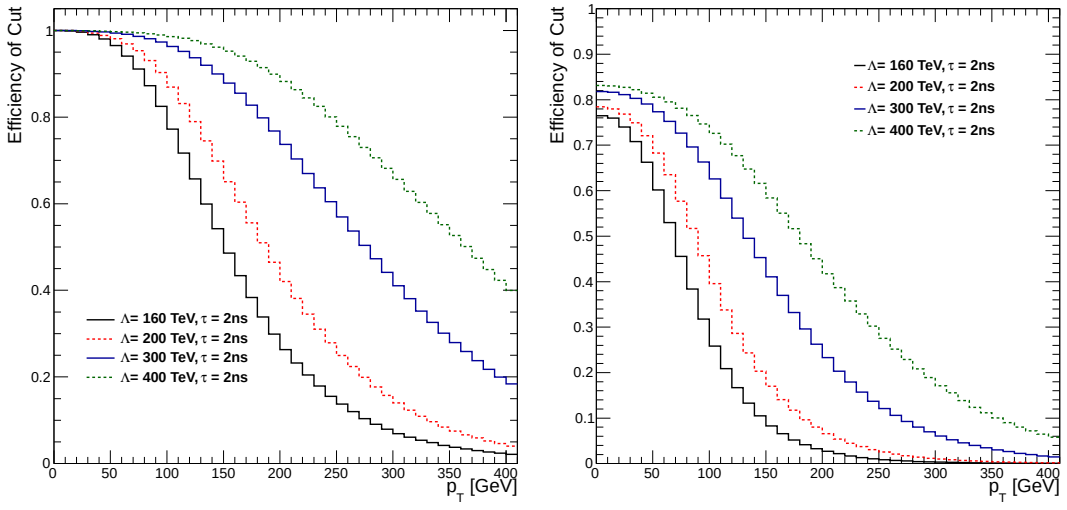

FIGURE 10.2: Efficiency of the leading (left) and sub-leading(right) photon in GMSB events passing a p_{T} cut as a function of the value of the p_{T} cut. Both plots were produced using signal MC produced for the 8 TeV analysis.

Figure 10.2 shows the efficiency of the leading and sub-leading photons in SPS8 events passing different p_{T} cuts for a range of Λ values. As expected, it can be seen that increasing the p_{T} cut above the value of 50 GeV used in the 7 TeV and 8 TeV analyses decreases the efficiency of photons from SPS8 events passing the cut. As for $E_{\mathrm{T}}^{\mathrm{miss}}$, this is more severe for samples with smaller Λ values, that have already been excluded for a

range of τ values, and is considered a conservative estimate since increasing the center of mass energy of the pp collisions should also increase the p_{T} of the photons. However, the single photon trigger with the lowest p_{T} requirements is currently set at 140 GeV which is expected to significantly reduce the efficiency of SPS8 events making it into the signal region.

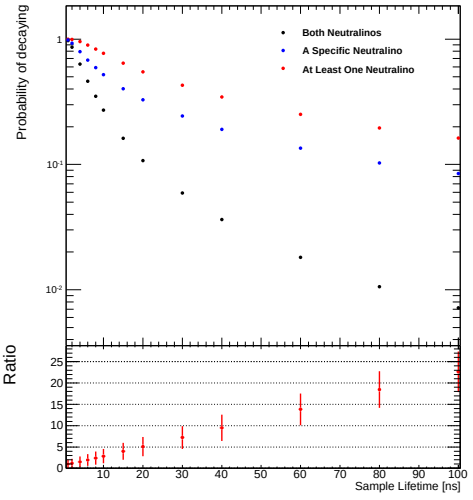

FIGURE 10.3: Probability that both neutralinos in an event (black), any single neutralino (blue), or at least one out of the two neutralinos (red) in an event decaying inside the ATLAS electromagnetic calorimeter for a range of neutralino lifetimes. The ratio shown in the lower third of the plot is the probability of at least one neutralino decaying over the probability of both neutralinos in the event decaying. This plot was created using toy MC with the kinematic distributions expected of neutralinos produced in 8 TeV SPS8 events with $\Lambda = 300$TeV.

There is, however, a significant benefit of moving to a single photon trigger. The right plot of figure 10.2 shows that the efficiency of the sub-leading photon passing the p_{T} cut remains less than 1 even if the p_{T} cut is reduced to 0 GeV. This is explained by many events containing neutralinos that decay after the EM calorimeter and therefore do not produce a sub-leading photon that will be reconstructed as a photon in the detector. Figure 10.3 shows how the probability of a neutralino decaying before the EM calorimeter decreases as the typical neutralino lifetime increases. A consequence of this is that the probability of having two neutralinos decaying before the EM calorimeter in an event, and therefore having two photons, decreases significantly as the typical lifetime increases. This reduces the expected signal yield at larger lifetimes, decreasing the sensitivity of the analysis. However, if a single photon trigger is used in the analysis, it is no longer necessary to require that both neutralinos decay in the detector and produce photons. If instead, a single photon analysis is performed then any event where

at least one neutralino decays will make it into the signal region. This could recover much of the lost signal yield, as shown in figure 10.3. However, moving to a single photon analysis will also increase the amount of background events so more study is required before a decision is made.

Chapter 11

Conclusions

A search for non-prompt photons produced from the decay of massive long lived neutral particles to a final state containing two photons and a large amount of missing transverse momentum has been presented. The data used in this search was collected from proton-proton collisions in the ATLAS detector at two center of mass energies: 4.8 fb^{-1}at $\sqrt{s} = 7$ TeV and 20.3 fb^{-1}at $\sqrt{s} = 8$ TeV. No significant excess is observed over the Standard Model predictions. Both datasets are interpreted in terms of the GMSB parameter space using the SPS8 benchmark model. In this scenario, the lightest neutralino is the next to lightest SUSY particle and the branching fraction to a gravitino and a photon is fixed to 100%. The only free parameters in this model are the lifetime of the neutralino and the effective SUSY breaking scale (Λ). Limits are set to a 95% CL on the excluded values of these two parameters with the range of lifetimes that are excluded varying for different Λ. In the analysis using the data collected at $\sqrt{s} = 7$ TeV, neutralinos with lifetimes varying from 250 ps to 50 ns in the Λ range 70 TeV to 170 TeV, corresponding to neutralino masses of between 95 GeV and 240 GeV, are excluded. In the analysis using data collected at $\sqrt{s} = 8$ TeV, neutralinos with lifetimes varying from 250 ps to 100 ns in the Λ range 80 TeV to 300 TeV, corresponding to neutralino masses of between 120 GeV and 440 GeV, are excluded.

Looking ahead to run 2 of the LHC, a similar search for non-prompt photons will be complicated by the triggers that are available. If a diphoton trigger is used the stricter photon ID requirements will likely reduce the efficiency of the analysis. However, moving

to a single photon analysis reduces the impact of neutralinos decaying outside of the detector, making the analysis more sensitive to neutralinos with longer lifetimes.

Appendix A

Event Selection

In this section the different objects that form the signal and control regions are defined for the 7 TeV and 8 TeV analyses separately.

A.1 7 TeV Analysis

In the following sub-sections a series of cuts and parameters are described that an object must satisfy. If the object fails any of these cuts it is removed from that particular sample of objects. This is to ensure that only good quality objects are considered in this analysis.

A.1.1 Photons

Photons are reconstructed in ATLAS as described in section 4.2. After the following cuts have been applied, events that contain a minimum of two photons that satisfy the Tight-Loose selection, as described in section 5.1.3, will populate the signal region and different diphoton control regions. In this analysis only the pointing measurement of the Loose (probe) photon will be used to distinguish between signal and background as described in section 7.1.1.

- Every photon is required to have a minimum p_{T} of 50 GeV. The Loose photon is required to have $|\eta| < 1.37$ due to the pointing resolution of the EM calorimeter

end-cap being worse than in the barrel (5.2.1). However, since the pointing measurement of the Tight photon is not used in the analysis the acceptance region is increased to $|\eta| < 2.37$, excluding the crack region, to increase the acceptance efficiency of the analysis. If both photons are Tight and only one is detected in the barrel this will be assigned the probe label. If, however, both photons are Tight and detected in the barrel, then the photon with the lowest energy will be given the probe label.

- All photons must be isolated, with the energy in a cone of $R < 0.4$ around the photon required to be less than 5 GeV.

- If the Tight photon is identified as a converted photon it must not share any pixel hits with a track that is associated to a track from another object. This is more strict than the standard converted photon identification rules in order to reduce the number of electrons that fake photons.

- At different points during the 7 TeV data taking period a number of the front end boards and high voltage regions were not operating as required. If the core of the photon cluster, defined as the 3×7 (3×5) cells for (un)converted photons in the barrel or 5×5 cells for photons in the EC, overlap with any of these regions the photon is excluded from the analysis. Additionally, if the core of the 3×3 cell cluster in the second layer of the calorimeter or the 8 central strips in the first layer of the calorimeter contain a dead cell, then the photon is also rejected [112].

- As described in [141], certain quality cuts are imposed to identify 'bad' photons. These photons are not removed from the sample but are involved in the event veto process (A.1.6). The Q-factor, given by equation 3.9, of all photons must be less than 0.8%. The cluster time must satisfy $|t| > (10 + 2/|E_{clus}|)$ where E_{clus} is the energy in the cluster and is measured in GeV, to exclude out of time and cosmic events. The IsEM variables R_ϕ or R_η must be less than or equal to 1.0 and 0.98 respectively.

A.1.2 Electrons

Electrons are reconstructed as described in section 4.2 and must meet the following requirements:

- All electrons must pass the Medium IsEM quality cuts.
- Electrons must have a minimum p_{T} of 25 GeV.
- The acceptance region for electrons is $|\eta| < 2.37$, excluding the crack region.
- The isolation requirement of electrons is identical to that of photons, with the energy in a cone of $R < 0.2$ around the electron required to be less than 5 GeV.
- The same requirement for the EM cluster not to be in dead regions or contain dead cells applies to electrons.
- Electrons are identified as 'bad' using the same cluster time method used for photons.

In the signal region and diphoton control regions there is no requirement to have any electrons that pass the above requirements in the final state.

A.1.3 Muons

Muons are reconstructed as described in section 4.4. All identification cuts follow the recommendations of the muon performance group for 7 TeV analyses [98] including:

- All muons must have a minimum p_{T} of 10 GeV.
- Muons must pass the Loose quality cuts [98].
- The acceptance range of muons is $|\eta| < 2.4$
- If the impact parameter of a muon along the z axis is greater than 1 mm or in the radial direction is greater than 0.2 mm then the muon is potentially a cosmic muon and identified as a bad muon.

In the signal region and control regions there is no requirement to have any muons that pass the above requirements in the final state.

A.1.4 Jets

Jets are reconstructed as described in section 4.3. All identification cuts follow the recommendations of the muon performance group for 7 TeV analyses [142] including:

- The transverse momentum of jets is measured at the electromagnetic jet energy scale ($p_{\mathrm{T}}^{\mathrm{EMJES}}$) [143] and required to be greater than 20 GeV.
- Jets are only accepted if they are detected within the $|\eta| < 2.8$ region.

It was found that a small number of jets could be the result of cosmic rays passing through the detector or due to noise in the calorimeter system faking jets. Therefore, a selection of cuts was devised (for more information on any of the cuts see [144]) to clean events. The cuts are applied to every jet in the event that passes the standard p_{T} threshold of $p_{\mathrm{T}}^{\mathrm{EMJES}} > 20$ GeV with no η requirement and also survives the overlap removal process (see section 4.6). If a jet meets any of the following requirements, the event it was detected in is vetoed from the data sample:

- More than 50% of the energy of the jet is in the hadronic end-cap and the absolute Q-factor of the jet is measured to be above 0.5.
- The sum of the energy of every cell with negative energy in the jet is less than -60 GeV
- The fraction of the jet energy deposited in the EM calorimeter is greater than 0.95 and the jet Q-factor is greater than 0.8. This applies to jets with $|\eta| < 2.8$.
- The energy squared weighted time of the jet differs from the expected value by more than 25 ns
- The fraction of the jet energy deposited in the EM calorimeter is less than 0.05. If the jet is detected with $|\eta| < 2.0$ then an additional requirement of the ratio of $\frac{\Sigma p_{\mathrm{T}}^{\mathrm{track}}}{p_{\mathrm{T}}^{\mathrm{calib}}} < 0.05$ where $p_{\mathrm{T}}^{\mathrm{track}}$ is the p_{T} of every track associated to the jet and $p_{\mathrm{T}}^{\mathrm{calib}}$ is the calibrated p_{T} of the jet.
- If a jet detected with $|\eta| < 2.0$ and more than 99% of its energy is deposited in a single layer of the calorimeter.

In the signal region and diphoton control regions there is no requirement to have any jets that pass the above requirements in the final state.

A.1.5 Missing Transverse Momentum

The $E_{\mathrm{T}}^{\mathrm{miss}}$ is calculated as described in section 4.5. The $E_{\mathrm{T}}^{\mathrm{miss}}$ requirements of the signal region and the different control regions is shown in table 6.3.

A.1.6 Event Veto

In the previous few sections bad photons/electrons/muons/jets where identified. These objects are due to detector effects such as noise or a cosmic event rather than a particle and will cause the $E_{\mathrm{T}}^{\mathrm{miss}}$ measurement to be inaccurate. Therefore, if an event contains any of these bad objects after overlap removal, the event is vetoed and not included in any of the signal or control region samples.

A.1.7 Cutflow

The cuts outlined above are applied to the data collected at 7 TeV in the following order to obtain the signal data used in this analysis:

- The good run list and trigger requirements outlined in section 6.1 are applied.
- All object related cuts are applied. Note, this does not result in any events being rejected only objects rejected from respective samples.
- Any events that are flagged by the event veto (section 6.1.1) due to a LAr error or data integrity error are removed.
- Overlap removal procedure is applied (section 4.6). Note, no events are rejected during this step.
- Any events containing jets that have been identified as 'bad' during the jet cleaning procedure described in section A.1.4 are removed.
- Any event which has a PV containing less than 5 associated tracks is removed.

- Any event containing a muon identified as bad in section A.1.3 is removed.
- The EM calorimeter hole veto (section 6.1.1) is applied.
- Any event that doesn't contain at least one Loose photon in the barrel is removed.
- Any event that doesn't satisfy the Tight-Loose selection, including the relevant η and p_{T} requirements, is removed.
- The relevant $E_{\mathrm{T}}^{\mathrm{miss}}$ requirement is applied.

The result of applying this cut flow to period K of the 7 TeV data, which was unblinded and used while developing the analysis strategy is shown in table A.1. Also shown is the cut flow for the full 2011 data, this result was kept blinded until the final stages of the analysis, as well as the cutflow for an example signal MC.

Selection	Data Period K	2011	SPS8 $\Lambda = 120$ TeV, τ =2 ns
All events	19683	153399	39999 (529.5)
GRL+Trigger	17866	142168	23344 (308.9)
LAr Error	17805	141644	23344 (308.9)
Jet Cleaning	17778	141460	22774 (301.4)
Vertex	17754	141220	22683 (300.2)
Muon veto	17743	141174	22543 (298.3)
LAr veto	17738	140926	22543 (298.3)
1 Loose Photon	12998	103642	19049 (252.1)
Diphoton	2894	23284	9155 (121.2)
$E_{\mathrm{T}}^{\mathrm{miss}} > 75$ GeV	3	46	6512 (86.2)

TABLE A.1: Cutflow table of data and a relevant SPS8 MC signal sample for the 7 TeV analysis. The numbers shown are the number of events after each selection step. The number in brackets is the number of signal events normalised to the luminosity of the 2011 data period. [57]

A.2 8 TeV Analysis

In the 8 TeV analysis the cuts were based on those used in the 7 TeV analysis but updated to meet the recommendations of the various performance groups. Any changes to the cuts used in the 7 TeV analysis are stated below.

A.2.1 Photons

- The energy in a cone around the photon with $\Delta R < 0.4$ is required to be less than 4 GeV after applying the appropriate recommendations from the egamma performance group [145].
- Photons with $|t_\gamma| > 4$ ns are removed from the sample. This is to ensure that photons produced in satellite collisions that will have a $|t_\gamma| \approx 5$ ns as explained in section 5.2.2.
- If the highest energy cell of a photon cluster is read out with LOW gain (see section 3.2.4.2) it is removed from the photon sample. This is because the timing calibration has not been optimised for LOW gain photons as described in section 5.2.2.

A.2.2 Electrons

- As for photons, if an electron is read out in LOW gain it is removed from the electron sample.

A.2.3 Muons

All identification cuts follow the recommendations of the muon performance group for 8 TeV analyses [99].

A.2.4 Jets

All identification cuts follow the recommendations of the jet performance group for 8 TeV analyses [146].

A.2.5 Missing Transverse Momentum

The $E_{\mathrm{T}}^{\mathrm{miss}}$ is calculated as described in section 4.5. The $E_{\mathrm{T}}^{\mathrm{miss}}$ cuts of the signal region and different control samples is the same as the 7 TeV analysis.

A.2.6 Event Veto

The event veto strategy is identical to the 7 TeV strategy

A.2.7 Cutflow

The cuts outlined above are applied to the data collected at 8 TeV in the following order to obtain the signal data used in this analysis:

- The good run list and trigger requirements outlined in section 6.1 are applied.
- All object related cuts are applied. Note: this does not result in any events being rejected, only objects were rejected from respective samples.
- Any event that does not contain at least two photons that pass all of the photon cuts is rejected.
- Overlap removal procedure is applied (section 4.6). Note, no events are rejected during this step.
- Any events containing jets that have been identified as 'bad' during the jet cleaning procedure described in section A.2.4 are removed. Events flagged by the event veto. (section 6.1.1) due to a LAr error or data integrity error are also removed.
- Any event which has a PV containing less than 5 associated tracks is removed.
- Any event containing a muon identified as bad in section A.2.3 is removed.
- Any event that doesn't contain at least one Loose photon in the barrel is removed.
- The relevant $E_{\mathrm{T}}^{\mathrm{miss}}$ requirement is applied.

The result of applying this cut flow to the full 8 TeV data is shown in table A.2. Also shown is the cut flow for the full 2012 data with the $E_{\mathrm{T}}^{\mathrm{miss}}$ cut separated into the different diphoton control regions and the signal region, the $E_{\mathrm{T}}^{\mathrm{miss}}$ range of each can be found in table 6.3. This information was blinded until the final stages of the analysis. Also shown is the cutflow for an example signal MC.

Cut	2012 Data			SPS8 $\Lambda = 300$ TeV, τ =2ns
Skimmed D3PD	2449621			40000 (13.6)
Good Run List	2332761			40000 (13.6)
Trigger	2332724			31666 (10.8)
2 Photons	122939			14582 (4.98)
LAr and Jet Cleaning	122585			14544 (4.96)
Vertex	122323			14485 (4.94)
Cosmic Muon veto	122309			14385 (4.93)
> 0 barrel photon	108972			14191 (4.84)
Region:	CR1:	CR2:	SR:	
BB	31182	2268	225	
BE	19569	1323	161	
Total	50751	3591	386	13252 (4.52)

TABLE A.2: Table showing the number of signal events entering the control regions and from a relevant SPS8 MC signal sample. The number of events in the signal region and diphoton control regions are broken down into the total number of BB and BE events. The number in brackets is the number of signal events normalised to the luminosity of the 2012 data period.

Appendix B

Lifetime Reweighting Procedure

The Monte Carlo signal samples used in this analysis were produced with Λ values that span the range of values that the analysis is expected to be sensitive to. For each Λ a range of τ were explored. Instead of using the computing intensive method of producing a separate sample for each τ a single reference sample was produced and then a reweighting technique (see Appendix A in Ref. [57]) utilized to transform this sample to the required τ.

The probability of a neutralino with a characteristic lifetime of $\tau = T$ decaying in proper time (t) is given by

$$p(t) = \frac{1}{T} \exp\left(-\frac{t}{T}\right) \tag{B.1}$$

To reweight the reference sample to the target lifetime (T') each neutralino that is recorded as decaying to a photon and gravitino is assigned a weight

$$w(t) = \frac{p'(t)}{p(t)} = \frac{T}{T'} * \exp\left[-t\left(\frac{1}{T'} - \frac{1}{T}\right)\right] \tag{B.2}$$

in order that the distribution of the proper decay times of the neutralinos in the reference sample matches the distribution expected in a sample with the target lifetime. Since there are two neutralinos produced in every event, each event is given a new weight:

$$w_{\gamma\gamma} = w_1 * w_2 \tag{B.3}$$

where w_1 and w_2 are the weights calculated for each neutralino from equation B.2. Figure B.1 shows that when the Λ= 160 TeV, T = 2 ns reference sample has been reweighted to T' = 6 ns the distribution of the proper decay time of the neutralinos agrees very well with the distribution seen in the Λ= 160 TeV, T= 6 ns reference sample before and after signal selection cuts have been made.

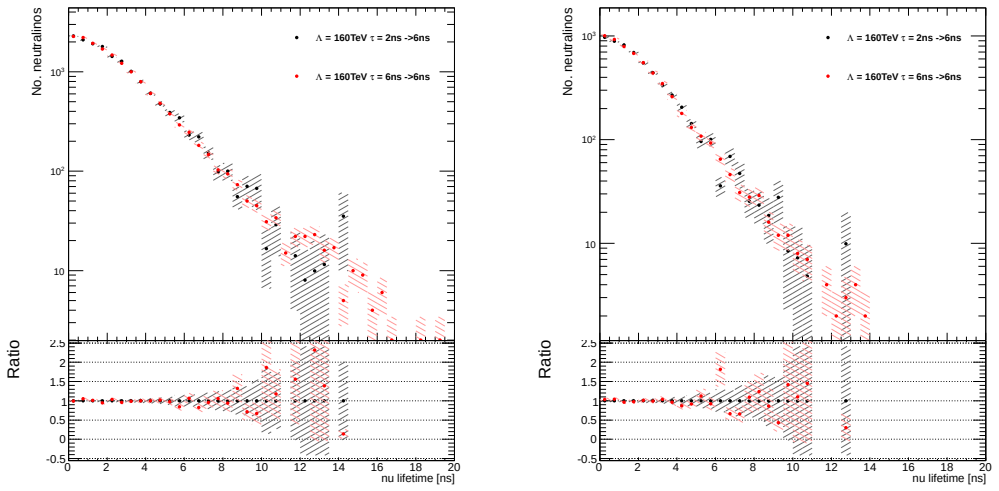

FIGURE B.1: Distribution of proper decay time of all neutralinos recorded as decaying in the Λ = 160 TeV, T = 6 ns reference sample and in the Λ =160 TeV, T = 2ns reference sample that has been reweighted to a target lifetime of T'=6 ns before (left) and after (right) signal selection cuts.

This reweighting method is valid for all neutralinos that are recorded as decaying to a photon and a gravitino. However, as shown in figure B.2 the decay will not be recorded if it occurs more than 3500 mm or 1150 mm from the center of the detector in the beam and transverse directions respectively. In the 7 TeV analysis it was assumed that if there was no decay information for a neutralino then it did not decay. In events where only one neutralino was recorded as decaying but two photons were detected, it was assumed that this was not a signal photon but the event still made it into the signal sample due to a real or fake photon from elsewhere in the decay chain. Since there is no input information for equation B.2 if a neutralino isn't recorded as decaying, a value of 1 was used for w_2 in equation B.3.

However, if a neutralino decays outside of this region, which corresponds to the inner detector (ID) of the ATLAS detector, and the photon produces a shower in the EM

calorimeter there will be a reconstructed photon but no information relating to the decay vertex or decay products will be recorded. In the 8 TeV analysis, a new validation sample was produced with identical settings as used to create the reference samples except that the decay information of all LLPs is recorded. Figure B.2 was produced using this new sample and verifies that neutralinos with longer lifetimes are decaying beyond the ID in the reference samples. However, as no information relating to the decay is stored in the reference samples it is not possible to use equation B.2 to reweight neutralinos that decay beyond the ID. It is assumed that the new cutoff, beyond which the decay of a neutralino will not produce a photon that can satisfy the photon selection requirements, is the start of the EM calorimeter. Beyond this point even a small angle between the direction of the neutralino and photon will result in the shower in the EM calorimeter being very wide compared to a prompt photon, causing the photon to fail the IsEM SSV cuts.

The proper decay time of a neutralino is related to the distance travelled in the lab frame (L) between the neutralino production and decay vertex according to $t = L/(c\beta\gamma)$, where $\beta = p/E$ and $\gamma = (1-\beta^2)^{-1/2}$. The probability of a neutralino decaying after travelling L can be written as

$$p(L) = \frac{1}{T} \exp\left(-\frac{L}{c\beta\gamma}\frac{1}{T}\right). \tag{B.4}$$

The probability of a neutralino decaying in this region depends on the maximum (L_{max}) and minimum (L_{min}) distance it can travel and still be in the volume between the ID and EM calorimeter according to

$$P_T = \exp\left(-\frac{L_{min}}{c\beta\gamma}\frac{1}{T}\right) - \exp\left(-\frac{L_{max}}{c\beta\gamma}\frac{1}{T}\right). \tag{B.5}$$

Figure B.3 was produced using the toy MC and shows how the fraction of neutralinos expected to decay in the volume between the ID and EM calorimeter is dependent on the τ of the sample. When reweighting the reference sample to lifetime T' each neutralino is assigned a weight

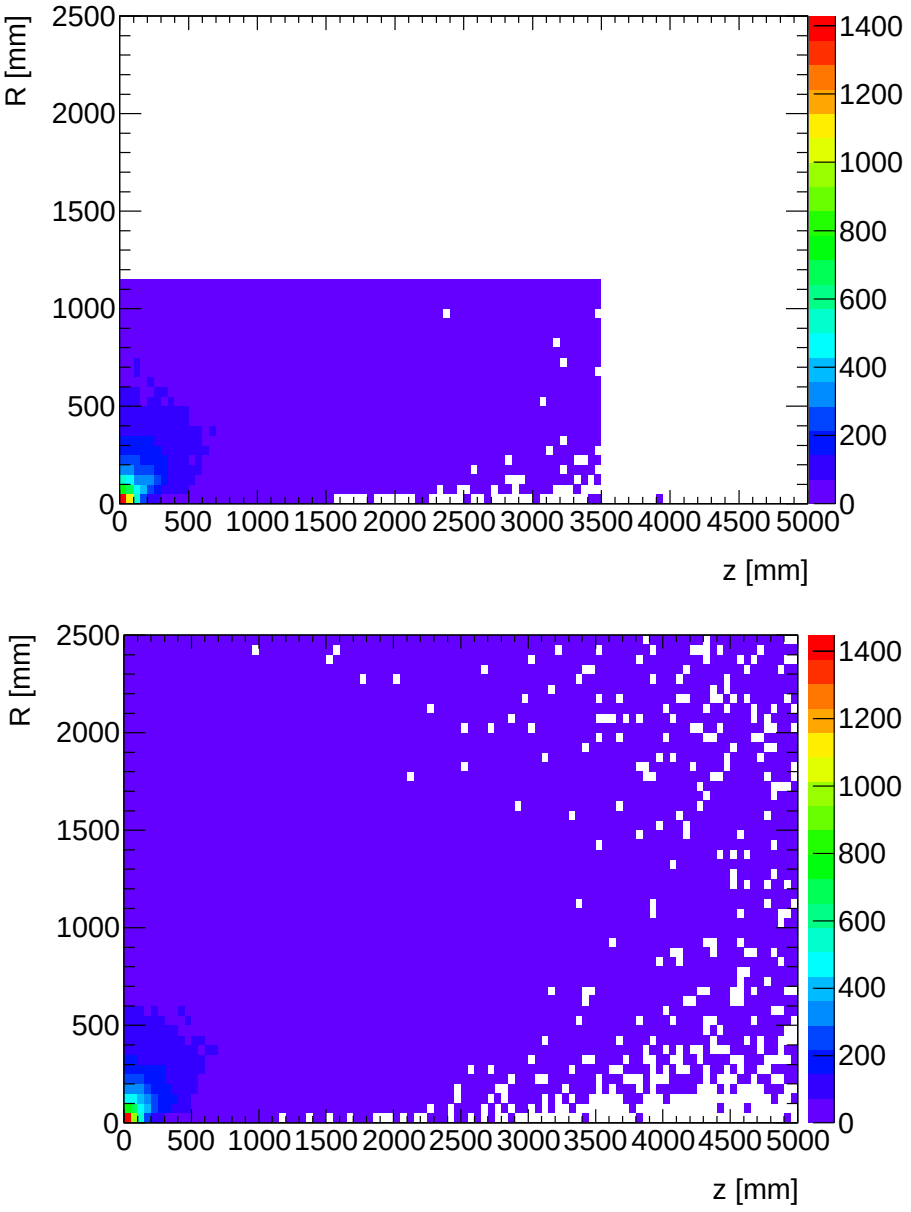

FIGURE B.2: (Left) decay vertex in mm of all neutralinos that are recorded as decaying in $\Lambda = 160$ TeV, T=2ns reference sample. (Right) decay vertex of all neutralinos that decay to a photon in new sample where decay vertex of all long lived particles is kept.

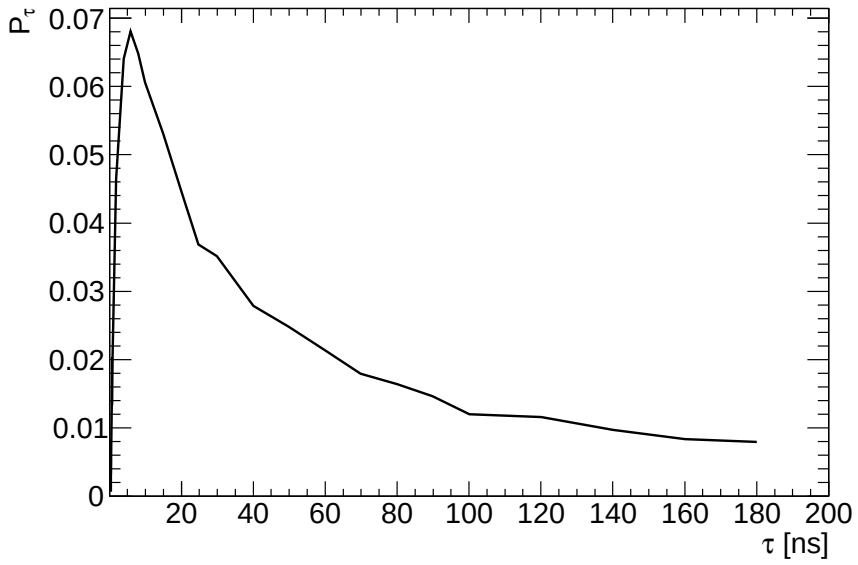

FIGURE B.3: Probability of a neutralino with $\Lambda = 160TeV$ decaying in the region between the ID and EM calorimeter as a function of $T = \tau$.

$$w(L) = \frac{P'_T}{P_T} = \frac{\exp\left(-\frac{L_{min}}{c\beta\gamma}\frac{1}{T'}\right) - \exp\left(-\frac{L_{max}}{c\beta\gamma}\frac{1}{T'}\right)}{\exp\left(-\frac{L_{min}}{c\beta\gamma}\frac{1}{T}\right) - \exp\left(-\frac{L_{max}}{c\beta\gamma}\frac{1}{T}\right)} \tag{B.6}$$

so that the fraction of neutralinos in the sample that decay in the volume between the ID and the EM calorimeter agree with that expected for a lifetime of T'. Figure B.4 shows that for the Λ = 160 TeV, T = 2 ns sample, $w(L)$ is at its largest at around T' = 7 ns but then decreases as T' increases before flattening out at large T'.

In this study the weight assigned to the two signal photons (w_1 and w_2) is combined with all other weights (w_{other}) that affect the event weight such as PU, sample cross-section etc. to get a single weight for each event. This event weight (W) is given by $W = w_{\gamma\gamma} * w_{other}$. It is then clear there will be three different sub categories of events depending on how many neutralinos are recorded as decaying inside the ID. In category 1 both neutralinos decay inside the ID and w_1 and w_2 are both calculated using equation B.2. In category 2 both neutralinos decay outside the ID and w_1 and w_2 are both calculated using equation B.6. In category 3, 1 neutralino decays in the ID and one decays outside the ID meaning that one weight will be calculated using equation B.2 and the other using equation B.6.

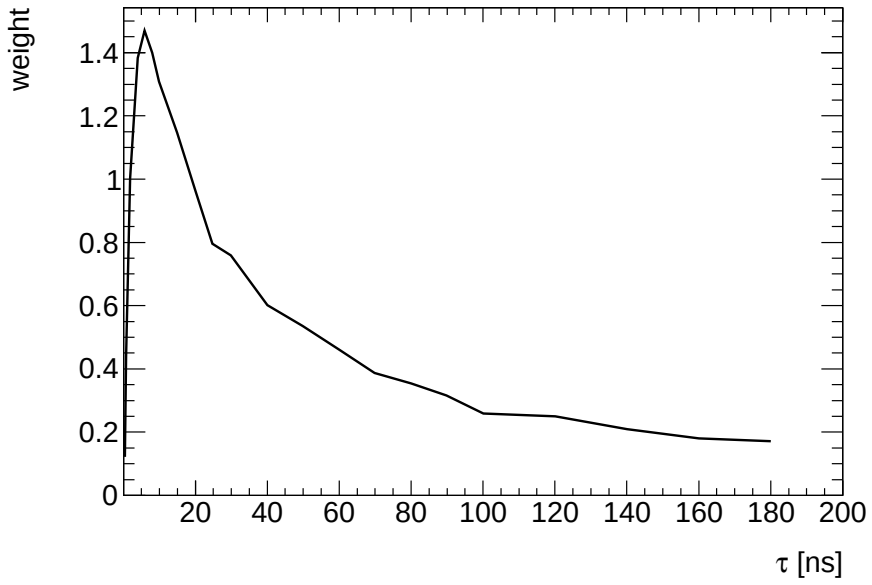

FIGURE B.4: Weight given to a neutralino that decays in the region between the ID and EM calorimeter when reweighting the $\Lambda = 160TeV$ T = 2 ns reference sample to $T' = \tau$.

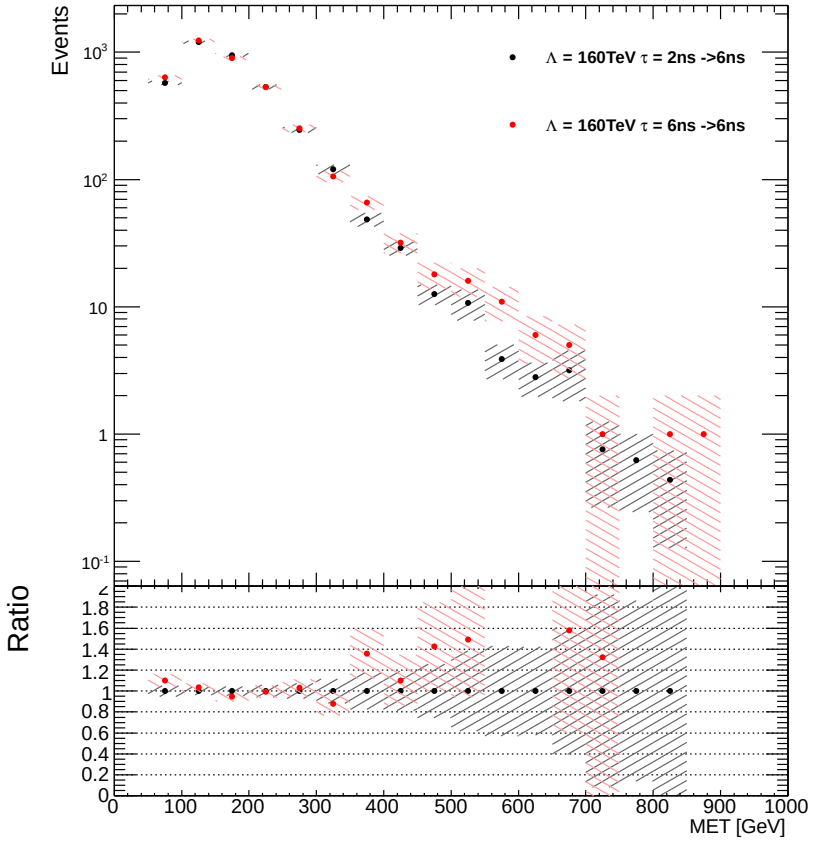

FIGURE B.5: $E_{\mathrm{T}}^{\mathrm{miss}}$ distribution after full signal selection for Λ = 160 TeV, T = 6 ns sample (red) and Λ = 160 TeV, T = 2 ns sample reweighted to T' = 6 ns(black).

Figure B.5 shows that when the reweighting procedure as described above is applied to all signal events in the Λ = 160 TeV, T = 2 ns sample to reweight to T' = 6 ns the $E_{\mathrm{T}}^{\mathrm{miss}}$ distribution agrees very well with the $E_{\mathrm{T}}^{\mathrm{miss}}$ distribution in the T = 6 ns sample. Figure B.6 shows that this agreement is still good when both samples are reweighted to larger T'.

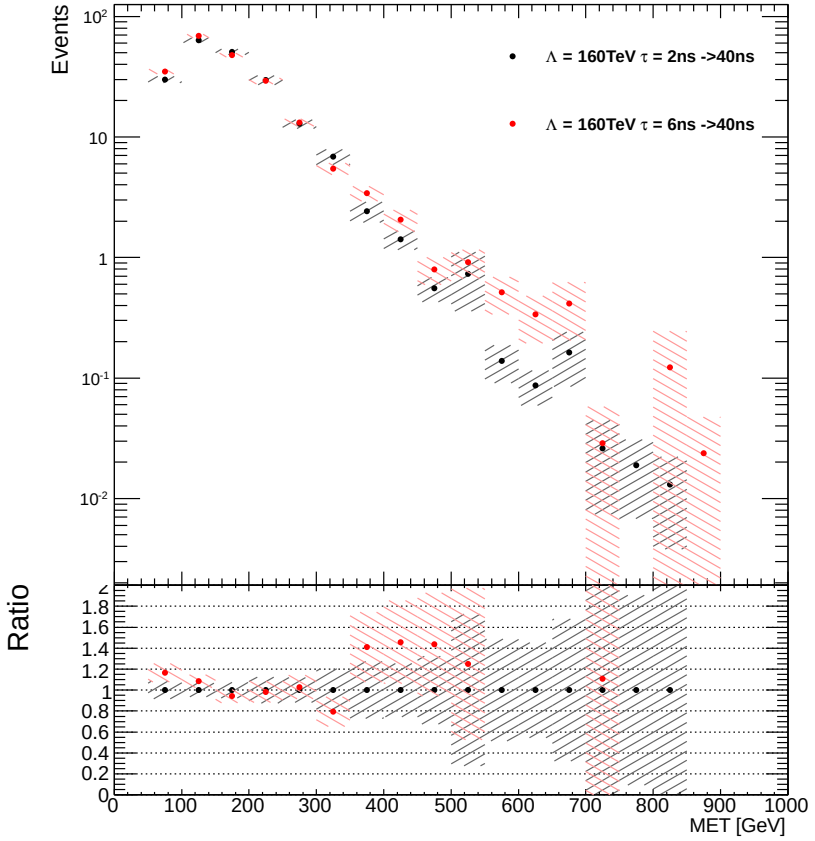

FIGURE B.6: $E_{\mathrm{T}}^{\mathrm{miss}}$ distribution after full signal selection for Λ = 160 TeV, T = 6 ns sample (red) and Λ = 160 TeV, T = 2 ns sample (black) both reweighted to T' = 40 ns.

To estimate a systematic uncertainty for category 1, two different reference samples (Λ = 160 TeV , T = 2 ns and T = 6 ns) were reweighted to a range of T' values as shown in figure B.7 with the ratio of the predicted numbers of events used as the error.

For category 2, the uncertainty comes from the uncertainty of the maximum radius (R) that a neutralino can decay and the daughter photon still pass all of the photon identification cuts. R is taken to be the start of the EM calorimeter (1500 mm) but it is conceivable that a photon produced after this point will still pass the Loose IsEM cuts if the angle of decay with the neutralino is very small and conversely a photon produced before this point would be expected to fail the Loose IsEM cuts if there is a large decay

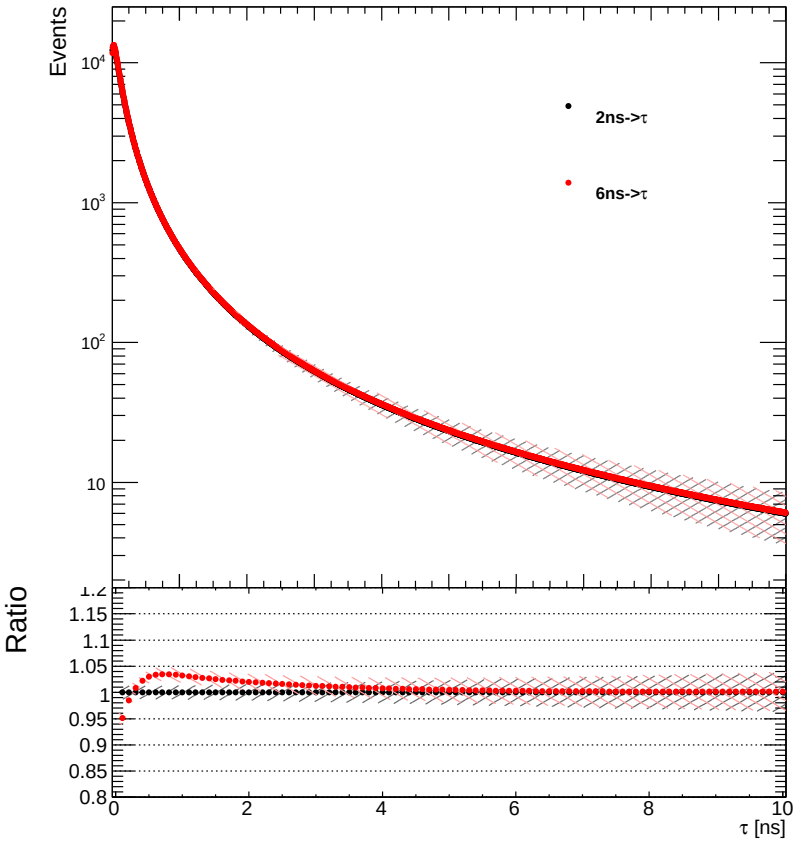

FIGURE B.7: Number of events with two neutralinos recorded as decaying in the ID using the $\Lambda = 160$ TeV, T = 2 ns (black) and $\Lambda = 160$ TeV, T = 6 ns (red) reweighted to T' = τ.

angle between the neutralino. A conservative estimate of the uncertainty is produced by varying R by $\pm$ 200 mm and calculating how the probability of decaying in this new region varies for different T' values as shown in B.8.

In category 3, one photon decays in the ID and one decays outside the ID, the uncertainty is therefore taken to be the average of the uncertainties on category 1 and category 2. To get an estimate of the uncertainty for the whole sample a weighted average of the uncertainties based on the number of events in each category is calculated as shown in figure B.9.

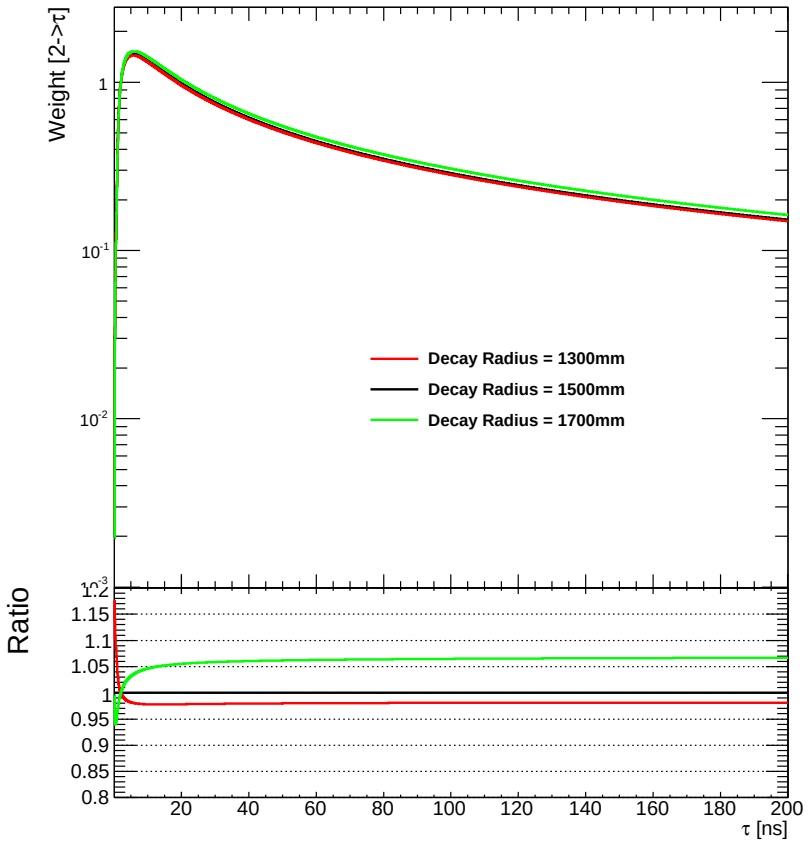

FIGURE B.8: Weight applied to neutralinos that aren't recorded as decaying in the ID if maximum decay radius is 1300 mm (red) 1500 mm (black) or 1700 mm (green) when reweighting from $\Lambda = 160$ TeV, T = 2 ns reference sample to T = τ.

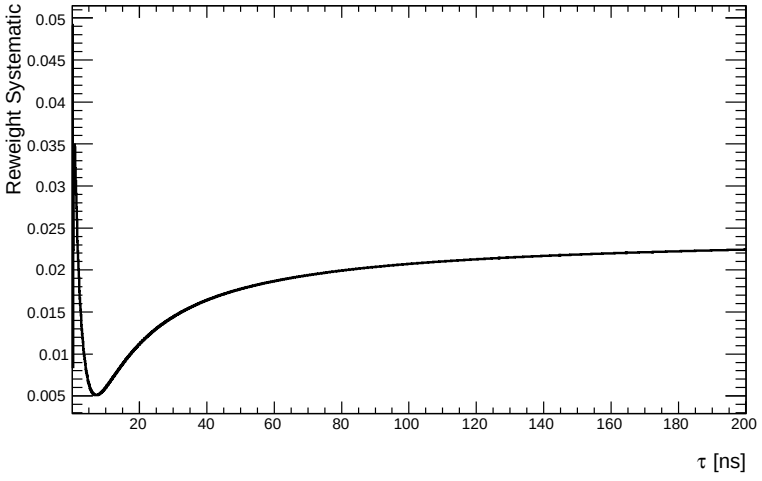

FIGURE B.9: Weight applied to neutralinos that aren't recorded as decaying in the ID if maximum decay radius is 1300 mm (red) 1500 mm (black) or 1700 mm (green) when reweighting from $\Lambda = 160$ TeV, T = 2 ns reference sample to T = τ.

Appendix C

Signal Efficiencies

Λ (TeV)	Neutralino lifetime (ns)													
	0	0.25	0.5	0.75	1	2	4	6	8	10	15	20	25	30
210		58.6 ±0.6	54.6 ±0.5	50.9 ±0.5	50.0 ±0.5	33.0 ±0.3	17.6 ±0.2	10.8 ±0.1	7.3 ±0.07	5.3 ±0.05	3.1 0.02	1.9 ±0.02	1.4 ±0.01	0.99 ±0.01
200		56.3 ±0.4	52.0 ±0.4	48.2 ±0.3	44.3 ±0.3	31.1 ±0.2	16.8 ±0.1	10.4 ±0.07	7.1 ±0.05	5.2 ±0.04	2.9 ±0.02	1.8 ±0.02	1.3 ±0.01	1.0 ±0.007
190		52.0 ±0.2	50.9 ±0.3	47.8 ±0.4	44.0 ±0.4	30.4 ±0.3	16.1 ±0.2	9.9 ±0.2	6.8 ±0.1	4.9 ±0.1	2.7 0.07	1.8 ±0.05	1.3 ±0.04	0.97 ±0.04
180		48.6 ±0.5	47.7 ±0.4	44.8 ±0.4	41.3 ±0.4	28.6 ±0.3	15.1 ±0.2	9.3 ±0.2	6.3 ±0.1	4.6 ±0.1	2.5 ±0.06	1.6 ±0.05	1.1 ±0.03	0.86 ±0.03
170		52.4 ±0.4	47.8 ±0.3	43.6 ±0.3	39.6 ±0.3	27.0 ±0.2	14.4 ±0.1	9.0 ±0.06	6.2 ±0.04	4.5 ±0.03	2.5 ±0.02	1.6 ±0.01	1.2 ±0.01	0.90 ±0.006
160		45.1 ±0.3	42.0 ±0.3	39.1 ±0.3	35.9 ±0.3	24.8 ±0.2	13.1 ±0.09	8.06 ±0.06	5.50 ±0.03	4.01 ±0.03	2.2 ±0.02	1.43 ±0.01	1.0 ±0.007	0.772 0.006
150		42.5 ±0.2	40.4 ±0.2	37.3 ±0.2	34.0 ±0.2	23.1 ±0.1	12.13 ±0.06	7.45 ±0.04	5.07 ±0.03	3.69 ±0.02	2.11 ±0.06	1.311 ±0.007	0.98 ±0.03	0.715 ±0.004
140		38.5 ±0.3	37.1 ±0.3	34.4 ±0.2	31.3 ±0.2	21.1 ±0.2	11.1 ±0.08	6.82 ±0.05	4.68 ±0.2	3.44 ±0.03	1.9 ±0.9	1.25 ±0.01	0.9 ±0.05	0.682 ±0.005
130		36.1 ±0.2	34.2 ±0.2	31.5 ±0.2	27.3 ±0.2	19.2 ±0.1	10.04 ±0.07	6.39 ±0.03	4.40 ±0.02	3.25 ±0.02	1.9 ±0.04	1.235 ±0.006	0.92 ±0.02	0.712 ±0.004
120	29.6 ±0.3	30.2 ±0.2	29.2 ±0.2	27.0 ±0.2	23.9 ±0.1	16.3 ±0.06	8.73 ±0.03	5.38 ±0.02	3.68 ±0.02	2.71 ±0.02	1.54 ±0.04	1.006 ±0.005	0.74 ±0.02	0.568 ±0.003
110		28.1 ±0.2	26.2 ±0.1	24.0 ±0.1	20.1 ±0.2	14.30 ±0.07	6.83 ±0.05	4.55 ±0.02	3.15 ±0.02	2.33 ±0.01	1.34 ±0.03	0.900 ±0.005	0.67 ±0.02	0.525 ±0.003
100		22.9 ±0.1	21.8 ±0.1	19.7 ±0.1	16.6 ±0.1	11.34 ±0.06	5.84 ±0.04	3.51 ±0.02	2.42 ±0.01	1.79 ±0.01	1.03 ±0.03	0.688 ±0.004	0.51 ±0.02	0.399 ±0.002
90		19.1 ±0.1	17.9 ±0.1	16.1 ±0.1	13.9 ±0.1	9.06 ±0.05	4.72 ±0.04	2.91 ±0.01	1.96 ±0.01	1.447 ±0.008	0.85 ±0.01	0.563 ±0.003	0.43 ±0.02	0.333 ±0.002
80		15.3 ±0.3	14.1 ±0.2	12.6 ±0.2	11.1 ±0.1	6.90 ±0.07	3.34 ±0.04	2.01 ±0.02	1.37 ±0.02	1.01 ±0.02	0.6 ±0.01	0.39 ±0.01	0.3 ±0.01	0.24 ±0.01
70		14.2 ±0.2	12.4 ±0.2	10.8 ±0.1	9.32 ±0.08	5.49 ±0.05	2.57 ±0.02	1.53 ±0.02	1.04 ±0.01	0.77 ±0.01	0.46 ±0.02	0.311 ±0.005	0.24 ±0.01	0.194 ±0.004

TABLE C.1: The efficiency, in percent, of the Tight-Loose photon selection and $E_{\mathrm{T}}^{\mathrm{miss}}$ cut for the 7 TeV signal grid, for neutralino lifetimes up to 30 ns [57].

Λ (TeV)	Neutralino lifetime (ns)			
	40	60	80	100
160	0.510 ±0.004	0.287 ±0.002	0.196 ±0.002	-
150	0.473 ±0.003	0.276 ±0.001	0.189 ±0.001	-
140	0.448 ±0.003	0.255 ±0.002	0.176 ±0.001	-
130	0.493 ±0.003	0.309 ±0.002	0.231 ±0.001	-
120	0.384 ±0.002	0.230 ±0.001	0.164 ±0.001	-
110	0.366 ±0.002	0.230 ±0.001	0.172 ±0.001	0.1470 ±0.0007
100	0.277 ±0.002	0.172 ±0.001	0.128 ±0.001	0.1040 ±0.0006
90	0.235 ±0.002	0.151 ±0.001	0.115 ±0.001	0.095 ±0.001
80	0.175 ±0.005	0.116 ±0.004	0.090 ±0.004	0.076 ±0.004
70	0.144 ±0.003	0.101 ±0.003	0.082 ±0.003	0.072 ±0.003

TABLE C.2: The efficiency, in percent, of the Tight-Loose photon selection and $E_{\mathrm{T}}^{\mathrm{miss}}$ cut for the 7 TeV signal grid, for neutralino lifetimes beyond 30 ns [57].

Λ	Neutralino lifetime (ns)											
(TeV)	0.1	0.3	0.5	0.7	1	2	4	6	8	10	15	20
350	47.5	47.4	48	47.1	44.7	33.9	19.6	12.6	8.79	6.5	3.59	2.28
	±0.4	±0.4	±0.4	±0.4	±0.4	±0.3	±0.2	±0.1	±0.08	±0.06	±0.03	±0.02
	±1.9	±0.81	±1.5	±1.6	±1.5	±0	±0.33	±0.17	±0.12	±0.094	±0.062	±0.045
320	46.2	46.3	46.4	45.4	43.1	33	19.3	12.5	8.72	6.45	3.56	2.26
	±0.4	±0.4	±0.4	±0.4	±0.4	±0.3	±0.2	±0.1	±0.08	±0.06	±0.03	±0.02
	±1.9	±0.79	±1.5	±1.6	±1.4	±0	±0.33	±0.17	±0.12	±0.093	±0.062	±0.045
310	47.2	46.6	45.7	44.5	42.2	32.5	19	12.3	8.57	6.35	3.51	2.23
	±0.4	±0.4	±0.4	±0.4	±0.4	±0.3	±0.2	±0.1	±0.08	±0.06	±0.03	±0.02
	±2	±0.8	±1.5	±1.6	±1.4	±0	±0.33	±0.17	±0.12	±0.092	±0.062	±0.044
300	43.7	43.5	44.2	43.6	41.7	31.9	18.4	11.8	8.26	6.1	3.36	2.14
	±0.4	±0.4	±0.4	±0.4	±0.4	±0.3	±0.2	±0.1	±0.07	±0.05	±0.03	±0.02
	±1.8	±0.75	±1.4	±1.5	±1.4	±0	±0.32	±0.16	±0.11	±0.089	±0.059	±0.043
290	42.1	43.8	44.5	43.8	41.7	31.8	18.3	11.7	8.18	6.04	3.32	2.11
	±0.4	±0.4	±0.4	±0.4	±0.4	±0.3	±0.2	±0.1	±0.07	±0.05	±0.03	±0.02
	±1.8	±0.76	±1.5	±1.5	±1.4	±0	±0.32	±0.16	±0.11	±0.088	±0.059	±0.042
270	42.2	42.1	42.6	42	40.2	30.8	17.8	11.4	7.93	5.85	3.22	2.04
	±0.4	±0.4	±0.4	±0.4	±0.4	±0.3	±0.2	±0.1	±0.07	±0.05	±0.03	±0.02
	±1.8	±0.73	±1.4	±1.5	±1.4	±0	±0.31	±0.16	±0.11	±0.086	±0.057	±0.041
260	40.1	42.9	43	42.1	40	30.7	17.8	11.5	8	5.91	3.26	2.07
	±0.4	±0.4	±0.4	±0.4	±0.4	±0.3	±0.2	±0.1	±0.07	±0.05	±0.03	±0.02
	±1.7	±0.75	±1.4	±1.5	±1.4	±0	±0.31	±0.16	±0.11	±0.087	±0.058	±0.042
250	39.9	41.4	41.8	41.1	39.3	30	17.3	11.1	7.75	5.71	3.14	1.99
	±0.4	±0.4	±0.4	±0.4	±0.4	±0.3	±0.2	±0.1	±0.07	±0.05	±0.03	±0.02
	±1.7	±0.73	±1.4	±1.5	±1.3	±0	±0.31	±0.16	±0.11	±0.085	±0.056	±0.04
240	48.8	43.2	42	40.7	38.5	29.2	16.9	10.8	7.55	5.58	3.08	1.96
	±0.5	±0.4	±0.4	±0.4	±0.4	±0.3	±0.2	±0.1	±0.07	±0.05	±0.03	±0.02
	±2.1	±0.76	±1.4	±1.5	±1.3	±0	±0.3	±0.15	±0.1	±0.083	±0.056	±0.04
230	44.2	41.2	40.7	39.7	37.9	29	16.8	10.8	7.5	5.53	3.04	1.93
	±0.4	±0.4	±0.4	±0.4	±0.4	±0.3	±0.2	±0.1	±0.07	±0.05	±0.04	±0.04
	±1.9	±0.73	±1.4	±1.4	±1.3	±0	±0.3	±0.15	±0.1	±0.083	±0.055	±0.039
220	39.2	39.4	39.1	38.1	36.3	27.7	15.9	10.2	7.08	5.22	2.87	1.82
	±0.4	±0.4	±0.4	±0.4	±0.3	±0.3	±0.2	±0.1	±0.07	±0.05	±0.03	±0.02
	±1.7	±0.71	±1.3	±1.4	±1.3	±0	±0.29	±0.15	±0.1	±0.079	±0.052	±0.037
210	34.4	38	37.9	37	35.2	26.9	15.6	10	6.99	5.16	2.85	1.81
	±0.3	±0.4	±0.4	±0.4	±0.3	±0.3	±0.2	±0.1	±0.07	±0.05	±0.03	±0.02
	±1.5	±0.68	±1.3	±1.4	±1.2	±0	±0.28	±0.14	±0.099	±0.079	±0.052	±0.038
200	39.4	37.7	37.3	36.2	34.3	26	15	9.65	6.73	4.97	2.74	1.75
	±0.4	±0.4	±0.4	±0.4	±0.3	±0.3	±0.1	±0.09	±0.07	±0.05	±0.03	±0.02
	±1.7	±0.69	±1.3	±1.3	±1.2	±0	±0.27	±0.14	±0.096	±0.077	±0.051	±0.037
190	39.1	36.2	35.6	34.6	32.7	24.6	14	8.88	6.15	4.52	2.47	1.56
	±0.4	±0.4	±0.4	±0.3	±0.3	±0.2	±0.1	±0.09	±0.06	±0.05	±0.02	±0.02
	±1.7	±0.67	±1.2	±1.3	±1.2	±0	±0.26	±0.13	±0.089	±0.071	±0.047	±0.033
180	44.4	38.7	37.8	36.5	34.3	25.7	14.7	9.37	6.5	4.78	2.62	1.66
	±0.4	±0.4	±0.4	±0.4	±0.3	±0.3	±0.1	±0.09	±0.06	±0.05	±0.03	±0.02
	±2	±0.71	±1.3	±1.4	±1.2	±0	±0.27	±0.14	±0.093	±0.074	±0.049	±0.035
170	35	32.7	32.1	31.3	29.6	22.4	12.8	8.2	5.7	4.19	2.3	1.46
	±0.4	±0.3	±0.3	±0.3	±0.3	±0.2	±0.1	±0.09	±0.06	±0.04	±0.02	±0.02
	±1.6	±0.62	±1.1	±1.2	±1.1	±0	±0.24	±0.12	±0.085	±0.067	±0.044	±0.032
160	28.9	30.4	30.2	29.2	27.5	20.5	11.6	7.35	5.06	3.71	2.01	1.26
	±0.3	±0.3	±0.3	±0.3	±0.3	±0.2	±0.1	±0.08	±0.06	±0.04	±0.02	±0.01
	±1.3	±0.59	±1.1	±1.1	±1	±0	±0.23	±0.11	±0.077	±0.06	±0.04	±0.028
150	25.8	26.8	27.2	26.4	25	18.7	10.6	6.74	4.67	3.43	1.87	1.18
	±0.3	±0.3	±0.3	±0.3	±0.3	±0.2	±0.1	±0.08	±0.05	±0.04	±0.02	±0.01
	±1.2	±0.53	±1	±1.1	±0.96	±0	±0.21	±0.11	±0.073	±0.057	±0.038	±0.027
140	38	27.9	25.9	24.4	22.5	16.3	9.03	5.64	3.86	2.81	1.51	0.945
	±0.8	±0.6	±0.5	±0.5	±0.5	±0.3	±0.2	±0.1	±0.08	±0.06	±0.03	±0.02
	±2.4	±0.74	±1.3	±1.3	±1.2	±0.65	±0.24	±0	±0.081	±0.063	±0.041	±0.029
130	35.3	25.5	23.3	21.7	20	14.4	7.96	4.97	3.4	2.48	1.33	0.833
	±0.8	±0.6	±0.5	±0.5	±0.4	±0.3	±0.2	±0.1	±0.08	±0.06	±0.03	±0.02
	±2.3	±0.7	±1.2	±1.2	±1.1	±0.6	±0.22	±0	±0.074	±0.058	±0.037	±0.026
120	23.2	24	22.5	20.7	18.5	12.8	6.99	4.37	2.99	2.18	1.18	0.737
	±0.6	±0.6	±0.5	±0.5	±0.4	±0.3	±0.2	±0.1	±0.07	±0.05	±0.03	±0.02
	±1.6	±0.68	±1.2	±1.2	±1	±0.55	±0.2	±0	±0.067	±0.052	±0.034	±0.024
90	12.9	11.4	11.6	11.1	10.1	6.82	3.58	2.2	1.5	1.09	0.582	0.364
	±0.4	±0.4	±0.4	±0.4	±0.3	±0.2	±0.1	±0.07	±0.05	±0.04	±0.02	±0.01
	±1.1	±0.38	±0.74	±0.76	±0.67	±0.35	±0.12	±0	±0.04	±0.031	±0.02	±0.014
80	8.34	8.5	8.35	7.9	7.25	5.07	2.75	1.72	1.18	0.862	0.468	0.294
	±0.3	±0.3	±0.3	±0.3	±0.3	±0.2	±0.1	±0.07	±0.04	±0.03	±0.02	±0.01
	±0.72	±0.31	±0.57	±0.58	±0.51	±0.27	±0.099	±0	±0.033	±0.026	±0.017	±0.012

TABLE C.3: The efficiency, in percent, of the Loose-Loose photon selection and $E_{\mathrm{T}}^{\mathrm{miss}}$ cut for the 8 TeV signal grid, for neutralino lifetimes up to 20 ns.

Λ	Neutralino lifetime (ns)					
(TeV)	25	30	40	60	80	100
350	1.58	1.16	0.706	0.341	0.2	0.132
	±0.01	±0.01	±0.006	±0.003	±0.002	±0.001
	±0.033	±0.026	±0.017	±0.0086	±0.0052	±0.0035
320	1.56	1.15	0.695	0.334	0.196	0.129
	±0.01	±0.01	±0.006	±0.003	±0.002	±0.001
	±0.033	±0.026	±0.017	±0.0085	±0.0052	±0.0035
310	1.55	1.14	0.691	0.334	0.196	0.129
	±0.01	±0.01	±0.006	±0.003	±0.002	±0.001
	±0.033	±0.026	±0.017	±0.0085	±0.0052	±0.0035
300	1.48	1.09	0.661	0.319	0.188	0.123
	±0.01	±0.01	±0.006	±0.003	±0.002	±0.001
	±0.032	±0.025	±0.016	±0.0082	±0.005	±0.0033
290	1.46	1.07	0.65	0.313	0.184	0.121
	±0.01	±0.01	±0.006	±0.003	±0.002	±0.001
	±0.031	±0.024	±0.016	±0.0081	±0.0049	±0.0033
270	1.41	1.04	0.627	0.302	0.177	0.116
	±0.01	±0.009	±0.006	±0.003	±0.002	±0.001
	±0.031	±0.024	±0.015	±0.0078	±0.0047	±0.0032
260	1.44	1.05	0.639	0.308	0.181	0.119
	±0.01	±0.01	±0.006	±0.003	±0.002	±0.001
	±0.031	±0.024	±0.016	±0.008	±0.0049	±0.0033
250	1.38	1.01	0.61	0.293	0.172	0.113
	±0.01	±0.009	±0.006	±0.003	±0.002	±0.001
	±0.03	±0.023	±0.015	±0.0077	±0.0046	±0.0031
240	1.36	0.996	0.604	0.291	0.171	0.113
	±0.01	±0.009	±0.006	±0.003	±0.002	±0.001
	±0.03	±0.023	±0.015	±0.0077	±0.0047	±0.0031
230	1.34	0.98	0.593	0.285	0.167	0.11
	±0.03	±0.02	±0.006	±0.003	±0.002	±0.001
	±0.029	±0.023	±0.015	±0.0075	±0.0046	±0.0031
220	1.26	0.922	0.558	0.268	0.157	0.103
	±0.01	±0.009	±0.005	±0.003	±0.001	±0.001
	±0.028	±0.022	±0.014	±0.0071	±0.0043	±0.0029
210	1.25	0.92	0.557	0.268	0.158	0.104
	±0.01	±0.009	±0.005	±0.003	±0.002	±0.001
	±0.028	±0.022	±0.014	±0.0072	±0.0044	±0.0029
200	1.21	0.889	0.54	0.26	0.153	0.101
	±0.01	±0.009	±0.005	±0.003	±0.002	±0.001
	±0.027	±0.021	±0.014	±0.007	±0.0043	±0.0029
190	1.08	0.788	0.476	0.228	0.134	0.0878
	±0.01	±0.008	±0.005	±0.002	±0.001	±0.0009
	±0.025	±0.019	±0.012	±0.0063	±0.0038	±0.0025
180	1.14	0.838	0.506	0.243	0.142	0.0935
	±0.01	±0.008	±0.005	±0.002	±0.001	±0.0009
	±0.026	±0.02	±0.013	±0.0066	±0.004	±0.0027
170	1.01	0.738	0.446	0.214	0.126	0.0826
	±0.01	±0.008	±0.005	±0.002	±0.001	±0.0009
	±0.024	±0.018	±0.012	±0.006	±0.0036	±0.0024
160	0.868	0.634	0.381	0.182	0.106	0.0697
	±0.01	±0.007	±0.004	±0.002	±0.001	±0.0008
	±0.021	±0.016	±0.01	±0.0052	±0.0032	±0.0021
150	0.818	0.6	0.362	0.174	0.102	0.067
	±0.009	±0.007	±0.004	±0.002	±0.001	±0.0008
	±0.02	±0.015	±0.01	±0.0051	±0.0031	±0.0021
140	0.648	0.472	0.283	0.135	0.0785	0.0514
	±0.01	±0.01	±0.006	±0.003	±0.002	±0.001
	±0.021	±0.016	±0.011	±0.0053	±0.0032	±0.0021
130	0.571	0.416	0.25	0.119	0.0694	0.0454
	±0.01	±0.009	±0.006	±0.003	±0.002	±0.001
	±0.02	±0.015	±0.0096	±0.0049	±0.0029	±0.002
120	0.506	0.369	0.222	0.106	0.0617	0.0404
	±0.01	±0.009	±0.005	±0.003	±0.001	±0.001
	±0.018	±0.014	±0.0088	±0.0045	±0.0027	±0.0018
90	0.249	0.182	0.109	0.0518	0.0302	0.0197
	±0.008	±0.006	±0.004	±0.002	±0.001	±0.0007
	±0.01	±0.008	±0.0051	±0.0026	±0.0016	±0.001
80	0.203	0.148	0.0893	0.0427	0.025	0.0164
	±0.008	±0.006	±0.003	±0.002	±0.001	±0.0006
	±0.009	±0.007	±0.0045	±0.0023	±0.0014	±0.00092

TABLE C.4: The efficiency, in percent, of the Loose-Loose photon selection and $E_{\mathrm{T}}^{\mathrm{miss}}$ cut for the 8 TeV signal grid, for neutralino lifetimes beyond 20 ns.

Appendix D

$E_{\mathrm{T}}^{\mathrm{miss}}$ Systematic Uncertainty

In this section more information is provided regarding the method used to estimate the systematic uncertainty on the $E_{\mathrm{T}}^{\mathrm{miss}}$ measurement in the 7 TeV analysis. This method follows the recipe developed by the prompt analysis [135][136] with three separate sources of uncertainty considered. These sources are described below and the systematic uncertainty is then given separately for every signal grid point in the tables that follow.

Topocluster Energy Scale

The uncertainty on the energy scale of the clusters used during particle identification and reconstruction is estimated by comparing energy and momentum measurements in data and MC [147]. This uncertainty is calculated by multiplying the topocluster energy by the following correction factor c:

$$c = \begin{cases} 1 \pm a \times \left(1 + \frac{b}{p_{\mathrm{T}}}\right) & |\eta_{clus}| < 2.3 \\ 1 \pm \sqrt{\left(a \times \left(1 + \frac{b}{p_{\mathrm{T}}}\right)\right)^2 + 0.05^2} & 2.3 < |\eta_{clus}| < 3.2 \\ 1 \pm \sqrt{\left(a \times \left(1 + \frac{b}{p_{\mathrm{T}}}\right)\right)^2 + 0.15^2} & 3.2 < |\eta_{clus}| < 4.5 \end{cases} \tag{D.1}$$

where $a = 5\%$, $b = 1.5$, and p_{T} is in GeV. This gives an uncertainty of approximately 20% for p_{T} in the sub-GeV energy range and approximately 5% for high p_{T} clusters.

$E_{\mathrm{T}}^{\mathrm{miss}}$ Resolution

The $E_{\mathrm{T}}^{\mathrm{miss}}$ resolution can be described by the function $\sigma\left(E_x^{miss}, E_y^{miss}\right) = \alpha\sqrt{\sum E_T}$ where α is the resolution parameter. A value of $\alpha = 0.49$ is measured from minimum bias events at $\sqrt{s} = 7$ TeV, and as $\alpha = 0.53$ when requiring at least one jet with $p_{\mathrm{T}} > 20$ GeV [148]. This uncertainty was estimated to be 14% [8].

Muon terms in $E_{\mathrm{T}}^{\mathrm{miss}}$

Studies [135][136] have shown that uncertainties on the p_{T} of muons have a negligible impact on the $E_{\mathrm{T}}^{\mathrm{miss}}$ of diphoton events.

Lambda (TeV)	τ (ps)	$E_{\mathrm{T}}^{\mathrm{miss}}$ Scale Fractional error	$E_{\mathrm{T}}^{\mathrm{miss}}$ Resolution Fractional error
70	100000	0.023	0.003
70	10000	0.061	0.12
70	1000	0.048	0.02
70	12000	0.060	0.01
70	14000	0.059	0.009
70	16000	0.058	0.008
70	18000	0.056	0.007
70	20000	0.055	0.006
70	2000	0.053	0.020
70	22000	0.053	0.005
70	24000	0.052	0.004
70	250	0.042	0.03
70	26000	0.050	0.004
70	30000	0.047	0.003
70	3000	0.057	0.02
70	35000	0.044	0.001
70	40000	0.042	0.00007
70	4000	0.059	0.02
70	45000	0.039	0.0007
70	5000	0.061	0.017
70	500	0.045	0.02
70	55000	0.035	0.002
70	60000	0.033	0.002
70	6000	0.062	0.02
70	65000	0.031	0.002
70	70000	0.030	0.002
70	7000	0.062	0.015
70	75000	0.028	0.003
70	750	0.046	0.022
70	80000	0.027	0.003
70	8000	0.062	0.014
70	90000	0.025	0.003
70	9000	0.062	0.0.13
80	100000	0.029	0.030
80	10000	0.051	0.028
80	1000	0.049	0.027
80	12000	0.050	0.029
80	14000	0.049	0.030
80	16000	0.049	0.031
80	18000	0.048	0.032
80	20000	0.047	0.032
80	2000	0.051	0.023
80	22000	0.047	0.033
80	24000	0.046	0.033
80	250	0.055	0.048
80	26000	0.045	0.034
80	30000	0.044	0.034
80	3000	0.052	0.023
80	35000	0.042	0.035
80	40000	0.041	0.035
80	4000	0.052	0.023
80	45000	0.040	0.035
80	5000	0.052	0.024
80	500	0.050	0.038
80	55000	0.037	0.034
80	60000	0.036	0.034
80	6000	0.052	0.025
80	65000	0.035	0.034
80	70000	0.034	0.033
80	7000	0.052	0.026
80	75000	0.033	0.033
80	750	0.049	0.031
80	80000	0.032	0.032
80	8000	0.052	0.026
80	90000	0.030	0.031
80	9000	0.051	0.027

TABLE D.1: Signal grid systematic errors due to the $E_{\mathrm{T}}^{\mathrm{miss}}$ scale and resolution uncertainties, for $\Lambda = 70, 80$TeV [57].

Lambda (TeV)	τ (ps)	$E_{\mathrm{T}}^{\mathrm{miss}}$ Scale Fractional error	$E_{\mathrm{T}}^{\mathrm{miss}}$ Resolution Fractional error
90	100000	0.062	0.034
90	10000	0.045	0.020
90	1000	0.053	0.014
90	12000	0.047	0.020
90	14000	0.048	0.020
90	16000	0.049	0.020
90	18000	0.050	0.020
90	20000	0.051	0.021
90	2000	0.051	0.012
90	22000	0.052	0.021
90	24000	0.052	0.021
90	250	0.030	0.016
90	26000	0.053	0.022
90	30000	0.054	0.022
90	35000	0.055	0.023
90	40000	0.056	0.024
90	4000	0.046	0.016
90	45000	0.057	0.025
90	500	0.040	0.023
90	55000	0.058	0.027
90	60000	0.059	0.028
90	6000	0.042	0.020
90	65000	0.059	0.029
90	70000	0.060	0.030
90	75000	0.060	0.031
90	750	0.043	0.022
90	80000	0.060	0.031
90	8000	0.044	0.020
90	90000	0.061	0.033
100	100000	0.065	0.035
100	10000	0.056	0.013
100	1000	0.042	0.018
100	12000	0.057	0.013
100	14000	0.057	0.014
100	16000	0.057	0.015
100	18000	0.058	0.015
100	20000	0.058	0.016
100	2000	0.039	0.016
100	22000	0.058	0.016
100	24000	0.058	0.017
100	250	0.004	0.00
100	26000	0.059	0.018
100	30000	0.059	0.019
100	35000	0.060	0.020
100	40000	0.060	0.021
100	4000	0.048	0.009
100	45000	0.060	0.023
100	500	0.020	0.002
100	55000	0.061	0.025
100	60000	0.062	0.027
100	6000	0.054	0.013
100	65000	0.062	0.028
100	70000	0.063	0.029
100	75000	0.063	0.030
100	750	0.026	0.005
100	80000	0.063	0.031
100	8000	0.055	0.013
100	90000	0.064	0.033

TABLE D.2: Signal grid systematic errors due to the $E_{\mathrm{T}}^{\mathrm{miss}}$ scale and resolution uncertainties, for $\Lambda = 90, 100$TeV [57].

Lambda (TeV)	τ (ps)	$E_{\mathrm{T}}^{\mathrm{miss}}$ Scale Fractional error	$E_{\mathrm{T}}^{\mathrm{miss}}$ Resolution Fractional error
110	100000	0.047	0.00
110	10000	0.045	0.002
110	1000	0.037	0.014
110	12000	0.046	0.002
110	14000	0.046	0.002
110	16000	0.046	0.001
110	18000	0.046	0.001
110	20000	0.046	0.001
110	2000	0.038	0.013
110	22000	0.046	0.000
110	24000	0.046	0.000
110	250	0.036	0.011
110	26000	0.046	0.000
110	30000	0.046	0.000
110	35000	0.046	0.00
110	40000	0.046	0.00
110	4000	0.038	0.021
110	45000	0.046	0.00
110	500	0.035	0.009
110	55000	0.046	0.00
110	60000	0.046	0.00
110	6000	0.045	0.004
110	65000	0.046	0.00
110	70000	0.046	0.00
110	75000	0.046	0.00
110	750	0.035	0.010
110	80000	0.046	0.00
110	8000	0.044	0.001
110	90000	0.046	0.00
120	10000	0.039	0.006
120	1000	0.027	0.012
120	15000	0.028	0.015
120	20000	0.027	0.015
120	2000	0.034	0.011
120	22000	0.027	0.015
120	24000	0.027	0.015
120	250	0.035	0.028
120	26000	0.027	0.015
120	28000	0.027	0.015
120	30000	0.027	0.014
120	35000	0.026	0.014
120	40000	0.026	0.014
120	4000	0.036	0.019
120	45000	0.026	0.014
120	500	0.033	0.019
120	55000	0.025	0.013
120	60000	0.025	0.013
120	6000	0.028	0.016
120	65000	0.024	0.013
120	70000	0.024	0.013
120	75000	0.024	0.012
120	750	0.033	0.016
120	80000	0.023	0.012
120	8000	0.028	0.016

TABLE D.3: Signal grid systematic errors due to the $E_{\mathrm{T}}^{\mathrm{miss}}$ scale and resolution uncertainties, for $\Lambda = 110, 120\mathrm{TeV}$ [57].

Lambda (TeV)	τ (ps)	$E_{\mathrm{T}}^{\mathrm{miss}}$ Scale Fractional error	$E_{\mathrm{T}}^{\mathrm{miss}}$ Resolution Fractional error
130	10000	0.038	0.008
130	1000	0.031	0.016
130	12000	0.038	0.007
130	14000	0.039	0.007
130	16000	0.040	0.006
130	18000	0.040	0.006
130	20000	0.041	0.005
130	2000	0.029	0.006
130	22000	0.042	0.005
130	24000	0.042	0.005
130	250	0.022	0.005
130	26000	0.043	0.004
130	28000	0.043	0.004
130	30000	0.044	0.004
130	35000	0.045	0.003
130	40000	0.046	0.003
130	4000	0.030	0.014
130	45000	0.047	0.002
130	500	0.024	0.007
130	55000	0.049	0.002
130	60000	0.050	0.001
130	6000	0.036	0.009
130	65000	0.051	0.001
130	70000	0.052	0.001
130	75000	0.053	0.001
130	750	0.025	0.007
130	80000	0.053	0.001
130	8000	0.037	0.008
140	10000	0.036	0.011
140	1000	0.027	0.010
140	12000	0.036	0.011
140	14000	0.036	0.010
140	16000	0.036	0.010
140	18000	0.036	0.009
140	20000	0.036	0.009
140	2000	0.032	0.011
140	22000	0.036	0.009
140	24000	0.036	0.008
140	250	0.016	0.010
140	26000	0.036	0.008
140	30000	0.036	0.007
140	3000	0.034	0.012
140	35000	0.036	0.007
140	40000	0.035	0.006
140	4000	0.035	0.012
140	45000	0.035	0.006
140	5000	0.035	0.012
140	500	0.022	0.010
140	55000	0.035	0.005
140	60000	0.035	0.004
140	6000	0.036	0.012
140	65000	0.035	0.004
140	70000	0.034	0.004
140	7000	0.036	0.012
140	75000	0.034	0.003
140	750	0.025	0.010
140	80000	0.034	0.003
140	8000	0.036	0.012
140	9000	0.036	0.011

TABLE D.4: Signal grid systematic errors due to the $E_{\mathrm{T}}^{\mathrm{miss}}$ scale and resolution uncertainties, for $\Lambda = 130, 140$TeV [57].

Lambda (TeV)	τ (ps)	$E_{\mathrm{T}}^{\mathrm{miss}}$ Scale Fractional error	$E_{\mathrm{T}}^{\mathrm{miss}}$ Resolution Fractional error
150	10000	0.031	0.017
150	1000	0.023	0.008
150	12000	0.032	0.018
150	14000	0.032	0.018
150	16000	0.032	0.019
150	18000	0.033	0.019
150	20000	0.033	0.019
150	2000	0.025	0.009
150	22000	0.033	0.019
150	24000	0.033	0.019
150	250	0.016	0.007
150	26000	0.033	0.019
150	30000	0.033	0.019
150	3000	0.027	0.011
150	35000	0.033	0.019
150	40000	0.032	0.019
150	4000	0.028	0.012
150	45000	0.032	0.018
150	5000	0.029	0.013
150	500	0.020	0.008
150	55000	0.031	0.018
150	60000	0.031	0.017
150	6000	0.029	0.014
150	65000	0.030	0.017
150	70000	0.030	0.017
150	7000	0.030	0.015
150	75000	0.030	0.016
150	750	0.022	0.008
150	80000	0.029	0.016
150	8000	0.031	0.016
150	9000	0.031	0.016
160	10000	0.018	0.009
160	1000	0.018	0.002
160	12000	0.018	0.010
160	14000	0.019	0.010
160	16000	0.019	0.010
160	18000	0.020	0.010
160	20000	0.020	0.010
160	2000	0.018	0.005
160	22000	0.021	0.010
160	24000	0.022	0.010
160	250	0.024	0.01
160	26000	0.023	0.010
160	30000	0.024	0.010
160	3000	0.018	0.006
160	35000	0.026	0.010
160	40000	0.028	0.010
160	4000	0.018	0.007
160	45000	0.030	0.010
160	5000	0.017	0.008
160	500	0.019	0.00
160	55000	0.034	0.009
160	60000	0.036	0.009
160	6000	0.017	0.008
160	65000	0.039	0.009
160	70000	0.041	0.009
160	7000	0.017	0.009
160	75000	0.043	0.009
160	750	0.018	0.000
160	80000	0.045	0.009
160	8000	0.018	0.009
160	9000	0.018	0.009

TABLE D.5: Signal grid systematic errors due to the $E_{\mathrm{T}}^{\mathrm{miss}}$ scale and resolution uncertainties, for $\Lambda = 150, 160$TeV [57].

Lambda (TeV)	τ (ps)	$E_{\mathrm{T}}^{\mathrm{miss}}$ Scale Fractional error	$E_{\mathrm{T}}^{\mathrm{miss}}$ Resolution Fractional error
170	10000	0.017	0.012
170	1000	0.018	0.011
170	12000	0.017	0.013
170	14000	0.017	0.013
170	16000	0.018	0.013
170	18000	0.018	0.013
170	20000	0.018	0.013
170	2000	0.017	0.010
170	22000	0.019	0.013
170	24000	0.019	0.013
170	250	0.020	0.008
170	26000	0.020	0.013
170	30000	0.021	0.013
170	3000	0.017	0.010
170	4000	0.017	0.011
170	5000	0.017	0.011
170	500	0.020	0.012
170	6000	0.017	0.011
170	7000	0.017	0.012
170	750	0.019	0.011
170	8000	0.017	0.012
170	9000	0.017	0.012
180	10000	0.017	0.002
180	1000	0.018	0.008
180	12000	0.017	0.001
180	14000	0.016	0.000
180	16000	0.016	0.00
180	18000	0.016	0.00
180	20000	0.016	0.00
180	2000	0.018	0.008
180	22000	0.016	0.00
180	24000	0.016	0.00
180	250	0.020	0.010
180	26000	0.016	0.00
180	30000	0.016	0.00
180	3000	0.018	0.008
180	4000	0.018	0.007
180	5000	0.017	0.006
180	500	0.019	0.009
180	6000	0.017	0.005
180	7000	0.017	0.004
180	750	0.018	0.008
180	8000	0.017	0.003
180	9000	0.017	0.003

TABLE D.6: Signal grid systematic errors due to the $E_{\mathrm{T}}^{\mathrm{miss}}$ scale and resolution uncertainties, for $\Lambda = 170, 180$TeV [57].

Lambda (TeV)	τ (ps)	$E_{\mathrm{T}}^{\mathrm{miss}}$ Scale Fractional error	$E_{\mathrm{T}}^{\mathrm{miss}}$ Resolution Fractional error
190	10000	0.019	0.004
190	1000	0.015	0.006
190	12000	0.019	0.004
190	14000	0.019	0.004
190	16000	0.019	0.004
190	18000	0.019	0.005
190	20000	0.019	0.005
190	2000	0.017	0.007
190	22000	0.019	0.006
190	24000	0.018	0.006
190	250	0.013	0.00
190	26000	0.018	0.007
190	30000	0.018	0.008
190	3000	0.018	0.006
190	4000	0.018	0.006
190	5000	0.019	0.005
190	500	0.013	0.004
190	6000	0.019	0.005
190	7000	0.019	0.004
190	750	0.014	0.006
190	8000	0.019	0.004
190	9000	0.019	0.004
200	10000	0.019	0.000
200	1000	0.014	0.004
200	12000	0.019	0.00
200	14000	0.019	0.00
200	16000	0.019	0.00
200	18000	0.018	0.00
200	20000	0.018	0.00
200	2000	0.017	0.007
200	22000	0.018	0.01
200	24000	0.018	0.01
200	250	0.011	0.00
200	26000	0.018	0.01
200	30000	0.018	0.01
200	3000	0.018	0.007
200	4000	0.018	0.006
200	5000	0.019	0.005
200	500	0.012	0.001
200	6000	0.019	0.004
200	7000	0.019	0.003
200	750	0.013	0.003
200	8000	0.019	0.002
200	9000	0.019	0.001
210	10000	0.012	0.003
210	1000	0.015	0.006
210	12000	0.012	0.003
210	14000	0.012	0.002
210	16000	0.012	0.002
210	18000	0.012	0.002
210	20000	0.012	0.002
210	2000	0.014	0.005
210	22000	0.012	0.002
210	24000	0.012	0.002
210	250	0.010	0.001
210	26000	0.012	0.002
210	30000	0.012	0.002
210	3000	0.014	0.005
210	4000	0.013	0.004
210	5000	0.013	0.004
210	500	0.014	0.004
210	6000	0.013	0.004
210	7000	0.013	0.003
210	750	0.015	0.005
210	8000	0.013	0.003
210	9000	0.012	0.003

TABLE D.7: Signal grid systematic errors due to the $E_{\mathrm{T}}^{\mathrm{miss}}$ scale and resolution uncertainties, for $\Lambda = 190, 200, 210$TeV [57].

Appendix E

7 TeV Signal Region Outlier

In section 9.1.2, an event containing a photon detected with $z_\gamma = 752$ mm was discussed. Figure E.1 is the event display for this event and the shower shape of this 'outlier' is displayed in the central panel at the bottom of the figure. It can be seen that the shower in the first layer of the EM calorimeter is fairly wide with two distinct peaks, which causes the photon to fail the Tight IsEM cuts. This shower is what would be expected if the object was a jet with a leading π^0, which decays to two photons, faking a Loose photon. This conclusion is supported by the timing information: a t_γ of 0.2 ps suggests that this object was promptly produced.

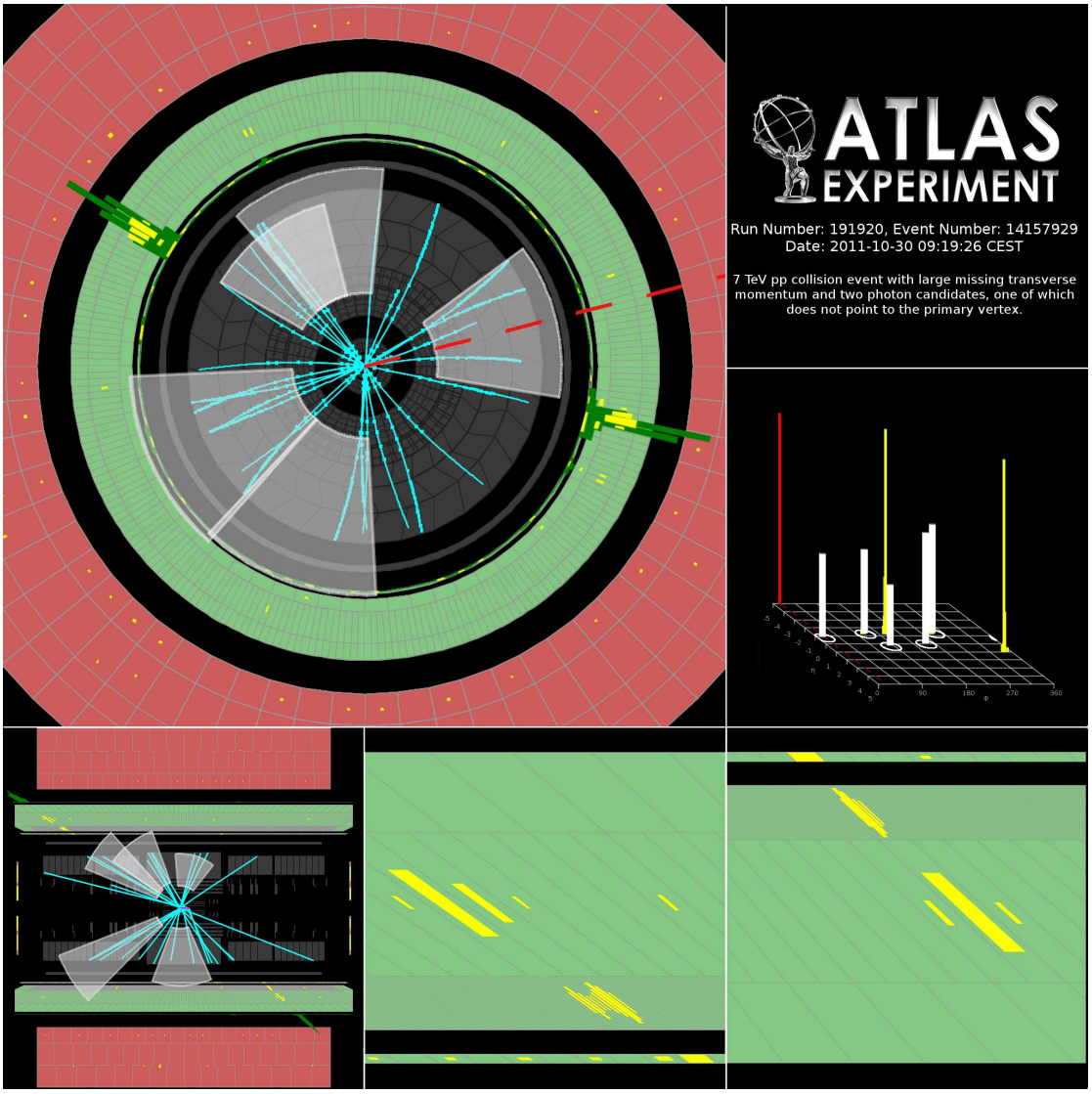

FIGURE E.1: Event display for run number 191920, event number 14157929. The middle panel at the bottom of the figure shows the shower shape of the photon detected with $z_\gamma = 752$ mm [57].

Bibliography

[1] ATLAS Collaboration, *Search for non-pointing photons in the diphoton and E_T^{miss} final state in $\sqrt{s}$ = 7 TeV proton-proton collisions using the ATLAS detector*, Phys. Rev. D **88** no. arXiv:1304.6310. CERN-PH-EP-2013-049, (2013) 012001. 26 p.

[2] ATLAS Collaboration, *Search for non-pointing and delayed photons in the diphoton and missing transverse momentum final state in 8 TeV pp collisions at the LHC using the ATLAS detector*, Phys. Rev. D **90** no. arXiv:1409.5542. CERN-PH-EP-2014-215, (2014) 112005. 16 p.

[3] E. D. Bloom et al., *High-Energy Inelastic e p Scattering at 6-Degrees and 10-Degrees*, Phys.Rev.Lett. **23** (1969) 930–934.

[4] M. Breidenbach et al., *Observed Behavior of Highly Inelastic electron-Proton Scattering*, Phys.Rev.Lett. **23** (1969) 935–939.

[5] Super-Kamiokande Collaboration, *Evidence For Oscillation Of Atmospheric Neutrinos*, Phys. Rev. Lett. **81** no. hep-ex/9807003. ICRR-422. BU-98-17. KEK-98-95. 8, (1998) 1562. `http://cds.cern.ch/record/473368`.

[6] Particle Data Group. Berkeley Collaboration, Beringer, J. et al., *Review of Particle Physics, 2012-2013. Review of Particle Properties*, Phys. Rev. D **86** no. 1, (2012) 177–198. `http://cds.cern.ch/record/1481544`.

[7] L. Canetti, M. Drewes, and M. Shaposhnikov, *Matter and Antimatter in the Universe*, New J.Phys. **14** (2012) 095012, `arXiv:1204.4186 [hep-ph]`.

[8] ATLAS Collaboration, G. Aad et al., *Search for diphoton events with large missing transverse momentum in 7 TeV proton-proton collision data with the ATLAS detector*, `arXiv:1209.0753 [hep-ex]`.

[9] S. L. Glashow, *Partial-symmetries of weak interactions*, Nuclear Physics 22 (1961)579 – 588.

[10] S. Weinberg, *Elementary particle theory of composite particles*, Phys. Rev 130 (1963)776–783.

[11] S. Weinberg, *A model of leptons*, Phys. Rev Lett 19 (1967)1264–1266.

[12] M. Gell-Mann, *A schematic model of baryons and mesons*, Phys. Rev Lett 8 (1964)579–588.

[13] G. Zweig, *An SU3 model for strong interaction symmetry and its breaking; Version 1*, Tech. Reo. CERN-TH-401, CERN (1964).

[14] A. Salam, *Elementary Particle Theory*, p. 367. Stockholm, 1969.

[15] P. Higgs, *Broken symmetries, massless particles and gauge fields*, Physics Letters 12 (1964) no.2132–133.

[16] F. Englert and R. Brout, *Broken symmetry and the Mass of Gauge Vector Mesons*, Physics Letters 13 (1964)321–323.

[17] G. S. Guralnik, C. R. Hagen, and T. W. B. Kibble, *Global Conservation Laws and Massless Particles*, Physics Letters 13585–587.

[18] Particle Data Group Collaboration, Olive, K. A. et al.

[19] E. Noether, *Invariant Variation Problems*, Gott.Nachr. **1918** (1918) 235–257, `arXiv:physics/0503066 [physics]`.

[20] Particle Data Group Collaboration, K. Olive et al., *Review of Particle Physics*, Chin.Phys. **C38** (2014) 090001.

[21] ATLAS Collaboration, *Observation of a new particle in the search for the Standard Model Higgs boson with the ATLAS detector at the LHC*, Phys. Lett. B **716** no. arXiv:1207.7214. CERN-PH-EP-2012-218, (2012) 1–29. 39 p. Comments: 24 pages plus author list (38 pages total), 12 figures, 7 tables, revised author list.

[22] CMS Collaboration, *Observation of a new boson at a mass of 125 GeV with the CMS experiment at the LHC*, Phys. Lett. B **716** no. arXiv:1207.7235. CMS-HIG-12-028. CERN-PH-EP-2012-220, (2012) 30–61. 59 p.

[23] A. Djouadi, *The anatomy of electroweak symmetry breaking Tome II: The Higgs bosons in the Minimal Supersymmetric Model*, Physics Reports**Volume 459, Issues 16** 1–241.

[24] V. Rubin, N. Thonnard, and J. Ford, W.K., *Rotational properties of 21 SC galaxies with a large range of luminosities and radii, from NGC 4605 /R = 4kpc/ to UGC 2885 /R = 122 kpc/*, Astrophys.J. **238** (1980) 471.

[25] R. Massey, T. Kitching, and J. Richard, *The dark matter of gravitational lensing*, Rept.Prog.Phys. **73** (2010) 086901, `arXiv:1001.1739 [astro-ph.CO]`.

[26] Blumenthal, G., *Formation of Galaxies and Large Scale Structure with Cold Dark Matter*, Nature **311** (1984) 517–525.

[27] Planck Collaboration, P. Ade et al., *Planck 2013 results. I. Overview of products and scientific results*, Astron.Astrophys. **571** (2014) A1, `arXiv:1303.5062 [astro-ph.CO]`.

[28] Askew, A. et al, *Searching for Dark Matter at Hadron Colliders*, Int. J. Mod. Phys. A **29** no. arXiv:1406.5662, (2014) 1430041. mult. p.

[29] M. Schumann, *Dark Matter 2013*, Tech. Rep. arXiv:1310.5217, Oct, 2013. Comments: 9 pages, 7 figures. To appear in the proceedings of ICRC 2013.

[30] P. Ramond, Phys. Rev. D **3**, 2415 (1971); A. Neveu and J.H. Schwarz, Nucl. Phys. B **31**, 86 (1971); J.L. Gervais and B. Sakita, Nucl. Phys. B **34**, 632 (1971).

[31] Yu. A. Golfand and E. P. Likhtman, JETP Lett. **13**, 323 (1971).

[32] J. Wess and B. Zumino, Nucl. Phys. B **70** (1974) 39.

[33] D.V. Volkov and V.P. Akulov, Phys. Lett. B **46**, 109 (1973).

[34] S. P. Martin, *A Supersymmetry primer*, Adv.Ser.Direct.High Energy Phys. **21** (2010) 1–153, `arXiv:hep-ph/9709356 [hep-ph]`.

[35] J. Wess and J. Bagger, *Supersymmetry and Supergravity.* Princeton Series in Physics, New Jersey, 1992.

[36] S. Martin, *Perspectives on Supersymmetr.* World Scientific, Singapore, 1998. `hep-ph/9709356`.

[37] P. B. Pal, *Dirac, Majorana and Weyl fermions*, Am. J. Phys. **79** (2011) 485–498, arXiv:1006.1718 [hep-ph].

[38] L. Brink, S. Deser, B. Zumino, P. Di Vecchia, and P. S. Howe, *Local Supersymmetry for Spinning Particles*, Phys.Lett. **B64** (1976) 435.

[39] A. H. Chamseddine, R. L. Arnowitt, and P. Nath, *Locally Supersymmetric Grand Unification*, Phys.Rev.Lett. **49** (1982) 970.

[40] P. Nath and R. L. Arnowitt, *Generalized Supergauge Symmetry as a New Framework for Unified Gauge Theories*, Phys.Lett. **B56** (1975) 177.

[41] Super-Kamiokande Collaboration, K. Abe et al., *Search for Proton Decay via $p \to \nu K^+$ using 260 kiloton·year data of Super-Kamiokande*, Phys.Rev. **D90** (2014) 072005, arXiv:1408.1195 [hep-ex].

[42] G. R. Farrar and P. Fayet, *Phenomenology of the Production, Decay, and Detection of New Hadronic States Associated with Supersymmetry*, Phys.Lett. **B76** (1978) 575–579.

[43] *Summary of ATLAS Supersymmetry public results including links to journal articles*,.

[44] *Summary of CMS Supersymmetry public results including links to journal articles*,.

[45] S. K. Dimopoulos and H. M. Georgi, *Softly broken supersymmetry and SU(5)*, Nucl. Phys. B **193** no. HUTP-81-A-022, (1981) 150. 25 p.

[46] J. L. Daz-Cruz, *The Supersymmetric Flavor Problem*, AIP Conf. Proc. **917** (2007) 277–284.

[47] F. Quevedo, S. Krippendorf, and O. Schlotterer, *Cambridge Lectures on Supersymmetry and Extra Dimensions*, arXiv:1011.1491 [hep-th].

[48] C. F. Kolda, *Gauge mediated supersymmetry breaking: Introduction, review and update*, Nucl.Phys.Proc.Suppl. **62** (1998) 266–275, arXiv:hep-ph/9707450 [hep-ph].

[49] L. O'Raifeartaigh, *Spontaneous symmetry breaking for chiral scalar superfields*, Nucl. Phys. B **96** no. DIAS-TP-75-9, (1975) 331. 31 p.

[50] P. Fayet and J. Iliopoulos, *Spontaneously Broken Supergauge Symmetries and Goldstone Spinors*, Phys.Lett. **B51** (1974) 461–464.

[51] D. Gorbunov, A. Khmelnitsky, and V. Rubakov, *Is gravitino still a warm dark matter candidate?*, J. High Energy Phys. **12** no. arXiv:0805.2836. INR-TH-05-08-18, (2008) 055. 16 p. Comments: 16 pages, 4 figures.

[52] N. Okada, *SuperWIMP dark matter and 125 GeV Higgs boson in the minimal GMSB*, Tech. Rep. arXiv:1205.5826, May, 2012. Comments: 4 pages, 2 figures.

[53] P. Bode, J. P. Ostriker, and N. G. Turok, *Halo Formation in Warm Dark Matter Models*, Astrophys. J. **556** no. astro-ph/0010389. 20, (2001) 93–107.

[54] N. E. Bomark and L. Roszkowski, *The 3.5 keV X-ray line from decaying gravitino dark matter*, Tech. Rep. arXiv:1403.6503, Mar, 2014. Comments: 8 pages Latex.

[55] S. P. Martin, *Generalized messengers of supersymmetry breaking and the sparticle mass spectrum*, Phys. Rev. D **55** no. hep-ph/9608224. 5, (1997) 3177.

[56] B. Allanach et al., *The Snowmass points and slopes: Benchmarks for SUSY searches*, Eur.Phys.J. **C25** (2002) 113–123, `arXiv:hep-ph/0202233 [hep-ph]`.

[57] Bhandari, R. et al, *Search for non-pointing photons in the diphoton and E_T^{miss} final state in $\sqrt{s} = 7$ TeV pp collisions at the LHC using the ATLAS detector*, Tech. Rep. ATL-PHYS-INT-2013-020, CERN, Geneva, Oct, 2013.

[58] *Collection of Feynman diagrams produced by the ATLAS SUSY group*,.

[59] S. Burdin et al., *Search for non-pointing photons in the diphoton and $E_{\mathrm{T}}^{\mathrm{miss}}$ final state in $\sqrt{s} = 8$ TeV pp collisions at the LHC using the ATLAS detector*, Tech. Rep. ATL-COM-PHYS-2014-203, CERN, Geneva, Mar, 2014.

[60] ATLAS Collaboration, *The ATLAS experiment at the CERN Large Hadron Collider*, JINST **3** (2008) S08003.

[61] Brning, O., *LHC Design Report*. CERN, Geneva, 2004.

[62] P. Lebrun, *Interim Summary Report on the Analysis of the 19 September 2008 Incident at the LHC*, tech. rep. `https://edms.cern.ch/file/973073/1/Report_on_080919_incident_at_LHC__2_.pdf`.

[63] UA1 Collaboration, *Experimental observation of isolated large transverse energy electrons with associated missing energy at $\sqrt{s} = 540$ GeV*,.

[64] UA1 Collaboration, *Experimental observation of lepton pairs of invariant mass around 95 GeV/c^2 at the CERN SPS collider*,.

[65] https://bigscience.web.cern.ch/bigscience/en/lhc/lhc2.html.

[66] ATLAS Collaboration, *Improved luminosity determination in pp collisions at $\sqrt{s}$ = 7 TeV using the ATLAS detector at the LHC*, Eur. Phys. J. C **73** no. arXiv:1302.4393. CERN-PH-EP-2013-026, (2013) 2518. 40 p.

[67] ATLAS Collaboration, *ATLAS public results on luminosity measurements*,. `https://twiki.cern.ch/twiki/bin/view/AtlasPublic/LuminosityPublicResults`.

[68] ATLAS Collaboration, *ATLAS public results: stand-alone event displays*,. `https://twiki.cern.ch/twiki/bin/view/AtlasPublic/EventDisplayStandAlone`.

[69] A. Jeff, C. Welsch, and A. Boccardi, *A Longitudinal Density Monitor for the LHC*. PhD thesis, Liverpool U., Dec, 2012.

[70] Boccardi, A. et al, *LHC Luminosity calibration using the Longitudinal Density Monitor*,.

[71] http://www.quantumdiaries.org/wp-content/uploads/2011/05/exp magnets.png.

[72] ATLAS Collaboration, *The ATLAS Inner Detector and commissioning and calibration*, Eur.Phys.J.C70:787-821,2010 **C70** (2010) 362–365, `arXiv:1004.5293 [physics.ins-det]`.

[73] A. Parker et al., *The material budget of the ATLAS Inner Detector*,.

[74] ATLAS Collaboration, *Energy Linearity and Resolution of the ATLAS Electromagnetic Barrel Calorimeter in an Electron Test-Beam*, Nucl. Instrum. Methods Phys. Res., A **568** no. physics/0608012, (2006) 601–623. `http://cds.cern.ch/record/976098`.

[75] ATLAS Collaboration, *Observation of an excess of events in the search for the Standard Model Higgs boson in the gamma-gamma channel with the ATLAS detector*, Tech. Rep. ATLAS-CONF-2012-091, CERN, Geneva, Jul, 2012.

[76] W. E. Cleland and E. G. Stern, *Signal Processing Considerations for Liquid Ionization Calorimeters in a High Rate Environment*, Nucl. Instrum. Methods Phys. Res., A **338** (1994) 467–497.

[77] ATLAS Collaboration, *ATLAS muon spectrometer: Technical Design Report.* Technical Design Report ATLAS. CERN, Geneva, 1997. `https://cds.cern.ch/record/331068`.

[78] ATLAS Collaboration, *Reconstruction of Photon Conversions, in Expected Performance of the ATLAS Experiment: Detector, Trigger and Physics*,.

[79] ATLAS Collaboration, *The ATLAS Level-1 Calorimeter Trigger*, JINST **3** (2008) P03001.

[80] N. Ellis, *Trigger and data acquisition*, `arXiv:1010.2942 [physics.ins-det]`.

[81] J. Pequenao and P. Schaffner, "An computer generated image representing how atlas detects particles." Jan, 2013.

[82] Cornelissen, T. et al, *Concepts, Design and Implementation of the ATLAS New Tracking (NEWT)*, Tech. Rep. ATL-SOFT-PUB-2007-007. ATL-COM-SOFT-2007-002, CERN, Geneva, Mar, 2007.

[83] D. Wicke, *A New Algorithm For Solving Track Ambiguities*, Tech. Rep. PROG 236 TRACK 92, 1998.

[84] ATLAS Collaboration, *Performance of primary vertex reconstruction in proton-proton collisions at* $\sqrt{s}$ *=7 TeV in the ATLAS experiment*, Tech. Rep. ATLAS-CONF-2010-069, CERN, Geneva, Jul, 2010.

[85] ATLAS Collaboration, *ATLAS public results on beam-spot measurements*,. `https://twiki.cern.ch/twiki/bin/view/AtlasPublic/BeamSpotPublicResults`.

[86] W. Lampl et al., *Calorimeter Clustering Algorithms: Description and Performance*, Tech. Rep. ATL-LARG-PUB-2008-002. ATL-COM-LARG-2008-003, CERN, Geneva, Apr, 2008.

[87] ATLAS Collaboration, *Expected performance of the ATLAS experiment: detector, trigger and physics.* CERN, Geneva, 2009.

[88] ATLAS Collaboration, *Measurements of the photon identification efficiency with the ATLAS detector using 4.9 fb^{-1} of pp collision data collected in 2011*, ATLAS-CONF-2012-123.

[89] ATLAS Collaboration, *Expected photon performance in the ATLAS experiment*, ATL-PHYS-PUB-2011-007. `https://cdsweb.cern.ch/record/1345329`.

[90] ATLAS Collaboration, *Electron reconstruction and identification efficiency measurements with the ATLAS detector using the 2011 LHC proton-proton collision data*, Eur.Phys.J. **C74** no. 7, (2014) 2941, `arXiv:1404.2240 [hep-ex]`.

[91] ATLAS Collaboration, *Electron performance measurements with the ATLAS detector using the 2010 LHC proton-proton collision data*, The European Physical Journal C **72** no. 3, (2012) 1–46. `http://dx.doi.org/10.1140/epjc/s10052-012-1909-1`.

[92] *Calibration recommendations for ATLAS analyses using the 7 TeV and 8 TeV datasets*,.

[93] ATLAS Collaboration, *Electron and photon reconstruction and identification in ATLAS: expected performance at high energy and results at 900 GeV*, Tech. Rep. ATLAS-CONF-2010-005, CERN, Geneva, Jun, 2010. `http://cds.cern.ch/record/1273197`.

[94] *Data/MC correction factors for photons*,.

[95] G. P. S. Matteo Cacciari and G. Soyez, *The anti-kt jet clustering algorithm*, JHEP04(2008)063.

[96] T. Lagouri et al., *A Muon Identification and Combined Reconstruction Procedure for the ATLAS Detector at the LHC at CERN*,. revised version number 1 submitted on 2003-10-30 18:34:15.

[97] D. Adams et al., *Track reconstruction in the ATLAS Muon Spectrometer with MOORE 007*, Tech. Rep. ATL-SOFT-2003-007, CERN, Geneva, May, 2003. revised version number 1 submitted on 2003-10-13 13:51:39.

[98] *ATLAS Muon Combined Performance Group Guidelines for Analyses of 7 TeV Data* ,.

[99] *ATLAS Muon Combined Performance Group Guidelines for Analyses of 8 TeV Data* ,.

[100] ATLAS Collaboration, *Performance of Missing Transverse Momentum Reconstruction in Proton-Proton Collisions at $\sqrt{s}$ = 7 TeV with ATLAS*, Eur. Phys. J. C **72** no. arXiv:1108.5602. CERN-PH-EP-2011-114, (2011) 1844. 33 p.

[101] Barillari, T. et al, *Local Hadronic Calibration*, Tech. Rep. ATL-LARG-PUB-2009-001-2. ATL-COM-LARG-2008-006. ATL-LARG-PUB-2009-001, CERN, Geneva, Jun, 2008.

[102] ATLAS Collaboration, *Performance of Missing Transverse Momentum Reconstruction in ATLAS studied in Proton-Proton Collisions recorded in 2012 at 8 TeV*, Tech. Rep. ATLAS-COM-CONF-2013-075, CERN, Geneva, Jun, 2013.

[103] ATLAS Collaboration, *The ATLAS Simulation Infrastructure*, Eur. Phys. J. C **70** no. arXiv:1005.4568. CERN-PH-EP-2010-044, (2010) 823–874. 53 p.

[104] GEANT4 Collaboration, *GEANT4: A Simulation toolkit*, Nucl. Instrum. Methods Phys. Res., A **506** no. CERN-IT-2002-003. SLAC-PUB-9350. 3, (2002) 250–303. 86 p.

[105] *Guidelines for Correctly Implementing the Extended Pileup Reweighting Corrections*,.

[106] Bahr, M. et al., *Herwig++ Physics and Manual*, Eur. Phys. J. C **58** no. arXiv:0803.0883. CAVENDISH-HEP-2008-03. CERN-PH-TH-2008-038. CP3-2008-05. DCPT-2008-22. IPPP-2008-11. KA-TP-2008-05. 4, (2008) 639–707. 143 p.

[107] A. Sherstnev and R. Thorne, *Parton Distributions for LO Generators*, Eur.Phys.J. **C55** (2008) 553–575, `arXiv:0711.2473 [hep-ph]`.

[108] H. Baer, H. et al and X. Tata, *ISAJET 7.69: A Monte Carlo event generator for pp, anti-p p, and e+e- reactions*, `arXiv:hep-ph/0312045 [hep-ph]`.

[109] N. Nikiforou and J. Parsons, *Timing Calibration of the Liquid Argon Electromagnetic Barrel Calorimeter and Timing Resolution Study of Electromagnetic Clusters Using 2011 Data*, Tech. Rep. ATL-COM-LARG-2012-003, CERN, Geneva, Mar, 2012.

[110] N. Nikiforou and J. Parsons, *Optimization of the Liquid Argon Calorimeter Timing Performance in the 2011 and 2012 pp Data*, Tech. Rep. ATL-COM-LARG-2014-004, CERN, Geneva, Mar, 2014.

[111] B. Cleland, N. Nikiforou, and J. Parsons, *Observation, Using Liquid Argon Calorimeter Timing, of Satellite-Satellite Collisions in the 2012 pp Dataset*, Tech. Rep. ATL-COM-LARG-2014-008, CERN, Geneva, Apr, 2014.

[112] Alasia, J. et al, *Search for a diphoton and E_T^{miss} final state in $\sqrt{s} = 7$ TeV pp collisions at the LHC using the ATLAS detector*, Tech. Rep. ATL-PHYS-INT-2011-095, CERN, Geneva, Nov, 2011.

[113] ATLAS Collaboration, *Performance of the ATLAS Electron and Photon Triggers in p-p Collisions at $\sqrt{s} = 8$ TeV in 2012*, Tech. Rep. ATL-COM-DAQ-2013-121, CERN, Geneva, Oct, 2013.

[114] *Recommendations for the Good Run Lists to be used by ATLAS Analyses*,.

[115] *Guidlines for Rejecting Bad Quality Clusters or Fake Clusters Originating from Calorimeter Problems*,.

[116] Asai, S. et al, *Search for Supersymmetry with jets and missing transverse momentum and one lepton at sqrt(s) = 7 TeV*,. `https://cds.cern.ch/record/1366095`.

[117] TOTEM Collaboration, *First measurement of the total proton-proton cross section at the LHC energy of s =7 TeV*, EPL **96** no. arXiv:1110.1395. CERN-PH-EP-2011-158. TOTEM-2011-02, (2011) 21002. 11 p. `http://cds.cern.ch/record/1383030`.

[118] ATLAS Collaboration, *Measurement of the inclusive $W^{\pm}$ and Z/γ cross sections in the electron and muon decay channels in pp collisions at $\sqrt{s} = 7$ TeV with the ATLAS detector*, Phys. Rev. D **85** no. arXiv:1109.5141. CERN-PH-EP-2011-143, (2011) 072004. 43 p. `http://cds.cern.ch/record/1385019`.

[119] ATLAS Collaboration, *Measurement of the inclusive isolated prompt photon cross-section in pp collisions at $\sqrt{s}$= 7 TeV using 35 pb^{-1} of ATLAS data*, Phys. Lett. B **706** no. arXiv:1108.0253. CERN-PH-EP-2011-115, (2011) 150–167. 19 p. `http://cds.cern.ch/record/1372177`.

[120] J. M. Campbell, J. W. Huston, and W. J. Stirling, *Hard Interactions of Quarks and Gluons: a Primer for LHC Physics*, Rep. Prog. Phys. **70** no. hep-ph/0611148, (2006) 89. 118 p.

[121] ATLAS Collaboration, *Performance of Missing Transverse Momentum Reconstruction in ATLAS with 2011 Proton-Proton Collisions at sqrts = 7 TeV*, Tech. Rep. ATLAS-CONF-2012-101, CERN, Geneva, Jul, 2012. `https://cds.cern.ch/record/1463915`.

[122] *Electron efficiency measurements with the ATLAS detector using the 2012 LHC proton-proton collision data*, Tech. Rep. ATLAS-CONF-2014-032, CERN, Geneva, Jun, 2014. `http://cds.cern.ch/record/1706245`.

[123] F. Alonso et al., *Search for a diphoton and $E_{\mathrm{T}}^{\mathrm{miss}}$ final state in $\sqrt{s} = 7$ TeV pp collisions at the LHC using the ATLAS detector*, Tech. Rep. ATL-COM-PHYS-2012-463, CERN, Geneva, Apr, 2012. `https://cds.cern.ch/record/1444875`.

[124] L. Moneta et al., *The RooStats Project*, PoS **ACAT2010** no. arXiv:1009.1003, (2010) 057. `http://cds.cern.ch/record/1289965`. Comments: 11 pages, 3 figures, ACAT2010 Conference Proceedings.

[125] A. L. Read, *Presentation of search results: The CL(s) technique*, J.Phys. **G28** (2002) 2693–2704.

[126] Cowan, G. et al, *Asymptotic formulae for likelihood-based tests of new physics*, Eur. Phys. J. **C71** (2011) 1554, `arXiv:1007.1727 [physics.data-an]`.

[127] G. Cowan, *Statistics for Searches at the LHC*, Tech. Rep. arXiv:1307.2487, Jul, 2013. `http://cds.cern.ch/record/1561011`. Comments: Lectures presented at the 69th Scottish Universities Summer School in Physics, St. Andrews, August-September 2012.

[128] ATLAS Collaboration, *Evidence for the spin-0 nature of the Higgs boson using ATLAS data*, Phys. Lett. B **726** no. arXiv:1307.1432. CERN-PH-EP-2013-102, (2013) 120–144. 15 p.

[129] S. S. Wilks, *The Large-Sample Distribution of the Likelihood Ratio for Testing Composite Hypotheses*, Ann. Math. Statist. **9** no. 1, (1938) 60–62. http://dx.doi.org/10.1214/aoms/1177732360.

[130] A. Wald, *Tests of Statistical Hypotheses Concerning Several Parameters When the Number of Observations is Large*, Transactions of the American Mathematical Society **54** no. 3, (1943) pp. 426–482. http://www.jstor.org/stable/1990256.

[131] S. van der Meer, *Calibration of the effective beam height in the ISR*, Tech. Rep. CERN-ISR-PO-68-31. ISR-PO-68-31, CERN, Geneva, 1968. https://cds.cern.ch/record/296752.

[132] C. Rubbia, *Measurement of the luminosity of $p\overline{p}$ collider with a (generalized) Van der Meer Method*, Tech. Rep. CERN-p$\overline{p}$-Note-38, CERN, Geneva, Nov, 1977. https://cds.cern.ch/record/1025746.

[133] T. Luminosity Group, *Preliminary Luminosity Determination in pp Collisions at sqrt(s) = 8 TeV using the ATLAS Detector in 2012*, Tech. Rep. ATL-COM-LUM-2012-013, CERN, Geneva, Nov, 2012.

[134] *Photon Identification Efficiencies with 8 TeV data*,.

[135] ATLAS Collaboration, "Search for Diphoton Events with Large Missing Transverse Momentum in 5 fb^1 of 7 TeV Proton-Proton Collision Data with the ATLAS Detector." Atl-com-phys-2012-770, 2012. https://cdsweb.cern.ch/record/1454143.

[136] ATLAS Collaboration, "Search for Diphoton Events with Large Missing Transverse Momentum in 5 fb^1 of 7 TeV Proton-Proton Collision Data with the ATLAS Detector." Atl-com-phys-2012-463, 2012. https://cdsweb.cern.ch/record/1444875.

[137] *Guidelines for Calculating the $E_{\mathrm{T}}^{\mathrm{miss}}$ Systematic Uncertainties when Analysing 8 TeV Data*,.

[138] *Photon + $E_{\mathrm{T}}^{\mathrm{miss}}$ Background Estimation*,.

[139]

[140] T. Hryn'ova and K. Nagano, *Trigger Menu Strategy for Run 2*, Tech. Rep. ATL-COM-DAQ-2014-054, CERN, Geneva, May, 2014.

[141] Carminati, L. et al, *Reconstruction and Identification Efficiency of Inclusive Isolated Photons*, Tech. Rep. ATL-PHYS-INT-2011-014, CERN, Geneva, Mar, 2011.

[142] *Official recommendations for analyses using jets in 7 TeV data and simulation*,.

[143] ATLAS Collaboration, *Jet energy scale and its systematic uncertainty for jets produced in proton-proton collisions at sqrt(s) = 7 TeV and measured with the ATLAS detector*, Tech. Rep. ATLAS-CONF-2010-056, CERN, Geneva, Jul, 2010.

[144] ATLAS Collaboration, *Data-Quality Requirements and Event Cleaning for Jets and Missing Transverse Energy Reconstruction with the ATLAS Detector in Proton-Proton Collisions at a Center-of-Mass Energy of sqrts = 7 TeV*, Tech. Rep. ATLAS-CONF-2010-038, CERN, Geneva, Jul, 2010.

[145] *Guidelines for applying corrections to the calorimeter isolation cones*,.

[146] *Official recommendations for analyses using jets in 8 TeV data and simulation*,.

[147] ATLAS Collaboration, *ATLAS Calorimeter Response to Single Isolated Hadrons and Estimation of the Calorimeter Jet Scale Uncertainty*, Tech. Rep. ATLAS-CONF-2011-028, CERN, Geneva, Mar, 2011. `https://cds.cern.ch/record/1337075`.

[148] M. Schott et al., "Supporting Document: Total inclusive W and Z boson cross-section measurements, cross-section ratios and combinations in the electron and muon decay channels at 7TeV based on $300nb^{-1}$." ATL-PHYS-INT-2010-125, 2010.